Weight Bearing Cone Beam Computed Tomography (WBCT) in the Foot and Ankle

A Scientific, Technical and Clinical Guide

Martinus Richter
Francois Lintz
Cesar de Cesar Netto
Alexej Barg
Arne Burssens
Scott Ellis

International WBCT Society

Springer

Weight Bearing Cone Beam Computed Tomography (WBCT) in the Foot and Ankle

Martinus Richter • Francois Lintz
Cesar de Cesar Netto • Alexej Barg
Arne Burssens • Scott Ellis

Weight Bearing Cone Beam Computed Tomography (WBCT) in the Foot and Ankle

A Scientific, Technical and Clinical Guide

Springer

Martinus Richter
Department for Foot and Ankle Surgery
Hospital Rummelsberg
Schwarzenbruck
Germany

Francois Lintz
Foot and Ankle Surgery Centre
Clinique de l'Union
Toulouse
France

Cesar de Cesar Netto
Department of Orthopedics and Rehab
University of Iowa
Iowa City, IA
USA

Alexej Barg
University Orthopedic Center
University of Utah
Salt Lake City, UT
USA

Arne Burssens
Department of Orthopedics and Trauma
University Hospital of Ghent
Ghent, OVL
Belgium

Scott Ellis
Department of Orthopedic Surgery
Hospital for Special Surgery
New York, NY
USA

ISBN 978-3-030-31948-9 ISBN 978-3-030-31949-6 (eBook)
https://doi.org/10.1007/978-3-030-31949-6

This Springer imprint is published by the registered company Springer Nature Switzerland AG
The registered company address is: Gewerbestrasse 11, 6330 Cham, Switzerland

Preface

Weight bearing cone beam computed tomography (WBCT) was introduced in 2012 for foot and ankle use as a new technology that allows 3D-imaging with full weight bearing that should be not influenced by projection and/or foot orientation. From the very beginning of device availability, scientific studies have been employed. In the early stages of the scientific work-up in different institutions, different methodologies, especially for the angle measurements, were inaugurated. No standard for the methodology for the image acquisition and measurement was defined, and different methods have been published. After ongoing discussion about the optimal approach for further research in this field, the International WBCT Study Group (WBCT ISG, www.wbctstudygroup.com) was founded by five investigators from five different institutions, who are the editors of this book. In the following two years, the group grew in membership from 5 at the beginning in July 2017 to more than 50 at the end of 2018. The scientific activities were extraordinary, resulting in 70 PubMed listed publications dealing with WBCT in foot and ankle at the end of 2018. During the same period, WBCT ISG organized scientific meetings at different foot and ankle conferences to spread the acquired knowledge among foot and ankle surgeons. Based on the fast-growing WBCT ISG and reflecting the increasing importance of WBCT, the founders of WBCT ISG decided to found the International WBCT Society (www.wbctsociety.org) and to transfer WBCT ISG into the International WBCT Society. The society was registered in Belgium and a secretariat was founded. Since then, the society is further growing and the member number as well as the number of Pubmed-listed publications by members both reached more than 100 by the end of 2019. The International WBCT Society can be considered as one of the most scientifically active societies. Meanwhile, the society also inaugurated educational activities as for example hands-on workshops. At the beginning of 2019, the board of the society discussed how to further spread the knowledge of WBCT in foot and ankle besides the scientific publications in all relevant scientific foot and ankle journals and scientific sessions at the most important foot and ankle conferences. The board then decided to write this book, which should be focused on scientific, technical, clinical, and educational content. In contrast to standard textbooks, the scientific content is emphasized and placed at the beginning to reflect the initial scientific approach of WBCT ISG and International WBCT Society.

The authors wish that this book serves all current and upcoming users of WBCT in foot and ankle to answer all scientific and technical questions, to educate and instruct the clinical use including measurements.

Schwarzenbruck, Germany — Martinus Richter, MD, PhD
Toulouse, France — Francois Lintz, MD, FEBOT
Iowa City, IA, USA — Cesar de Cesar de Netto, MD, PhD
Salt Lake City, UT, USA — Alexej Barg, MD
Ghent, OVL, Belgium — Arne Burssens, MD
New York, NY, USA — Scott Ellis, MD

The original version of this book was revised. The correction to this chapter can be found at https://doi.org/10.1007/978-3-030-31949-6_24

Contents

Part I History and Scientific Overview of Weight Bearing Cone Beam Computed Tomography

1 Background of Weight Bearing Cone Beam Computed Tomography 3
Introduction 3
Weight Bearing CT International Study Group (WBCT ISG) 6
International WBCT Society 7
References 8

2 Scientific Overview of Weight Bearing Cone Beam Computed Tomography 9
General Thoughts on Foot and Ankle Imaging 9
Studies on Normal Controls 10
Studies on Pathologic Conditions 13
Radiographic Measurements Using Weight Bearing CT 19
Future Directions 21
Standardization of Measurements Using WBCT 21
WBCT vs. Plain Films 21
Conclusions 23
References 23

Part II Scientific Background of Weight Bearing Cone Beam Computed Tomography

3 Weight Bearing CT Allows for More Accurate Bone Position (Angle) Measurement than Radiographs or CT 27
Introduction 27
Methods 27
Inclusion and Exclusion Criteria: Ethics 29
Image Acquisition 29
Time Spent 29

Angle Measurements 30
Statistics 31
Results 31
Time Spent 31
Angle Measurement: Differences Between Methods 32
Angle Measurement: Intra- and Interobserver Reliability 32
Discussion 33
Time Spent 33
Angle Measurement: Differences between Methods 33
1st–2nd Intermetatarsal Angle 34
TMT Dorsoplantar 34
TMT Lateral 34
Hindfoot Angle 35
Calcaneal Pitch Angle 35
Angle Measurement: Intra- and Interobserver Reliability 35
Shortcomings of the Study 35
Radiation Dose 36
Cost 37
Approval for Use 37
Standard Imaging? 38
References 39

4 Combination of Weight Bearing CT (WBCT) with Pedography Shows No Statistical Correlation of Bone Position with Force/Pressure Distribution 41
Introduction 41
Methods 43
Inclusion and Exclusion Criteria: Ethics 43
Image Acquisition 44
Pedography 44
Measurements of Bone Position (Angles and Distances) 44
Measurement of Pedographic Parameters 46
Correlation Analysis of WBCT Parameters with Pedography Parameters 47
Statistics 48
Results 48
Measurements of Bone Position (Angles and Distances): Intra- and Interobserver Reliability 48
Correlation of WBCT Parameters with Pedography Parameters 48
Discussion 50
Angle Measurement: Intra- and Interobserver Reliability 50
Correlation of WBCT Parameters with Pedography Parameters 51
Shortcomings of the Study 51
Radiation Dose 52
References 52

5 Combination of Weight Bearing CT (WBCT) with Pedography Shows Relationship Between Anatomy-Based Foot Center (FC) and Force/Pressure-Based Center of Gravity (COG) 55
Introduction 55
Methods 56
Inclusion and Exclusion Criteria, Ethics 56
Image Acquisition: Foot Center (FC) 57
Pedography: Center of Gravity (COG) 57
Comparison of FC/COG 57
Statistics 59
Results 59
Discussion 62
Center of Gravity (COG) 62
Foot Center (FC) 62
Shortcomings of the Study 64
Radiation Dose 65
References 65

6 A New Concept of 3D Biometrics for Hindfoot Alignment Using Weight Bearing CT 67
Introduction 67
Methods 68
Statistical Analysis 70
Results 70
Discussion 70
References 73

7 3D Biometrics for Hindfoot Alignment Using Weight Bearing Computed Tomography: A Prospective Assessment of 249 Feet . . . 77
Introduction 77
Materials and Methods 78
Study Population and Design 78
Patient Assessment 78
Statistical Analysis 81
Results 81
Discussion 81
References 85

8 Relationship Between Chronic Lateral Ankle Instability and Hindfoot Varus Using Weight Bearing Cone Beam Computed Tomography: A Retrospective Study 87
Introduction 87
Material and Methods 88
Study Design 88
Study Population 88

Investigations and Measurements . . . 89
Statistical Analysis . . . 90
Results . . . 90
Discussion . . . 91
References . . . 95

9 Normal Hindfoot Alignment Assessed by Weight Bearing CT: Presence of a Constitutional Valgus? . . . 97
Introduction . . . 97
Materials and Methods . . . 98
Study Population and Design . . . 98
Patient Characteristics . . . 98
Statistical Analysis . . . 101
Results . . . 101
Hindfoot Alignment . . . 101
ROI Density Analysis . . . 103
Hindfoot Characteristics . . . 103
Discussion . . . 103
References . . . 104

10 Reliability and Correlation Analysis of Computed Methods to Convert Conventional 2D Radiological Hindfoot Measurements to 3D Equivalents Using Weight Bearing CT . . . 107
Introduction . . . 107
Materials and Methods . . . 108
Study Population, Design, and Measurement Protocol . . . 108
Statistical Analysis . . . 113
Results . . . 114
Hindfoot Alignment . . . 114
Ankle and Hindfoot Characteristics . . . 114
Discussion . . . 116
References . . . 118

11 The Hind- and Midfoot Alignment Analyzed After a Medializing Calcaneal Osteotomy Using a 3D Weight Bearing CT . . . 121
Introduction . . . 121
Material and Methods . . . 122
Study Population, Design, and Measurement Protocol . . . 122
Surgical Procedure . . . 127
Statistical Analysis . . . 127
Results . . . 128
Hindfoot Alignment . . . 128
Midfoot Alignment . . . 128
Discussion . . . 130
References . . . 132

12 Is Load Application Necessary when Using Computed Tomography Scans to Diagnose Syndesmotic Injuries? A Cadaver Study 135
Introduction 135
Methods 136
Data Source 136
Experimental Setting 139
Imaging and Measurements 140
Statistical Analysis 140
Results 142
Discussion 143
References 148

13 Use of Weight Bearing Computed Tomography in Subtalar Joint Instability: A Cadaver Study 151
Introduction 151
Methods 152
Data Source and Specimens 152
Experimental Setting 153
Imaging and Measurements 155
Statistical Analysis 156
Results 157
Digitally Reconstructed Radiographs 157
Computed Tomography Scans 158
Discussion 161
References 164

14 Is Torque Application Necessary When Using Computed Tomography Scans to Diagnose Syndesmotic Injuries? A Cadaver Study 167
Introduction 167
Methods 168
Data Source 168
Experiments 168
Imaging and Measurements 169
Statistical Analysis 171
Results 172
Digitally Reconstructed Radiographs 172
Weight Bearing CT Scans 175
Discussion 175
References 178

15 Flexible Adult-Acquired Flatfoot Deformity: Comparison Between Weight Bearing and Non-weight Bearing Measurements Using Cone Beam Computed Tomography 181
Introduction 181

Materials and Methods 182
Study Design 182
Subjects 182
CBCT Imaging Technique 182
Measurements 183
Axial Plane Measurements 184
Coronal Plane Measurements 184
Sagittal Plane Measurements 186
Statistical Analysis 187
Source of Funding 187
Results 187
Discussion 191
References 196

16 Hindfoot Alignment of Adult-Acquired Flatfoot Deformity: A Comparison of Clinical Assessment and Weight Bearing Cone Beam CT Examinations 199
Introduction 199
Materials and Methods 200
Study Design 200
Subjects 201
CBCT Imaging Technique 201
WB CBCT Measurements 202
Statistical Analysis 203
Results 203
Discussion 206
References 209

17 Influence of Investigator Experience on Reliability of Adult-Acquired Flatfoot Deformity Measurements Using Weight Bearing Computed Tomography 213
Introduction 213
Material and Methods 214
Study Design 214
Subjects 214
WBCT Imaging Technique 214
Measurements 215
Axial Plane Measurements 215
Coronal Plane Measurements 215
Sagittal Plane Measurements 217
Statistical Analysis 217
Results 218
Intraobserver Reliability 218

Interobserver Reliability 218
Measurement Differences 218
Discussion 223
References 225

18 Results of More Than 11,000 Scans with Weight Bearing CT: Impact on Costs, Radiation Exposure, and Procedure Time 229
Introduction 229
Methods 229
Study Design 229
Control Group 230
Data Acquisition 230
Imaging Time (T) 230
Radiation Dose (RD) 230
Cost-Effectiveness 230
Data Analysis/Control Group 231
Statistics 231
Results 231
Discussion 232
Shortcomings of the Study 234
References 235

Part III Technical Guide to Weight Bearing Cone Beam Computed Tomography

19 Technology of Weight Bearing Cone Beam Computed Tomography 241
Introduction 241
How It Works 243
A 3D Environment 244
DRRs: Digitally Reconstructed Radiographs 245
Biases of Conventional Radiography 246
References 247

20 Weight Bearing Computed Tomography Devices 249
Beginning of Weight Bearing Computed Tomography Devices 249
Foot and Ankle Weight Bearing Computed Tomography Devices 249
Knee Weight Bearing Computed Tomography Devices 251
The Future of Weight Bearing Computed Tomography Devices 251
References 253

21 Measurements in Weight Bearing Computed Tomography 255
Adult-Acquired Flatfoot Measurements 255
Hindfoot Alignment Measurements 256

Subtalar Joint Alignment Measurements 257
Distal Tibiofibular Syndesmotic Measurements 258
Hallux Valgus Measurements 259
References 260

22 Clinical Examples of Weight Bearing Computed Tomography 265

23 Future Developments in Weight Bearing Computed Tomography 305
References 306

Correction to: Weight Bearing Cone Beam Computed Tomography (WBCT) in the Foot and Ankle C1

Index 307

Part I
History and Scientific Overview of Weight Bearing Cone Beam Computed Tomography

Chapter 1
Background of Weight Bearing Cone Beam Computed Tomography

Martinus Richter

Introduction

The standard for diagnostic radiographic imaging in foot and ankle surgery until 2012 was radiographs with full weight bearing without any useful alternative [1–3]. The three-dimensional position of bones and relationships between bones in the foot (e.g., angles) are difficult to assess with standard radiographs due to superimposition of the different bones [2, 4]. The reason is the "reduction" of a three-dimensional body (foot) to a two-dimensional image (conventional radiograph). Angle measurements with conventional radiographs could be inaccurate due to inaccuracies of the projection (orientation of (central) beam) and/or foot orientation (Fig. 1.1) [2, 5–7]. 3D imaging with conventional computed tomography (CT) allows for exact analysis within the 3D data that is not influenced by projection and/or foot orientation but lacks weight bearing (Fig. 1.2) [2, 4, 8]. Weight bearing cone beam computed tomography (WBCT) was introduced in 2012 for foot and ankle use as a new technology that allows 3D imaging with full weight bearing which should be not influenced by projection and/or foot orientation [2]. The cone beam technology as such (Chap. 19) is similar to previous applications, for example, intraoperative 3D imaging (Fig. 1.3) or maxillofacial 3D imaging (Fig. 1.4) [9, 10]. Different devices from different companies became available (Chap. 20). Several measurement possibilities had been provided with different software solutions (Chap. 21). Many clinical application possibilities have been shown (Chap. 22). From the very beginning of the device availability, scientific studies have been employed. Most of the studies investigated the accuracy of the bone position assessment, i.e., different measurement of angles between bones and position of bones (Chaps. 2, 3, 4, 5, 6, 7, 8, 9, 10, 11, 12, 13, 14, 15, 16, 17, and 18). Shortly after, additional measurements, for example, pedography, were added (Chaps. 19, 20, 21, 22, and 23).

M. Richter et al., *Weight Bearing Cone Beam Computed Tomography (WBCT) in the Foot and Ankle*, https://doi.org/10.1007/978-3-030-31949-6_1

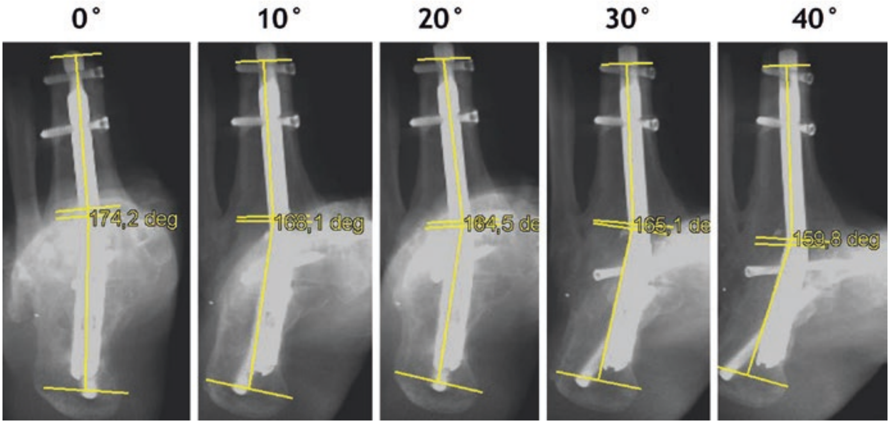

Fig. 1.1 Conventional radiographs for measurement of hindfoot alignment in a patient with healed tibio-talo-calcaneal arthrodesis with retrograde nail. The healed arthrodesis ensures uniform hindfoot position during repetitive radiographic assessment. Radiographs with different internal rotations (0–40°) of the foot in relation to the central beam were obtained, and the hindfoot angle is measured. The measured hindfoot angles ranged from 5.8° to 21.2°. The different angles are not influenced by the "real" hindfoot angle (healed arthrodesis plus nail) but only be different orientation (internal rotation) of the foot and ankle during radiographic assessment

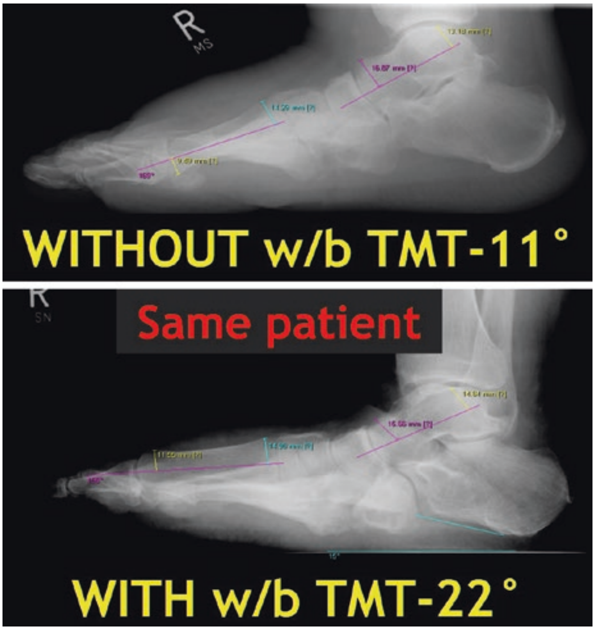

Fig. 1.2 Lateral radiographs of the right foot from a patient with Charcot arthropathy without weight bearing (top) and with weight bearing (bottom). The lateral talo-first metatarsal angle (TMT) was measured. This was −11° without and −22° with weight bearing showing the influence of weight bearing on the relationship of the bones (angles)

Fig. 1.3 Cone beam technology application for intraoperative 3D imaging (ISO-C-3D, Siemens, Erlangen, Germany). (**a**) shows the device in the operating theater and (**b**) a monitor with a few examples. The monitor shows intraoperative imaging after open reduction and internal fixation of a calcaneal fracture. 3D reformations are shown (parasagittal, top left; coronal, top right; axial, bottom)

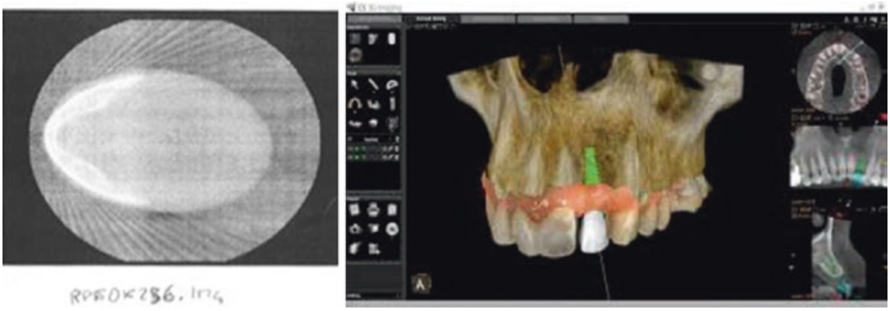

Fig. 1.4 Evolution of cone beam CT

Weight Bearing CT International Study Group (WBCT ISG)

In the early stage of the scientific workup in different institutions, different methodologies especially for the angle measurements were inaugurated. No standard for the methodology for the image acquisition and measurement was defined, and different methods have been published (Chaps. 2, 3, 4, 5, 6, 7, 8, 9, 10, 11, 12, 13, 14, 15, 16, 17, and 18). After ongoing discussion about the optimal approach for further research in this field, the International WBCT Study Group (WBCT ISG, www.wbctstudygroup.com) was founded by five investigators from five different institutions who are the editors of this book. The tasks of this group were defined as follows:

- To promote and improve research using 3D radiographic imaging with WBCT
- To standardize the methodology regarding measurement methods
- To serve as a platform of communication for foot and ankle surgeons and to inform of educational events
- To offer guidelines and reviews regarding the indications and use of WBCT at an international level

The WBCT ISG was planned to comprise active and passive members from relevant international surgical and radiology foot and ankle societies. Research projects were planned to be conducted and published together. This group was completely independent from the industry but cooperates with the different manufacturers of different WBCT devices (Chap. 20). In the following 2 years, the group was growing regarding membership from 5 at the beginning in July 2017 to more than 50 at the end of 2018. In addition to active and standard members that were limited to foot and ankle surgeons (orthopedic and podiatric), representatives from radiology specialty and so-called academic affiliates were included. Academic affiliates represent researchers that are not foot and ankle surgeons. The scientific activities were extraordinary, resulting in 70 PubMed listed publications dealing with

WBCT in foot and ankle at the end of 2018. During the same period, WBCT ISG organized scientific meetings at different foot and ankle conferences to spread the acquired knowledge among foot and ankle surgeons. A cooperation with the international foot and ankle societies was started, and representatives from the societies were invited to the board (Asian Federation of Foot & Ankle Surgeons (AFFAS, www.naraseikei.com/affas); European Foot and Ankle Society (EFAS, www.efas.co); Latin American Federation of Medicine and Surgery of the Foot and Leg (FLAMECIPP, www.flamecipp.org); North American Federation of Foot & Ankle Societies (NAFFAS, www.aofas.org)).

International WBCT Society

Based on the fast-growing WBCT ISG and reflecting the increasing importance of WBCT, the founders of the WBCT ISG decided to found the International WBCT Society (www.wbctsociety.org) and to transfer WBCT ISG into the International WBCT Society. The membership types were uniformed to "member" without differentiation between active and standard members and academic affiliates. The society was registered in Belgium, and a secretariat was founded. The founding board of the society discussed how to further spread the knowledge of WBCT in foot and ankle besides the scientific publications in all relevant scientific foot and ankle journals (*Foot and Ankle International*, *Foot and Ankle Surgery*, *Journal of Foot and Ankle Surgery*, *Techniques in Foot and Ankle Surgery*, *Fuss und Sprunggelenk*) and scientific sessions at the most important foot and ankle conferences (EFAS, FLAMECIPP, AFFAS, IFFAS (International Federation of Foot and Ankle Societies (www.iffas.org), AOFAS (American Orthopaedic Foot and Ankle Society; www.aofas.org), DAF (German Orthopaedic Foot and Ankle Society (www.daf-online.de)) and also general orthopaedic conferences (AAOS (American Academy of Orthopaedic Surgeons; www.aaos.org); EFORT (European Federation of Orthopaedics and Traumatology, www.efort.org); DKOU (German Society for Orthopaedic and Trauma Surgery; www.dkou.org)). Meanwhile, the society was further growing and the member number as well as the number of Pubmed-listed publications by members both reached more than 100 by the end of 2019. By then, the International WBCT Society could be considered as one of the most scientifically active societies. The society also inaugurated educational activities as for example hands-on workshops. At the beginning of 2019, the board decided to write a book which should be focused on scientific, technical, clinical, and educational content. In contrast to standard textbooks, the scientific content should be emphasized and placed at the beginning to reflect the initial scientific approach of WBCT ISG and International WBCT Society. Chapter 2 gives a scientific overview, and Chaps. 3, 4, 5, 6, 7, 8, 9, 10, 11, 12, 13, 14, 15, 16, 17, and 18 comprise 16 scientific landmark studies. On this scientific basis, the technical guide (Chaps. 19, 20, 21, 22, and 23) gives technical background (Chap. 19), introduces the different devices (Chap. 20), and gives insight in the actual measurement possibilities including the initial software solutions for automatic measurements (e.g., angles between bones, Chap. 21). Chapter 22 shows typical clinical examples. Finally, Chap. 23 gives an outlook to future developments such as dynamic scans and measurements or hologram-like visualization. The authors wish that this book serves all current and upcoming users of WBCT in foot and ankle to answer all scientific and technical questions, to educate and instruct the clinical use including measurements.

References

1. Rammelt S, Amlang M, Zwipp H. Standardröntgendiagnostik an Fuß und Sprunggelenk. Fuss Sprungg. 2010;8(2):80–91.
2. Richter M, Seidl B, Zech S, Hahn S. PedCAT for 3D-imaging in standing position allows for more accurate bone position (angle) measurement than radiographs or CT. Foot Ankle Surg. 2014;20:201–7.
3. Richter MZS, Hahn S. PedCAT for radiographic 3D-imaging in standing position. Fuss Sprungg. 2015;13:85–102.
4. Ferri M, Scharfenberger AV, Goplen G, Daniels TR, Pearce D. Weightbearing CT scan of severe flexible pes planus deformities. Foot Ankle Int. 2008;29(2):199–204.
5. Johnson JE, Lamdan R, Granberry WF, Harris GF, Carrera GF. Hindfoot coronal alignment: a modified radiographic method. Foot Ankle Int. 1999;20(12):818–25.
6. Richter M. Computer aided surgery in foot and ankle: applications and perspectives. Int Orthop. 2013;37(9):1737–45.
7. Richter M. Computer based systems in foot and ankle surgery at the beginning of the 21st century. Fuss Sprungg. 2006;4(1):59–71.
8. Kido M, Ikoma K, Imai K, Maki M, Takatori R, Tokunaga D, Inoue N, Kubo T. Load response of the tarsal bones in patients with flatfoot deformity: in vivo 3D study. Foot Ankle Int. 2011;32(11):1017–22.
9. Richter M, Geerling J, Zech S, Goesling T, Krettek C. Intraoperative three-dimensional imaging with a motorized mobile C-arm (SIREMOBIL ISO-C-3D) in foot and ankle trauma care: a preliminary report. J Orthop Trauma. 2005;19(4):259–66.
10. Mozzo P, Procacci C, Tacconi A, Martini PT, Andreis IA. A new volumetric CT machine for dental imaging based on the cone-beam technique: preliminary results. Eur Radiol. 1998;8(9):1558–64.

Chapter 2
Scientific Overview of Weight Bearing Cone Beam Computed Tomography

Alexej Barg

General Thoughts on Foot and Ankle Imaging

Imaging remains highly valuable in diagnosing, treating, and assessing outcomes in patients with disorders of the foot and ankle [1]. Available modalities include conventional radiographs, fluoroscopy, computed tomography (CT), scintigraphy, single-photon emission computed tomography-CT (SPECT-CT), magnetic resonance imaging (MRI), and ultrasonography. Most diagnostic imaging workups start with conventional weight-bearing radiographs because pathologies such as subtle arch collapse and loss of cartilage are more reliably identified with weight-bearing. Further imaging may be required for better assessment of the underlying pathology as well as to guide treatment planning. The choice of the best imaging modality is usually based on several factors that include (1) reliability with regard to the diagnosis under consideration; (2) local availability; (3) patient concerns, such as cost, convenience, and discomfort; (4) safety risks including radiation dose (Table 2.1) and contrast sensitivity; and (5) cost [2].

CT technology is commonly used to evaluate skeletal pathology. Modern multidetector CT technology provides high-resolution thin-slice images that can be obtained in any plane providing excellent visualization of fractures, degenerative changes, osseous union at a site of arthrodesis, internal fixation of fractures, or osteotomies [2]. One major limitation of conventional CT has been the inability to obtain weight-bearing images. Without weight-bearing during CT assessment, true alignment may not be fully appreciated. Pathology such as impingement, joint space narrowing, and malalignment that may be apparent only with load may also go undiagnosed [3].

Based on Barg A, Bailey T, Richter M, de Cesar Netto C, Lintz F, Burssens A, Phisitkul P, Hanrahan CJ, Saltzman CL. Weight-bearing Computed Tomography of the Foot and Ankle. *Foot Ankle Int* 2018; 39(3): 376–86.

M. Richter et al., *Weight Bearing Cone Beam Computed Tomography (WBCT) in the Foot and Ankle*, https://doi.org/10.1007/978-3-030-31949-6_2

Table 2.1 Typical effective radiation dose [2]

Average US background radiation/yr	3.0 mSv
Single trans-Atlantic flight	0.04 mSv
Radiograph: chest (p.a.)	0.02 mSv
Radiograph: foot (single exposure)	0.001 mSv
Conventional computed tomography: pelvis	15 mSv
Conventional computed tomography: ankle	0.07 mSv
Weight-bearing cone beam computed tomography: foot/ankle	0.01–0.03 mSv
Isotope (tc-99 m-MDP) bone scan	6.3 mSv

MDP methylene diphosphonate, *mSV* millisievert, *p.a.* posteroanterior

The idea of visualizing the relative alignment of the bones of the foot and ankle with a weight-bearing CT (WBCT) imaging is not new. Several investigators have developed methods to simulate weight-bearing using custom-made loading frames to assess foot and ankle pathologies (Table 2.2). The limitations of simulated weight-bearing conditions have been well articulated by these authors. First, only partial weight bearing can be applied so the observed deformities or pathologies are potentially underestimated as compared to normal standing [3–8]. Second, the loading devices are generally passive, applying external loads without the muscle forces active when standing [9–11].

In the last decade, cone beam CT technology has helped with both supine and standing weight-bearing imaging of the lower extremity due to improved designs with flexible gantry movements [19, 20]. This imaging technology has several advantages, including the ability to obtain images with the patient standing, high contrast resolution and spatial resolution, fast image acquisition time, decreased radiation, a relatively small scanner size with portable design, and generally less capitalization cost than conventional CT scan technology [19, 20].

Studies on Normal Controls

Colin et al. [21] performed WBCT in 59 patients without any history of hindfoot or ankle pathology to describe the subtalar joint configuration. The shape of the posterior facet and the subtalar vertical angle was measured in three different coronal planes (center of the subtalar joint, 5 mm anterior, and 5 mm posterior to the center). In this patient cohort, the posterior facet was concave in 88% of feet and flat in the remaining 12%. In the middle coronal plane, the posterior facet was oriented in valgus in 90% and in varus in 10% of cases. However, substantial intraindividual differences in the subjects were observed with the subtalar vertical angle increasing in valgus when the measurement was performed more posteriorly [6].

Table 2.2 Literature review addressing the use of simulated weight-bearing computed tomography in patients with foot and ankle disorders [1]

Study	Patients	Study objectives	Methods	Findings
Ananthakrisnan et al. [3]	4 healthy controls 8 patients with flatfoot deformity and rupture of PTT	3D position of the talocalcaneal joint in patients with flatfoot deformity	75 N axial force with a custom loading frame in supine position	Patients with PTTD had decreased contact surface in talocalcaneal joint
Apostle et al. [4]	20 healthy controls 20 patients with peritalar subluxation	Morphology of the subtalar joint axis	75 N axial force with a custom loading frame in supine position	Subtalar joint axis orientation was more valgus in patients with peritalar subluxation
Ferri et al. [5]	8 healthy controls 15 patients with symptomatic flatfoot deformity	Forefoot and hindfoot alignment	Special loading device with load of 50% of body weight	Forefoot arch angle 29% lower in flatfeet during non-weight-bearing and 52% lower during weight-bearing
Geng et al. [12]	10 healthy controls 10 patients with HV deformity	Mobility of the 1st TMT joint	Special frame with full weight-bearing in supine position	1st TMT joint more dorsiflexed and more supinated in HV
Greisberg et al. [6]	37 patients with flatfoot deformity	Assessment of deformity and degenerative changes	75 N axial force with a custom loading frame in supine position	Mean TN angle −1° (10° to −34°) Mean naviculocuneiform angle −15° (−1° to −30°) Average TMT subluxation 9% (0–20%)
Katsui et al. [13]	142 patients with HV deformity (269 feet)	Alignment of the tibial sesamoid	Special frame with one third of patient's weight loading	Sesamoid position: grade 1 (tibial sesamoid medial to axis of 1st metatarsal) 34 feet, grade 2 (tibial sesamoid below the axis of 1st metatarsal) 116 feet, grade 3 (tibial sesamoid lateral to axis of 1st metatarsal) 119 feet
Kido et al. [10]	21 healthy controls 21 patients with flatfoot deformity	Bone rotation of hindfoot joints	A custom foot loading device with 99.4 ± 11.6% of the body weight	Patients with flatfoot deformity: talus 1.7° more plantarflexed, navicular 2.3° more everted, calcaneus 1.1° more dorsiflexed and 1.7° more everted

(continued)

Table 2.2 (continued)

Study	Patients	Study objectives	Methods	Findings
Kido et al. [11]	20 healthy controls 24 patients with flatfoot deformity	Bone rotation of each joint in the medial longitudinal arch	Special frame with full weight-bearing in supine position	Patients with flatfoot deformity: 1st metatarsal more dorsiflexed, navicular and calcaneus more everted, and TN joint more rotated
Kim et al. [14]	138 patients (166 feet) with HV deformity 19 healthy controls (19 feet)	1st metatarsal pronation and sesamoid position	Special frame with half of full weight-bearing in supine position	Significant difference in α angle with 21.9° (HV group) vs. 13.8° (control group)
Kimura et al. [15]	10 patients with HV deformity 10 healthy controls	3D mobility of the first ray	Special frame with full weight-bearing in supine position	Patients with HV deformity: TN and 1st TMT joints more dorsiflexed
Ledoux et al. [7]	10 healthy controls 10 patients with pes cavus deformity 10 patients with asymptomatic pes planus deformity 10 patients with symptomatic pes planus deformity	Differences in bone-to-bone relationships between different foot types	Special frame with 20% of weight-bearing in supine position	Significant differences were found in all measurements regarding midfoot and hindfoot alignment
Malicky et al. [8]	5 healthy controls 19 patients with symptomatic flatfoot deformity with lateral pain	Osseous relationships in patients with flatfoot deformity and to evaluate subfibular impingement	75 N axial force with a custom loading frame in supine position	Prevalence of sinus tarsi impingement 92% vs. 0% in controls Prevalence of calcaneofibular impingement 66% vs. 5% in controls
Van Bergeyk et al. [16]	12 healthy controls 11 patients with chronic lateral instability	Radiographic differences with respect to hindfoot varus/valgus between patients with chronic lateral instability and controls	Special frame with full weight-bearing in supine position	Hindfoot alignment angle was different in both groups: 6.4° ± 4° varus (patients with instability) vs. 2.7° ± 5° varus (controls)

Table 2.2 (continued)

Study	Patients	Study objectives	Methods	Findings
Yoshioka et al. [17]	10 healthy controls 10 patients with stage II PTTD flatfoot deformity	Forefoot and hindfoot alignment	Special frame with full weight-bearing in supine position	Méary angle was significantly lower in flatfeet 1st metatarsal more everted in flatfeet Calcaneus was more everted and abducted in flatfeet
Zhang et al. [18]	15 healthy controls 15 patients with stage II PTTD flatfoot deformity	Rotation and translation of hindfoot joints	Special frame with full weight-bearing in supine position	Significant differences in position of talus, navicular, and calcaneus between both groups

3D three-dimensional, *HV* hallux valgus, *PTT* posterior tibial tendon, *PTTD* posterior tibial tendon dysfunction, *TMT* tarsometatarsal, *TN* talonavicular

Meanwhile, Lepojärvi et al. [22] used WBCT to investigate the normal anatomy and rotational dynamics of the distal tibiofibular joint under physiological conditions in a cross-sectional study including 32 asymptomatic subjects. Imaging acquisition was performed in three different positions of the ankle: neutral, internal, and external rotation. Measured parameters included sagittal translation of the fibula, anterior and posterior widths of the distal tibiofibular syndesmosis, tibiofibular clear space, and rotation of the fibula. In subjects with the ankle in a neutral position, the fibula was located anteriorly in the tibial incisura in 88% of all measurements. During ankle rotation, the mean anteroposterior motion was 1.5 mm, and the mean rotation of the fibula was 3° [22].

In another study, Lepojärvi et al. [23] performed WBCT in the same subject cohort to assess the rotational dynamics of the talus. The rotation of the talus, medial clear space, anterior and posterior widths of the tibiotalar joint, translation of the talus, and talar tilt were measured. When the ankle was rotated with a moment of 30 Nm, a talus rotation of 10° without substantial widening of the medial clear space was observed [23].

Studies on Pathologic Conditions

In total, eight studies were reviewed (Table 2.3). All were published between 2013 and 2017 with four prospective and four retrospective studies. All studies but one were single-center in design. For the included investigations, the level of evidence ranged from II to IV. There was one level II study, five level III studies, and two level IV studies.

Table 2.3 Description of eight studies included into systematic literature review [1]

Study	Study type	Data collection	Level of evidence	Conflict of interest	Subjects
Burssens et al. [9]	Multicenter	Retrospective	III	None	60 patients (30 valgus and 30 varus malalignment)
Cody et al. [24]	Single-center	Retrospective	III	None	45 patients with adult-acquired flatfoot deformity 17 healthy controls
Collan et al. [25]	Single-center	Prospective	II	None	10 patients with bilateral hallux valgus deformity 5 healthy controls
Hirschmann et al. [13]	Single-center	Prospective	IV	n.r.	22 patients with different hindfoot pathologies
Krähenbühl et al. [26]	Single-center	Retrospective	III	None	40 patients with subtalar osteoarthritis 20 healthy controls
Lintz et al. [27]	Multicenter	Retrospective	III	Yes[a]	135 patients: normal (57), varus (38), and valgus (40) alignment
Richter et al. [28]	Single-center	Prospective	IV	Yes[b]	30 patients with foot/ankle disorders
Richter et al. [29]	Single-center	Prospective	IV	Yes[b]	First study: 30 patients Second study: 50 patients

n.r. not reported
[a]The corresponding author received personal fees from CurveBeam during the conduct of the study
[b]The corresponding author is a consultant of Stryker, Intercus, and CurveBeam, proprietor of R-innovation, and joint proprietor of 1st Worldwide Orthopedics

Collan et al. [25] used CT in weight-bearing and non-weight-bearing conditions in ten patients with hallux valgus and five asymptomatic controls to assess the alignment of the first metatarsal bone. There were significant differences between weight-bearing and non-weight bearing measurements of the first metatarsal alignment in patients with hallux valgus deformity. For instance, the 3D hallux valgus angle was 35° ± 3° in the weight bearing vs. 46° ± 5° in the non-weight bearing conditions [25].

Hirschmann et al. [13] performed a prospective study comparing CT of the hindfoot in the supine non-weight-bearing position vs. the upright weight-bearing position. Hindfoot alignment was independently measured by two musculoskeletal radiologists in 22 patients with different indications for CT assessment including osteoarthritis of the hindfoot ($n = 8$), osteochondral defects of the talus ($n = 6$), evaluation of foot pain ($n = 5$), and others ($n = 3$). Significant differences were found for all measurements except the hindfoot alignment angle and tibiocalcaneal distance when comparing weight-bearing and non-weight-bearing images.

These included differences in fibulocalcaneal distance, lateral talocalcaneal joint space, talocalcaneal overlap, and naviculocalcaneal distance [13]. The hindfoot alignment angle was comparable when measured with and without weight bearing (21.0° ± 7.9° vs. 19.0° ± 9.0°) [13]. These findings suggest that radiographic assessment of impingement (e.g., using fibulocalcaneal distance) should be performed using weight bearing conditions.

Kim et al. [14] used semi-WBCT to assess the preoperative forefoot alignment in 138 patients (166 feet) with hallux valgus deformities and compared the results to a control group with 19 patients (19 feet). In all persons, the α angle (first metatarsal pronation angle) was measured to assess the forefoot alignment in coronal view. Furthermore, the sesamoid position was evaluated using a four-stage grading system. The α angle was significantly different between the hallux valgus and control groups (21.9° and 13.8°, respectively). Four different classification groups of hallux valgus deformity were developed based on the first metatarsal pronation and sesamoid subluxation, leading the authors to suggest that the use of semi-WBCT may be helpful to assess the forefoot deformity in the coronal plane and guide treatment choice.

Richter et al. [28, 29] recently published two studies examining WBCT. In the first study, 30 consecutive patients were prospectively enrolled to assess forefoot and hindfoot alignment using WBCT (Figs. 2.1 and 2.2), CT without weight-bearing, and conventional weight-bearing radiographs [28]. Significant differences were

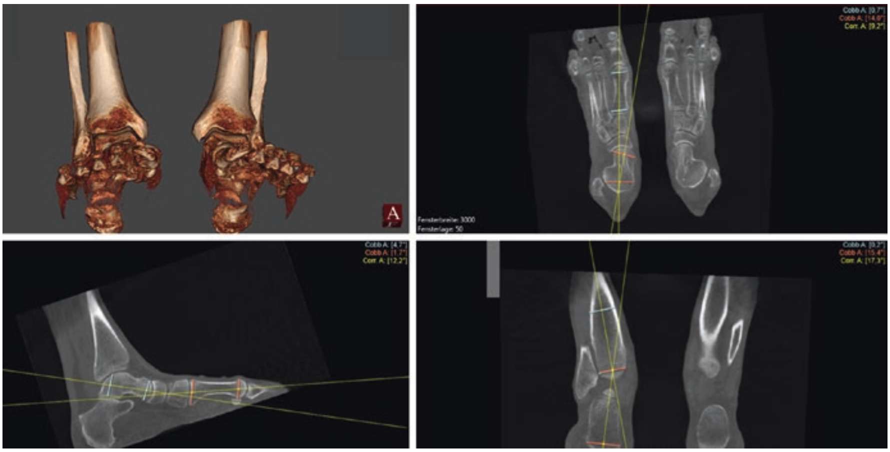

Fig. 2.1 PedCAT angle measurements. The 3D reformation (top left) demonstrates how the 3D dataset was virtually rotated to allow for exact congruency of the plane of the reformations with the bone axes as described before. Measurement of the dorsoplantar tarsometatarsal angle in horizontal plane (top right) and in sagittal plane (bottom left). Hindfoot alignment measurement (bottom right). The lines that define the centers of the bones proximally and distally are exactly 50% of the measured bone thickness distance [1]

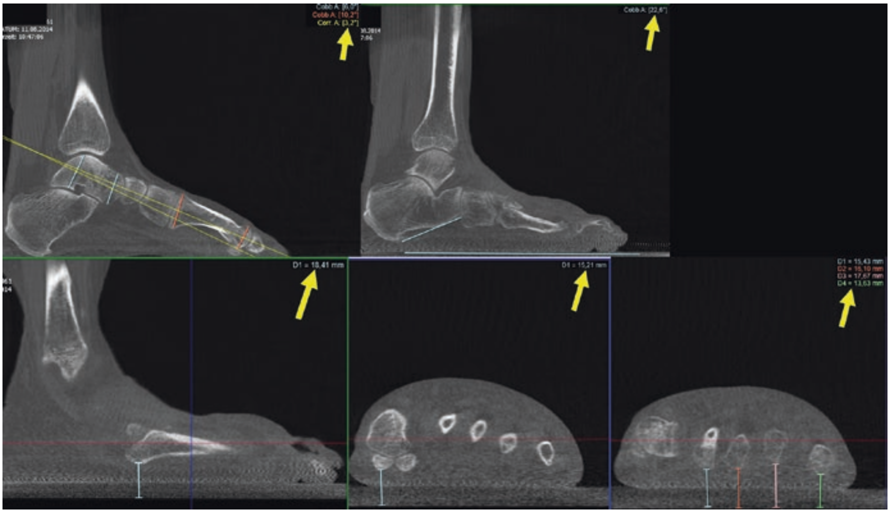

Fig. 2.2 PedCAT angle and distance measurements. (**a**) Lateral tarsometatarsal angle in sagittal plane. (**b**) Calcaneal pitch angle in sagittal plane. (**c**) Minimum distance between 5th metatarsal bone to footplate in sagittal plane. (**d**) Height of medial sesamoid in coronal plane. (**e**) Height of 2nd–5th metatarsal heads in coronal plane [1]

found in measured angles between imaging modalities (Table 2.4) [28]. For instance, hindfoot alignment angle on WBCT was 10.1° ± 7.1° while 5.4° ± 5.6° on conventional CT and 2.4° ± 6.9° on weight-bearing radiographs. The second study was a prospective consecutive study of 50 patients who underwent WBCT and simultaneous pedography [29]. The pedography consisted of the following computerized mapping: hindfoot, midfoot, 1st metatarsal head/sesamoids, 2nd metatarsal head, 3rd metatarsal head, 4th metatarsal head, 5th metatarsal head, 1st toe, 2nd toe, and 3rd–5th toes. No substantial correlation was found between WBCT measurements and pedography values, leading the authors to conclude that WBCT is not useful in assessing plantar force and pressure distributions [29].

Burssens et al. [9] recently described a clinically relevant and reproducible method to measure hindfoot alignment using WBCT. Sixty patients were enrolled into this prospective study including two groups: 30 patients with varus alignment and 30 patients with valgus alignment. Hindfoot alignment was measured using three different angles (Fig. 2.3): by the bisector of the Achilles tendon and the calcaneus (HAACL), by standard method using an inclination set at 45° (to simulate the long axial view) (HAALA), and a novel method by combining the inclination of the tibia (anatomical axis) and inclination of the talus and calcaneus (talocalcaneal angle) (HAANOV). The novel hindfoot angle assessment demonstrated a positive correlation with previous hindfoot angles, a high correlation with clinical alignment assessment, and an excellent reliability. The authors concluded that WBCT can be used to objectively measure hindfoot alignment similar to plain films [9].

Table 2.4 Radiographic assessment of the forefoot using weight-bearing computed tomography [1]

Radiographic measurement	Interobserver reliability	Intraobserver reliability	Correlation with other measurements	Clinical findings
α angle (1st MT pronation angle)	n.a.	n.a.	vs. HVA, 0.076[b]; *P* value <0.1 [14] vs. IMA, 0.144[b]; *P* value <0.1 [14] vs. sesamoid position, 0.019[b]; *P* value <0.1 [14]	HV group, 21.9°; control group, 13.8° [14] HV group, 8° ± 2° (4°–12°); control group, 2° ± 3° (−4°-8°) [25]
1st MT/ground angle	n.a.	n.a.	n.a.	HV group, 18° ± 1°; control group, 21° ± 1° [25]
HVA (2D)	n.a.	n.a.	n.a.	HV group, 35° ± 3°; control group, 13° ± 4° [25]
HVA (3D)	n.a.	n.a.	vs. HVA on plain radiographs, 0.95[a]; *P* value <0.05 [25] vs. HVA (2D), 0.94[a]; *P* value <0.05 [25]	HV group, 35° ± 3° (WB), 46° ± 5° (NWB); control group, 15° ± 4° (WB), 32° ± 8° (NWB) [25]
IMA (2D)	n.a.	n.a.	n.a.	HV group, 19° ± 1°; control group, 11° ± 1° [25]
IMA (3D)	n.a.	n.a.	vs. IMA on plain radiographs, 0.72[a]; *P* value <0.05 [25] vs. IMA (2D), 0.81[a]; *P* value <0.05 [25]	HV group, 17° ± 1° (WB), 14° ± 1° (NWB); control group, 11° ± 1° (WB), 8° ± 2° (NWB) [25] 9.3° ± 3.5° (WB), 7.8° ± 3.9° (NWB) [29]
Max. horizontal width (mm)	n.a.	n.a.	n.a.	HV group, 98 ± 1 (WB), 89 ± 2 (NWB); control group, 86 ± 2 (WB), 78 ± 3 (NWB) [25]
Sesamoid position in coronal plane	n.a.	n.a.	vs. α angle, 0.019[b]; *P* value <0.1 [14] vs. HVA, 0.477[b]; *P* value <0.01 [14]	HV group: true sesamoid subluxation 71.7%, no sesamoid subluxation 28.3% [14]
TMT angle dorsoplantar	n.a.	n.a.	n.a.	−5.0° ± 12.0° (WB), 4.3° ± 10.0° (NWB) [29]
TMT angle lateral	n.a.	n.a.	n.a.	−7.6° ± 8.2° (WB), 0.5° ± 8.4 (NWB) [29]

HV hallux valgus, *HVA* hallux valgus angle, *IMA* intermetatarsal angle, *MT* metatarsal, *n.a.* not available, *NWB* non-weight-bearing, *TMT* talo-1st metatarsal, *WB* weight-bearing
[a]Pearson correlation coefficient
[b]Spearman rank correlation coefficient

Fig. 2.3 Hindfoot alignment measurements in weight-bearing computed tomography. (**a**) HAA_{CL}: According to the clinical position by the intersection of the bisecting axis through the Achilles tendon and calcaneal surfaces measured in posteroanterior view. (**b**) HAA_{LA}: Hindfoot alignment measured using a simulated long axial view. (**c**) HAA_{NOV}: Determined by combination of the tibia inclination (blue line, anatomical tibial axis) and inclination of the talus and calcaneus (orange line, talocalcaneal axis connecting the inferior calcaneus point and the middle of the talar dome) in a person with neutral alignment in anteroposterior view. (**d**) HAA_{NOV} in a patient with varus alignment. (**e**) HAA_{NOV} in a patient with valgus alignment. (**f**) HAA_{NOV} in a patient following surgical correction of valgus alignment [1]

Cody et al. [24] used WBCT to analyze the talar anatomy and subtalar joint alignment in patients with adult-acquired flatfoot deformity. In total, 45 patients with stage II flatfoot deformity and 17 control patients were enrolled into this study. The subtalar joint alignment was assessed using two angles: (1) angle between the inferior facet of the talus and the horizontal and (2) angle between the inferior and superior facets of the talus. Both angles were significantly different in both groups. Specifically, it was demonstrated that patients with flatfoot deformity had more innate valgus in their talar anatomy and more valgus alignment of the subtalar joint. This information might potentially be used to identify patients who have a higher risk for underlying deformity progression [24].

Krähenbühl et al. [26] analyzed the orientation of the subtalar joint in 40 patients with tibiotalar osteoarthritis and 20 healthy controls. The subtalar joint was assessed by measurement of the subtalar vertical angle using WBCT. When comparing varus and valgus joints, significant differences of the subtalar vertical angle were found when comparing to healthy controls. The findings of this study suggest that the orientation of the subtalar joint may be an important factor in the development of ankle joint osteoarthritis [26].

Lintz et al. [27] described a new 3D biometric tool for hindfoot alignment assessment using WBCT. Datasets from 135 patients were analyzed: 57 with normal hindfoot alignment, 38 with varus hindfoot alignment, and 40 with valgus hindfoot alignment. Foot and ankle offset represents the lever arm of the torque generated in the ankle from the combined actions of body weight and ground reaction force. It was measured using a specific software. In patients with neutral hindfoot alignment, the offset was 2.3% ± 2.9%. In patients with valgus varus and valgus alignment, the offset was −11.6% ± 6.9% and 11.4% ± 5.7%, respectively. The findings of this pilot study suggest that the measurement of the foot and ankle offset can be used as a tool for hindfoot alignment assessment. However, further clinical studies should highlight its importance and relevance in clinical use. Furthermore, it needs to be addressed whether WBCT is superior to plain films with regard to assessment of hindfoot alignment [27].

Radiographic Measurements Using Weight Bearing CT

In the available literature, several measurements have been described to assess the forefoot alignment (Table 2.4) and midfoot/hindfoot alignment (Table 2.5) using WBCT (Fig. 2.4). The forefoot measurements include specifically assessment of hallux valgus deformity (α angle, hallux valgus angle, intermetatarsal angle, and tarsometatarsal angle). The hindfoot measurements include foot and ankle offset, hindfoot alignment angle, and osseous relationship (e.g., talocalcaneal overlap and tibiocalcaneal distance).

Table 2.5 Radiographic assessment of the midfoot and hindfoot using weight-bearing computed tomography [1]

Radiographic measurement	Interobserver reliability	Intraobserver reliability	Correlation with other measurements	Clinical findings
Calcaneal pitch angle	n.a.	n.a.	n.a.	17.8° ± 5.4° (WB), 16.5° ± 5.0° (NWB) [29]
Calcaneofibular distance (mm)	0.61[a] [13]	n.a.	n.a.	0.3 ± 6.0 (WB), 3.6 ± 5.2 (NWB) [13]
Foot and ankle offset (%)	0.99 ± 0.00[c] [27]	0.97 ± 0.02 [27]	n.a.	2.3 ± 2.9 (95% CI: 1.5–3.1) (patients with neutral alignment) [27] −11.6 ± 6.9 (95% CI: −13.9 to −9.4) (patients with varus alignment) [27] 11.4 ± 5.7 (95% CI: 9.6–13.3) (patients with valgus alignment) [27]
HAA	0.83[a] [13]	n.a.	n.a.	21.0° ± 7.9 (WB), 19.0° ± 9.0° (NWB) [13] 10.1° ± 7.1° (WB), 5.4° ± 5.6° (NWB) [29]

(continued)

Table 2.5 (continued)

Radiographic measurement	Interobserver reliability	Intraobserver reliability	Correlation with other measurements	Clinical findings
HAA_{CL}	0.72 (valgus), 0.69 (varus)[c] [9]	0.73 (valgus), 0.67 (varus) [9]	n.a.	25.2° (valgus), 22° (varus) [9]
HAA_{LA}	0.7 (valgus), 0.71 (varus)[c] [9]	0.71 (valgus), 0.72 (varus) [9]	n.a.	16.4° (valgus), 11.9° (varus) [9]
HAA_{NOV}	0.69 (valgus), 0.6 (varus)[c] [9]	0.67 (valgus), 0.67 (varus) [9]	n.a.	17.7° (valgus), 13.5° (varus) [9]
Lateral talocalcaneal joint space width (mm)	0.82[a] [13]	n.a.	n.a.	2.2 ± 1.1 (WB), 2.9 ± 1.7 (NWB) [13]
Naviculocalcaneal distance (mm)	0.85[a] [13]	n.a.	n.a.	15.3 ± 4.7 (WB), 13.5 ± 4.0 (NWB) [13]
Subtalar inferior facet-horizontal angle	n.a.	n.a.	No correlation with any weight-bearing radiographic measures [24]	Stage II AAFD group, 15.9° ± 5.7°; control group, 5.7° ± 6.7° [24]
Subtalar inferior-superior facet angle	n.a.	n.a.	vs AP coverage angle: *P* value 0.003 [24] vs. AP talar-first MT angle: *P* value 0.003 [24] vs. calcaneal pitch: *P* value 0.014 [24] vs. Méary angle: *P* value <0.001 [24] vs. medial column height: *P* value 0.007 [24]	Stage II AAFD group, 21.2° ± 6.7°; control group, 10.7° ± 6.4° [24]
Subtalar vertical angle	0.975[a] [26] 0.72 (valgus), 0.73 (varus)[c] [9]	0.989 [26] 0.77 (valgus), 0.78 (varus) [9]	n.a.	91° (72°–109°) (varus OA group), 109° (97°–120°) (valgus OA group), 98° (85°–114°) (controls) [26] 74.3° (valgus), 69.1° (varus) [9]
Talar tilt	0.92 (valgus), 0.89 (varus)[c] [9]	0.89 (valgus), 0.89 (varus) [9]	n.a.	5.9° (valgus), 4.8° (varus) [9]
Talar translation (mm)	0.86 (valgus), 0.82 (varus)[c] [9]	0.87 (valgus), 0.88 (varus) [9]	n.a.	21 (valgus), 19 (varus) [9]

Table 2.5 (continued)

Radiographic measurement	Interobserver reliability	Intraobserver reliability	Correlation with other measurements	Clinical findings
Talocalcaneal overlap (mm)	0.81[b] [13]	n.a.	n.a.	1.4 ± 3.9 (WB), 4.1 ± 3.9 (NWB) [13]
Tibiocalcaneal distance (mm)	0.72[b] [13]	n.a.	n.a.	20.6 ± 4.2 (WB), 21.7 ± 6.2 (NWB) [13]

AAFD adult-acquired flatfoot deformity, *AP* anteroposterior, *HAA* hindfoot alignment angle, HAA_{CL} hindfoot alignment angle measured by the bisector of the Achilles tendon and the calcaneus [9], HAA_{LA} hindfoot alignment angle measured using an inclination set at 45° to simulate the long axial view [9], HAA_{NOV} hindfoot alignment angle measured by combining the inclination of the tibia (anatomical axis) and inclination of the talus and calcaneus (talocalcaneal angle) [9], *MT* metatarsal, *n.a.* not available, *NWB* non-weight-bearing, *WB* weight-bearing

[a]Intraclass correlation coefficient to assess the interobserver reliability (measurements of one orthopedic resident, one medical student, and one scientific associate)

[b]Intraclass correlation coefficient to assess the interobserver reliability (measurements of two musculoskeletal radiologists)

[c]Intraclass correlation coefficient to assess the interobserver reliability (measurement of two independent observers)

Future Directions

Standardization of Measurements Using WBCT

First, all forefoot, midfoot, and hindfoot alignment measurements using WBCT should be standardized by reliable identification of anatomic landmarks. All measurements should be then performed in healthy asymptomatic person to identify the normal values. Furthermore, the intraobserver and interobserver reliability for all measurements at different training levels including research associate, medical student, orthopedic resident, orthopedic foot and ankle surgeon, and musculoskeletal radiologist should be assessed. Finally, clinical studies should clarify whether forefoot, midfoot, and hindfoot measurements using WBCT are clinically relevant and superior to using plain films.

WBCT vs. Plain Films

All forefoot, midfoot, and hindfoot alignment measurements using WBCT should be correlated with those using conventional weight-bearing radiographs. It still remains unclear whether weight bearing has a substantial influence on alignment measurements. WBCT offers the possibility to use digitally reconstructed radiographs; however, those radiographs should be correlated with conventional plain films.

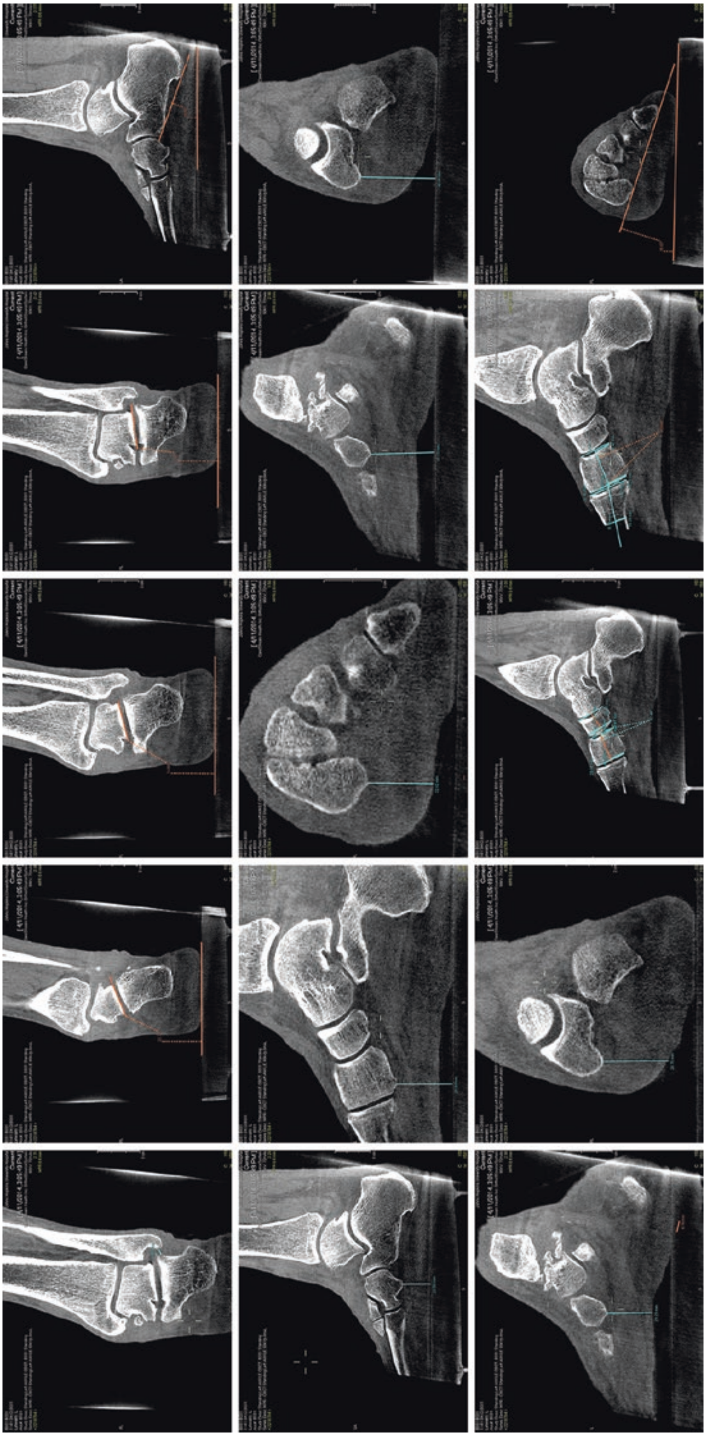

Fig. 2.4 Hindfoot, midfoot, and forefoot alignment measurements using weight-bearing computed tomography. (**a**) Calcaneofibular distance in coronal plane. (**b**) Subtalar horizontal angle in coronal plane. (**c**) Calcaneal inclination angle in sagittal plane. (**d**) Cuboid-floor distance in sagittal plane. (**e**) Cuneiform-floor distance in sagittal plane. (**f**) Cuneiform-skin distance in coronal plane. (**g**) Navicular-floor distance in sagittal and coronal planes. (**h**) Navicular-skin distance in sagittal and coronal planes. (**i**) Navicular-cuneiform angle in sagittal plane. (**j**) Cuneiform-1st metatarsal angle in sagittal plane. (**k**) Forefoot arch angle in coronal plane

Conclusions

The use of WBCT has steadily increased over the last 5 years. WBCT has been shown to offer several advantages including imaging in the physiological standing position, high spatial resolution, fast imaging acquisition time, low radiation dose, and modest costs. Cone beam CT technology with current design and flexible gantry movements allows both supine and standing weight-bearing imaging of the lower extremity with comparable quality but lower radiation than with conventional CT scanning. WBCT can be used to investigate the normal anatomy and dynamics (e.g., rotational dynamics) of the hindfoot [22, 23]. In the clinic, WBCT can be used to assess forefoot and hindfoot alignment. Further work needs to be done to validate and standardize measurement approaches which will facilitate communication between investigators and clinicians on the nature and treatment of foot and ankle deformities.

References

1. Barg A, Bailey T, Richter M, de Cesar Netto C, Lintz F, Burssens A, Phisitkul P, Hanrahan CJ, Saltzman CL. Weightbearing computed tomography of the foot and ankle: emerging technology topical review. Foot Ankle Int. 2018;39(3):376–86.
2. Linklater JM, Read JW, Hayter CL. Chapter 3 imaging of the foot and ankle. In: Mann's surgery of the foot and ankle. 9th ed. Philadelphia: Elsevier Saunders; 2014. p. 61–120.
3. Ananthakrisnan D, Ching R, Tencer A, Hansen ST Jr, Sangeorzan BJ. Subluxation of the talocalcaneal joint in adults who have symptomatic flatfoot. J Bone Joint Surg Am. 1999;81(8):1147–54.
4. Apostle KL, Coleman NW, Sangeorzan BJ. Subtalar joint axis in patients with symptomatic peritalar subluxation compared to normal controls. Foot Ankle Int. 2014;35(11):1153–8.
5. Ferri M, Scharfenberger AV, Goplen G, Daniels TR, Pearce D. Weightbearing CT scan of severe flexible pes planus deformities. Foot Ankle Int. 2008;29(2):199–204.
6. Greisberg J, Hansen ST Jr, Sangeorzan B. Deformity and degeneration in the hindfoot and midfoot joints of the adult acquired flatfoot. Foot Ankle Int. 2003;24(7):530–4.
7. Ledoux WR, Rohr ES, Ching RP, Sangeorzan BJ. Effect of foot shape on the three-dimensional position of foot bones. J Orthop Res. 2006;24(12):2176–86.
8. Malicky ES, Crary JL, Houghton MJ, et al. Talocalcaneal and subfibular impingement in symptomatic flatfoot in adults. J Bone Joint Surg Am. 2002;84(11):2005–9.
9. Burssens A, Peeters J, Buedts K, Victor J, Vandeputte G. Measuring hindfoot alignment in weight bearing CT: a novel clinical relevant measurement method. Foot Ankle Surg. 2016;22(4):233–8.
10. Kido M, Ikoma K, Imai K, Maki M, Takatori R, Tokunaga D, Inoue N, Kubo T. Load response of the tarsal bones in patients with flatfoot deformity: in vivo 3D study. Foot Ankle Int. 2011;32(11):1017–22.
11. Kido M, Ikoma K, Imai K, Tokunaga D, Inoue N, Kubo T. Load response of the medial longitudinal arch in patients with flatfoot deformity: in vivo 3D study. Clin Biomech (Bristol, Avon). 2013;28(5):568–73.
12. Geng X, Wang C, Ma X, Wang X, Huang J, Zhang C, Xu J, Yang J. Mobility of the first metatarsal-cuneiform joint in patients with and without hallux valgus: in vivo three-dimensional analysis using computerized tomography scan. J Orthop Surg Res. 2015;10:140.

13. Katsui R, Samoto N, Taniguchi A, et al. Relationship between displacement and degenerative changes of the sesamoids in hallux valgus. Foot Ankle Int. 2016;37(12):1303–9.
14. Kim Y, Kim JS, Young KW, Naraghi R, Cho HK, Lee SY. A new measure of tibial sesamoid position in hallux valgus in relation to the coronal rotation of the first metatarsal in CT scans. Foot Ankle Int. 2015;36(8):944–52.
15. Kimura T, Kubota M, Taguchi T, Suzuki N, Hattori A, Marumo K. Evaluation of first-ray mobility in patients with hallux valgus using weight-bearing CT and a 3-D analysis system: a comparison with normal feet. J Bone Joint Surg Am. 2017;99(3):247–55.
16. Van Bergeyk AB, Younger A, Carson B. CT analysis of hindfoot alignment in chronic lateral ankle instability. Foot Ankle Int. 2002;23(1):37–42.
17. Yoshioka N, Ikoma K, Kido M, Imai K, Maki M, Arai Y, Fujiwara H, Tokunaga D, Inoue N, Kubo T. Weight-bearing three-dimensional computed tomography analysis of the forefoot in patients with flatfoot deformity. J Orthop Sci. 2016;21(2):154–8.
18. Zhang Y, Xu J, Wang X, Huang J, Zhang C, Chen L, Wang C, Ma X. An in vivo study of hindfoot 3D kinetics in stage II posterior tibial tendon dysfunction (PTTD) flatfoot based on weight-bearing CT scan. Bone Joint Res. 2013;2(12):255–63.
19. Carrino JA, Al Muhit A, Zbijewski W, Thawait GK, Stayman JW, Packard N, Senn R, Yang D, Foos DH, Yorkston J, Siewerdsen JH. Dedicated cone-beam CT system for extremity imaging. Radiology. 2014;270(3):816–24.
20. Tuominen EK, Kankare J, Koskinen SK, Mattila KT. Weight-bearing CT imaging of the lower extremity. AJR Am J Roentgenol. 2013;200(1):146–8.
21. Colin F, Horn Lang T, Zwicky L, Hintermann B, Knupp M. Subtalar joint configuration on weightbearing CT scan. Foot Ankle Int. 2014;35(10):1057–62.
22. Lepojarvi S, Niinimaki J, Pakarinen H, Leskela HV. Rotational dynamics of the normal distal tibiofibular joint with weight-bearing computed tomography. Foot Ankle Int. 2016;37(6):627–35.
23. Lepojarvi S, Niinimaki J, Pakarinen H, Koskela L, Leskela HV. Rotational dynamics of the talus in a normal tibiotalar joint as shown by weight-bearing computed tomography. J Bone Joint Surg Am. 2016;98(7):568–75.
24. Cody EA, Williamson ER, Burket JC, Deland JT, Ellis SJ. Correlation of talar anatomy and subtalar joint alignment on weightbearing computed tomography with radiographic flatfoot parameters. Foot Ankle Int. 2016;37(8):874–81.
25. Collan L, Kankare JA, Mattila K. The biomechanics of the first metatarsal bone in hallux valgus: a preliminary study utilizing a weight bearing extremity CT. Foot Ankle Surg. 2013;19(3):155–61.
26. Krähenbühl N, Tschuck M, Bolliger L, Hintermann B, Knupp M. Orientation of the subtalar joint: measurement and reliability using weightbearing CT scans. Foot Ankle Int. 2016;37(1):109–14.
27. Lintz F, Welck M, Bernasconi A, Thornton J, Cullen NP, Singh D, Goldberg A. 3D biometrics for hindfoot alignment using weightbearing CT. Foot Ankle Int. 2017;38(6):684–9.
28. Richter M, Seidl B, Zech S, Hahn S. PedCAT for 3D-imaging in standing position allows for more accurate bone position (angle) measurement than radiographs or CT. Foot Ankle Surg. 2014;20(3):201–7.
29. Richter M, Zech S, Hahn S. PedCAT for radiographic 3D-imaging in standing position. Fuss Sprungg. 2015;13(2):85–102.

Part II
Scientific Background of Weight Bearing Cone Beam Computed Tomography

Chapter 3
Weight Bearing CT Allows for More Accurate Bone Position (Angle) Measurement than Radiographs or CT

Martinus Richter

Introduction

The standard for diagnostic radiographic imaging in foot and ankle surgery is radiographs with full weight bearing [1, 2]. The three-dimensional relationships of the bones in the foot are difficult to assess with standard radiographs due to superimposition of the different bones [1, 3]. Angle measurements with standard radiographs could be inaccurate due to inaccuracies of the projection (orientation of (central) beam) and/or foot orientation [1, 4–6]. 3D imaging with conventional computed tomography (CT) allows for exact analysis within the 3D data that is not influenced by projection and/or foot orientation but lacks weight bearing [1, 3, 7]. WBCT (PedCAT, CurveBeam, Warrington, USA) is a new technology that allows 3D imaging with full weight bearing which should be not influenced by projection and/or foot orientation (Figs. 3.1 and 3.2) [1].

The aim of this study was to compare time spent on the image acquisition, and comparison of specific angle measurements between the three methods (radiographs, CT, WBCT), and to analyze and compare inter- and intraobserver reliability.

Methods

In a prospective consecutive study, 30 patients in which standard digital radiographs with full weight bearing in standing position, CT without weight bearing in supine position, and WBCT with full weight bearing in standing position were included, starting July 1, 2013 [1]. The potential pathologies of the feet were registered but not further analyzed.

Based on Richter M, Seidl B, Zech S, Hahn S. PedCAT for 3D-Imaging in Standing Position Allows for More Accurate Bone Position (Angle) Measurement than Radiographs or CT. *Foot Ankle Surg* 2014;20(3): 201–207.

M. Richter et al., *Weight Bearing Cone Beam Computed Tomography (WBCT) in the Foot and Ankle*, https://doi.org/10.1007/978-3-030-31949-6_3

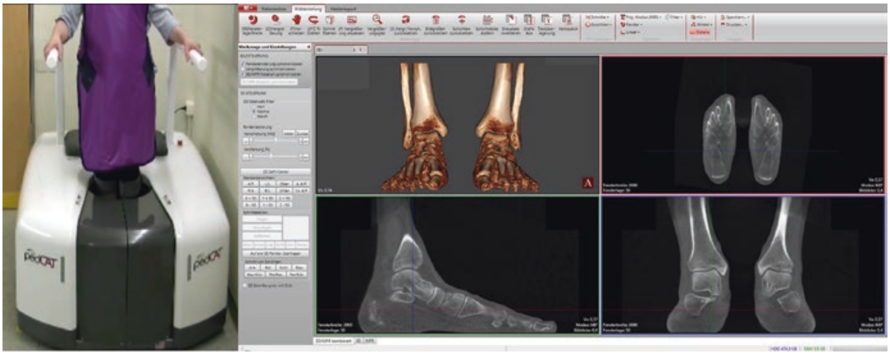

Fig. 3.1 WBCT scan and software screen. An X-ray emitter and a flat panel sensor on the opposite side are rotating horizontally around the feet. Resolution and contrast which are the principal parameters for image quality are comparable with modern conventional CT. Left, patient positioned in WBCT during scan. Sitting position is also possible for patients that are not allowed or able to stand. The gray part is a sliding door that is opened before and after the scan. The patient can walk into the device of the door is open. Right, software screen view with 3D reformation (top left), axial reformation (top right, red frame), parasagittal reformation (bottom left, green frame), and coronal reformation (bottom right, blue frame). The standard view is with 1 mm slice thickness, shown by the red, green, and blue lines. The red lines are corresponding to the axial reformation in the red frame, the green lines are corresponding to the parasagittal reformation in the green frame, and the blue lines are corresponding to the coronal reformation in the blue frame

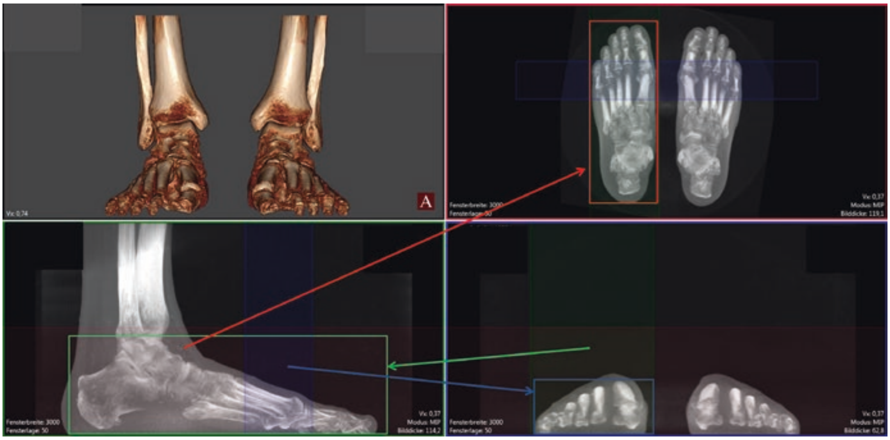

Fig. 3.2 WBCT software screen view with increased slice thickness to create virtual radiographs. Top right, in red frame, virtual dorsoplantar radiograph created by increased slice thickness that contains entire foot (red arrow). Bottom left, in green frame, virtual lateral radiograph created by increased slice thickness that contains entire foot (green arrow). Bottom right, in blue frame, virtual metatarsal head skyline view radiograph created by increased slice thickness that contains the metatarsal heads (blue arrow)

Inclusion and Exclusion Criteria: Ethics

The inclusion criteria were age ≥18 years, presentation at the local foot and ankle outpatient clinic, and indication for radiographs and 3D imaging (CT, WBCT). The indication for radiograph and 3D imaging (CT, WBCT) was defined following the local standard. For example, no indication for 3D imaging (CT, WBCT) was given for isolated forefoot deformities, whereas indication for 3D imaging (CT, WBCT) was given for deformities in the midfoot and/or hindfoot region.

The exclusion criteria were age <18 years, no indication for radiograph and/or 3D imaging (CT, WBCT) and participation in other studies.

All three methods (radiographs, CT, WBCT) were approved by the relevant authority for diagnostic use at the local institution. Approval from the local ethical committee was granted for simultaneous use of all three methods (radiograph, CT, WBCT) based on the indications as described above. Informed consent was obtained from all subjects.

Image Acquisition

The radiographic image acquisition followed a standardized protocol with a fully digital device (Model Buck Diagnost, Philips, Hamburg, Germany) [2, 8]. The patient was positioned on a special step with a holding apparatus for the digital film, the X-ray emitter was adjusted, and the images were taken (feet bilateral dorsoplantar and lateral views and Saltzman hindfoot view) [8]. The radiation exposure time was approximately 1/10th of a second for each image. For CT (Model Optima 520, General Electric Healthcare, Solingen, Germany; helical technique, 20 lines), the patient was positioned in supine position, and the feet were placed in a special holding device to ensure neutral foot and ankle position [9]. Both feet and ankles were scanned from 10 cm proximal to the ankle level. The slice thickness was adjusted to 1 mm, and the pure scanning time was 60 seconds. For WBCT (PedCAT, CurveBeam, Warrington, USA), the patient walked into the device and was positioned in bipedal standing position as shown in Fig. 3.1. Technically, an X-ray emitter and a flat panel sensor on the opposite side are rotating horizontally around the feet. Resolution and contrast which are the principal parameters for image quality are comparable with modern conventional CT. The scanning time was 68 seconds.

Time Spent

The time spent on the image acquisition was registered. Time spent was defined as the sum of the time needed for positioning the patient for the imaging and the time needed for the imaging as such as described above. The time for epidemiological data entry was not included. For the radiograph group, the times for all four images (feet bilateral dorsoplantar, right foot lateral, left foot lateral, Saltzman hindfoot view bilateral) were added up to a total time.

Angle Measurements

The angles were digitally measured with specific software (Radiographs, JiveX, VISUS, Bochum, Germany; CT, Syngo XS version VE31GSL19P21VC10ASL129P167SP1, Siemens, Erlangen, Germany; PedCAT, CubeVue, version 2.4.0.5, CurveBeam, Warrington, USA).

The following angles were measured for the right foot by three different investigators three times: 1st–2nd intermetatarsal angle, talo-1st metatarsal (TMT) angle dorsoplantar and lateral projection, hindfoot angle, and calcaneal pitch angle [8, 10].

The 1st–2nd intermetatarsal angle was defined as the angle created between the axis of the 1st and the 2nd metatarsal in the dorsoplantar view (radiograph) or axial/horizontal reformation (CT, WBCT). For CT and WBCT, the plane for the measurement was virtually rotated within the 3D dataset to achieve an exact congruency to the bone axes of first and second metatarsals.

The TMT angle was defined as the angle created between the axis of the 1st metatarsal and the talus [10] (Fig. 3.3, image top right and bottom left). The dorsoplantar TMT angle was measured in the dorsoplantar view (radiograph) or axial/

Fig. 3.3 WBCT software screen showing an example of some angle measurements. The 3D reformation (top left) shows how the 3D dataset was virtually rotated to allow for exact congruency of the plane of the reformations with the bone axes as described in the methods section. Top right, measurement of the dorsoplantar TMT angle; bottom left, measurement of the dorsoplantar TMT angle; bottom right, measurement of the hindfoot angle also as described in the methods section. The hindfoot angle measurement was typically performed in another plane which cannot be displayed simultaneously with planes for the dorsoplantar and lateral TMT angles. This modified presentation was chosen for this figure for to allow simultaneous presentation of three angles within one figure. The lines that define the centers of the bones proximally or distally are exactly 50% of the measured entire bone thickness

horizontal reformation (CT, WBCT) (Fig. 3.3, image top right). The lateral TMT angle was measured in the lateral view (radiograph) or parasagittal reformation (CT, WBCT) (Fig. 3.3, image bottom left). For CT and WBCT, the plane for the measurement was virtually rotated within the 3D dataset to achieve an exact congruency to the bone axis of talus and 1st metatarsal.

The hindfoot angle was defined as the angle created between the axis of the distal tibia and the line between the center of the talar dome and the posterior calcaneal process (Fig. 3.3, image bottom right). This angle is defined to be positive for hindfoot valgus and negative for hindfoot varus. It is measured Saltzman view (radiograph) or coronal reformation (CT, WBCT). For CT and WBCT the plane for the measurement was virtually rotated within the 3D dataset to achieve an exact congruency to the bone axis of the tibia and the axis of the hindfoot. This was typically the case when this plane was congruent with the axis of the ankle, i.e. a line between medial and lateral malleolus comparable to a mortise orientation but within a 3D pace. Figure 3.3 (image bottom right) shows the orientation within the 3D dataset as described above with the adjusted rotation with the fibula and tibia aligned in the same virtual plane comparable to a mortise view.

The calcaneal pitch angle was defined as the angle created between a horizontal line, between the lowest part of the posterior calcaneal process and the lowest part of the anterior calcaneal process. The calcaneal pitch was measured in the lateral view (radiograph) or parasagittal reformation (CT, WBCT). For CT and WBCT the plane for the measurement was virtually rotated within the 3D dataset to achieve an exact congruency to an exactly parasagittal plane.

All bone axes (tibia, talus, metatarsals) were defined as the straight line between the centers of the bones proximally and distally. These bone centers were defined by linear measurements (Fig. 3.3). The TMT angles were defined to be negative for abduction in the dorsoplantar radiograph and for dorsiflexion in the lateral radiographs [10].

Statistics

The parameters were compared to intra- and interobserver and between the different methods (radiograph, CT, WBCT) (ANOVA with post hoc Scheffe test). The null hypothesis at a significant level of 0.05 was formulated that the different angles did not differ between the three methods. For nonsignificant findings, a power analysis was indicated. Sufficient power was defined as ≥0.8.

Results

Time Spent

The time spent for the image acquisition was 902 ± 70 seconds for radiographs, 415 ± 46 seconds for CT and 270 ± 44 seconds for WBCT on average (ANOVA, $p < 0.001$).

Angle Measurement: Differences Between Methods

The angles differed between radiographs, CT, and WBCT (ANOVA, all $p \leq 0.01$) (Table 3.1). The angles differed between WBCT and both radiographs and CT (post hoc Scheffe test, each $p \leq 0.05$) except for TMT dorsoplantar and calcaneal pitch angles for WBCT versus radiographs. The null hypothesis was rejected for all angles except for TMT dorsoplantar and calcaneal pitch angles between WBCT and radiograph.

Angle Measurement: Intra- and Interobserver Reliability

Regarding intraobserver reliability, the angles did not differ between measurement 1, measurement 2, and measurement 3 for all three investigators and for all three methods (radiograph, CT, WBCT) (ANOVA, each $p > 0.9$, power > 0.8).

Regarding interobserver reliability, the angles did not differ between the three investigators for measurement 1, measurement 2, and measurement 3 for all three methods (radiograph, CT, WBCT) (ANOVA, each $p > 0.9$, power > 0.8).

Table 3.1 One-way ANOVA radiographs versus CT versus WBCT and post hoc test WBCT versus radiographs and CT

One-way ANOVA							
Parameter	**Radiographs**		**CT**		**WBCT**		***p***
	Mean	**STD**	**Mean**	**STD**	**Mean**	**STD**	
IM-angle	7.7	3.3	7.8	3.9	9.3	3.5	<0.001
TMT dorsoplantar	−6.2	12.4	4.3	10.0	−5.0	12.0	<0.001
TMT lateral	−5.2	8.2	0.5	8.4	−7.6	8.2	<0.001
Hindfoot angle	2.4	6.9	5.4	5.6	10.1	7.1	<0.001
Calcaneal pitch angle	17.5	6.3	16.5	5.0	17.8	5.4	0.01
Post hoc Scheffe test							
Parameter	**WBCT vs.**	***p***					
IM-angle	Radiographs	<0.001					
	CT	<0.001					
TMT dorsoplantar	Radiographs	0.561					
	CT	<0.001					
TMT lateral	Radiographs	0.003					
	CT	<0.001					
Hindfoot angle	Radiographs	<0.001					
	CT	<0.001					
Calcaneal pitch angle	Radiographs	0.701					
	CT	0.013					

IM 1st–2nd intermetatarsal angle, *TMT* talo-1st metatarsal angle, *STD* standard deviation

Discussion

This is the first study comparing bone position (angle) measurements between standard radiographs with weight bearing, standard CT without weight bearing and 3D imaging with weight bearing (WBCT).

Time Spent

The image acquisition with WBCT (270 seconds) is 70% faster than with radiographs (902 seconds) and 35% faster than with CT (270). This difference is not caused by the scanning time as such which is much lower for radiographs (four times 1/10 of a second) than for CT (60 seconds) or WBCT (68 seconds). The positioning of the patient and the adjustment of the X-ray emitter comprise the time spent of the positioning of the patient and the adjustment of the device, specifying the scan area and sliding the patient to the correct position for the scan for CT. For the WBCT the patient positioning is the fastest and no further adjustments are needed so that only pushing pressing a button is necessary to perform the scan.

Angle Measurement: Differences between Methods

The angles differed between radiographs, CT and WBCT. The difference as such is a fact, but the difference does not show which one of the methods measures correctly. However, when considering technical issues, it is obvious that only WBCT is able to detect the correct angles because WBCT obtains a 3D dataset which is independent of foot position and projection. Consequently, the significant different angles (Table 3.1) measured with radiographs or CT in comparison with WBCT imply that radiographs or CT do not allow for correct angle measurement. The incorrect angles measured with radiographs are probably caused by inaccuracies of projection and foot orientation and the incorrect angles measured with CT by missing weight bearing (see detailed discussion below). WBCT includes weight bearing in contrast to CT. WBCT countervails inaccuracies of projection and foot orientation in contrast to radiographs due to the 3D dataset which is principally independent from projection and foot orientation. If a malposition of the foot during image acquisition exists, the planes of the WBCT reformations (also CT) could be rotated as described above to ensure exact angle measurement despite foot malposition. We did not quantitatively assess the extent of plane rotation needed, but the investigators' interpretation was that the least plane rotation was needed for dorsoplantar TMT and calcaneal pitch angles and more plane rotation for the other angles. This reflects the results that radiographs were not different for calcaneal pitch angle and dorsoplantar TMT angles that are obviously less likely to be influenced by inaccurate foot position and/or projection which is also an issue for radiographs. Inaccuracy of the projection, i.e., the (central) beam(s), is obviously an underestimated problem for radiographic imaging. We were not able to isolate the factors inaccurate foot position or inaccurate projection. The resulting different angles in comparison with WBCT reflect probably a combination of both inaccuracies.

1st–2nd Intermetatarsal Angle

This angle was lower for radiographs (7.7) and CT (7.8) than for WBCT (9.3). We believe that the different angles for radiographs in comparison with WBCT reflect a combination of both factors inaccurate foot position and inaccurate projection of the radiographic image acquisition. A slight supination of the foot might cause this as well as the bilateral dorsoplantar imaging that is performed with a central beam in the middle between both feet and minimally oblique beams at both feet. For CT, the missing weight bearing will probably cause a true lower angle because CT is independent of foot position and projection as WBCT.

TMT Dorsoplantar

This angle was lower for radiographs (−6.2) and WBCT (−5.0) than for CT (4.3). The higher or better less negative angles for CT than for radiographs and WBCT are obviously caused by the missing weight bearing. For radiographs, inaccuracies of foot position and projection are either not relevant or might abrogate each other. We believe that these inaccuracies are more likely not relevant because the investigators' interpretation was that the least plane rotation for measurement within the WBCT data was needed for this angle (see above).

TMT Lateral

This angle was higher for radiographs (−5.2) and much higher for CT (0.5) than for WBCT (−7.6). The much higher of much less negative angles for CT than for radiographs and WBCT are obviously caused by the missing weight bearing. For radiographs, a slight supination of the foot could possibly increase the angle or better decrease the negative value of this angle. More probable seems to be that the axis of the talus is "sticking out" of the plane of the 2D radiograph based on the abduction of the mid- and forefoot in a flatfoot which is then positioned with the mid- and forefoot parallel to the film but the talus in slight internal rotation and not parallel to the film.

Hindfoot Angle

This angle was lower for radiographs (2.4) and CT (5.4) than for WBCT (10.1). Again, the higher angles for CT than for radiographs and WBCT are obviously caused by the missing weight bearing. For, radiographs, the foot position with both feet parallel to each other and the longitudinal foot axes perpendicular to the film might be the most important reason for the lower angles. This position is typically not a mortise view which would be more internal rotation of the ankle and foot. For WBCT the plane for the measurement was virtually rotated within the 3D dataset to achieve an exact congruency to the bone axis of the tibia and the axis of the hindfoot. This was typically the case when this plane was congruent with the axis of the ankle, i.e. a line between medial and lateral malleolus comparable to a mortise orientation but within a 3D space. This is virtually more internally rotated than in the radiograph group resulting in a higher angle at least for all hindfeet with valgus position which were the majority of the cases as shown by the positive values on average.

Calcaneal Pitch Angle

This angle was higher for radiographs (17.5) and WBCT (17.8) than for CT (16.5). The lower angles for CT than for radiographs and WBCT are obviously caused by the missing weight bearing. For radiographs, inaccuracies of foot position and projection are either not relevant or might abrogate each other. We believe that these inaccuracies are more likely not relevant because the investigators' interpretation was that the least plane rotation for measurement within the WBCT data was needed for this angle (see above).

Angle Measurement: Intra- and Interobserver Reliability

The intra- and interobserver reliability is sufficient for all three methods. This is probably based on the digital software based measurements, and the experience of all three investigators regarding these kind of digital measurements. Based on the sufficient intra- and interobserver reliability for all three methods, differences between the methods are not influenced by differences in intra- and interobserver reliability.

Shortcomings of the Study

The shortcomings of this study are not the typical ones like missing analysis of intra- and/or interobserver reliability or missing power analysis of the statistical test. The low case number might be a shortcoming. We fell that a (much) higher case number would have led to significant differences of the dorsoplantar TMT and calcaneal pitch angles comparing radiographs with WBCT. All other angles differed already which led to the conclusions, so a higher case number would probably not change the conclusions. The angular measurement as such could possibly be influenced by the investigators in that manner that the investigators would have desired that one method, for example, the WBCT, would perform better than the other methods. However, this kind of influence principally results in a low intra- and/or interobserver reliability which were sufficient for all three methods. We did not measure how difficult and time-consuming the measurements were. The reason for this is that the type of software and version and above all the experience of the investigator might influence this time much more than the method as such. Another shortcoming might that we were not able to isolate the factors inaccurate foot or inaccurate projection of the radiographs group. The radiographic image acquisition followed a standardized protocol which was not further assessed [2]. Finally, the potential foot pathologies of the subjects were registered but not analyzed. The pathological angles (not neutral or 0 for TMT dorsoplantar and lateral, hindfoot and calcaneal pith angle on average) imply that relevant pathologies were present which are also based on the inclusion criteria. However, we did not want to investigate different pathologies but the technical parameters of the different imaging methods.

Radiation Dose

A comparison of the radiation dose of the WBCT with radiographs and a standard CT scan was not performed in our study. The applied energy (product of amperage, voltage, and time) is typically adjusted and registered during a CT scan, radiographs, or WBCT. However, the dose as such depends on the structure of the scanned object and is not measured during the imaging. Recently, the dose of foot/ankle radiographs, CT and WBCT was measured and analyzed using a foot and ankle phantom [11]. The dose for adults for three radiographs from one foot (anteroposterior/dorsoplantar + lateral + oblique) was 0.7 μSv, the dose for a bilateral WBCT scan 4.3 μSv, and the dose for conventional CT of one foot/ankle 25 μSv [11]. This means that a bilateral WBCT scan has a comparable dose of 18 unilateral radiographs of the foot and 17% of a unilateral CT of the foot and ankle [11]. This study did also measure the dose of a unilateral WBCT scan which was 1.4 μSv comparable to six unilateral radiographs of the foot and 5.6% of a unilateral CT of the foot and ankle [11]. For the later clinical use this radiation dose is relativized because virtual radiography could be created from the WBCT data as shown in Fig. 3.1.2. We have created the following virtual radiographs from the WBCT scan data: entire foot dorsoplantar and lateral views, ankle dorsoplantar, mortise and lateral views, Saltzman views, metatarsal head skyline views, and Broden's views (all views bilateral).

Cost

Another issue is cost as always. A device for radiography is around 75,000 Euros, a WBCT device is 150,000 Euros, and a CT device is starting at 200,000 Euros (all prices exclusive VAT). However, devices for radiographs and CT can be used for other body regions also, whereas the WBCT can only be used for the foot and ankle region. The reimbursement is different for different countries and types of insurance. In the country in which this study has taken place, the reimbursement for a WBCT scan is comparable with a CT scan and 15 radiographs. Time spent is also a cost factor. In our study the time spent for the WBCT scan was 70% faster than radiographs and 35% faster than a CT scan. Still, a WBCT-device might be cost-effective for institutions with one foot and ankle surgeon, but we think that groups with two or more foot and ankle surgeons or foot and ankle departments might not only be able to run a WBCT cost-effectively but create profit even when the quality of the imaging is not taken into consideration. It has been demonstrated in many US institutions and private practices that a single foot and ankle surgeon can operate the WBCT cost-effectively and generate a sizable surplus. The same should apply to other parts of the world. This can also be established by comparing the WBCT's typical lease or finance cost (between 3000 and 4000 Euros per month depending on the lease terms) and reimbursement per scan (around 200 Euros). These example figures would permit a practice to justify the cost with 15–20 scans a month, which should be achievable even with a single surgeon. This model has been well established for almost similar CBCT devices for dental/maxillofacial/ENT imaging, with hundreds of such devices installed with single practitioners in Germany and across Europe.

Approval for Use

Approval for imaging is specific for the WBCT. Actually, most countries classify the device as a CT. However, a more common trend is to differentiate between conventional CT and cone beam CT and apply exemptions for CBCT from typical CT requirements due to its specialized and limited applications, coupled with low dose and dramatically less complexity. This same model is very common and already established with CBCT devices for maxillofacial and ENT imaging.

In some countries like the one where the institution of authors is located, this device is not classified as a CT which allows non-radiologists to prosecute a WBCT in their institution in contrast to CT which is mostly only approved for prosecution by radiologists. In conclusion, everybody who is approved to run his or her radiograph device will be allowed to run a WBCT.

Standard Imaging?

When considering the potential of the WBCT as faster image acquisition and more accurate bone position representation than radiographs and CT with acceptable radiation dose and cost-effectiveness, one could conclude the WBCT might have the potential to become the standard diagnostic imaging in foot and ankle surgery. When a WBCT-device is available as in our institution, CT which has no better image quality (resolution and contrast) but 10 times radiation dose, 1.5 times time spent for image acquisition, higher device cost, and radiologist needed is almost obsolete. Since September 2013, we limited the use of a conventional CT to patients with acute injury that are not able to stand or sit in the WBCT. We compared the numbers of CT and WBCT over a 6-month period in which both were available at our institution (September 2013 to February 2014) with a 6-month period in which only CT was available (September 2012 to February 2013). In the period with only CT, 148 CT scans were obtained, and in the period with both 16 CT scans and 135 WBCT scans. This corresponds to a reduction of conventional CT scans of almost 90%. We are expecting the same development with conventional radiographs. We have not performed the same transposition from radiographs to WBCT as for CT to WBCT because we do not have enough WBCT workstations for creation, presentation, and printout of the virtual radiographs. We do plan to switch completely from conventional radiographs to virtual radiographs when these technical requirements are fulfilled.

The results of this study call into question if the existing standard angles of angles for pathology classification are also correct for the WBCT. The answer is no, and the reason is obvious because the WBCT measures different angles as measured with radiographs. For example, the 1st–2nd intermetatarsal angles were 7.7° on average for radiographs and 9.3° on average for WBCT with a difference of 1.6° (Table 3.1). What caused this difference? Again, we believe that the different angles in comparison with WBCT reflect a combination of both factors inaccurate foot position and inaccurate projection of the radiographic image acquisition as discussed above in detail. What does this mean? Are we able to perform a distal osteotomy of the 1st metatarsal for hallux valgus correction in cases with 1st–2nd intermetatarsal angle 17.6° measured with WBCT comparing with 16° with radiographs? What about the significant differences of the hindfoot angles? When it comes to implantation of total ankle replacements and/or surgical corrections of the hindfoot, this might be important information. We cannot answer these questions at this stage, but we believe that the standard angles and angles for classification of pathologies need to be defined for WBCT comparable technologies. Another important part of the discussion based on the results of this study is whether conventional radiographs could still serve as standard diagnostic imaging. The logical answer from a scientific point of view is no because the angles that are measured with conventional radiographs are not correct. Nevertheless, we believe that conventional devices for radiographs will not disappear for a long time and this will be the same with all the non-validated foot and ankle scores that are used again and again even though everybody knows that they are not validated, i.e., they are not correctly measuring. In the end, conventional devices for radiographs might disappear as non-validated scores, but nobody knows when validated scores and new imaging technologies like WBCT might be used instead as already in our institution.

In conclusion, the bone position represented by the measured angles differed between radiographs, CT, and WBCT, indicating that only WBCT is able to detect the correct angles. WBCT includes weight bearing in contrast to CT. WBCT prevents inaccuracies of projection and foot orientation in contrast to radiographs due to the 3D dataset which is principally independent from projection and foot orientation. WBCT or a similar technology has the potential to become the standard diagnostic imaging.

References

1. Richter M, Seidl B, Zech S, Hahn S. PedCAT for 3D-imaging in standing position allows for more accurate bone position (angle) measurement than radiographs or CT. Foot Ankle Surg. 2014;20:201–7.
2. Rammelt S, Amlang M, Zwipp H. Standardröntgendiagnostik an Fuß und Sprunggelenk. Fuss Sprungg. 2010;8(2):80–91.
3. Ferri M, Scharfenberger AV, Goplen G, Daniels TR, Pearce D. Weightbearing CT scan of severe flexible pes planus deformities. Foot Ankle Int. 2008;29(2):199–204.
4. Johnson JE, Lamdan R, Granberry WF, Harris GF, Carrera GF. Hindfoot coronal alignment: a modified radiographic method. Foot Ankle Int. 1999;20(12):818–25.
5. Richter M. Computer aided surgery in foot and ankle: applications and perspectives. Int Orthop. 2013;37(9):1737–45.
6. Richter M. Computer based systems in foot and ankle surgery at the beginning of the 21st century. Fuss Sprungg. 2006;4(1):59–71.
7. Kido M, Ikoma K, Imai K, Maki M, Takatori R, Tokunaga D, Inoue N, Kubo T. Load response of the tarsal bones in patients with flatfoot deformity: in vivo 3D study. Foot Ankle Int. 2011;32(11):1017–22.
8. Saltzman CL, el-Khoury GY. The hindfoot alignment view. Foot Ankle Int. 1995;16(9):572–6.
9. Richter M, Zech S. Intraoperative 3D imaging in foot and ankle trauma. The first clinical experience with a second device generation (ARCADIS-3D). J Orthop Trauma. 2009;23(3):213–20.
10. Richter M, Zech S. Lengthening osteotomy of the calcaneus and flexor digitorum longus tendon transfer in flexible flatfoot deformity improves Talo-1st metatarsal-index, clinical outcome and pedographic parameter. Foot Ankle Surg. 2012;19(1):56–61.
11. Ludlow BW, Ivanovic M. Weightbearing CBCT, MDCT, and 2D imaging dosimetry of the foot and ankle. Int J Diagn Imaging. 2014;1(2):1–9.

Chapter 4
Combination of Weight Bearing CT (WBCT) with Pedography Shows No Statistical Correlation of Bone Position with Force/Pressure Distribution

Martinus Richter

Introduction

Analyzing the position of the bones radiographically allows conclusions regarding the biomechanics of the foot [1–9]. However, static and dynamic pedography is more effective for the analysis of the biomechanics of the foot [8, 10–12].

WBCT (PedCAT, CurveBeam, Warrington, USA) is a new technology that allows 3D imaging with full weight bearing which should be not influenced by projection and/or foot orientation (Figs. 4.1 and 4.2) [9]. In an earlier study, specific bone position (angle) measurements with WBCT were compared with measurements of conventional radiographs with weight bearing and CT without weight bearing (radiographs, CT, WBCT) [9]. The angles differed between radiographs, CT, and WBCT, indicating that only WBCT is able to detect the correct angles [9]. WBCT includes weight bearing in contrast to CT. WBCT prevents inaccuracies of projection and foot orientation in contrast to radiographs due to the 3D dataset which is principally independent from projection and foot orientation [9]. Pedography is a measurement of the force distribution under the sole of the foot which can be performed in a static or dynamic way [13, 14]. Over the years, a variety of methods have been employed to study foot pressure [15–17]. Many of these techniques have already improved our understanding of the foot and its function and have had an impact on the way we practice [8, 11, 15, 18]. The correlation between 3D bone position and pedographic measurements, i.e., force and pressure (distribution), has not been shown so far. For this study a customized pedography sensor (Pliance, Novel, Munich, Germany) was inserted into the WBCT. The aim of this study was to analyze the correlation of bone position and force/pressure distribution.

Based on Richter M, Zech S, Hahn S, Naef I, Merschin D. Combination of PedCAT for 3D imaging in standing position with pedography shows no statistical correlation of bone position with force/pressure distribution. J Foot Ankle Surg. 2015;55(2): 240–246.

M. Richter et al., *Weight Bearing Cone Beam Computed Tomography (WBCT) in the Foot and Ankle*, https://doi.org/10.1007/978-3-030-31949-6_4

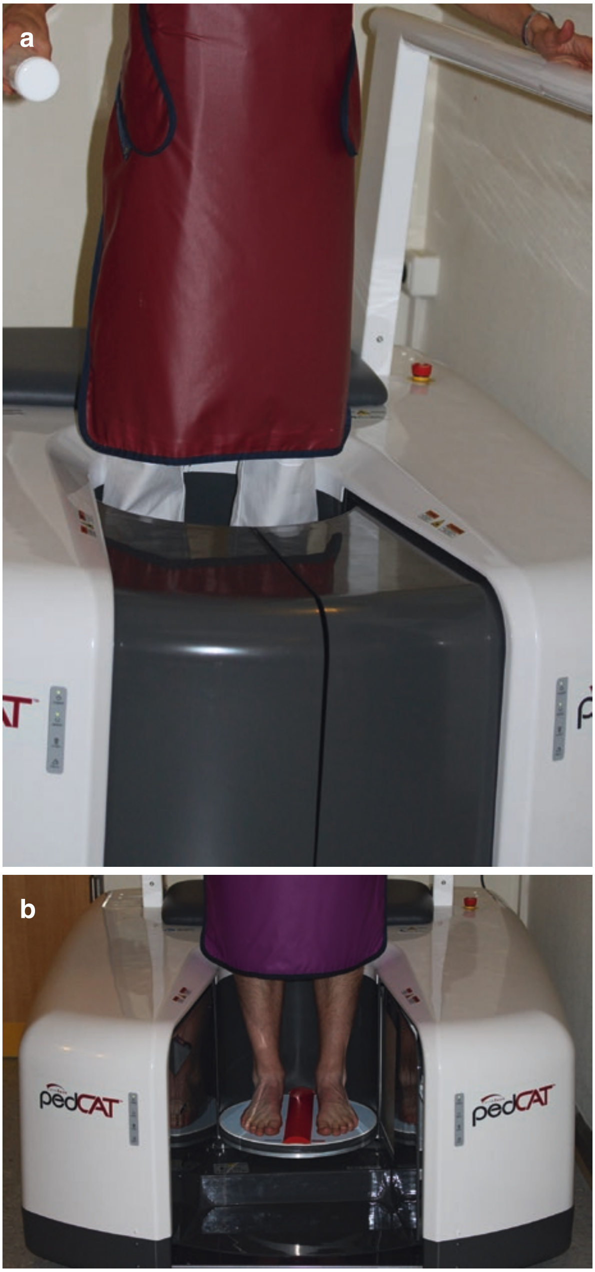

Fig. 4.1 WBCT with pedography sensor. An X-ray emitter and a flat panel sensor on the opposite side are rotating horizontally around the feet. Resolution and contrast which are the principal parameters for image quality are comparable with modern conventional CT. (**a**) Shows a patient positioned in WBCT during scan. Sitting position is also possible for patients that are not allowed or able to stand. The gray part is a sliding door that is opened before and after the scan. The patient can walk into the device when the door is open. (**b**) The WBCT with the sliding door open

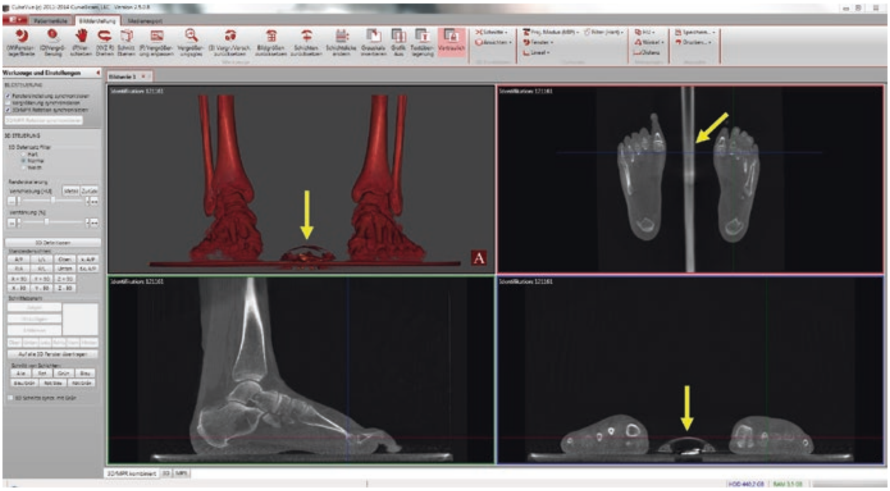

Fig. 4.2 WBCT software screen view with 3D reformation (top left), axial reformation (top right, red frame), parasagittal reformation (bottom left, green frame), and coronal reformation (bottom right, blue frame). The standard view is with 1 mm slice thickness. The red lines (bottom left and bottom right) are corresponding to the axial reformation in the red frame (top right), the green lines (top right and bottom right) are corresponding to the parasagittal reformation in the green frame (bottom left), and the blue lines (bottom left and top right) are corresponding to the coronal reformation in the blue frame (bottom right). The arrows show the illustration of the pedography sensor hardware

Methods

In a prospective consecutive study starting July 28, 2014, 50 patients were included. A WBCT scan with simultaneous pedography of both feet under full weight bearing in standing position was performed. A customized pedography sensor (Pliance, Novel, Munich, Germany) was inserted into the WBCT and connected to a PC with the standard software installed (Expert, Novel, Munich, Germany). The potential pathologies of the feet were registered but not further analyzed.

Inclusion and Exclusion Criteria: Ethics

The inclusion criteria were age ≥18 years, presentation at the local foot and ankle outpatient clinic, and indication for WBCT. The indication for WBCT was defined following the local standard [9]. For example, no indication for 3D imaging with WBCT was given for isolated forefoot deformities, whereas indication was given for deformities in the midfoot and/or hindfoot region.

The exclusion criteria were age <18 years, no indication for WBCT imaging and participation in other studies.

Approval from the local ethical committee was granted based on the indications as described above. Informed consent was obtained from all subjects.

Image Acquisition

The patient walked into the device and was positioned in bipedal standing position as shown in Fig. 4.1a. Technically, an X-ray emitter and a flat panel sensor on the opposite side are rotating horizontally around the feet. Resolution and contrast which are the principal parameters for image quality are comparable with modern conventional CT [9]. The scanning time was 68 seconds.

Pedography

The data of the pedography sensor (Fig. 4.1b) was gathered for the first 30 seconds of the WBCT scan.

Measurements of Bone Position (Angles and Distances)

The bone positions (angles and distances) were digitally measured with standard WBCT software (Cubevue, CurveBeam, Warrington, USA).

The following angles and distances were measured for the right foot by three different investigators three times: lateral talo-1st metatarsal angle (TMT), calcaneal pitch angle, minimum height of 5th metatarsal base, and 2nd–5th metatarsal heads and medial sesamoid. The medial sesamoid was chosen instead of the first metatarsal head because it is regularly closer to the foot sole/ground. The medial sesamoid was chosen instead of the lateral sesamoid because it is less likely to completely dislocate from underneath the 1st metatarsal head in forefoot deformities such as hallux valgus [19, 20].

The lateral TMT angle was defined as the angle created between the axis of the first metatarsal and the talus (Fig. 4.3a) [9, 21]. The plane for the measurement was virtually rotated within the 3D dataset to achieve an exact congruency to the bone axis of talus and first metatarsal.

The calcaneal pitch angle was defined as the angle created between a straight line, a line between the lowest part of the posterior calcaneal process and the lowest part of the anterior calcaneal process (Fig. 4.3b) [9]. The plane for the measurement was virtually rotated within the 3D dataset to achieve an exact congruency to a parasagittal plane.

Bone axes (talus, first metatarsal) were defined as the straight line between the centers of the bones proximally and distally. These bone centers were defined by

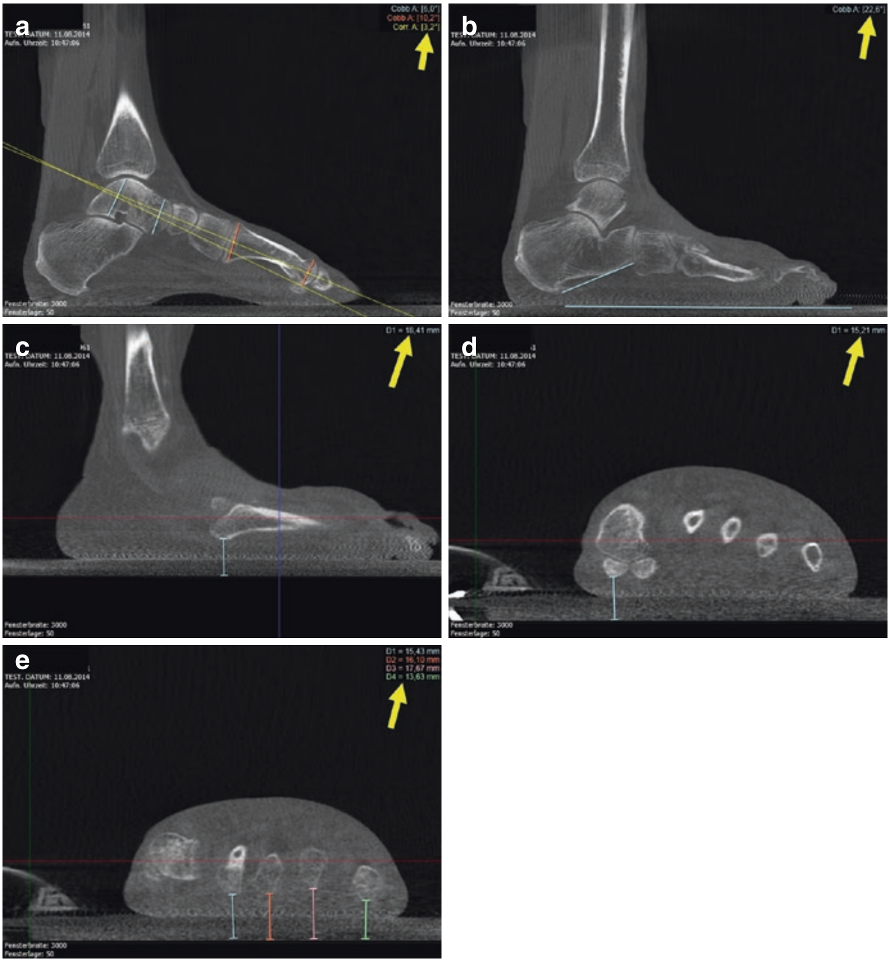

Fig. 4.3 WBCT software screens showing examples of some angle and distance measurements. (**a**) Lateral TMT angle (arrow); (**b**) calcaneal pitch angle; (**c**) minimum height 5th metatarsal base to footplate; (**d**) height medial sesamoid; (**e**) height 2nd–5th metatarsal heads. The lines that define the centers of the bones proximally or distally are exactly 50% of the measured entire bone thickness

linear measurements (Fig. 4.3a). The TMT angles were defined to be negative for angle corresponding to a dorsiflexion [21].

The minimum height of 5th metatarsal base, 2nd–5th metatarsal heads, and medial sesamoid was defined as the minimum distance between the footplate and the 5th metatarsal base (Fig. 4.3c), medial sesamoid (Fig. 4.3d), and 2nd–5th metatarsal heads and (Fig. 4.3e). The plane for the measurement was virtually shifted within the 3D dataset to display the lowest part of the relevant bone.

Measurement of Pedographic Parameters

A standard computerized mapping to create a distribution into the following foot regions was performed with the standard software (Automask, Novel, Munich, Germany): hindfoot, midfoot, 1st metatarsal head/sesamoids area, 2nd metatarsal head, 3rd metatarsal head, 4th metatarsal head, 5th metatarsal head, 1st toe, 2nd toe, and 3rd–5th toe (Fig. 4.4) [22]. This mapping process does not include manual determination of landmarks [22]. The outlines of the foot and the different regions are determined by the software using an algorithm as reported [17]. This software algorithm is based on geometric characteristics of a maximum pressure picture using an individual sensing threshold [22]. The following parameters were registered within the defined foot regions: midfoot contact area, maximum force midfoot, maximum force midfoot lateral, maximum force entire foot, and maximum pressure 1st to 5th metatarsal head area. The parameter maximum force midfoot was defined as the maximum force in the entire midfoot region (Fig. 4.4). The parameter maximum force midfoot lateral was defined as maximum force in the lateral sensor row of the midfoot region (Fig. 4.4).

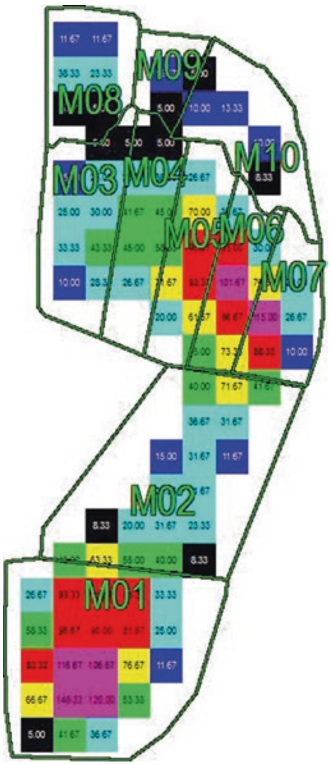

Fig. 4.4 Image from the pedography after computerized mapping. The following regions are defined by the mapping process: M1, hindfoot; M2, midfoot; M3, 1st metatarsal head/sesamoids area; M4, 2nd metatarsal head; M5, 3rd metatarsal head; M6, 4th metatarsal head; M7, 5th metatarsal head; M8, 1st toe; M9, 2nd toe; M10, 3rd–5th toe

Correlation Analysis of WBCT Parameters with Pedography Parameters

Lateral TMT, calcaneal pitch angle, and minimum height of fifth metatarsal base were each correlated with midfoot contact area, maximum force midfoot, maximum force midfoot lateral, and maximum force entire foot (Fig. 4.5). The minimum height of 2nd–5th metatarsal heads and medial sesamoid was correlated with the maximum pressure of the corresponding 1st to 5th metatarsal head area.

Fig. 4.5 Correlation of WBCT ((**a**) slice thickness increased for better visualization) and pedography (**b**). The height of the medial sesamoid was 20.3 mm (mean), and the height of the 2nd–5th metatarsals was higher (2nd, 27.6 mm; 3rd, 27.4 mm; 4th, 27.0 mm; 5th, 26.4 mm, measurement not shown). The maximum pressures were 116.7 kPa for the 1st metatarsal and lower for the 2nd–5th metatarsals (2nd, 73.3 kPa; 3rd, 45.0 kPa; 4th, 30.0 kPa; 5th, 13.3 kPa). In conclusion, the lower 1st metatarsal/medial sesamoid resulted in higher pressure than the higher 2nd–5th metatarsals

Statistics

The statistical analysis was performed in cooperation with the Institute for Biometry and Statistics of the affiliated university with IBM® SPSS® Statistics (Version 22.0.0.0, IBM, Armonk, NY, USA). The WBCT parameters were compared for intra- and interobserver (ANOVA with post hoc Scheffe test). The correlation of the WBCT parameters with the pedography parameters was performed with Pearson test. Significant correlation was considered as $p < 0.05$. Sufficient correlation was considered as $r > 0.8$ or <-0.8.

Results

Table 4.1 shows the descriptive statistics of all WBCT and pedography parameters.

Measurements of Bone Position (Angles and Distances): Intra- and Interobserver Reliability

Regarding intraobserver reliability, the angles and distances did not differ between measurement 1, measurement 2, and measurement 3 of all measured WBCT parameters for all three investigators (ANOVA, each $p > .8$, power >.8).

Regarding interobserver reliability, the angles and distances did not differ between the three investigators for measurement 1, measurement 2, and measurement 3 of all measured WBCT parameters (ANOVA, each $p > .8$, power >.8).

Correlation of WBCT Parameters with Pedography Parameters

Table 4.2 shows the correlation of WBCT parameters with pedography parameter. The correlation between angles and heights from the WBCT data with force/pressure distribution from the pedography data was not significant (each $p > 0.05$) except for lateral talo-first metatarsal (TMT) angle versus midfoot contact area ($p = 0.02$) and maximum force entire foot ($p = 0.01$) and minimum height fifth metatarsal base versus maximum force midfoot lateral ($p = 0.05$). The correlation coefficient for these correlations was not sufficient (lateral talo-first metatarsal (TMT) angle versus midfoot contact area ($r = -0.32$) and maximum force entire foot ($r = 0.38$) and minimum height fifth metatarsal base versus maximum force midfoot lateral ($r = -0.27$)). In conclusion, no sufficient correlation was found.

Table 4.1 Descriptive statistics of all measured WBCT and pedography parameters

	TL (°)	C (°)	H5P (mm)	H1 (mm)	H2 (mm)	H3 (mm)	H4 (mm)	H5 (mm)	MC (cm^2)	MF (N)	MFLAT (N)	FMAX (N)	P1 (kPa)	P2 (kPa)	P3 (kPa)	P4 (kPa)	P5 (kPa)
Mean	−8.3	18.1	21.5	16.4	19.1	18.2	17.5	16.0	18.7	41.7	33.6	375.3	56.5	50.7	50.0	43.8	34.5
Min	−38.0	5.4	15.7	12.8	14.5	13.2	13.6	12.4	3.4	2.8	1.5	52.4	0.0	0.0	0.0	0.0	0.0
Max	14.3	33.5	47.4	28.2	25.9	26.6	25.8	25.4	44.0	203.5	112.8	563.2	355.0	120.0	103.3	100.0	256.7
Std	9.3	5.4	5.2	2.9	2.5	2.1	2.1	2.2	8.5	41.8	28.4	98.2	58.7	27.2	23.4	22.5	38.0

TL lateral talo-1st metatarsal (TMT) angle, *C* calcaneal pitch angle, *H5P* minimum height 5th metatarsal base, *H1* height medial sesamoid, *H2–H5* height 2nd–5th metatarsal heads, *MC* midfoot contact area, *MF* maximum force midfoot, *MFLAT* maximum force midfoot lateral, *FMAX* maximum force entire foot, *P1–P5* maximum pressure 1st to 5th metatarsal, *Min* minimum, *Max* maximum, *Std* standard deviation

Table 4.2 Correlation of WBCT parameters with pedography parameters

		MC (cm^2)	MF (N)	MFLAT (N)	FMAX (N)	
TL (°)	r	−0.32	−0.14	−0.14	−0.38	
	p	**0.02**	0.34	0.33	**0.01**	
C (°)	r	−0.11	−0.13	−0.11	0.00	
	p	0.46	0.37	0.44	0.98	
H5P (mm)	r	−0.24	−0.26	−0.27	0.06	
	p	0.09	0.07	**0.05**	0.68	
		P1 (kPa)	P2 (kPa)	P3 (kPa)	P4 (kPa)	P5 (kPa)
H1 (mm)	*r*	−0.02				
	p	0.90				
H2 (mm)	*r*		−0.22			
	p		0.13			
H3 (mm)	*r*			−0.11		
	p			0.45		
H4 (mm)	*r*				−0.22	
	p				0.12	
H5 (mm)	*r*					−0.14
	p					0.35

The bold values are statistically significant values
Parameters, *TL* lateral talo-1st metatarsal angle (TMT) angle, *C* calcaneal pitch angle, *H5P* minimum height 5th metatarsal base, *H1* height medial sesamoid, *H2–H5* height 2nd–5th metatarsal heads, *MC* midfoot contact area, *MF* maximum force midfoot, *MFLAT* maximum force midfoot lateral, *FMAX* maximum force entire foot, *P1–P5* maximum pressure 1st to 5th metatarsal

Discussion

This is the first study analyzing the direct correlation of bone position and force/pressure distribution with simultaneous radiographic 3D imaging and pedography and full weight bearing. This correlation as such seems to be logical, but it has not been shown from a scientific point of view.

Angle Measurement: Intra- and Interobserver Reliability

The intra- and interobserver reliability was sufficient for the measurements with WBCT. This is probably based on the digital software-based measurements and the experience of all three investigators regarding these kinds of digital measurements. In the future, an automatic software-based angular measurement between bones in the 3D dataset will be implemented. This will allow for investigator-independent analysis of these angles. The advantage of investigator-independent definition of parameters has been shown for the pedography as described above [17].

Correlation of WBCT Parameters with Pedography Parameters

The correlation between angles/heights from the WBCT data with force/pressure distribution from the pedography data was not significant except for lateral talo-first metatarsal (TMT) angle versus midfoot contact area and maximum force entire foot and minimum height fifth metatarsal base versus maximum force midfoot lateral. However, the correlation coefficient for these correlations was not sufficient with −0.32, −0.38, and −0.27. In conclusion, no sufficient correlation was found. When analyzing all single cases in more detail, some typical associations between bone position and pressure or force distribution were observed as, for example, shown in Fig. 4.5. Still, these case limited parameters did not lead to statistical significant ($p < 0.05$) and sufficient ($r > 0.8$ or <-0.8) correlation. This finding is very surprising and disturbing. Everybody would expect, as we did before the study, that there must be a high correlation between bone position and force/pressure distribution. We did extensively discuss the reasons for the missing statistical correlation within our study group. We could not find a convincing explanation. We wondered if we possibly choose the wrong parameters. One could argue that parameters like lateral TMT angle or calcaneal pitch angle might not be appropriate. However, the height of the metatarsal heads, medial sesamoid, or proximal fifth metatarsal seems to be very comprehensive parameters to correlate with forces and pressures under these bony structures. We thought that different body weight might influence the results. So we also used individual multiplication factors to standardize all pedography parameters patients to a standard weight or better total force (data not shown). However, this did also not lead to any statistical sufficient correlation.

There is no comparison of our results with results from the literature possible because no such measurement has been performed and reported so far.

Shortcomings of the Study

The shortcomings of this study are not the typical ones like missing analysis of intra- and/or interobserver reliability or missing power analysis of the statistical test. The low case number might be a shortcoming. We feel that a (much) higher case number would also not have led to more significant correlations of WBCT parameters with pedography parameters. With 50 patients, we "reached" very low correlation coefficients of less than 0.4 (or more than −0.4, respectively), which questions if any higher case number may lead to a sufficient correlation of >0.8 or <−0.8. We did not measure how difficult and time consuming the WBCT measurement were. The reason for this is that the type of software and version and above all the experience of the investigator might influence this time much more than the method as such. Finally, the potential foot pathologies of the subjects were registered but not analyzed. The pathological angles (lateral TMT angle, −8.3°, calcaneal pitch angle, 18.1° on average) imply that relevant pathologies were present which is also based on the inclusion criteria. However, we did not want to investigate different pathologies but the correlation of WBCT parameters with pedography parameters. Pedography to date is a dynamic method utilized for the detection and analysis of the entire stance phase during gait and not only for standing position, i.e., static pedography. We measured a static quality of the foot, and we are aware that this is not directly related to the dynamic mechanics of the foot [9]. We did not design the introduced method to mimic a dynamic pedography [9]. It has been previously shown and was discussed above that a static pedography also allows conclusion about the biomechanics of the foot [8, 9, 13, 14].

Radiation Dose

The radiation dose of the WBCT was not investigated in this study. However, the radiation dose is a principal concern [9]. Recently, the dose of foot/ankle radiographs, CT, and WBCT was measured and analyzed using a foot and ankle phantom [23]. The dose for adults for three radiographs from one foot (dorsoplantar + lateral + oblique) was 0.7 μSv, the dose for a bilateral WBCT scan 4.3 μSv, and the dose for conventional CT of one foot/ankle 25 μSv [23]. This means that a bilateral WBCT scan has a comparable dose of 18 unilateral radiographs of the foot and 17% of a unilateral CT of the foot and ankle [23]. This study did also measure the dose of a unilateral WBCT scan which was 1.4 μSv comparable to six unilateral radiographs of the foot and 5.6% of a unilateral CT of the foot and ankle [23]. For the later clinical use, this radiation dose is relativized because virtual radiography could be created from the WBCT data [9]. We have created the following virtual radiographs from the WBCT scan data: entire foot dorsoplantar and lateral views, ankle dorsoplantar, mortise and lateral views, Saltzman views, metatarsal head skyline views, and Broden's views (all views bilateral) [9].

In conclusion, 3D bone position did not correlate with force and pressure distribution under the foot sole during simultaneous WBCT scan and pedography. Consequently, the bone positions measured with WBCT do not allow conclusions about the force and pressure distribution. Vice versa static pedography parameters do not allow conclusions about the 3D bone position. Further investigations with higher case number and more parameters should be carried out to further validate these surprising findings.

References

1. Richter M, Zech S, Hahn S, Naef I, Merschin D. Combination of pedCAT for 3D imaging in standing position with pedography shows no statistical correlation of bone position with force/pressure distribution. J Foot Ankle Surg. 2016;55(2):240–6.
2. Zwipp H. Biomechanik der Sprunggelenke. Unfallchirurg. 1989;92(3):98–102.

3. Zwipp H. Chirurgie des Fusses. Wien, New York: Springer; 1994.
4. Marti RK, de Heus JA, Roolker W, Poolman RW, Besselaar PP. Subtalar arthrodesis with correction of deformity after fractures of the os calcis. J Bone Joint Surg Br. 1999;81(4):611–6.
5. Easley ME, Trnka HJ, Schon LC, Myerson MS. Isolated subtalar arthrodesis. J Bone Joint Surg Am. 2000;82(5):613–24.
6. Rammelt S, Grass R, Zawadski T, Biewener A, Zwipp H. Foot function after subtalar distraction bone-block arthrodesis. A prospective study. J Bone Joint Surg Br. 2004;86(5):659–68.
7. Trnka HJ, Easley ME, Lam PW, Anderson CD, Schon LC, Myerson MS. Subtalar distraction bone block arthrodesis. J Bone Joint Surg Br. 2001;83(6):849–54.
8. Richter M, Zech S. Leonard J. Goldner Award 2009. Intraoperative pedobarography leads to improved outcome scores: a Level I study. Foot Ankle Int. 2009;30(11):1029–36.
9. Richter M, Seidl B, Zech S, Hahn S. PedCAT for 3D-imaging in standing position allows for more accurate bone position (angle) measurement than radiographs or CT. Foot Ankle Surg. 2014;20:201–7.
10. Rosenbaum D, Becker HP, Sterk J, Gerngross H, Claes L. Functional evaluation of the 10-year outcome after modified Evans repair for chronic ankle instability. Foot Ankle Int. 1997;18(12):765–71.
11. Cavanagh PR, Henley JD. The computer era in gait analysis. Clin Podiatr Med Surg. 1993;10(3):471–84.
12. Cavanagh PR, Rodgers MM, Iiboshi A. Pressure distribution under symptom-free feet during barefoot standing. Foot Ankle. 1987;7(5):262–76.
13. Grieve DW, Rashdi T. Pressures under normal feet in standing and walking as measured by foil pedobarography. Ann Rheum Dis. 1984;43(6):816–8.
14. Inman VT, Ralston HJ, Todd F. Human walking. Baltimore: Williams & Wilkins; 1981.
15. Alexander IJ, Chao EY, Johnson KA. The assessment of dynamic foot-to-ground contact forces and plantar pressure distribution: a review of the evolution of current techniques and clinical applications. Foot Ankle. 1990;11(3):152–67.
16. Becker HP, Rosenbaum D, Zeithammer G, Gerngross H, Claes L. Gait pattern analysis after ankle ligament reconstruction (modified Evans procedure). Foot Ankle Int. 1994;15(9):477–82.
17. Cavanagh PR, Ulbrecht JS, Caputo GM. Elevated plantar pressure and ulceration in diabetic patients after panmetatarsal head resection: two case reports. Foot Ankle Int. 1999;20(8):521–6.
18. Rosenbaum D, Engelhardt M, Becker HP, Claes L, Gerngross H. Clinical and functional outcome after anatomic and nonanatomic ankle ligament reconstruction: Evans tenodesis versus periosteal flap. Foot Ankle Int. 1999;20(10):636–9.
19. Talbot KD, Saltzman CL. Assessing sesamoid subluxation: how good is the AP radiograph? Foot Ankle Int. 1998;19(8):547–54.
20. Yildirim Y, Cabukoglu C, Erol B, Esemenli T. Effect of metatarsophalangeal joint position on the reliability of the tangential sesamoid view in determining sesamoid position. Foot Ankle Int. 2005;26(3):247–50.
21. Richter M, Zech S. Lengthening osteotomy of the calcaneus and flexor digitorum longus tendon transfer in flexible flatfoot deformity improves talo-1st metatarsal-index, clinical outcome and pedographic parameter. Foot Ankle Surg. 2012;19(1):56–61.
22. Richter M, Frink M, Zech S, Vanin N, Geerling J, Droste P, Krettek C. Intraoperative pedography: a validated method for static intraoperative biomechanical assessment. Foot Ankle Int. 2006;27(10):833–42.
23. Ludlow BW, Ivanovic M. Weightbearing CBCT, MDCT, and 2D imaging dosimetry of the foot and ankle. Int J Diagnostic Imaging. 2014;1(2):1–9.

Chapter 5
Combination of Weight Bearing CT (WBCT) with Pedography Shows Relationship Between Anatomy-Based Foot Center (FC) and Force/Pressure-Based Center of Gravity (COG)

Martinus Richter

Introduction

Weight bearing CT (WBCT) is a technology that allows 3D imaging with full weight bearing which is not influenced by projection and/or foot orientation [1, 2]. In the first published study, specific bone position (angle) measurements using WBCT were compared with conventional weight bearing radiographs and conventional non weight bearing CT [2]. The angles differed between radiographs, CT, and WBCT, indicating that only WBCT is able to detect the correct angles, i.e., bone position [2]. In a subsequent study, the correlation between 3D bone position and pedographic measurements, i.e., force and pressure (distribution), has been investigated [3]. In that study, 3D bone position did not correlate with force and pressure distribution under the foot sole during simultaneous WBCT scan and pedography [3]. Consequently, the bone positions measured with WBCT did not allow conclusions about the force and pressure distribution in this static configuration [3]. Vice versa, pedography parameters did not allow conclusions about the 3D bone position [3]. One conclusion was that further investigations with higher case number and more other parameters should be carried out to further validate these surprising findings [3]. Meanwhile, center of gravity (COG) and foot center (FC) were discussed to be important parameters for biomechanical assessment around foot and ankle and consequently as basis for diagnostics and planning of corrective surgeries and/or joint replacement [4, 5]. In particular, a semiautomatic system (TALAS, CurveBeam, Warrington PA, USA) designed to measure hindfoot alignment as a 3D biometric uses the anterior midline of the forefoot (which joins the FC with the midpoint between the first and the fifth metatarsal heads) as a landmark for hindfoot alignment [4]. The aim of this study was to analyze the difference between

Based on Richter M, Lintz F, Zech S, Meissner SA. Combination of PedCAT weight bearing CT with pedography shows relationship between anatomy-based foot center (FC) and force/pressure-based center of gravity (COG). Foot Ankle Int. 2018;39(3): 361–368.

M. Richter et al., *Weight Bearing Cone Beam Computed Tomography (WBCT) in the Foot and Ankle*, https://doi.org/10.1007/978-3-030-31949-6_5

morphology- and anatomy (bone/WBCT)-based FC, calculated as the intersection of the median lines of the triangular-based pyramid model of the foot and force/pressure (pedography)-based COG. Motion of COG during WBCT/pedography scan should also be assessed as potential source for bias. For this study, a customized pedography sensor (Pliance, Novel, Munich, Germany) was inserted into a WBCT as described previously [3]. Our hypothesis was that the FC should be a good predictor of mediolateral position of the COG but not longitudinal since the anatomy of the hindfoot allows free anteroposterior movement but limited mediolateral.

Methods

In a prospective, comparative, and consecutive study starting November 28, 2016, 90 patients (180 feet) were included [6]. A WBCT scan with simultaneous pedography with full weight bearing in standing position was performed (Fig. 5.1). A customized pedography sensor (Pliance, Novel, Munich, Germany) was inserted into the WBCT and connected to a PC with the standard software installed (Expert, Novel, Munich, Germany) (Fig. 5.1) [3]. Demographic data and underlying foot and ankle pathologies were registered.

Inclusion and Exclusion Criteria, Ethics

The inclusion criteria were age ≥18 years, presentation at the local foot and ankle outpatient clinic, and indication for WBCT. The indication for WBCT was defined according to local practice as described previously [2]. These indications have recently evolved to include all the patients presenting at our institution except initial postoperative follow-up radiographs without weight bearing.

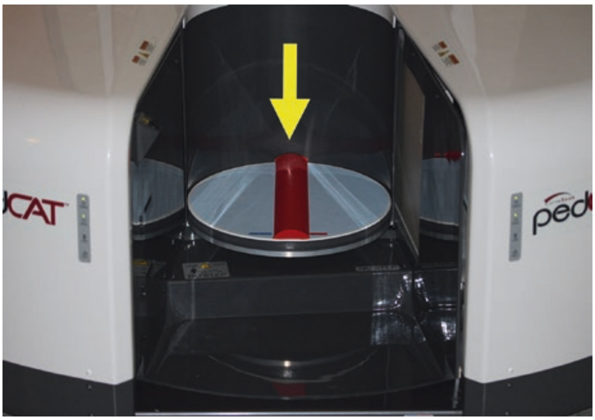

Fig. 5.1 WBCT with pedography sensor (arrow). An X-ray emitter and a flat panel sensor on the opposite side are rotating horizontally around the feet. Resolution and contrast which are the principal parameters for image quality are comparable with modern conventional CT

The exclusion criteria were age <18 years, no indication for WBCT imaging, and participation in other studies.

Approval from the local ethical committee was granted based on the indications as described above. Informed consent was obtained from all subjects.

Image Acquisition: Foot Center (FC)

The patients walked into the device and were positioned in bipedal standing position (Fig. 5.1). Technically, an X-ray emitter and a flat panel sensor on the opposite side are rotating horizontally around the feet. Resolution and contrast which are the principal parameters for image quality are comparable with modern conventional CT [2]. The acquisition time was 52 seconds. The morphology-based definition of the FC was performed with the WBCT data following the Torque Ankle Lever Arm System (TALAS) algorithm (Fig. 5.2a) [4]. The software takes four bony landmarks into consideration (lowest point of posterior calcaneal process, center of ankle joint, lowest or weight bearing points of metatarsal heads 1 and 5). These landmarks are manually pointed out by the clinician using the MPR windows. This remains necessary as part of a semiautomatic process with the early version of the TALAS (CurveBeam, Warrington PA, USA) software used for this study. Future versions of this will include automatic detection of the landmarks. This defines a 3D volume as opposed to a 2D angle and allows for precise evaluation of hindfoot alignment, given as the foot ankle offset (FAO) (Fig. 5.2b) [4]. The software includes a semiautomatic database (requiring manual input of the clinical record) which stores the 3D coordinates of the points, allowing further anonymous retrieval of the latter and secondary calculation of FC position.

Pedography: Center of Gravity (COG)

The data of the pedography sensor was gathered during the entire WBCT scan (52 seconds). The force/pressure-based COG was defined with the pedography data using a software-based algorithm (Fig. 5.3) [3]. COG motion during data acquisition was recorded and analyzed.

Comparison of FC/COG

The images with the FC (Fig. 5.4a) and COG (Fig. 5.4b) were semiautomatically superimposed (Fig. 5.4c). The average position of COG during acquisition time was used for this superimposition. The distance between FC and COG (Fig. 5.4c) and the direction of a potential shift (distal-proximal; mediolateral) were measured and

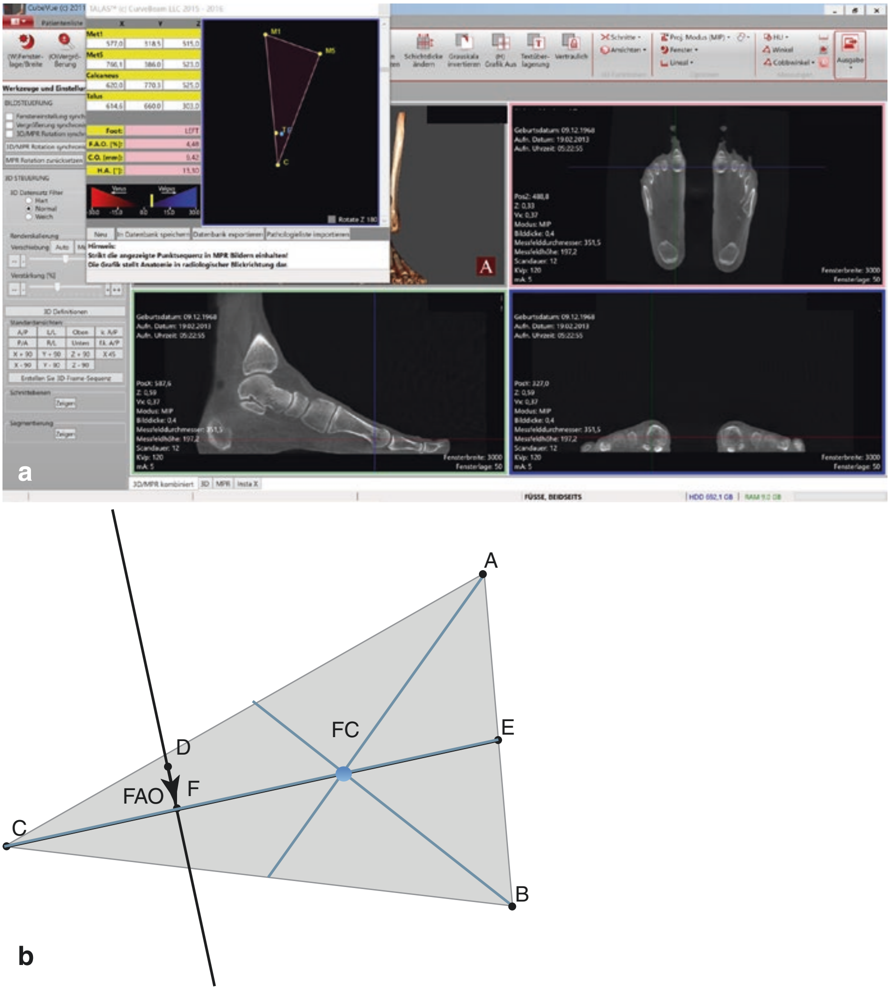

Fig. 5.2 (**a**) The WBCT software screen view with foot center (FC) definition with TALAS (top left), axial reformation (top right, red frame), parasagittal reformation (bottom left, green frame) and coronal reformation (bottom right, blue frame). The standard view is with 1 mm slice thickness. For the definition of FC (F in image), the following landmarks are used: lowest point of posterior calcaneal process (C), center of talar dome/tibial plafond (T), lowest point of the first metatarsal head (M1), and lowest point of the fifth metatarsal head (M5). (**b**) The triangular-based pyramid model of the foot with foot ankle offset (where D is the projection of the center of the ankle, C the calcaneus weight bearing point, A the first metatarsal head, B the fifth metatarsal head), FC (foot center), E is the midpoint between M1 and M5

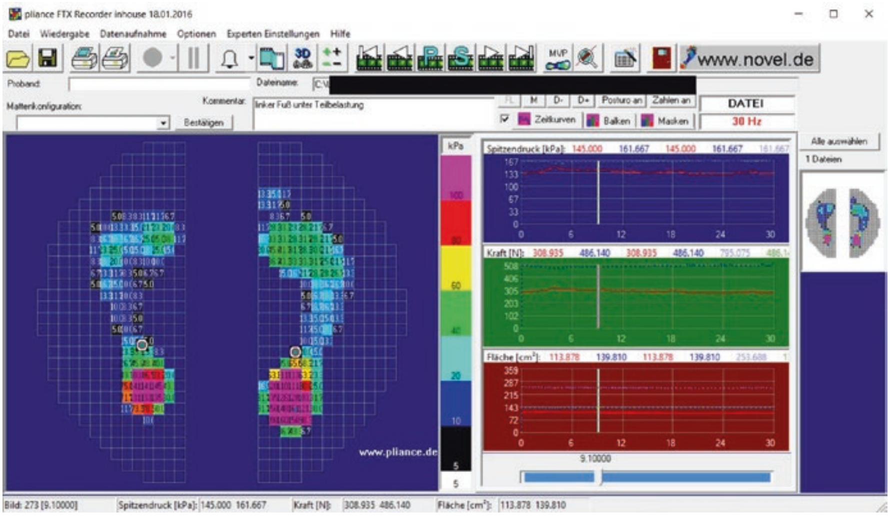

Fig. 5.3 Pedography software screen view showing the center of gravity (COG) for each foot (circles)

analyzed. The pedographic images include a raster with 10 × 10 mm squares that correspond to the different sensor fields with this exact geometric size (e.g., Fig. 5.3b, c). This raster was used as reference for the measurements.

Statistics

The statistical analysis was performed with Microsoft Excel 2016 (Microsoft, Redmond, WA, USA) and SPSS 24.0 (IBM, Rochester, MN, USA). The data (distances/shift between FC and COG) was successfully tested for normal distribution with a Shapiro-Wilk test. A bilateral paired t-test was used to compare data from the left to the right foot. One-way ANOVA with potential post hoc Scheffe test was used for data comparison between different pathologies. Pearson test (two sided) was used for correlation of BMI with measured data (distances/shift between FC and COG). Correlation was defined as significant when $p < 0.05$ and when significant then sufficient when $r > 0.5$ or $r < -0.5$.

Results

Mean age of patients was 53.8 on average (range, 17–84) years, and 57 (63%) were female. Height was 171 cm on average (range 169–184), weight 71.4 kg (range, 43–108), and BMI 24.3 kg/m^2 (range, 15.6–34.8). Table 5.1 shows the registered

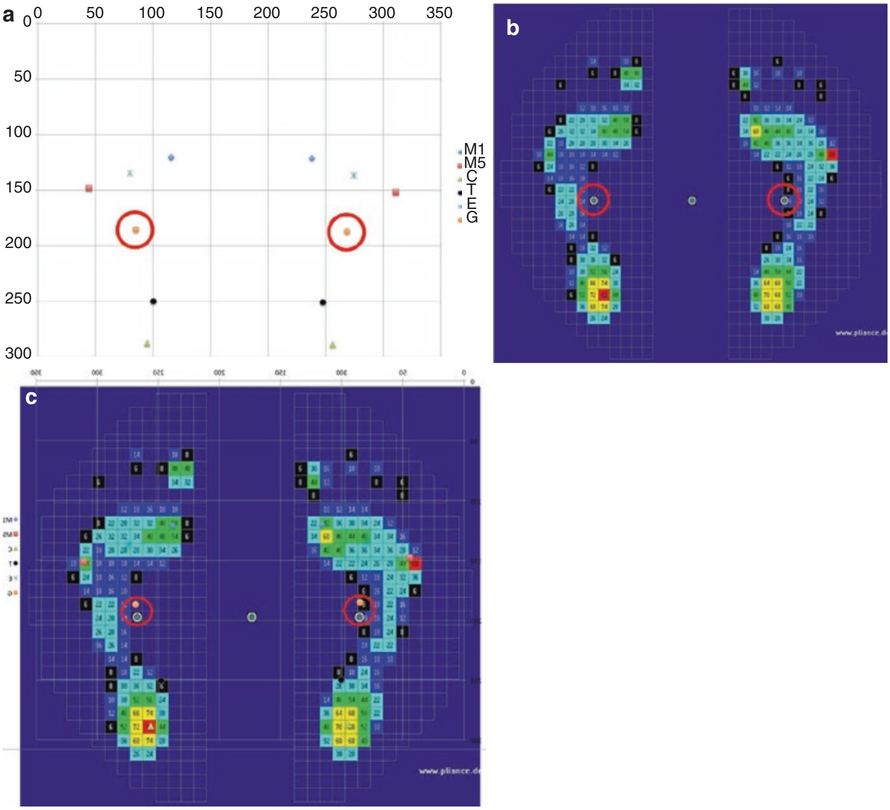

Fig. 5.4 (**a**) An exported image from TALAS with FC of both feet (yellow points in red circles, labelled with G). The right foot is displayed on the left side. For the definition of FC, the following landmarks are used: lowest point of posterior calcaneal process (C, green triangles), center of talar dome/tibial plafond (T, black point), lowest point of the first metatarsal head (M1, blue rhombus), and lowest point of the fifth metatarsal head (M5, red square). (**b**) An exported image from the pedography software with the COG (white/blue points in red circles) of each foot. The right foot is displayed on the right side. The squares have a size of 10 × 10 mm. The numbers in some squares show the measured pressure (kPa), and the different colors are coding different pressure values. (**c**) The superimposition of the TALAS and pedography images (**a**, **b**). FC (red points) and COG (white/blue points) both surrounded by red circle. The TALAS image was horizontally mirrored for superimposition of the same foot side. The right foot is displayed on the right side for the TALAS and pedography image

pathologies. Fifty-two patients (29%) had unilateral pathologies and 128 (71%) bilateral pathologies. Maximum COG motion during the 68 seconds pedography scan was 1.2 mm on average (range, 0–4.8 mm). Table 5.2 shows measurements of position differences of COG and FC. The distance between FC and COG was 28.7 mm on average (range, 0–60). FC was distal to COG in 175 feet (97%) (mean, 27.5 mm; range, −15 to 60) and lateral in 112 feet (52%; mean, 2.0 mm; range, −18 to 20). No distal or proximal shift of FC occurred in 4 feet (2%) and proximal shift

Table 5.1 Registered foot and ankle pathologies in 180 feet in 90 patients

Pathology	*n*	%
Isolated hallux valgus	10	6
Complex forefoot deformity	24	13
Hallux rigidus	5	3
Flatfoot	18	10
Cavus foot	10	6
Other combined deformities	18	10
Ankle instability	20	11
Osteoarthritis without relevant deformity	23	13
None	52	29

Complex forefoot deformity, hallux valgus plus lesser ray deformities. Hallux rigidus, only cases without deformity, i.e., hallux valgus. Flatfoot might include hindfoot valgus. Cavus foot might include hindfoot varus. Ankle instability, only cases without relevant deformity such as hindfoot valgus/varus

Table 5.2 Measurements of position differences of the center of gravity (COG) and foot center (FC)

Parameter		Right ($n = 90$)	Left ($n = 90$)	Bilateral ($n = 180$)	t-test r/l
		mm	mm	mm	P
Distal-proximal	Mean	27.3	27.8	27.5	0.8
	std	13.3	13.4	13.3	
	min	0	−15	−15	
	max	60	60	60	
Mediolateral	Mean	1.8	2.2	2.0	0.5
	std	4.9	4.5	4.7	
	min	−18	−11	−18	
	max	10	20	20	
Distance	Mean	28.1	29.0	28.7	0.7
	std	13.4	12.8	12.9	
	min	−16	0	0	
	max	60	60	60	

Parameter *distal-proximal*, distance in exact distal to proximal direction between COG and FC. Positive value means that COG is *proximal* to FC and negative value that COG is *distal* to FC
Parameter *mediolateral*, distance in exact medial to lateral direction between COG and FC. Positive value means that COG is *medial* to FC and negative value that COG is *lateral* to FC
Parameter *distance*, distance between COG and FC. Negative value not possible, value "0" means no distance between COG and FC
std standard deviation, *min* minimum, *max* maximum, *t-test r/l* t-test right foot versus left foot

in 1 (1%). No lateral or medial shift of FC occurred in 35 feet (19%) and medial shift in 33 (18%). The variation was high as shown by high standard deviations. No difference between the right and left side occurred (t-test, each $p \geq 0.5$). No difference between pathology groups occurred (One-way ANOVA, distance FC/COG, $p = 0.62$; mediolateral shift, $p = 0.48$; distal-proximal shift, $p = 0.53$, post hoc test not applicable). No significant correlation with BMI occurred (Pearson, distance FC/COG, $p = 0.36$; mediolateral shift, $p = 0.91$; distal-proximal shift, $p = 0.20$, R-value irrelevant due to missing significance).

Discussion

This is the first study analyzing the correlation between the positions of the force/pressure-based COG and the anatomy/morphology-based FC.

Center of Gravity (COG)

COG is an important biomechanical parameter [7–11]. It is principally a function of force, related to body weight (COG force (N) = body weight (Kg) × g (acceleration of gravity). COG is typically related to the entire body which is the typical case during unipedal stand or the stance phase during gait [7–11]. During bipedal stand, each foot can be considered for a COG. It correlates with axes of the entire leg, tibia (lower leg), and hindfoot axis. It is influenced by deformities of the leg (varus/valgus/antecurvation/recurvation) and/or foot (hindfoot valgus/valgus, flatfoot, etc.) [12]. It changes its position in relation to the foot during the stance phase of gait. COG has itself influence on forces/torques/moments, for example, in the ankle with or without replacement. COG is adequately defined with software-based analysis of pedography data [13]. It can be considered that strictly from the point of view of physics, if we do not take into account the actions of the muscles and the soft tissues, the COG of the whole body has to be situated vertically above the mathematical center of gravity of the weight bearing surface of the foot [14]. However, in reality, the activity of the muscles will have an influence on the position of COG. In this case, what should be observed is that this activity maintains the COG laterally. The longitudinal position should be more variable since the anteroposterior axis corresponds to the main degree of freedom of the ankle joint.

Foot Center (FC)

FC is defined based on a "function" of the morphology of the foot and mainly the bone shape and position [15, 16]. It corresponds to the mathematical center of a simple, triangular-based pyramid model of the foot. As COG, it is principally an important biomechanical parameter [4]. It is influenced by foot deformities (hindfoot valgus/valgus, flatfoot, etc.) [12]. In contrast to COG, FC is not influenced by deformities of the leg above the ankle (varus/valgus/antecurvation/recurvation) and does not change during the gait stance phase [16]. As COG, FC has influence on forces/torques/moments, for example, in the ankle with or without total joint replacement. FC is adequately defined with a semiautomatic software (TALAS, CurveBeam, Warrington PA, USA) based on WBCT data and a mathematical algorithm [4]. TALAS was designed to provide computerized, semiautomatic, and automatic 3D biometrics of the foot and ankle [4].

As outlined above, both COG and FC are potentially important parameters for foot morphology and especially biomechanics. Both have been investigated but not together in one investigation as far as we know [4, 7–11, 13, 15, 16]. The technical possibilities have not been present before 2016, the combination of WBCT and pedography has been firstly established in 2014, and TALAS was developed in 2016 [3, 4]. One would expect that COG and FC are not completely congruent because they are a function of different parameters (force/morphology). As expected, there was a spatial difference between FC and COG. This "expected" finding was quantified with this study (Table 5.2). The shift between COG and FC in the investigated 180 feet was relevant in the longitudinal axis (FC was 27.5 mm distal to COG) and relatively minor in the mediolateral axis (average shift of 2 mm) with a high variability, which probably accounts for individual variations of the rest position among patients. FC was distal to COG in 175 feet (97%) and lateral in 112 feet (52%; mean, 2.0 mm; range, −18 to 20). No difference between the right and left side occurred. The interpretation of this data is difficult, and no comparable data have been reported in the literature so far. COG is the more biomechanical parameter and is located proximally in almost all investigated feet and medially in the majority of the feet in relation to FC, representing the more morphology-based parameter. This finding is just a fact but what does this mean? We formulate the following explanation: mediolateral shift is symmetrical, indicating simple oscillations of the mean rest position across our population, which has a 50/50% chance of being measured lateral or medial, while the anterior shift is explained by a spontaneous anterior shift at rest to balance posterior chain muscular balancing mediated by the Achilles tendon. Our practical interpretation and recommendation is that this data and findings stand alone to date as additional research and clinical parameters for foot and ankle. The data could be a basis for prediction of COG based on FC without additional pedography. The definition of COG might be taken into consideration for planning and follow-up for corrections/fusion around the hindfoot and for total ankle replacement.

In respect to the potential upcoming rise of weight bearing CT as the new standard for foot and ankle imaging beyond the recent/current golden standard conventional radiographs, these findings confirm the relationship between the TALAS algorithm and the physics of gravitation as described by Newton. In this model, the foot is considered as its own referential in which weight (force) is repeatedly applied on the center of the ankle joint and ground reaction force from the calcaneus weight bearing point on strike, moving anteriorly throughout to the gait to the center of gravity of the forefoot (approximated by the midpoint between M1 and M5), along a straight line. This line has previously been found to be concurrent with experimental findings in the literature and was called "gravitational line" (GL) [11, 14, 17]. According to the TALAS theory, the COG has not to remain over the FC to maintain a standing posture, but over the GL during gait and in a static posture. Any other configuration would cause the body falling over to one side. In normally aligned feet, this means that the center of the ankle joint has to be also in over the GL. In fact, as confirmed by a previous clinical validation study, it is slightly medial in a static position to accommodate the fact that the ankle joint is solidly contained by the medial collateral ligaments and the fibular malleolus which acts as a lateral strut [4]. So, although the WBCT imaging is static, and the FAO a static measurement of hindfoot alignment, this study confirms that it provides relevant information on the biomechanical structure of the foot and ankle, which directly influence its dynamic behavior. One can formulate the hypothesis that if a more precise approximation of the forefoot center of gravity can be integrated in the TALAS software, and the data merged with dynamic pedography, an even closer correlation may be found in the future. Upcoming studies might also investigate different foot and ankle pathologies, i.e., FC/COG and potential spatial differences. We investigated the potential influence of the underlying pathology on the measurements. An influence of different deformities, for example, was expected. However, different pathologies did not show different measurements. Also, a correlation between BMI and the measurements did not occur.

Shortcomings of the Study

The main shortcoming of the study is the semiautomatic superimposition of the different images with the FC from the WBCT/TALAS system and the COG from the pedography system. It would be desirable that the superimposition is fully automatic based on markers that are visible in both datasets (WBCT and pedography). Also, FC definition using data from the TALAS software is also semiautomatic, since the landmarks (lowest point of posterior calcaneal process, center and summit of the talar dome, lowest point of metatarsal heads 1 and 5) are pointed out freehandedly by the user. Even though this method has demonstrated excellent inter- and intraobserver reliability (0.99 and 0.97, respectively), a fully automatic software-based definition of the landmarks and consequently FC would be desirable, less time-consuming, and probably even more reproducible than the current version which still relies on human intervention [4]. Pedography to date is a dynamic method utilized for the detection and analysis of the entire stance phase during gait and not only for standing position, i.e., static pedography. We measured a static state of the foot, and we are aware that this is not directly related to the dynamic mechanics of the foot [3, 17]. We did not design the introduced method to mimic a dynamic pedography [3, 17]. It has been previously shown and was discussed above that a static pedography also allows conclusion about the biomechanics of the foot [17–19]. Another possible shortcoming could have been relevant motion of COG during the 68 seconds of the data acquisition caused by patient’s motion. Our measurements show that the COG did move 1.2 mm on average with a maximum of 4.8 mm which was considered to be not relevant. However, individual variations of the rest position between patients (patients settling down more anteriorly or more posteriorly or inclining more to one side than the other) may explain the observed variations. We did not investigate difference in pressure loading left versus right foot in this study. An earlier study dealing with pedography in bipedal stand showed no pressure differences between the left and right foot [17].

Radiation Dose

The radiation dose of the WBCT was not investigated in this study. However, it remains a concern to provide the best and less invasive methods of investigation for our patients [2, 3]. Recently, the dose of foot/ankle radiographs, CT, and WBCT was measured and analyzed using a foot and ankle phantom [20]. The dose for adults for three radiographs from one foot (dorsoplantar + lateral + oblique) was 0.7 μSv, the dose for a bilateral WBCT scan 4.3 μSv, and the dose for conventional CT of one foot/ankle 25 μSv [20]. This means that a bilateral WBCT scan has a comparable dose as 18 unilateral radiographs of the foot and 17% of a unilateral CT of the foot and ankle [20]. This study did also measure the dose of a unilateral WBCT scan which was 1.4 μSv comparable to six unilateral radiographs of the foot and 5.6% of a unilateral CT of the foot and ankle [20]. For later clinical use, this radiation dose is relativized because virtual radiography can be created from the WBCT data [2].

In conclusion, despite the COG not relevantly moving during combined WBCT/pedography scan in the investigated 180 feet, there was an anterior/distal translation of COG relative to the FC. This expected finding was quantified with this study. FC was 27.5 mm distally and 2 mm laterally relative to FC on average with a high variability. The data could be a basis for prediction of COG based on FC without additional pedography. It also validates the use of TALAS as a relevant and informative hindfoot alignment measure in relation to the forces at stake in the foot and ankle, at least from a static standpoint. Definition of COG might be taken into consideration for planning and follow-up for corrections/fusion around the hindfoot and for total ankle replacement, implying that it would be useful to systematically associate WBCT imaging and pedography or try to merge data from dynamic pedography with WBCT images. Upcoming studies might also investigate different foot and ankle pathologies, i.e., FC/COG and potential spatial difference. Future studies should also evaluate which parameter should be used in the future for preoperative planning and for postoperative control.

References

1. Richter M, Lintz F, Zech S, Meissner SA. Combination of PedCAT weightbearing CT with pedography assessment of the relationship between anatomy-based foot center and force/pressure-based center of gravity. Foot Ankle Int. 2018;39(3):361–8.
2. Richter M, Seidl B, Zech S, Hahn S. PedCAT for 3D-imaging in standing position allows for more accurate bone position (angle) measurement than radiographs or CT. Foot Ankle Surg. 2014;20:201–7.

3. Richter M, Zech S, Hahn S, Naef I, Merschin D. Combination of pedCAT for 3D imaging in standing position with pedography shows no statistical correlation of bone position with force/pressure distribution. J Foot Ankle Surg. 2016;55(2):240–6.
4. Lintz F, Welck M, Bernasconi A, Thornton BJ, Cullen NP, Singh D, Goldberg A. 3D biometrics for hindfoot alignment using weightbearing CT. Foot Ankle Int. 2017;38(6):684–9. https://doi.org/10.1177/1071100717690806.
5. Baverel L, Brilhault J, Odri G, Boissard M, Lintz F. Influence of lower limb rotation on hindfoot alignment using a conventional two-dimensional radiographic technique. Foot Ankle Surg. 2017;23(1):44–9.
6. Richter M, Lintz F, Zech S, Meissner SA. Combination of PedCAT weight bearing CT with pedography shows relationship between anatomy based foot center (FC) and force/pressure based center of gravity (COG). Foot Ankle Int. 2018;39(3):361–8.
7. Davis BL, Cavanagh PR, Perry JE. Locomotion in a rotating space station: a synthesis of new data with established concepts. Gait Posture. 1994;2:157–65.
8. Yu J, Lee G. Comparison of pathway and center of gravity of the calcaneus on non-involved and involved sides according to eccentric and concentric strengthening in patients with Achilles tendinopathy. J Sports Sci Med. 2012;11(1):136–40.
9. Tanaka T, Takeda H, Izumi T, Ino S, Ifukube T. Age-related changes in postural control associated with location of the center of gravity and foot pressure. Phys Occup Ther Geriatr. 1997;15(2):1–14.
10. Salathe EP, Arangio GA. A biomechanical model of the foot: the role of muscles, tendons, and ligaments. J Biomech Eng. 2002;124(3):281–7.
11. Caron O, Gelat T, Rougier P, Blanchi JP. A comparative analysis of the center of gravity and center of pressure trajectory path lengths in standing posture: an estimation of active stiffness. J Appl Biomech. 2000;16(3):234–47.
12. Van Boerum DH, Sangeorzan BJ. Biomechanics and pathophysiology of flat foot. Foot Ankle Clin. 2003;8(3):419–30.
13. Cavanagh PR, Ulbrecht JS, Caputo GM. Elevated plantar pressure and ulceration in diabetic patients after panmetatarsal head resection: two case reports. Foot Ankle Int. 1999;20(8):521–6.
14. Lintz F, Barton T, Millet M, Harries WJ, Hepple S, Winson IG. Ground reaction force calcaneal offset: a new measurement of hindfoot alignment. Foot Ankle Surg. 2012;18(1):9–14.
15. Whittaker EC, Aubin PM, Ledoux WR. Foot bone kinematics as measured in a cadaveric robotic gait simulator. Gait Posture. 2011;33(4):645–50.
16. Morris JM. Biomechanics of the foot and ankle. Clin Orthop Relat Res. 1977;(122):10–7.
17. Richter M, Frink M, Zech S, Vanin N, Geerling J, Droste P, Krettek C. Intraoperative pedography: a validated method for static intraoperative biomechanical assessment. Foot Ankle Int. 2006;27(10):833–42.
18. Grieve DW, Rashdi T. Pressures under normal feet in standing and walking as measured by foil pedobarography. Ann Rheum Dis. 1984;43(6):816–8.
19. Inman VT, Ralston HJ, Todd F. Human walking. Baltimore: Williams & Wilkins; 1981.
20. Ludlow BW, Ivanovic M. Weightbearing CBCT, MDCT, and 2D imaging dosimetry of the foot and ankle. Int J Diagnostic Imaging. 2014;1(2):1–9.

Chapter 6
A New Concept of 3D Biometrics for Hindfoot Alignment Using Weight Bearing CT

Francois Lintz

Introduction

The importance of hindfoot alignment (HFA) in the setting of hindfoot surgery has been described and demonstrated in the literature due to the relationship between alignment and surgical outcome [1–3], as in ankle arthrodesis and arthroplasty [4–11] or in knee arthroplasty [12–16]. HFA measures based on 2D radiographs are flawed by many anatomical and operator-related bias which have been extensively investigated in the literature [17–29]. These include projection and rotation issues [30, 31] mostly with regard to the use of the tibia as a reference axis [32]. Previous studies on the HFA have focused on which technique to use and measurement methods [32–45].

Furthermore, 2D measures traditionally do not account for the contribution of the forefoot in ankle biomechanics. Recently, two publications from different authors [17, 31] have used HFA measures using the forefoot rather than the tibia as a reference, which seems to be one step forward in reducing the bias related to projection and rotation. However, these techniques were still based on 2D radiographs and were complicated to measure and thus were not usable in daily practice.

Today, 3D weight bearing computed tomography (3D WBCT) provides an opportunity to solve the problems associated with 2D biometrics [46, 47]. This could be done by creating a new generation of HFA measures or 3D biometrics based on 3D coordinates rather than trying to force apply older HFA measurements based on 2D angles to this new 3D environment. The ideal criteria for this new kind of tool would be physically meaningful, designed for 3D WBCT, computerized, and verifiable by data.

In this study, we investigated the efficacy of a new system: Torque Ankle Lever Arm System (TALAS™, CurveBeam LLC, 175 Titus Ave, Suite 300, Warrington,

Based on Lintz F, Welck M, Bernasconi A, Thornton J, Cullen NP, Singh D, Goldberg A. 3D biometrics for hindfoot alignment using weight bearing CT. Foot Ankle Int. 2018;38(6): 684–689

M. Richter et al., *Weight Bearing Cone Beam Computed Tomography (WBCT) in the Foot and Ankle*, https://doi.org/10.1007/978-3-030-31949-6_6

PA 18976, USA) designed to satisfy those requirements and used to calculate a computerized, semiautomatic 3D biometric—the foot ankle offset (FAO). It represents the lever arm or the torque generated in the ankle from the combined actions of body weight and ground reaction force. This technique had been previously validated in a simulated 3D weight bearing (WB) environment on 2D radiographs, at a time when 3D WBCT was not readily available [31]. The objective of this study was to describe the distribution of FAO in a series of anonymized datasets from clinically normal, varus, and valgus cases. We hypothesized that normal, varus, and valgus cases should be significantly different and that the distribution should be Gaussian in the normal population. We also assessed the interobserver and intraobserver reliability of the FAO measurement.

Methods

This is a comparative study looking retrospectively at existing data captured as part of routine clinical care. The study was conducted with institutional review board approval.

We analyzed 135 anonymized consecutive datasets, of which 57 were from patients with normal hindfoot alignment (42%), 38 from patients with varus hindfoot alignment (28%), and 40 from patients with valgus hindfoot alignment (30%). All scans were obtained from WBCT scans using the PedCAT™ unit (CurveBeam LLC, 175 Titus Ave, Suite 300, Warrington, PA 18976, USA) installed in the outpatients sector of an orthopedic Foot and Ankle Surgery referral center. The datasets were obtained using the following cone beam scanner settings: voxel size, 0.37 mm; field of view diameter, 350 mm; field of view height, 200 mm; exposure time, 9 seconds; total scan time, 54 seconds. The datasets were extracted from the existing database, containing the 3D image data (Fig. 6.1) and patient demographics limited to side and clinical morphotype.

Datasets were screened by two independent observers using the built-in software, CubeView™ (CurveBeam LLC, 175 Titus Ave, Suite 300, Warrington, PA 18976, USA) and collected the 3D coordinates of specific anatomical landmarks required for the software to process and calculate FAO. Two independent observers collected the 3D coordinates (x, y, z), for the following landmarks: First metatarsal head WB point (A), Fifth metatarsal head WB point (B), Calcaneus WB point (C), Talus centermost and highest point respectively in the coronal and sagittal planes (D1). The WB point was defined in the ground plane by its x and y coordinates as the lowest point (z coordinate nearest to 0) on the surface of the calcaneus and metatarsal WB surfaces. The center of the talus was defined as the highest point (z coordinate furthest to 0) on the talus in the centermost sagittal plane.

All these values were collected and stored anonymously in a spreadsheet, which a third investigator then ran the through a beta version of the Torque Ankle Lever Arm System, which calculated FAO values using an algorithm based on the inverted 3D pyramid model [31] (Fig. 6.2).

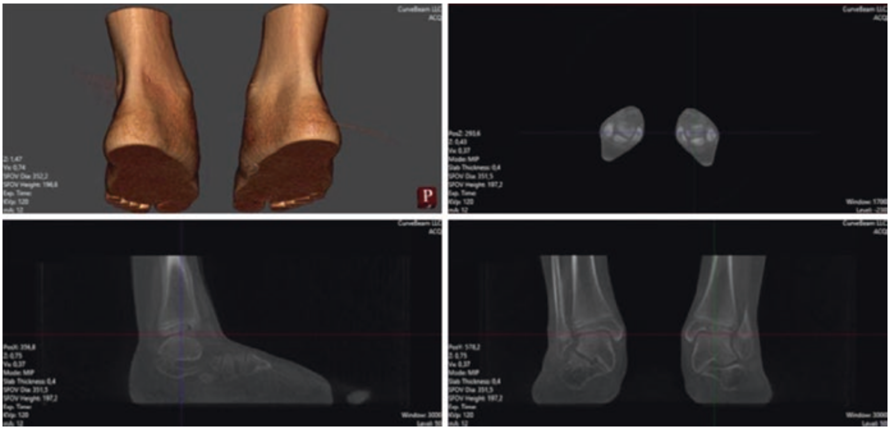

Fig. 6.1 3D views obtained by the WBCT built in software

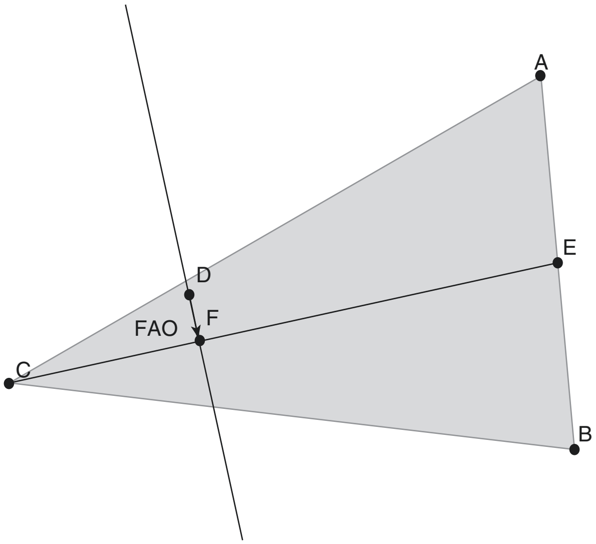

Fig. 6.2 Schematic representation of FAO in the transversal plane (see the text for abbreviations)

"A," "B," "C," and "D1" are defined as, respectively, the WB points of the first metatarsal head, the fifth metatarsal head, the calcaneus, and the talus; the midpoint "E" between "A" and "B" is found; the "CE" line is found, and the "CE" distance is called "foot length"; "D" is the orthogonal projection of "D1" on the ABC plane (i.e., the position of the center of the talus in the ground plane); the perpendicular line to "CE," which includes "D,' is found (i.e., the line from the center of the talus to the midline of the foot on the ground plane); "F" is the intersection of these two lines, and thus "DF" is found, being positive when "D" is medial to "F" and negative when lateral; FAO is DF/CE × 100 and is given as a percentage.

FAO therefore corresponds to the offset between the hindfoot-to-forefoot midline and the talus. It is therefore given as a percentage of foot length and is theoretically representative of the torque, which is produced in the ankle by this offset. This conversion to percentage of foot length is done to normalize the FAO value to foot size so that it is comparable between feet of different sizes, since the FAO is a metric, not an angle.

Statistical Analysis

FAO values in three groups were compared using a one-way ANOVA test. Normality test was performed using the Kolmogorov-Smirnov test method on the normal foot group. An intraclass correlation coefficient (ICC) two-way mixed model was used to assess the intraobserver and interobserver reliability of FAO values. ICCs were calculated with the measurements performed twice by two independent observers on datasets in the three different groups: normal, varus, and valgus. ICC values range from 0 to 1, with a higher value indicating a better reliability. ICCs below 0.40 were considered poor, 0.40–0.59 fair, 0.60–0.74 good, and 0.75–1.00 excellent.

Data are presented as mean, standard deviation, range, and 95% confidence intervals (CI 95%). All analyses were carried out using STATA statistical software package (Version 12.0, StataCorp, 2011). A P value <0.05 was considered to indicate statistical significance.

Results

In normal cases, the mean value for FAO was 2.3% ± 2.9 (CI 95%, 1.5–3.1; range, −3.2 to 9.0), whereas in varus and valgus cases, the mean was −11.6% ± 6.9 (CI 95%, −13.9 to −9.4; range, −26.4 to −1.0) and 11.4% ± 5.7 (CI 95%, 9.6–13.3; range, 2.0–24.5), respectively. The difference was statistically significant among the three groups ($P < 0.001$). FAO values distribution in the normal population was normal ($P > 0.81$) (Fig. 6.3).

The interobserver and intraobserver reliability of FAO measure were excellent, with small standard deviations; the global mean ICC was 0.99 ± 0.002 (CI 95%, 0.99–1.00) and 0.97 ± 0.02 (CI 95%, 0.92–1.02) for the inter- and intraobserver assessment, respectively. ICC values for the normal, varus, and valgus groups are showed in Table 6.1.

Discussion

This study confirmed our hypothesis: in a series of anonymized and independently reviewed 3D WBCT datasets, the FAO was successful in discriminating clinically normal from varus and valgus hindfoot alignment cases using a novel 3D biometric

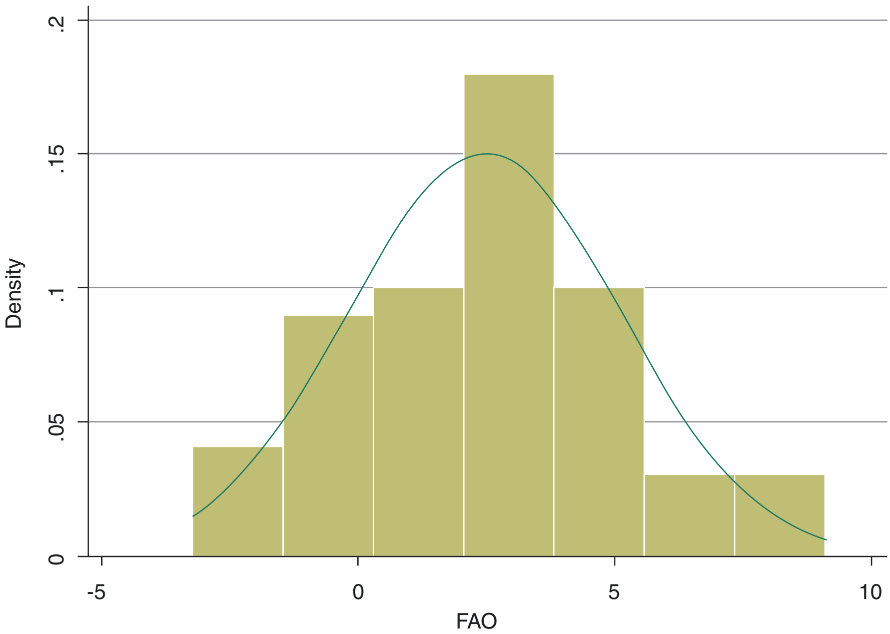

Fig. 6.3 Gaussian distribution of FAO values in the normal population

Table 6.1 Inter- and intraobserver reliability of FAO measurement in different groups

	ICC	SD	95% Cl
Overall			
Interobserver	0.99	0.00	0.99–1.00
Intraobserver	0.97	0.02	0.92–1.02
Normal			
Interobserver	0.95	0.06	0.83–1.07
Intraobserver	0.96	0.04	0.88–1.05
Varus			
Interobserver	0.98	0.02	0.94–1.02
Intraobserver	0.93	0.09	0.75–1.11
Valgus			
Interobserver	0.99	0.00	0.99–1.00
Intraobserver	0.95	0.05	0.84–1.07

Abbreviations: *FAO* foot and ankle offset, *ICC* intraclass correlation coefficient, *SD* standard deviation

computerized, semiautomatic measurement. The distribution of FAO in the normal population was Gaussian. Additionally, intra- and interobserver reliability has proven excellent in all groups of normal, valgus, and varus cases.

In the authors' opinion, the originality of this study lies in the description of an entirely new concept (3D biometrics) for measuring HFA which avoids projection, rotation, and operator errors related to traditional 2D methods. This is concurrent with previous literature in which Richter et al. [47] stated that WBCT imaging is a more accurate method of measuring angles because it is not subject to rotation and projection bias and because it is weight bearing.

Our technique's purpose is to limit the drawbacks of 2D measurement relating to rotational, projectional, and operative issues. With respect to HFA, there is no gold standard or "true" measurement [30–32]. Rotation and other potential bias influence the value of HFA measurements [30]. However, in most studies, reliability is assessed using intra- and interobserver reliability carried out on the same radiograph for each patient. So it is logical that the same observer (intraobserver), or two observers (interobserver), given the same instructions, the same value is found. The real question is rather if two radiographs of the same patient taken at different times would result in the same value. To really assess reliability, the radiographs would therefore have to be repeated on each patient, which would be ethically difficult to explain. This was done in a previous study using a cadaveric setup [30] where a 30° difference in rotation of the foot could result in a 50% difference in HFA value. So repeatability truly lies in the radiographic setting. In setups where the position of the foot, the height of the X-ray source (including angle), the distance of the X-ray source, the individual practice of the radiographer, and the measurement technique all influence the end result, repeatability may be impaired. Weight bearing CT may permit better control over these variables through regular assessment, as is enforced by international regulation by scanning templates which incorporate markers of known length, angle, and spatial distribution so that it may be checked, without consequences for the patients, that measurements made by the machine are reliable. There are other advantages including reduced spatial footprint, radiation dose (comparable to a series of five conventional radiographs), and time for acquisition (52 seconds). However, the clinical and economic efficiency of this technology still remains to be proven.

The clinical relevance for this study is therefore to report the possibility of developing dedicated 3D biometrics to provide more accurate measurement tools for planning foot and lower limb surgery in the future. This technology should also enable reliable and accurate data recording for the purposes of research and clinical audit. The software here described is a framework, in which 3D biometric tools such as FAO may be adapted suitably for WBCT.

The authors acknowledge some limitations in this study such as the absence of a post hoc sample size calculation and the absence of a gold standard comparator, which is always an issue when developing new measurements. We did not compare our measurements with traditional HFA measurements, for example, as determined by the Saltzman view, which is generally accepted as the main method to assess HFA alignment. This would have required additional irradiation of patients which could not be justified in this study setting. In addition, since there is no "true" or "gold standard" measure for HFA, it would not necessarily be an appropriate comparison.

We believe that establishment of the "true" HFA measurement that has relevance in clinical practice requires fully automatic measurement tools. A fully automated system may enable the gathering of data in great quantities in order to correlate varying pathologies. A “better” HFA measure will be one that improves the discrimination of a normal case from a pathological one. In the meantime, an international collaborative effort has to be made to adapt traditional 2D measurements to WBCT and validate their use in a clinical setting. This would provide the basic tools and guidelines to evaluate and validate 3D biometrics.

In the future, the involvement of reference centers will be required to conduct cost- and clinical-effectiveness analyses for this technology. Such an evolution was seen over the last 15 years in the dental arena [48, 49].

In conclusion, a semiautomatic software was successfully used to assess HFA using a 3D biometric measurement, FAO. This new concept may represent the way forward to make the best of WBCT. Further research is warranted in order to properly validate such tools for clinical use. An international effort is required in order to adapt traditional 2D HFA measurements so that a set of guidelines for assessing new tools can be published. This is essential to make the research reproducible and comparable.

References

1. Richardson ML, Van Vu M, Vincent LM, Sangeorzan BJ, Benirschke SK. CT measurement of the calcaneal varus angle in the normal and fractured hindfoot. J Comput Assist Tomogr. 1992;16(2):261–4.
2. Van Bergeyk AB, Younger A, Carson B. CT analysis of hindfoot alignment in chronic lateral ankle instability. Foot Ankle Int. 2002;23(1):37–42.
3. Waldecker U, Hofmann G, Drewitz S. Epidemiologic investigation of 1394 feet: coincidence of hindfoot malalignment and Achilles tendon disorders. Foot Ankle Surg. 2012;18(2):119–23.
4. Baxter JR, Demetracopoulos CA, Prado MP, Tharmviboonsri T, Deland JT. Lateral column lengthening corrects hindfoot valgus in a cadaveric flatfoot model. Foot Ankle Int. 2015;36(6):705–9.
5. Braito M, Dammerer D, Reinthaler A, Kaufmann G, Huber D, Biedermann R. Effect of coronal and sagittal alignment on outcome after mobile-bearing total ankle replacement. Foot Ankle Int. 2015;36(9):1029–37.
6. Frigg A, Nigg B, Hinz L, Valderrabano V, Russell I. Clinical relevance of hindfoot alignment view in total ankle replacement. Foot Ankle Int. 2010;31(10):871–9.
7. Hobson SA, Karantana A, Dhar S. Total ankle replacement in patients with significant preoperative deformity of the hindfoot. J Bone Joint Surg Br. 2009;91(4):481–6.
8. Lewis JS, Adams SB, Queen RM, DeOrio JK, Nunley JA, Easley ME. Outcomes after total ankle replacement in association with ipsilateral hindfoot arthrodesis. Foot Ankle Int. 2014;35(6):535–42.
9. Paul J, Hinterwimmer S, Vavken P, Wörtler K, Imhoff AB. Association between hindfoot alignment and localisation of osteochondral lesions of the talus. Z Orthop Unfall. 2014;152(4):389–92.
10. Queen RM, Adams SB, Viens NA, Friend JK, Easley ME, Deorio JK, Nunley JA. Differences in outcomes following total ankle replacement in patients with neutral alignment compared with tibiotalar joint malalignment. J Bone Joint Surg Am. 2013;95(21):1927–34.
11. Wang B, Saltzman CL, Chalayon O, Barg A. Does the subtalar joint compensate for ankle malalignment in end-stage ankle arthritis? Clin Orthop Relat Res. 2015;473(1):318–25.
12. Chandler JT, Moskal JT. Evaluation of knee and hindfoot alignment before and after total knee arthroplasty: a prospective analysis. J Arthroplasty. 2004;19(2):211–6.

13. Nakada I, Nakamura I, Juji T, Ito K, Matsumoto T. Correlation between knee and hindfoot alignment in patients with rheumatoid arthritis: the effects of subtalar joint destruction. Mod Rheumatol. 2015;25(5):689–93.
14. Norton AA, Callaghan JJ, Amendola A, Phisitkul P, Wongsak S, Liu SS, Fruehling-Wall C. Correlation of knee and hindfoot deformities in advanced knee OA: compensatory hindfoot alignment and where it occurs. Clin Orthop Relat Res. 2015;473(1):166–74.
15. Okamoto Y, Otsuki S, Jotoku T, Nakajima M, Neo M. Clinical usefulness of hindfoot assessment for total knee arthroplasty: persistent post-operative hindfoot pain and alignment in pre-existing severe knee deformity. Knee Surg Sports Traumatol Arthrosc. 2017;25(8):2632–9.
16. Takenaka T, Ikoma K, Ohashi S, Arai Y, Hara Y, Ueshima K, Sawada K, Shirai T, Fujiwara H, Kubo T. Hindfoot alignment at one year after total knee arthroplasty. Knee Surg Sports Traumatol Arthrosc. 2016;24(8):2442–6.
17. Arunakul M, Amendola A, Gao Y, Goetz JE, Femino JE, Phisitkul P. Tripod index: a new radiographic parameter assessing foot alignment. Foot Ankle Int. 2013;34(10):1411–20.
18. Duggal N, Paci GM, Narain A, Bournissaint LG, Nazarian A. A computer assessment of the effect of hindfoot alignment on mechanical axis deviation. Comput Methods Prog Biomed. 2014;113(1):126–32.
19. Glasoe WM, Allen MK, Ludewig PM. Measuring forefoot alignment with a table-mounted goniometric device. Aust J Physiother. 2002;48(1):51–3.
20. Haight HJ, Dahm DL, Smith J, Krause DA. Measuring standing hindfoot alignment: reliability of goniometric and visual measurements. Arch Phys Med Rehabil. 2005;86(3):571–5.
21. Hara Y, Ikoma K, Arai Y, Ohashi S, Maki M, Kubo T. Alteration of hindfoot alignment after total knee arthroplasty using a novel hindfoot alignment view. J Arthroplast. 2015;30(1):126–9.
22. Lee W-C, Moon J-S, Lee HS, Lee K. Alignment of ankle and hindfoot in early stage ankle osteoarthritis. Foot Ankle Int. 2011;32(7):693–9.
23. Mendicino RW, Catanzariti AR, John S, Child B, Lamm BM. Long leg calcaneal axial and hindfoot alignment radiographic views for frontal plane assessment. J Am Podiatr Med Assoc. 2008;98(1):75–8.
24. Perera A, Guha A. Clinical and radiographic evaluation of the cavus foot: surgical implications. Foot Ankle Clin. 2013;18(4):619–28.
25. Saltzman CL, el-Khoury GY. The hindfoot alignment view. Foot Ankle Int. 1995;16(9):572–6.
26. Sensiba PR, Coffey MJ, Williams NE, Mariscalco M, Laughlin RT. Inter- and intraobserver reliability in the radiographic evaluation of adult flatfoot deformity. Foot Ankle Int. 2010;31(2):141–5.
27. Stevens PM. Effect of ankle valgus on radiographic appearance of the hindfoot. J Pediatr Orthop. 1988;8(2):184–6.
28. Strash WW, Berardo P. Radiographic assessment of the hindfoot and ankle. Clin Podiatr Med Surg. 2004;21(3):295–304.
29. Tuijthof GJM, Herder JL, Scholten PE, van Dijk CN, Pistecky PV. Measuring alignment of the hindfoot. J Biomech Eng. 2004;126(3):357–62.
30. Baverel L, Brilhault J, Odri G, Boissard M, Lintz F. Influence of lower limb rotation on hindfoot alignment using a conventional two-dimensional radiographic technique. Foot Ankle Surg. 2017;23(1):44–9.
31. Lintz F, Barton T, Millet M, Harries WJ, Hepple S, Winson IG. Ground reaction force calcaneal offset: a new measurement of hindfoot alignment. Foot Ankle Surg. 2012;18(1):9–14.
32. Buck FM, Hoffmann A, Mamisch-Saupe N, Espinosa N, Resnick D, Hodler J. Hindfoot alignment measurements: rotation-stability of measurement techniques on hindfoot alignment view and long axial view radiographs. AJR Am J Roentgenol. 2011;197(3):578–82.
33. Barg A, Harris MD, Henninger HB, Amendola RL, Saltzman CL, Hintermann B, Anderson AE. Medial distal tibial angle: comparison between weightbearing mortise view and hindfoot alignment view. Foot Ankle Int. 2012;33(8):655–61.
34. Frigg A, Jud L, Valderrabano V. Intraoperative positioning of the hindfoot with the hindfoot alignment guide: a pilot study. Foot Ankle Int. 2014;35(1):56–62.

35. Frigg A, Nigg B, Davis E, Pederson B, Valderrabano V. Does alignment in the hindfoot radiograph influence dynamic foot-floor pressures in ankle and tibiotalocalcaneal fusion? Clin Orthop Relat Res. 2010;468(12):3362–70.
36. Hastings MK, Sinacore DR, Mercer-Bolton N, McCormick JJ, Hildebolt CF, Prior FW, Johnson JE. Precision of foot alignment measures in Charcot arthropathy. Foot Ankle Int. 2011;32(9):867–72.
37. Ikoma K, Noguchi M, Nagasawa K, Maki M, Kido M, Hara Y, Kubo T. A new radiographic view of the hindfoot. J Foot Ankle Res. 2013;6(1):48.
38. Johnson JE, Lamdan R, Granberry WF, Harris GF, Carrera GF. Hindfoot coronal alignment: a modified radiographic method. Foot Ankle Int. 1999;20(12):818–25.
39. Liu H, Sugamoto K, Itohara T, Tomita T, Hashimoto J, Yoshikawa H. In vivo three-dimensional skeletal alignment analysis of the hindfoot valgus deformity in patients with rheumatoid arthritis. J Orthop Res. 2007;25(3):330–9.
40. Melamed EA. Intoeing Harris view for accessory navicular visualization and hindfoot alignment: technique tip. Foot Ankle Int. 2010;31(12):1122–4.
41. Min W, Sanders R. The use of the mortise view of the ankle to determine hindfoot alignment: technique tip. Foot Ankle Int. 2010;31(9):823–7.
42. Reilingh ML, Beimers L, Tuijthof GJM, Stufkens SAS, Maas M, van Dijk CN. Measuring hindfoot alignment radiographically: the long axial view is more reliable than the hindfoot alignment view. Skelet Radiol. 2010;39(11):1103–8.
43. Sutter R, Pfirrmann CWA, Espinosa N, Buck FM. Three-dimensional hindfoot alignment measurements based on biplanar radiographs: comparison with standard radiographic measurements. Skelet Radiol. 2013;42(4):493–8.
44. Tanaka Y, Takakura Y, Fujii T, Kumai T, Sugimoto K. Hindfoot alignment of hallux valgus evaluated by a weightbearing subtalar x-ray view. Foot Ankle Int. 1999;20(10):640–5.
45. Williamson ERC, Chan JY, Burket JC, Deland JT, Ellis SJ. New radiographic parameter assessing hindfoot alignment in stage II adult-acquired flatfoot deformity. Foot Ankle Int. 2015;36(4):417–23.
46. Hirschmann A, Pfirrmann CWA, Klammer G, Espinosa N, Buck FM. Upright cone CT of the hindfoot: comparison of the non-weight-bearing with the upright weight-bearing position. Eur Radiol. 2014;24(3):553–8.
47. Richter M, Seidl B, Zech S, Hahn S. PedCAT for 3D-imaging in standing position allows for more accurate bone position (angle) measurement than radiographs or CT. Foot Ankle Surg. 2014;20(3):201–7.
48. Tsolakis IA, Venkat D, Hans MG, Alonso A, Palomo JM. When static meets dynamic: comparing cone-beam computed tomography and acoustic reflection for upper airway analysis. Am J Orthod Dentofac Orthop. 2016;150(4):643–50.
49. Tyndall DA, Kohltfarber H. Application of cone beam volumetric tomography in endodontics. Aust Dent J. 2012;57(Suppl 1):72–81.

Chapter 7
3D Biometrics for Hindfoot Alignment Using Weight Bearing Computed Tomography: A Prospective Assessment of 249 Feet

Francois Lintz

Introduction

Hindfoot malalignment is a common cause of foot and ankle disability [1, 2]. A reliable and precise measurement of hindfoot alignment (HA) is paramount for the diagnosis and treatment of various foot and ankle pathologies, although the best way to reach a correct assessment is still a matter of debate. Traditionally, HA can be assessed from weight bearing measurements on plain radiographic views, such as the calcaneal long axial view and HA view. These methods are used worldwide for preoperative planning and postoperative evaluations [2–5]. However, radiography has many flaws such as perspective distortion due to lower limb rotation, bone superimposition because of two-dimensional (2D) visualization and some operator related bias, which all affect the method of measurement making it imprecise and at times unreliable [5–8].

The recent development of new radiographic imaging equipment such as 3D weight bearing computed tomography (WBCT) has the potential to provide more accurate anatomical information on full bipedal weight bearing scans, allowing for more precise measurements with a similar total amount of radiation [9–13]. Recent studies have shown how the different angles used to assess HA may differ substantially between radiographs, traditional CT, and WBCT, suggesting that 3D weight bearing measurements represent a major step forward to detect the "true alignment" [2, 14, 15]. In addition, this technology can provide a digitally reconstructed radiograph, similar to traditional radiography with the advantage of no rotation bias [9, 16]. Common measurements, such as the long axial view (termed HACT), can be taken using this reconstruction to evaluate HA.

Based on Zhang JZ, Lintz F, Bernasconi A; Weight Bearing CT International Study Group, Zhang S. 3D biometrics for hindfoot alignment using weightbearing computed tomography. Foot Ankle Int. 2019;40(6):720–726.

M. Richter et al., *Weight Bearing Cone Beam Computed Tomography (WBCT) in the Foot and Ankle*, https://doi.org/10.1007/978-3-030-31949-6_7

A novel parameter used to assess HA on WBCT images is foot ankle offset (FAO) [5, 17]. Technically, this is a semiautomatic 3D biometrics and is calculated using semiautomatic software: Torque Ankle Lever Arm System or TALAS™ (CurveBeam®, Warrington, PA). This measurement considers the forefoot rather than the tibia as the reference since the forefoot interacts with the ground like the hindfoot and contributes to ankle biomechanics [5, 18]. In a previous retrospective study, Lintz et al. found that FAO had excellent inter- and intraobserver reliability and concluded that it was a precise and discriminating tool for measuring HA [5]. However, the clinical efficiency of FAO and the reference values for normal, varus, and valgus hindfoot have not yet been confirmed.

The aim of this study was to assess FAO and HACT on a large population of patients. We hypothesized that FAO would be a clinically relevant and reproducible method and that the values would be comparable to previously published data in normal, varus, and valgus cases.

Materials and Methods

Study Population and Design

Between September 2017 and April 2018, all consecutive patients undergoing a WBCT investigation in our department as part of their standard care were enrolled in this prospective comparative study.

Based on a standard physical examination, the patients were divided into three groups: clinically normally aligned hindfoot group (G1); valgus alignment group (G2); and varus alignment group (G3). This division was based on clinical examination by two experienced foot and ankle specialist orthopedic surgeons (one of the two). When the assessment of the hindfoot alignment was unclear, a goniometer was applied on the posterior aspect of the ankle and the hindfoot, measuring the standing tibiocalcaneal angle (angle between the bisectors of the calf and the calcaneus). Values between 0 and 7 degrees of valgus were considered normal. If greater than 0 degrees, the hindfoot was varus. If lower than −7, it was valgus.

Clinical indications to perform bilaterally WBCT scans were the same as with a conventional radiographic setup (obtaining comparative images).

The study was approved by the relevant Ethics Committee and was compliant with the Health Insurance Portability and Accountability Act (HIPAA) and the Declaration of Helsinki. Informed consent was signed by all participants to be included in the study.

Patient Assessment

WBCT images were obtained from scans performed using a PedCAT® unit (CurveBeam®, Warrington PA, USA) installed in the outpatients department of the Foot and Ankle Orthopaedic Surgery and Paedorthic Centre of our institution.

The data sets were obtained using the following cone beam scanner settings: voxel size, 0.37 mm; field of view diameter, 350 mm; field of view height, 200 mm; exposure time, 9 seconds; and total scan time, 54 seconds. Using WBCT patient datasets, 3D coordinates (x, y, z) required for the built-in software to process and calculate FAO were manually collected for the following landmarks: first metatarsal head WB point, fifth metatarsal head WB point, calcaneus WB point, and talus centermost and highest point. To identify WB points, images were scrolled through until the smallest contact area can be observed on the axial slice closest to the ground plane. This was usually possible until the last voxel of bone. When it was not, the center of the smallest area of contact was chosen. The software processed and calculated FAO automatically, as described previously (Fig. 7.1) [5].

HACT was measured on digitally reconstructed radiographs provided by the software, selecting the sagittal view where the foot was aligned with the second ray and inclined 45 degrees (Fig. 7.2). The same method used to measure the long axial view on standard radiographs was adopted [19]. Angular measurement of FAO and HACT was performed on the same day by two experienced investigators (in two independent settings) and repeated 14 days later.

Our analysis included only patients who had a bilateral WBCT, in order to minimize the risk of a nonphysiological static loading of the foot. Among these, feet which had a previous surgery with some important metal artifacts were excluded.

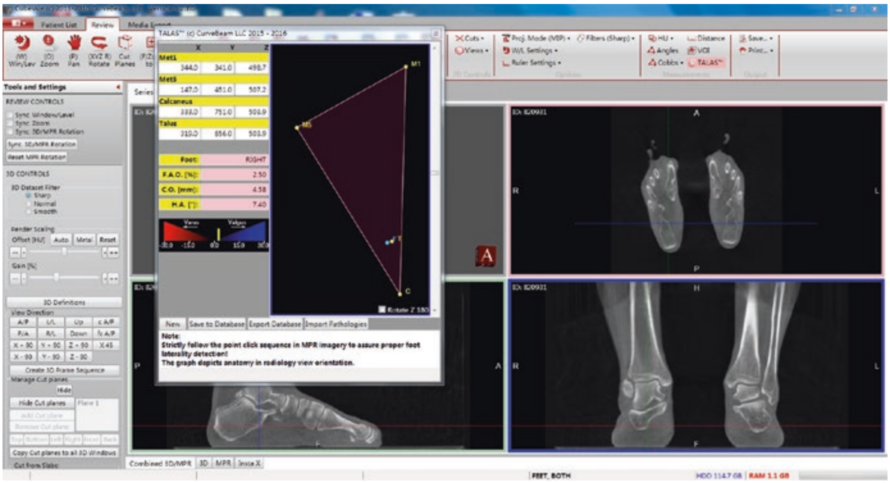

Fig. 7.1 PedCAT® software screen view with the Torque Ankle Lever Arm System (TALAS™) (top left). For the definition of FAO, three-dimensional coordinates (x, y, z planes) were harvested for the following landmarks: first metatarsal head WB point (Met1 or M1), fifth metatarsal head WB point (Met5 or M5), calcaneus WB point (C), and talus centermost and highest point (T). F represents the ideal position of the center of rotation of the ankle joint that lies on a bisecting line of the tripod

Fig. 7.2 Measurement method for the long axial view on digitally reconstructed radiographs. (**a**) Dorsoplantar radiograph from weight bearing CT (HACT); (**b**) foot aligned with the second ray and inclined towards 45 degrees, and (**c**) then visualized from the back to assess the hindfoot alignment. The mid-diaphyseal axis of the tibia was identified by bisecting the tibia into two mid-diaphyseal points (lines A and B) 30 mm apart (line E). The mid-diaphyseal axis of the calcaneus was defined by a line through two points in the calcaneus. At a distance of 7 mm from the most distal part of the calcaneus, a horizontal line was drawn (line D) and divided into a 40%: 60% ratio (where the length of the 40% line was measured from the lateral side). Another line (line C) was drawn horizontally, 30 mm from the posterior edge of the calcaneus. The calcaneus axis (line F) was drawn by connecting the 40% mark at line D and the bisected line C. The hindfoot alignment (G) was defined by the angle between lines E and F

Statistical Analysis

Quantitative variables are reported as mean ± standard deviation (SD), range, and 95% confidence intervals [95% CIs]. The Kolmogorov-Smirnov test was performed to investigate the distribution of the normal foot group (G1). Regression analysis was performed to calculate the correlation between FAO and HACT using Spearman's coefficient and visualization of a corresponding scatterplot.

To assess the reproducibility of FAO and HACT, inter- and intraobserver variability expressed by the intraclass correlation coefficient (ICC) was calculated. ICC values range from 0 to 1, with a higher value indicating better reliability. An ICC value >0.7 indicates good reliability and a value >0.9 excellent reliability. All analyses were carried out using SPSS 20.0 software (Standard version; IBM, Armonk, NY, USA). The significance level was set at $p < 0.05$.

Results

Overall, 249 feet (126 patients) were included in the study: G1 = 115, G2 = 78, and G3 = 56 feet. Three feet from three patients were excluded from the analysis. The mean values for FAO and HACT in the three groups are reported in Table 7.1 (Fig. 7.3).

Kolmogorov-Smirnov analysis showed a normal distribution for both FAO and HACT in G1 ($p > 0.05$) (Fig. 7.4).

The correlation between FAO and HACT was good (Spearman's correlation coefficient = .863). Linear regression analysis showed a good linear relationship between FAO and HACT ($R^2 = 0.744$), and the regression slope was 1.064 (Fig. 7.5).

The intraobserver and interobserver ICC values demonstrated excellent reliability for FAO measurements and good to excellent reliability for HACT (Table 7.2).

Discussion

In our study population, foot and ankle offset values assessed on WBCT images correlated well throughout the spectrum of HAs. Furthermore, the cases considered clinically to be normal were found to have a normal distribution. The FAO and

Table 7.1 Measurements of the foot and ankle offset (FAO) and hindfoot alignment through a long axial view (HACT) in the three groups, expressed as mean value, standard deviation (SD), 95% confidence interval (95%CI), and range of values

	Mean		SD		95% CI		Range	
Groups	FAO	HAct	FAO	HAct	FAO	HAct	FAO	HAct
1	1.17	3.18	2.82	3.12	0.65 to 1.70	2.60 to 3.76	−4.49 to 9.40	−4.70 to 10.5
2	8.10	9.69	3.69	4.85	7.27 to 8.93	8.59 to 10.8	3.35 to 19.07	2.1 to 24.5
3	−6.64	−8.15	4.83	6.62	−7.93 to −5.35	−9.92 to −6.37	−27.2 to 2.29	−29.3 to 4.9

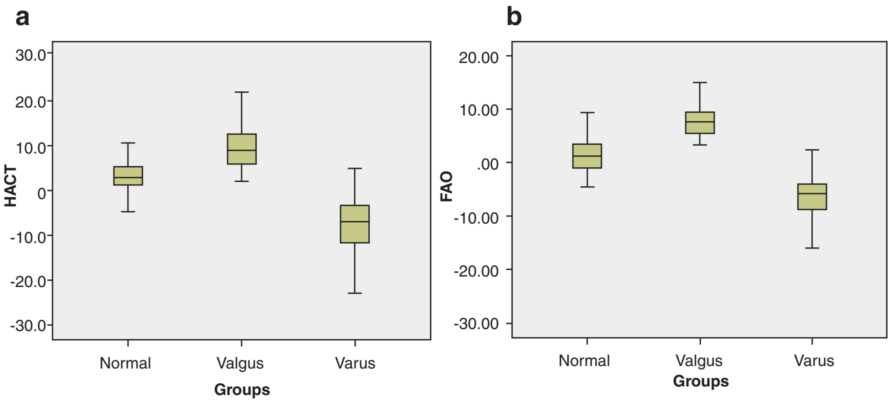

Fig. 7.3 Boxplots showing (**a**) HACT and (**b**) FAO values in the three groups of our cohort. On each box, the central mark indicates the mean value, and the bottom and top edges of the box indicate 95%CI. The whiskers extend to the most extreme data points in the range (minimum and maximum values)

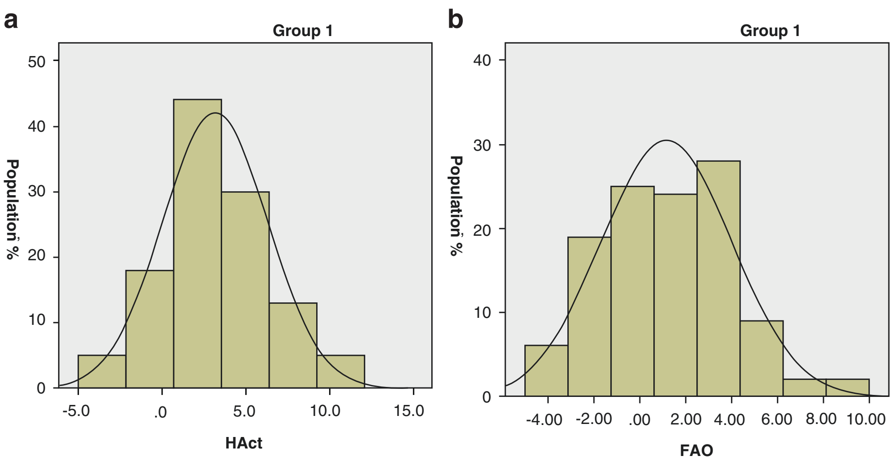

Fig. 7.4 (**a**) Gaussian distribution of the hindfoot alignment assessed through a long axial view (HACT) (**b**) and foot and ankle offset (FAO) values in the normal population

HACT mean values were very close to data published previously (mean value for clinically normal cases of 2% valgus FAO [5] and 9 degrees of valgus HACT [15]) (Fig. 7.3). Intra- and interobserver reliability was excellent, equivalent for both measurements, however slightly superior for FAO (being excellent in the overall and group analysis, while HACT was only good in the group analysis).

Different radiographic methods and measurements have been described to evaluate hindfoot malalignment, such as the Méary view, HA view (Saltzman view), and long axial view [20–22]. However, these tools have shown poor inter-test correlation [23]. These methods greatly depend on the accuracy of positioning the X-ray

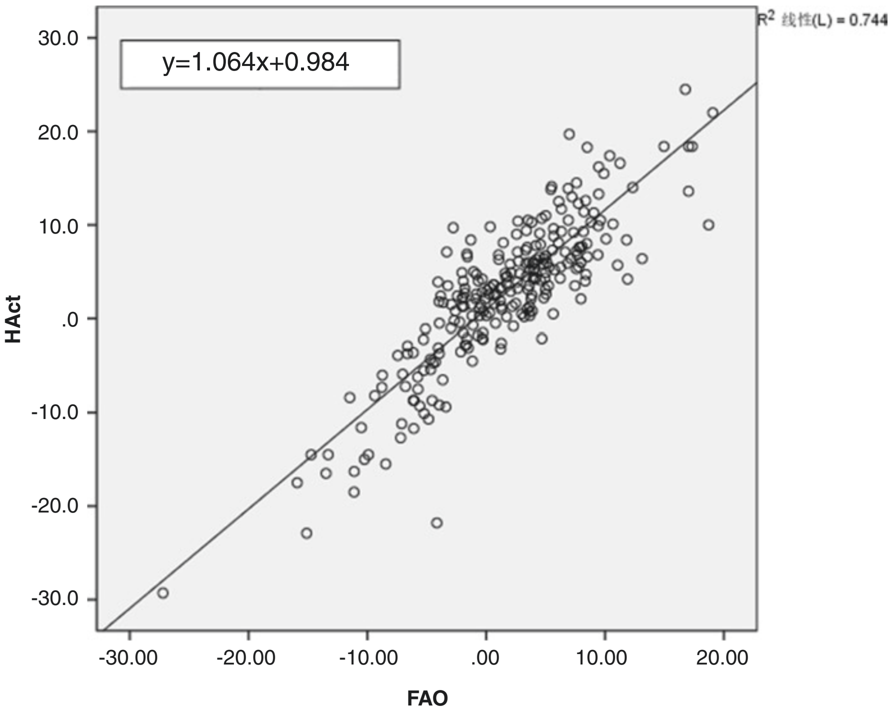

Fig. 7.5 Linear regression analysis of long axial view (HACT) and foot and ankle offset (FAO) values

Table 7.2 Intra- and interobserver reliability of foot and ankle offset (FAO) and hindfoot alignment through the long axial view (HACT) measurement in different groups, expressed as intraclass correlation coefficient values and 95%CI

	Intraobserver		Interobserver	
Groups	FAO	HAct	FAO	HAct
Overall	0.987	0.949	0.988	0.949
1	0.949	0.809	0.941	0.756
2	0.976	0.837	0.969	0.858
3	0.949	0.866	0.972	0.927

beam projection, which is difficult to standardize. In order to make projections more reliable, authors have repeatedly published modifications and new techniques such as the lateral Fick correction method, the metal wire and malleolar pincers on Méary view, and the modified Van Dijk and Robinson correction on HA view, with little success [8, 24]. Dagneaux et al. recently reported that the Fick correction did not counteract the influence of tibial rotation and caused a greater range of results with a mean ICC of 0.59 [8]. Therefore, there is currently no golden standard method to evaluate HA.

WBCT has inherent advantages including the absence of rotational and projection bias and of technical and operative mistakes. This is due to industrial standardizing processes such as quality assurance testing. In these procedures, templates with known density and dimensions are used to regularly test that the machine accurately measures known values. This increased reproducibility led to the development of novel measurement methods in WBCT, such as the FAO [5, 16]. Lintz et al. suggested that FAO is a reliable measurement of HA when acquired using a semiautomatic software tool in varus and valgus deformity, with excellent interobserver (0.99) and intraobserver (0.97) reproducibility [5].

In clinical practice, an accurate and reproducible method of measuring HA is essential for diagnosis and treatment, especially in certain subtle ankle conditions. Colville has demonstrated how in a chronically unstable ankle treated by surgical reconstruction a varus hindfoot may predispose to failure, given the severe inversion forces [25]. Similarly, Van Bergeyk found a correlation between a varus alignment of the hindfoot and chronic lateral ankle instability using a simulated weight bearing condition [26]. However, as reported in a recent review, this kind of simulation also presents a few biases, essentially because of the lack of physiological muscular contraction and the application of a partial load [9].

Our findings in terms of FAO values confirm the reference values reported previously in the literature [5], with the mean of normal cases of around 2%. As a 3D biometrics, FAO has overcome the inherent errors in 2D measurements, which makes it possible to develop more 3D tools to plan foot and lower limb surgery with greater accuracy in the future. However, larger number of patients and multicenter studies are required to distinguish between different degrees of hindfoot malalignment as precisely as possible, targeting the "true alignment."

Our study has several limitations. The use of a simulated long axial view as a control for FAO is open to debate since it does not represent the current gold standard for HA. As mentioned previously, it is hard to describe "true" HA without 3D biometrics. Long axial view is one of the most widely used tools for the clinical assessment of HA, and for that reason we selected it for comparison with FAO. Secondly, no sample size calculation was performed prospectively in this study. However, we feel that our findings on over 240 feet are appropriate to support our conclusions.

In conclusion, our study is the first prospective assessment of FAO as a 3D biometric tool. It shows that FAO has excellent reproducibility and good correlation with clinical findings, confirming the values reported previously. The use of WBCT can help to characterize HA objectively using semiautomatic software or digitally reconstructed radiographs. Future research in this field will define the reference values further and open future perspectives for larger data sets and multivariate analysis in foot and ankle pathologies.

Funding
This work was supported by The National Key Research and Development Program of China (2017YFC0108100).

References

1. Vienne P, Schöniger R, Helmy N, Espinosa N. Hindfoot instability in cavovarus deformity: static and dynamic balancing. Foot Ankle Int. 2007;28(1):96–102.
2. de Cesar Netto C, Schon LC, Thawait GK, da Fonseca LF, Chinanuvathana A, Zbijewski WB, Siewerdsen JH, Demehri S. Flexible adult acquired flatfoot deformity. J Bone Joint Surg. 2017;99(18):e98.
3. Aebi J, Horisberger M, Frigg A. Radiographic study of pes planovarus. Foot Ankle Int. 2017;38(5):526–31.
4. Hintermann B, Ruiz R, Barg A. Novel double osteotomy technique of distal tibia for correction of asymmetric varus osteoarthritic ankle. Foot Ankle Int. 2017;38(9):970–81.
5. Lintz F, Welck M, Bernasconi A, Thornton J, Cullen NP, Singh D, Goldberg A. 3D biometrics for hindfoot alignment using weightbearing CT. Foot Ankle Int. 2017;38(6):684–9.
6. Barg A, Amendola RL, Henninger HB, Kapron AL, Saltzman CL, Anderson AE. Influence of ankle position and radiographic projection angle on measurement of supramalleolar alignment on the anteroposterior and hindfoot alignment views. Foot Ankle Int. 2015;36(11):1352–61.
7. Baverel L, Brilhault J, Odri G, Boissard M, Lintz F. Influence of lower limb rotation on hindfoot alignment using a conventional two-dimensional radiographic technique. Foot Ankle Surg. 2017;23(1):44–9.
8. Dagneaux L, Moroney P, Maestro M. Reliability of hindfoot alignment measurements from standard radiographs using the methods of Meary and Saltzman. Foot Ankle Surg. 2019;25(2):237–41.
9. Barg A, Bailey T, Richter M, de Cesar Netto C, Lintz F, Burssens A, Phisitkul P, Hanrahan CJ, Saltzman CL. Weightbearing computed tomography of the foot and ankle: emerging technology topical review. Foot Ankle Int. 2018;39(3):376–86.
10. Burssens A, Peeters J, Buedts K, Victor J, Vandeputte G. Measuring hindfoot alignment in weight bearing CT: a novel clinical relevant measurement method. Foot Ankle Surg. 2016;22(4):233–8.
11. Colin F, Horn Lang T, Zwicky L, Hintermann B, Knupp M. Subtalar joint configuration on weightbearing CT scan. Foot Ankle Int. 2014;35(10):1057–62.
12. Hirschmann A, Pfirrmann CWA, Klammer G, Espinosa N, Buck FM. Upright cone CT of the hindfoot: comparison of the non-weight-bearing with the upright weight-bearing position. Eur Radiol. 2014;24(3):553–8.
13. Lawlor MC, Kluczynski MA, Marzo JM. Weight-bearing cone-beam CT scan assessment of stability of supination external rotation ankle fractures in a cadaver model. Foot Ankle Int. 2018;39(7):850–7. https://doi.org/10.1177/1071100718761035.
14. Richter M, Seidl B, Zech S, Hahn S. PedCAT for 3D-imaging in standing position allows for more accurate bone position (angle) measurement than radiographs or CT. Foot Ankle Surg. 2014;20(3):201–7.
15. Burssens A, Van Herzele E, Leenders T, Clockaerts S, Buedts K, Vandeputte G, Victor J. Weightbearing CT in normal hindfoot alignment — presence of a constitutional valgus? Foot Ankle Surg. 2018;24(3):213–8.
16. Burssens A, Peeters J, Peiffer M, Marien R, Lenaerts T, Vandeputte G, Victor J, Victor J. Reliability and correlation analysis of computed methods to convert conventional 2D radiological hindfoot measurements to a 3D setting using weightbearing CT. Int J Comput Assist Radiol Surg. 2018;13(12):1999–2008.
17. Richter M, Lintz F, Zech S, Meissner SA. Combination of PedCAT weightbearing CT with pedography assessment of the relationship between anatomy-based foot center and force/pressure-based center of gravity. Foot Ankle Int. 2018;39(3):361–8.
18. Arunakul M, Amendola A, Gao Y, Goetz JE, Femino JE, Phisitkul P. Tripod index. Foot Ankle Int. 2013;34(10):1411–20.

19. Reilingh ML, Beimers L, Tuijthof GJM, Stufkens SAS, Maas M, van Dijk CN. Measuring hindfoot alignment radiographically: the long axial view is more reliable than the hindfoot alignment view. Skelet Radiol. 2010;39(11):1103–8.
20. Buck FM, Hoffmann A, Mamisch-Saupe N, Espinosa N, Resnick D, Hodler J. Hindfoot alignment measurements: rotation-stability of measurement techniques on hindfoot alignment view and long axial view radiographs. Am J Roentgenol. 2011;197(3):578–82.
21. Méary R, Filipe G, Aubriot JH, Tomeno B. Functional study of a double arthrodesis of the foot. Rev Chir Orthop Reparatrice Appar Mot. 1977;63(4):345–59.
22. Saltzman CL, El-Khoury GY. The hindfoot alignment view. Foot Ankle Int. 1995;16(9):572–6.
23. Neri T, Barthelemy R, Tourné Y. Radiologic analysis of hindfoot alignment: comparison of Méary, long axial, and hindfoot alignment views. Orthop Traumatol Surg Res. 2017;103(8):1211–6.
24. Robinson I, Dyson R, Halson-Brown S. Reliability of clinical and radiographic measurement of rearfoot alignment in a patient population. Foot. 2001;11(1):2–9.
25. Colville MR. Surgical treatment of the unstable ankle. J Am Acad Orthop Surg. 1998;6(6):368–77.
26. Van Bergeyk AB, Van Younger A, Van Carson B. CT analysis of Hindfoot alignment in chronic lateral ankle instability. Foot Ankle Int. 2002;23(1):37–42.

Chapter 8
Relationship Between Chronic Lateral Ankle Instability and Hindfoot Varus Using Weight Bearing Cone Beam Computed Tomography: A Retrospective Study

Francois Lintz

Introduction

Ankle sprain is one of the most common pathologies in orthopedic practice, accounting for 15–20% of all athletic injuries [1]. It is usually treated successfully with conservative protocols (rest, ice, compression, and elevation), even though 15–20% of cases may develop chronic ankle lateral instability (CLAI) [1]. A few studies have investigated intrinsic predictors of CLAI; however, to date only the severity of the initial sprain and participation in physical training seem to predict re-sprain [2, 3]. The value of hindfoot alignment (HFA) in the setting of CLAI has been reported in the literature, [4, 5] with a varus hindfoot deformity suggested as a possible risk factor [5–10]. Study of the relationship between the varus alignment and clinical instability has usually relied on 2D plain radiographs, which are commonly used in daily practice. However, these are flawed by anatomical bias, which includes projection, rotation distortion, and a fan effect, as well as operator-related technical bias [11, 12]. In 2002, Van Bergeyk suggested computed tomography (CT) as a better imaging method to evaluate HFA being reliable, accurate, and reproducible [5]. In his study, he used a footrest to simulate weight-bearing conditions as no other technology was available at that time [5].

Recently introduced weight-bearing cone beam CT (WBCT) has been described as a major step forward in lower limb imaging and analysis, as it provides images comparable to ordinary CT scans but with a reduced radiation dose and under physiologically loaded conditions.1 In addition, new HFA measurements such as the foot and ankle offset (FAO), which is performed through 3D structural analysis of the foot-ankle complex using a semi-automated software (Talas®, CurveBeam, LLC),

Based on Lintz F, Bernasconi A, Baschet L, Fernando C, Mehdi N; Weight Bearing CT International Study Group, de Cesar Netto C. Relationship between chronic lateral ankle instability and hindfoot varus using weight-bearing cone beam computed tomography. Foot Ankle Int. 2019:1071100719858309. doi: 10.1177/1071100719858309. [Epub ahead of print].

M. Richter et al., *Weight Bearing Cone Beam Computed Tomography (WBCT) in the Foot and Ankle*, https://doi.org/10.1007/978-3-030-31949-6_8

have proven to be reliable and reproducible in the clinical setting, demonstrating excellent intra- (0.97–0.98) and interobserver (0.98–0.99) agreement [11–13].

The primary objective of our study was to analyze HFA in relation to CLAI using the FAO measurement on WBCT images. We hypothesized that there is a positive correlation between varus alignment and history of CLAI.

Material and Methods

Study Design

This comparative, retrospective, and nonselective study analyzed existing data recorded prospectively as part of routine clinical care. All procedures were performed in accordance with the ethical standards of the institutional research committee and with the 1964 Helsinki declaration and its later amendments or comparable ethical standards. Ethical approval from the relevant Institutional Review Board was obtained (IRB number OS-RGDS-2017-10-001).

Study Population

Datasets were obtained for 370 consecutive feet (189 patients) referred to a specialized orthopedic surgery center in our institution between July 2016 and October 2018, who underwent a WBCT investigation. Weight bearing cone beam CT was performed on patients requiring comparative weight bearing imaging when adequate imaging had not already been provided elsewhere. Indications to perform a WBCT were the same as a conventional comparative bilateral radiographic assessment.

History of CLAI was based on medical history, clinical symptoms, physical examination, and imaging studies including radiography (weight-bearing anteroposterior and lateral views, varus stress test, radiological anterior drawer test), arthro-CT, or MRI and ultrasonography, according to each patient's follow-up. For this study we included patients who had reported at least three repeated episodes of ankle "giving way" in the previous 6 months, complaining of ankle instability associated with pain or not, with at least one prior initial ankle sprain requiring active treatment. Patients who had pain and discomfort but no history of ankle giving way were not diagnosed with CLAI. Clinical examination was performed by a senior orthopedic surgeon and was independent from hindfoot alignment measurements.

Out of 378 feet investigated through WBCT, one foot from a patient with medial ankle instability, one with syndesmotic instability, and those (six) who had a history of hindfoot realignment surgery or traumatic malalignment were excluded. Feet were divided into two groups: (i) patients with CLAI and (ii) all other patients. Out of 370 feet, 43 (12%) had CLAI, in 34 patients (18%). No extra investigation other than the standard of care in our institution was required in this study.

Investigations and Measurements

WBCT scans were performed using a PedCAT™ unit (CurveBeam LLC, 175 Titus Ave, Suite 300, Warrington, PA 18976, USA) installed in the outpatient department. The datasets were obtained using the following cone beam scanner settings: voxel size, 0.37 mm; field of view diameter, 350 mm; field of view height, 200 mm; exposure time, 9 sec; and total scan time, 54 sec. The datasets were extracted from the existing database, containing the 3D image data and patient demographics including age, sex, body mass index (BMI), and history of CLAI and other clinical conditions. Datasets were screened using the manufacturer's visualization (CubeView™) and measurement (Talas®) softwares, and FAO was calculated using specific software, as described previously [12]. FAO is a semiautomated tool that measures offset between the center of the ankle joint and the center of the foot weight-bearing surface (Fig. 8.1). The offset is given as a percentage to normalize

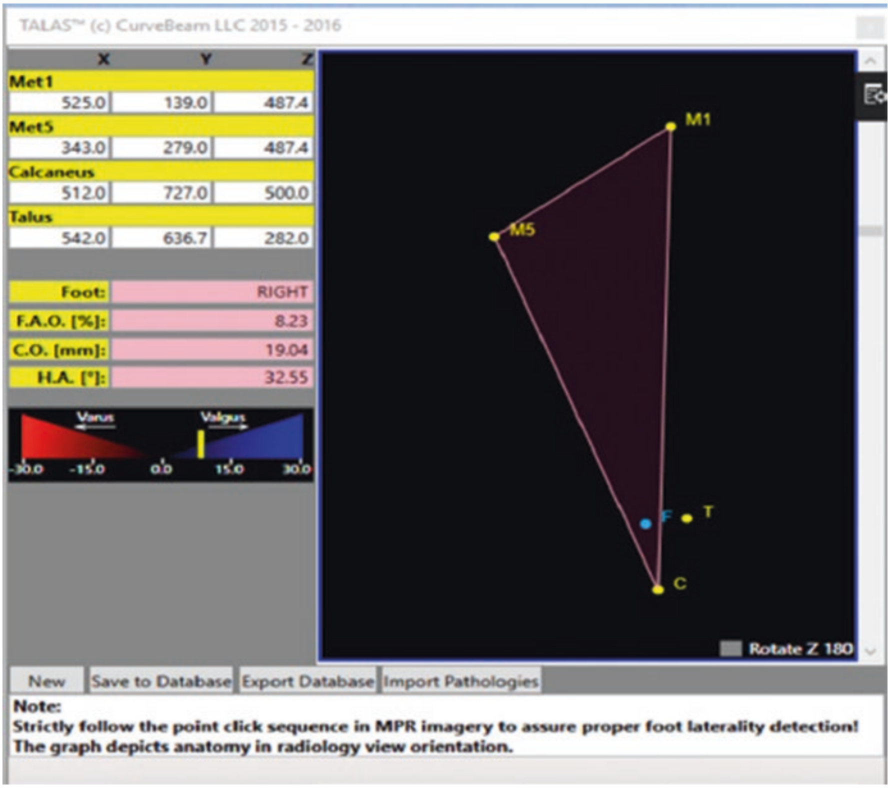

Fig. 8.1 A picture showing the basic elements required to calculate the foot and ankle offset (FAO). The following landmarks must be identified: the first metatarsal head WB point (M1), the fifth metatarsal head WB point (M2), the calcaneus WB point (C), and the talus centermost and highest point, respectively, in the coronal and sagittal planes (T). These values are elaborated through a specific software (Talas®; CurveBeam LLC), which calculates FAO values using an algorithm based on the inverted 3D pyramid model

its value according to foot length. In the first published study, normally aligned feet had a FAO value of 2.3 ± 2.9% [12]. We also recorded the calcaneal offset (CO) and hindfoot angle. CO represents the distance (in mm) between a theoretically neutral position of the calcaneus (in terms of mechanical lever arm at the level of the ankle) and the actual position of the calcaneus. Hindfoot angle is an angle whose end-points are the apex of the center of the talar dome projected on the ground plane (as the vertex), the ideal position of the calcaneus, and the actual position of the calcaneus, which is comparable to mainstream hindfoot angles used on 2D traditional radiographs.

Statistical Analysis

Data are reported as mean, standard deviation, and range values (min-max). Univariate analysis was conducted to compare patients with and without CLAI against the following variables: sex (Fisher test) and age and BMI (Student's t-test). To compare feet with and without CLAI against FAO, generalized mixed model was used to take into account correlation between the 2 feet of the same patient, unadjusted and adjusted on age and sex. A subgroup analysis was performed to assess the relationship between (1) a negative FAO and clinical varus and (1) a negative FAO and diagnosis of CLAI (Fisher test). $p = 0.05$ was considered significant. All statistical analyses were performed by an independent statistician using SAS for Windows (Version 9.4; SAS Institute Inc.).

Results

The final analysis included 43 (12%) feet with CLAI in 34 patients (18%). The main characteristics of the two groups are shown in Table 8.1.

Sex ($p = 0.012$) and age ($p = 0.0003$) were risk factors to have CLAI in at least one side; patients with CLAI were mostly men (59.8%) compared to patients without CLAI (65.2% of women) and were 10 years younger. FAO ($p = 0.0008$) was a significant risk factor for CLAI in univariate analysis (Table 8.2).

The proportion of patients with CLAI who were female was higher than those without CLAI (65.2% vs. 41.2%, respectively). Mean age was 46 years ± 14 and 56 years ± 15 for patients with and without history of CLAI, respectively. Mean FAO was −2.2% ± 5.4 (varus) and 2.6% ± 4.7 (valgus) in feet with and without a history of CLAI, respectively (Fig. 8.2). No significant differences in BMI were observed.

After verification of log-linearity between the odds ratio (OR) for CLAI and FAO, multivariable logistic generalized model, adjusted for sex and age, demonstrated a 35% increase in OR for CLAI per 1% decrease in FAO value (towards varus) [adjusted OR = 0.64; 95%CI, 0.49–0.84; $p = 0.001$] (Fig. 8.3) and no significant effect of sex [adjusted OR = 0.52; 95%CI, 0.04–6.80; $p = 0.617$] and age

Table 8.1 Demographic characteristics of the patients enrolled in this study

Parameters	CLAI	Other	Total	*p* value[a]
No. of patients (%)[b]	34 (18)	155 (82)	189	
Age, y				
Mean ± SD	45.6 ± 14.1	56.0 ± 15.2	54.1 ± 15.5	**.0003**[c]
Range	25–76	16–86	16–86	
Females, *n* (%)	14 (41.2)	101 (65.2)	115 (60.8)	**.0018**[d]
BMI				
Mean ± SD	26.8 ± 4.3	25.9 ± 4.1	26.1 ± 4.2	**.2875**[c]
Range	19–37	17–37	17–37	
Patient pathologies (several possible), *n* (%)				
Pes cavus (varus)	13 (38.2)	17 (11.0)	30 (15.9)	
Pes planus (valgus)	3 (8.8)	50 (32.3)	53 (28.0)	
Others	18 (52.9)	128 (82.6)	146 (77.2)	
No. of feet	43 (12)	327 (88)	370	
Side, R/L	21/22	162/165		
FAO, %				
Mean ± SD	−2.2 ± 5.4	2.6 ± 4.7	2.0 ± 5.0	**<.0001**[e]
Range	−19.3 to 9.43	−18.1 to 19.8	−19.3 to 19.8	
CO, mm				
Mean ± SD	−3.2 ± 8.4	6.7 ± 9.8	4.3 ± 10.4	**<.0001**[e]
Range	−21.2 to 16.3	−20 5 to 37.1	−20.5 to 37.1	
HA, degrees				
Mean ± SD	−5.9 ± 15.8	10.6 ± 16.0	6.5 ± 17.4	**<.0001**[e]
Range	−39.1 to 30.8	−38.9 to 59.3	−39.1 to 59.3	

Abbreviations: *BMI* body mass index, *CLAI* chronic lateral ankle instability, *CO* calcaneal offset, *FAO* foot and ankle offset, *HA* hindfoot angle, *L* left, *R* right, *SD* standard deviation
[a]Significant *p* values are in bold
[b]At least I side
[c]Student *t* test
[d]Fisher exact test
[e]Linear mixed model taking into account correlation between patients' feet

[adjusted OR = 0.94; 95%CI, 0.86–1.03; $p = 0.165$] (Table 8.2). In this study, there was a significant association between negative FAO and clinical varus hindfoot ($p < 0.001$) and between negative FAO and diagnosis of CLAI ($p < 0.001$) (Table 8.3).

Discussion

This study is the first to describe a positive linear relationship between hindfoot varus and the risk of developing CLAI. The modern tool represented by WBCT in association with semiautomated HFA and a clinical database proved effective at

Table 8.2 Univariate and multivariable generalized mixed model to predict risk of chronic lateral ankle instability ($N = 370$)[a]

Variable	Unadjusted OR (95% CI)	*p* value	Adjusted OR (95% CI)	*p* value
FAO (%) (by additional unit)	0.63 (0.49–0.83)	<.001	0.65 (0.50–0.84)	.001
Sex (F vs. M)	0.35 (0.04–2.98)	.346	0.52 (0.04–6.80)	.617
Age (years) (by additional unit)	0.95 (0.89–1 02)	.189	0.94 (0.86–1.03)	.165

Abbreviations: *CI* confidence intervals, *F* female, *FAO* foot ankle offset, *M* male, *OR* odds ratio
[a]Random effect on patients to take into account correlation between feet. Logit link of risk of chronic ankle instability

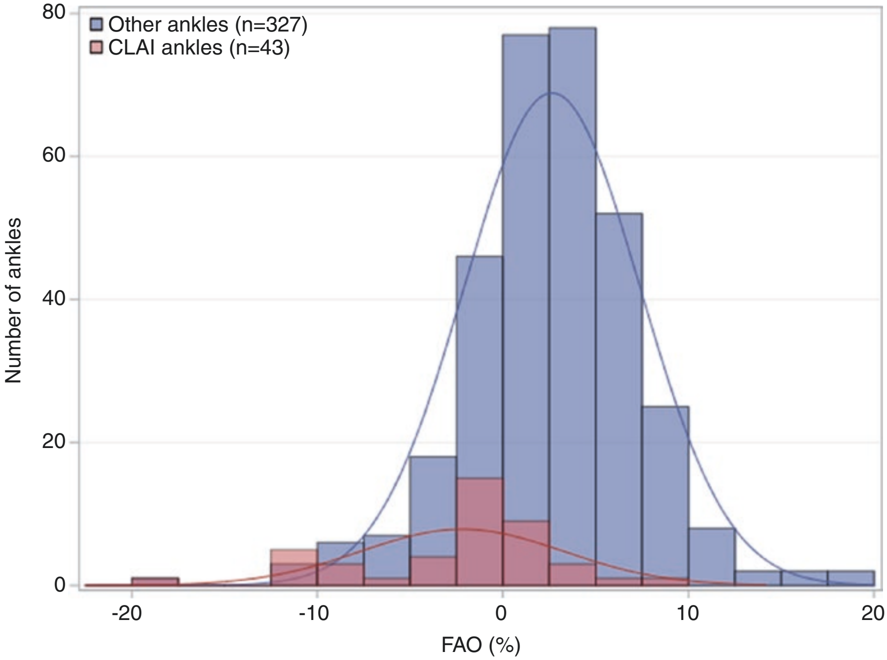

Fig. 8.2 Comparison of foot and ankle offset value distribution curves between subjects diagnosed with chronic lateral ankle instability and controls

achieving this objective using a retrospective study approach. This seems to match previous hypotheses based on clinical and radiographic evaluations but never demonstrated in a three-dimensional environment under physiological loading conditions [5–10]. The relationship between a varus momentum and risk of instability has a well-known rationale. In terms of biomechanics, a varus hindfoot is universally recognized as a "stiff" hindfoot, compared to a valgus/flatfoot morphotype, which is considered "supple." This stiffness contributes to reduced shock absorption power and also increases the risk of damage to the lateral structures of the hindfoot through increased supinating moment. As a result, weakened lateral support becomes a predisposing factor for recurrent inversion injuries [6].

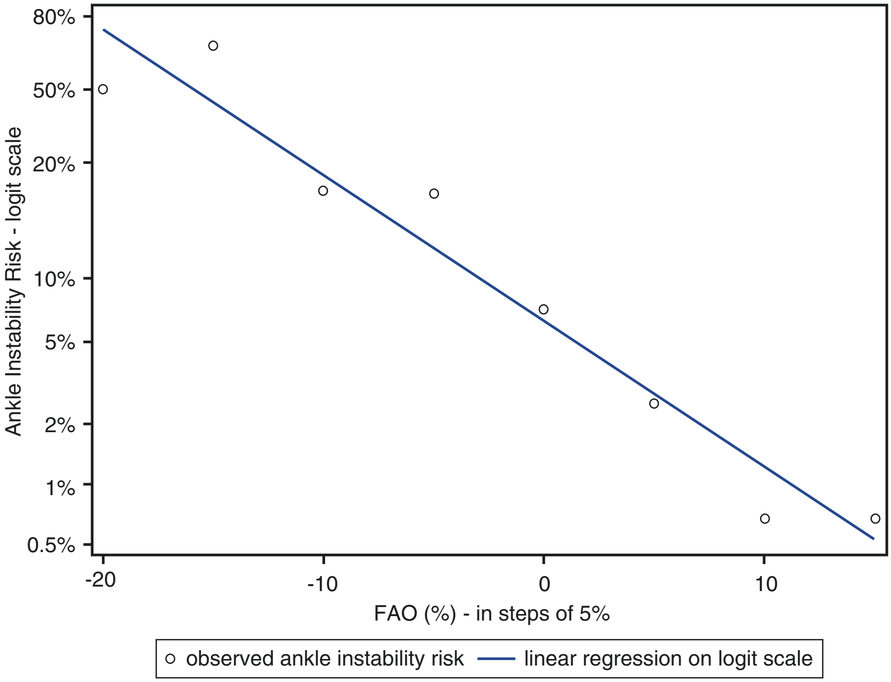

Fig. 8.3 Relation between the log odds of chronic lateral ankle instability and foot and ankle offset values

Table 8.3 Relationship between (1) FAO sign and clinical assessment and (2) FAO sign and diagnosis of CLAI (*N* = 370)

	Total	Clinically varus	Clinically neutral or valgus	*p* value	CLAI	No of CLAI	*p* value
Total	370	49	321	<.001	43	327	<.001
Positive FAO, *n* (%)	260 (70.3)	3 (6.1)	257 (80.1)		14 (32.6)	246 (75.2)	
Negative FAO, *n* (%)	110 (29.7)	46 (93.9)	64 (19.9)		29 (67.4)	81 (24.8)	

Abbreviations: *CLAI* chronic lateral ankle instability, *FAO* foot ankle offset
Hindfoot alignment assessment was primarily based on clinical examination. When unclear, a goniometer was applied on the posterior aspect of the ankle and the hindfoot, measuring the standing tibiocalcaneal angle (angle between the bisectors of the calf and the calcaneus). Values between 0° and 7° of valgus were considered normal. If greater than 0°, the hindfoot was varus. If lower than −7°, it was valgus

Up to a few years ago, there was little evidence for this, mainly due to flaws related to the clinical and radiographic assessment of HFA [11]. The idea that CT might enhance our understanding and diagnostic power around the hindfoot dates back over three decades [14, 15]. Non-loading conditions and the significant difference in amount of radiation when compared to plain radiographs have always limited the usefulness of CT in this field. However, this has been overcome by the recent development and expansion of WBCT [11, 12]. Some authors have already documented its role in common foot and ankle pathologies, such as ankle fractures, hallux valgus, hallux rigidus, peritalar subluxation, and flatfoot [16–20]. To the best of our knowledge, no study has investigated the relationship between a varus hindfoot and CLAI using the WBCT technology.

In 2002, Van Bergeyk stated that hindfoot varus was more common in patients with CLAI compared with normal controls [5]. These authors found a statistically significant difference in the central calcaneal varus angle (CCVA) between varus hindfeet and controls. In this study, a footrest was utilized to simulate weight-bearing conditions. A few years later, Strauss retrospectively assessed 180 ankles diagnosed with CLAI, focusing on various extra-articular related conditions and found clinical hindfoot varus alignment in 15 cases (8%). Interestingly, among those requiring revision after surgery, 28% had a varus hindfoot [5].

Our analysis represents a step forward from Van Bergeyk's work, for at least three reasons. First, the use of a WBCT machine helped to overcome the flaws related to weight-bearing simulation, namely, the application of a partial load and the absence of active muscle contraction [11]. Second, our approach enabled us to define an individual continuous predictive value for FAO towards CLAI and not just a difference between the groups. Finally, measurement of FAO has excellent intra- and interobserver reliability (0.97–0.98 and 0.98–0.99, respectively) [12, 13], as opposed to CCVA (0.62 and 0.49) used in the previous study [5]. Bearing in mind Strauss' considerations, WBCT would definitely help in the recognition of some associated intra- (osteochondral lesions) or extra-articular conditions, such as os trigonum lesions, os subfibulare, and other ossicles, anterior tibial spurs, and tarsal coalitions that are often underestimated and could be addressed at the same time as CLAI if properly diagnosed [4]. In our case, WBCTs were all part of standard follow-up for these patients, and no extra cost was generated. They were bilateral when a bilateral assessment was required, as it would have been using a conventional radiographic setup.

Noteworthy, in this study we found that about 94% of clinically varus hindfoot had negative FAO (Table 8.3). Although two studies have already well focused on the relationship between FAO and clinical assessment of hindfoot [12, 13], no specific study has been published on WBCT measurements in cavovarus feet so far. A recent analysis by de Cesar Netto et al. has suggested that WBCT measurements of hindfoot alignment may demonstrate significantly more pronounced valgus than the clinical evaluation, potentially explaining the positive value of FAO in 6% of clinically varus hindfeet [17].

Our study has several limitations. First, its retrospective design. Second, measurements were performed by a single author, which did not allow us to assess intra- or interobserver reproducibility. However, this was not an aim of the current analysis, and the latter has been assessed previously in the literature [12, 13]. Third, we investigated HFA in a relatively small sample size (only 43 feet with CLAI); however, the results were statistically significant and support the pertinence of our approach. No power estimation was done a priori to the study; however, performing an a posteriori analysis with power of 90%, a Type I error at 5%, and a normal distribution with mean 2 and standard deviation 5, for 12% feet with ankle instability, the required sample size for 0.85 odds ratio associated with each additional FAO unit would be 160. Fourthly, we included patients with a history of three ankle sprains over a 6-month period, corresponding to the criterion that we adopt in our clinical practice. To the best of our knowledge, CLAI is usually described as a combination of pain or discomfort, sensation of instability, and recurrent episodes (imprecise number) of ankle giving way [21, 22]. The lack of an unambiguous definition of CLAI and the absence of international consensus guidelines make certainly more difficult to define standardized inclusion criteria for a study on this condition. Lastly, we are aware that our results were generated from a specific population (patients referred to a specialized center). As such, an alternative explanation to our results might be that, among patients having CLAI, those with a varus morphotype would have a higher risk to become symptomatic and to seek medical attention. We acknowledge that the design of our study does not allow to disprove this scenario, and for this we encourage further research on ankle instability.

In conclusion, our study found that a varus hindfoot represents a risk factor for CLAI, with a 35% increased OR per 1% reduction of FAO (towards varus). The use of WBCT coupled with semiautomated measurements and a dedicated clinical database may improve the diagnostic accuracy and prognostic power while enabling the assessment of associated conditions in order to address all components of CLAI. Future research will need to focus on the development of intelligent software to improve exhaustiveness of clinical data collection and to render the measurement systems fully automatic.

References

1. Clanton TO, Campbell KJ, Wilson KJ, Michalski MP, Goldsmith MT, Wijdicks CA, LaPrade RF. Qualitative and quantitative anatomic investigation of the lateral ankle ligaments for surgical reconstruction procedures. J Bone Joint Surg Am. 2014;96(12):e98.
2. McCriskin BJ, Cameron KL, Orr JD, Waterman BR. Management and prevention of acute and chronic lateral ankle instability in athletic patient populations. World J Orthop. 2015;6(2):161–71.
3. Pourkazemi F, Hiller CE, Raymond J, Nightingale EJ, Refshauge KM. Predictors of chronic ankle instability after an index lateral ankle sprain: a systematic review. J Sci Med Sport. 2014;17(6):568–73.
4. Strauss JE, Forsberg JA, Lippert FG. Chronic lateral ankle instability and associated conditions: a rationale for treatment. Foot Ankle Int. 2007;28(10):1041–4.
5. Van Bergeyk AB, Younger A, Carson B. CT analysis of hindfoot alignment in chronic lateral ankle instability. Foot Ankle Int. 2002;23(1):37–42.
6. Bosman HA, Robinson AHN. Treatment of ankle instability with an associated cavus deformity. Foot Ankle Clin. 2013;18(4):643–57.
7. Fortin PT, Guettler J, Manoli A. Idiopathic cavovarus and lateral ankle instability: recognition and treatment implications relating to ankle arthritis. Foot Ankle Int. 2002;23(11):1031–7.
8. Klammer G, Benninger E, Espinosa N. The varus ankle and instability. Foot Ankle Clin. 2012;17(1):57–82.

9. Sugimoto K, Samoto N, Takakura Y, Tamai S. Varus tilt of the tibial plafond as a factor in chronic ligament instability of the ankle. Foot Ankle Int. 1997;18(7):402–5.
10. Vienne P, Schöniger R, Helmy N, Espinosa N. Hindfoot instability in cavovarus deformity: static and dynamic balancing. Foot Ankle Int. 2007;28(1):96–102.
11. Barg A, Bailey T, Richter M, de Cesar Netto C, Lintz F, Burssens A, Phisitkul P, Hanrahan CJ, Saltzman CL. Weightbearing computed tomography of the foot and ankle: emerging technology topical review. Foot Ankle Int. 2018;39(3):376–86.
12. Lintz F, Welck M, Bernasconi A, Thornton J, Cullen NP, Singh D, Goldberg A. 3D biometrics for hindfoot alignment using weightbearing CT. Foot Ankle Int. 2017;38(6):684–9.
13. Zhang JZ, Lintz F, Bernasconi A, Weight Bearing CT International Study Group, Zhang S. 3D biometrics for hindfoot alignment using weightbearing computed tomography. Foot Ankle Int. 2019;40(6):720–6.
14. Martinez S, Herzenberg JE, Apple JS. Computed tomography of the hindfoot. Orthop Clin North Am. 1985;16(3):481–96.
15. Smith RW, Staple TW. Computerized tomography (CT) scanning technique for the hindfoot. Clin Orthop Relat Res. 1983;177:34–8.
16. Cheung ZB, Myerson MS, Tracey J, Vulcano E. Weightbearing CT scan assessment of foot alignment in patients with hallux rigidus. Foot Ankle Int. 2018;39(1):67–74.
17. de Cesar Netto C, Schon LC, Thawait GK, da Fonseca LF, Chinanuvathana A, Zbijewski WB, Siewerdsen JH, Demehri S. Flexible adult acquired flatfoot deformity: comparison between weight-bearing and non-weight-bearing measurements using cone-beam computed tomography. J Bone Joint Surg Am. 2017;99(18):e98.
18. Kimura T, Kubota M, Taguchi T, Suzuki N, Hattori A, Marumo K. Evaluation of first-ray mobility in patients with hallux valgus using weight-bearing CT and a 3-D analysis system: a comparison with normal feet. J Bone Joint Surg Am. 2017;99(3):247–55.
19. Lawlor MC, Kluczynski MA, Marzo JM. Weight-bearing cone-beam CT scan assessment of stability of supination external rotation ankle fractures in a cadaver model. Foot Ankle Int. 2018;39(7):850–7.
20. Probasco W, Haleem AM, Yu J, Sangeorzan BJ, Deland JT, Ellis SJ. Assessment of coronal plane subtalar joint alignment in peritalar subluxation via weight-bearing multiplanar imaging. Foot Ankle Int. 2015;36(3):302–9.
21. de Vries JS, Krips R, Sierevelt IN, Blankevoort L, van Dijk CN. Interventions for treating chronic ankle instability. Cochrane Database Syst Rev. 2011;(8):CD004124.
22. Karlsson J, Eriksson BI, Bergsten T, Rudholm O, Swärd L. Comparison of two anatomic reconstructions for chronic lateral instability of the ankle joint. Am J Sports Med. 1997;25(1):48–53.

Chapter 9
Normal Hindfoot Alignment Assessed by Weight Bearing CT: Presence of a Constitutional Valgus?

Arne Burssens

Introduction

Hindfoot alignment has classically been determined using a long axial or hindfoot alignment view [1]. Studies using these radiographic methods in normal asymptomatic feet report values between 2° and 5° of valgus in the general population [2]. Clinical measurements of the hindfoot are situated between 5.61° and 6.50° of valgus [3]. These findings give the impression of a physiological valgus alignment of the hindfoot. However, results are based on small cohorts [2, 4], lack a clear correlation between clinical/radiographical data [5], and impose important measurement errors due to bony superposition present in plane weight bearing radiographs [6]. The latter is currently overcome by the use of weight bearing CT which provides an accurate bone position and allows a natural stance of the patient [7]. Various methods now have been described to determine hindfoot alignment using weight-bearing CT [7, 8]. This study will use a method composed out of the anatomical axis of the tibia and the talocalcaneal axis based on the inferior point of the calcaneus as described previously [9]. To investigate not only the radiological relevance of this point but also a possible biomechanical role, a density analysis will be performed. An increased ossification around the inferior point would indicate a higher load application as stated by Wolff's law [10]. Currently the measurement method was only used in malalignments of the hindfoot and lacks reference values. Therefore, the goal of this study is to obtain measurements from a population with clinical and radiological absence of hindfoot pathology. These will be compared to hindfoot measurements obtained from the long axial view based on the anatomical axis of the tibia and the calcaneal axis, to point out possible differences attributed to the measurement method [1]. Although surgical hindfoot corrections are frequently performed either extra-articular by osteotomies or intra-articular by arthrodesis, still

---

Based on Burssens A, Van Herzele E, Leenders T, Clockaerts S, Buedts K, Vandeputte G, et al. Weight bearing CT in normal hindfoot alignment—Presence of a constitutional valgus? *Foot and Ankle Surgery* 2018;24(3) 213–218.

M. Richter et al., *Weight Bearing Cone Beam Computed Tomography (WBCT) in the Foot and Ankle*, https://doi.org/10.1007/978-3-030-31949-6_9

numerous debate exists on the amount of correction and the ideal foot position after arthrodesis [11, 12]. Per-operative tools are already used to obtain a more accurate correction [13] or a physiological load distribution [14], but a preoperative planning remains paramount. This study will contribute to the preoperative planning by providing further insights into a physiological hindfoot alignment. The null hypothesis is the existence of an overall physiological valgus alignment in the hindfoot.

Materials and Methods

Study Population and Design

Forty-eight patients, mean age of 39.6 ± 13.2 years, with clinical and radiological absence of hindfoot pathology were included. Indications for imaging consisted out of minor foot and ankle trauma with persistent complaints in purpose to rule out an occult fracture, but appeared to be negative or nonsignificant ($n = 31$), suspicion of osteoartrosis but not detectible on weight bearing CT imaging ($n = 11$), and MTP I fusion to assess consolidation ($n = 4$) (Table 9.1).

Patient Characteristics

Each time the contralateral not affected foot was used for analysis. This was performed using CurveBeam® software applied on the images retrieved from the weight bearing CT (pedCAT®). Ethical committee gave permission in performing the study (OG10601102015). Following imaging protocol was used: radiation source was set at 4 mAs and 50 kV, with a focus distance of 100 cm, with the beam pointed at the ankle joint. PedCAT used the following settings: tube voltage, 96 kV; tube current, 7.5 mAs; CTDIvol 4.3 mGy; matrix, 160,160,130; pixel size, 0.4 mm; and slice interval 0.4 mm. At the department of radiology, patients were asked to attain a natural stance with both feet parallel to each other and straight ahead at shoulder width.

Hindfoot measurements were performed by two authors AB and EDV. Each measurement was repeated three times; after the complete set of measurements, the mean out of three measurements was used for further analysis. The hindfoot angle was

Table 9.1 Patient characteristics

Characteristic	Total (N = 48)
Age (±) SD	39.6 ± 13.2 years
Sex (M/F)	28/20
Minor trauma	31
Absence osteoarthritis	11
MTP I fusion	4

determined based on the inferior point of the calcaneus (HA_{IC}) as described previously [9]. In brief the foot is positioned according to the second ray, and the angle is composed out of the intersection between the anatomical tibial axis (TA_x) and the talocalcaneal axis (TCA_x) (Figs. 9.1a and 9.2a). The latter is formed by connecting the inferior point of the calcaneus with the middle of the upper surface of the talus (Fig. 9.3a, b). This will be compared to the hindfoot angle measured on the long axial view (HA_{LA}), for which firstly the foot needed to be aligned with second ray and inclined 45° by applying the reconstruction mode built in to the used software (Figs. 9.1b and 9.2b, c). Secondly the calcaneus needed to be divided 50–50% in the

Fig. 9.1 (**a**) Overview of the measurement method (HA_{IC}) based on the inferior calcaneal point (lower right quadrant) after alignment of the foot according to second ray (upper right quadrant, green line) (**b**). In comparison to the long axial method (HA_{LA}) based on dividing the calcaneus (lower right quadrant) after inclination of the feet towards 45° and aligning with the second ray (upper right quadrant, green line)

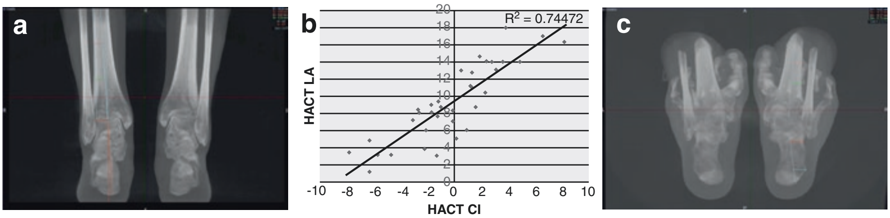

Fig. 9.2 (**a**–**c**) Correlation between both measurement methods showed to be good with an $R^2 = 0.74$, indicating that both can be used to determine hindfoot alignment but with higher valgus values obtained in the HA_{LA}

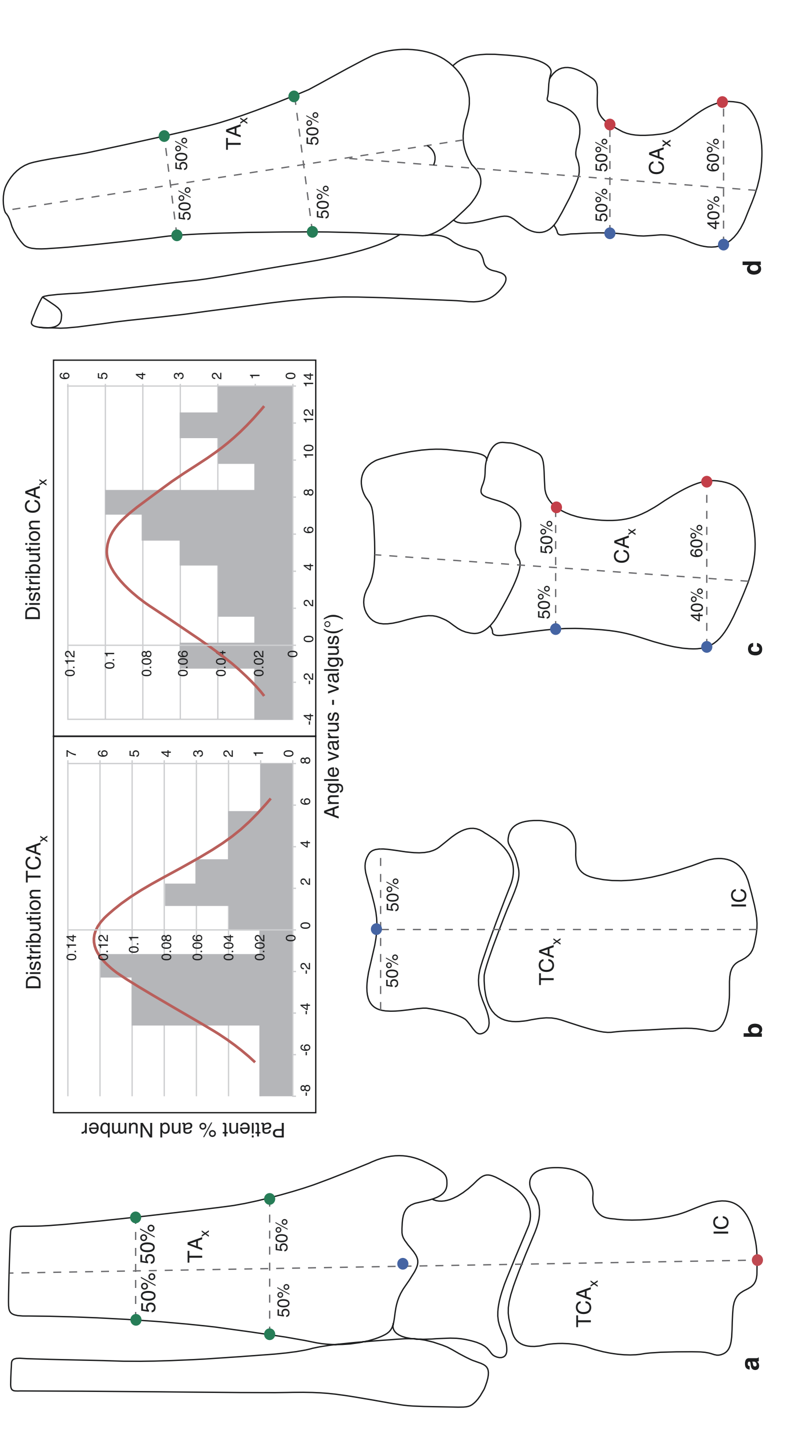

Fig. 9.3 Schematic overview of both hindfoot measurement methods (**a**). HA_{IC} composed out of the anatomical tibia axis (TA_x), by dividing the tibia shaft 50–50% each one third (green points) and talocalcaneal axis (TCA_x) by connecting the inferior calcaneus point (IC, red point) with the middle of the talar dome (blue point) (**b**). Distribution of the (TCA_x) (**c**). Distribution of the (CA_x) pointing out a shift towards a valgus value (**d**). HA_{LA} composed out of the anatomical tibia axis (TA_x) and the calcaneal axis (CA_x) after dividing the calcaneus and inclining the foot 45°

upper part and 40–60% in the lower part to determine the calcaneal axis (CA_x) as described by van Dijk et al. [1] (Fig. 9.3c). The HA_{LA} was composed out of the intersection between the TA_x and the CA_x on the inclined foot (Fig. 9.3d).

To investigate the relevance of the inferior calcaneus point, a bone density analysis was performed by calculating the pixel density of this region of interest (ROI) in the coronal plane and comparing it to a regional area with the same surface window by using an OsiriX®-based plug in software (Fig. 9.4a, b). A higher pixel density would concur with an increased calcium/bone density, and by applying Wolff's law, this would indicate a higher load exposure [10]. To avoid the influence of traction exerted by the fascia plantaris on the bone formation in this inferior calcaneal region, the ROI was set at a distance of 5 mm from the medial calcaneal tuberosity in the sagittal plane (Fig. 9.4c, d).

Hindfoot characteristics in the tibiotalar joint were measured as the talar tilt (TT) and the tibial inclination (TI) of the articular surface towards the horizontal axis as described previously [9]. In the subtalar joint the subtalar vertical angle (SVA) was measured in the middle coronal plane when started at the level of the highest point of the talar dome according to the method described by Knupp et al. [15]

Statistical Analysis

A Kolmogorov-Smirnov test was used to analyze if the data were normally distributed. Depending on the outcome, a parametric Student's t-test or a nonparametric Wilcoxon signed rank test will be conducted to compare the means of the two used hindfoot angles. Regression analysis was performed to correlate the relative change of both angles by calculation of the Spearman's coefficient and visualization of a corresponding scatterplot. To assess the density analysis between the inferior calcaneus point and the regional calcaneal area, the dependent Student's t-test was used. Inter- and intraobserver variability of the obtained measurements was analyzed using interclass correlation coefficient (ICC). This was interpreted as follows: ICC < 0.4, poor; 0.4 < ICC < 0.59, acceptable; 0.6 < ICC < 0.74, good; and ICC > 0.74, excellent [16]. The SPSS (release 20.0.0. standard version, SPSS, Inc., Chicago, IL, USA) statistical package was used to analyze the results. A probability level of $P < 0.05$ was considered significant.

Results

Hindfoot Alignment

Kolmogorov-Smirnov analysis shows a $P > 0.05$ for both hindfoot parameters indicating that the measurements are normally distributed, and therefore further parametric testing could be used. The mean HAIC equaled 0.79° of valgus ± 3.2 with a

Fig. 9.4 (**a**) 3D overview (**b**). Density of the WBC compared to the regional calcaneal area (**c**). ROI was set at a distance of 5 mm from the medial calcaneal tuberosity to avoid bone formation by traction influence of the fascia plantaris (**d**). Measurement of the hindfoot angle based on the osteosclerotic weight bear point (WBC) of the calcaneus

Table 9.2 Mean hindfoot measurements in degrees and concomitant intraclass correlation coefficients

	Hindfoot measurements	SD (±)	ICC_{inter}	ICC_{intra}
HA_{IC}	0.79	3.2	0.73	0.81
TA_X	2.7	2.1	0.76	0.83
TCA_X	0.61	2.9	0.85	0.82
HA_{LA}	9.1	4.8	0.71	0.74
TA_X	3.8	2.9	0.81	0.78
CA_X	5.2	4.1	0.71	0.79
TI	2.4	0.84	0.81	0.86
TT	1.9	0.86	0.83	0.82
SVA	96.1	5.7	0.73	0.76

mean TACT of 2.7° varus ± 2.1 and a mean TCAx of 0.61° varus ± 2.9 (Table 9.2, Figs. 9.2a and 9.3). The mean HALA equaled 9.1° of valgus ± 4.8° with a mean TAx of 3.8° varus ± 2.9 and a mean CAx of 5.2° valgus ± 4.1.

Comparing both pointed out that HALA was significantly different $P < 0.001$ from the HAIC by showing an increased valgus value (Tables 9.2 and 9.3), whereas the HAIC showed a more neutral alignment (Figs. 9.2 and 9.3). Correlation between both was shown to be good by a Spearman's correlation coefficient = 0.74.

Table 9.3 Results of independent Student t-testing

	HACT $_{CT\ IC}$/HA$_{CT\ CL}$	ROIcalc med/ROIcalc lat
t-value	<0.001	<0.001
P-value	<0.001	<0.001

ROI Density Analysis

The mean density of the WBP equaled 271.3 ± 84.1 and was significantly higher than the regional lateral calcaneal area 109.4 ± 63.2 ($P < 0.001$).

Hindfoot Characteristics

Measurements in the tibiotalar joined showed a mean TI = 1.9° ± 0.81° and a mean TT = 2.4° ± 0.86°. Measurements in the subtalar joint showed a mean SVA = 96,1° ± 5.7°.

Discussion

This study shows a more neutral alignment of the hindfoot when applying the measurement method based on the inferior point of the calcaneus (HAIC). Therefore, the anatomical tibia axis and the inferior point as described by Saltzman in the hindfoot alignment view were used [17]. Additionally, the talus was incorporated in the measurement method, as an important component of the hindfoot and due to its visibility on weight bear CT, as opposed to plane weight bear radiographs, where it's often superimposed by the midfoot [1, 17, 18]. The obtained results couldn't retain the null hypothesis of a physiological valgus alignment in the hindfoot as reported by previous literature [2, 3]. This can be attributed to either the used measurement method or to a physiological neutral configuration of the talus and calcaneus towards the tibia. Previous studies and this study show that by using a measurement based on dividing the calcaneus (HA$_{LA}$), an increased valgus alignment will be obtained [12]. Additionally, it is pointed out that by altering the foot position towards an increased endo-rotation, an overestimation of the valgus alignment occurs [12, 19, 20]. This advocates using the inferior calcaneus point, as it requires no additional steps, such as dividing the calcaneus in half, and hence avoiding possible measurement errors. Another relevance of the inferior weight bear point is shown by the presence of an increased bone formation as shown by the pixel density analysis suggesting an increased load exposure when following Wolff's law [10]. This makes it an interesting landmark as a reference point when planning an osteotomy, considering that the goal of this procedure is to shift the load towards a biomechanical more favorable position [13, 21]. An important disadvantage of the used method is the absence of complete 3D measurement. Although each foot was positioned using the same method according to three planes, the actual hindfoot angle was only determined in the coronal plane, possibly missing valuable spatial data in the sagittal and transversal plane such as the calcaneal shape [21]. Further translation of this method towards computer calculation of the inferior calcaneus point therefore can take place when using 3D segmented models, which are currently used for morphological characterization or joint configuration [22–24]. Another shortcoming can be attributed to the study population. Although the number is comparable to previous studies [17], the population was mostly taken from patients with persisting pain symptoms after sustaining a minor trauma such as an ankle distortion. Although not shown to be a primary risk factor [25], this population could have an intrinsic varus configuration and therefore be more prone in sustaining an ankle distortion. However, the obtained results are comparable to previous findings in healthy subjects [17], and the load-bearing area was found on the medial side of the calcaneus, which concurred with static podography study of Cavanagh et al. [26] Despite this concordance, it was pointed out recently by Richter et al. that a correlation between weight bearing CT images and podography was absent when using an incorporated pressure plate [27]. Further research can therefore analyze the influence of various types of hindfoot alignments on their bone distribution pattern using weight bearing CT compared to findings obtained from pressure plates both statically and dynamically [27]. In conclusion this paper shows a more neutral configuration of the hindfoot in the above population when using the HAIC based on the inferior point of the calcaneus. This method is supported by previous literature, a high reproducibility, and a load-bearing relevance as pointed out by the pixel bone density analysis [9, 17]. Future research should be aimed at translating the obtained measurement methods towards 3D segmented models to allow a higher accuracy. This will aid in preoperative planning and allow for a postoperative evaluation after multiplanar reconstructions. These findings should be combined with patient reported outcome measures (PROMs) and podographic and gait analysis to answer the question if the obtained neutral configuration should also be used in surgical hindfoot correction or fusion as compared to the proposed valgus position [12, 28].

References

1. Reilingh ML, Beimers L, Tuijthof GJM, Stufkens SAS, Maas M, van Dijk CN. Measuring hindfoot alignment radiographically: the long axial view is more reliable than the hindfoot alignment view. Skelet Radiol. 2010;39(11):1103–8.
2. Strash WW, Berardo P. Radiographic assessment of the hindfoot and ankle. Clin Podiatr Med Surg. 2004;21(3):295–304.
3. Haight HJ, Dahm DL, Smith J, Krause DA. Measuring standing hindfoot alignment: reliability of goniometric and visual measurements. Arch Phys Med Rehabil. 2005;86(3):571–5.
4. Robinson I, Dyson R, Halson-Brown S. Reliability of clinical and radiographic measurement of rearfoot alignment in a patient population. Foot. 2001;11(1):2–9.

5. Lamm BM, Mendicino RW, Catanzariti AR, Hillstrom HJ. Static rearfoot alignment: a comparison of clinical and radiographic measures. J Am Podiatr Med Assoc. 2005;95(1):26–33.
6. Tuijthof GJ, Herder JL, Scholten PE, Van Dijk CN, Pistecky PV. Measuring alignment of the hindfoot. J Biomech Eng. 2004;126(3):357–62.
7. Richter M, Seidl B, Zech S, Hahn S. PedCAT for 3D-imaging in standing position allows for more accurate bone position (angle) measurement than radiographs or CT. Foot Ankle Surg. 2014;20(3):201–7.
8. Hirschmann A, Pfirrmann CWA, Klammer G, Espinosa N, Buck FM. Upright cone CT of the hindfoot: comparison of the non-weight-bearing with the upright weight-bearing position. Eur Radiol. 2013;24(3):553–8.
9. Burssens A, Peeters J, Buedts K, Victor J, Vandeputte G. Measuring hindfoot alignment in weight bearing CT: a novel clinical relevant measurement method. Foot Ankle Surg. 2016;22(4):233–8.
10. Wolff J. The classic: on the inner architecture of bones and its importance for bone growth. Clin Orthop Relat Res. 2010;468(4):1056–65.
11. Chan JY, Williams BR, Nair P, Young E, Sofka C, Deland JT, et al. The contribution of medializing calcaneal osteotomy on hindfoot alignment in the reconstruction of the stage II adult acquired flatfoot deformity. Foot Ankle Int. 2013;34(2):159–66.
12. Frigg A, Nigg B, Davis E, Pederson B, Valderrabano V. Does alignment in the hindfoot radiograph influence dynamic foot-floor pressures in ankle and tibiotalocalcaneal fusion? Clin Orthop Relat Res. 2010;468(12):3362–70.
13. Richter M, Zech S. Computer assisted surgery (CAS) guided arthrodesis of the foot and ankle: an analysis of accuracy in 100 cases. Foot Ankle Int. 2008;29(12):1235–42.
14. Richter M, Frink M, Zech S, Vanin N, Geerling J, Droste P, et al. Intraoperative pedography: a validated method for static intraoperative biomechanical assessment. Foot Ankle Int. 2006;27(10):833–42.
15. Colin F, Lang TH, Zwicky L, Hintermann B, Knupp M. Subtalar joint configuration on weight-bearing CT scan. Foot Ankle Int. 2014;35(10):1057–62.. 1071100714540890.
16. Shrout PE, Fleiss JL. Intraclass correlations: uses in assessing rater reliability. Psychol Bull. 1979;86(2):420.
17. Saltzman CL, El-Khoury GY. The hindfoot alignment view. Foot Ankle Int. 1995;16(9):572–6.
18. Cobey JC. Posterior roentgenogram of the foot. Clin Orthop Relat Res. 1976;118:202–7.
19. Leemrijse T, Besse J-L, Devos Bevernage B, Vande Berg B, Vandeputte G. Chapitre 3: Imagerie du pied et de la cheville: mode d'emploi. In: Pathologie du pied et de la cheville. Paris: Elsevier Masson; 2015.
20. Barg A, Amendola RL, Henninger HB, Kapron AL, Saltzman CL, Anderson AE. Influence of ankle position and radiographic projection angle on measurement of supramalleolar alignment on the anteroposterior and hindfoot alignment views. Foot Ankle Int. 2015;36(11):1352–61.. 1071100715591091.
21. Hamel J. Calcaneal Z osteotomy for correction of subtalar hindfoot varus deformity. Oper Orthop Traumatol. 2015;27(4):308.
22. Gutekunst DJ, Liu L, Ju T, Prior FW, Sinacore DR. Reliability of clinically relevant 3D foot bone angles from quantitative computed tomography. J Foot Ankle Res. 2013;6(1):1.
23. Qiang M, Chen Y, Zhang K, Li H, Dai H. Measurement of three-dimensional morphological characteristics of the calcaneus using CT image post-processing. J Foot Ankle Res. 2014;7(1):1.
24. Zhang Y, Xu J, Wang X, Huang J, Zhang C, Chen L, et al. An in vivo study of hindfoot 3D kinetics in stage II posterior tibial tendon dysfunction (PTTD) flatfoot based on weight-bearing CT scan. Bone Joint Res. 2013;2(12):255–63.
25. Willems TM, Witvrouw E, Delbaere K, Mahieu N, De Bourdeaudhuij I, De Clercq D. Intrinsic risk factors for inversion ankle sprains in male subjects a prospective study. Am J Sports Med. 2005;33(3):415–23.

26. Cavanagh PR, Rodgers MM. Pressure distribution under symptom-free feet during barefoot standing. Foot Ankle Int. 1987;7(5):262–78.
27. Richter M, Zech S, Hahn S, Naef I, Merschin D. Combination of pedCAT® for 3D imaging in standing position with pedography shows no statistical correlation of bone position with force/pressure distribution. J Foot Ankle Res. 2016;55(2):240–6.
28. Cöster MC, Bremander A, Rosengren BE, Magnusson H, Carlsson Å, Karlsson MK. Validity, reliability, and responsiveness of the Self-reported Foot and Ankle Score (SEFAS) in forefoot, hindfoot, and ankle disorders. Acta Orthop. 2014;85(2):187–94. Burssens A, Van Herzele E, Leenders T, Clockaerts S, Buedts K, Vandeputte G, et al. Weightbearing CT in normal hindfoot alignment—presence of a constitutional valgus? Foot Ankle Surg. 2018;24(3):213–218.

Chapter 10
Reliability and Correlation Analysis of Computed Methods to Convert Conventional 2D Radiological Hindfoot Measurements to 3D Equivalents Using Weight Bearing CT

Arne Burssens

Introduction

Exact radiographic assessment of hindfoot alignment remains a challenge [1, 2]. The various measurement techniques and hindfoot views (either inclined anteroposterior (AP) or posterioranterior (PA)) reflect the lack of a standardized and accurate methodology [3]. All current methodologies try to overcome two main inaccuracies: the superposition caused by the osseous structures in the midfoot and the rotational errors created during the positioning of the foot, as demonstrated by several recent studies [4–6]. Weight bearing CT (WBCT) of the foot and ankle has been shown to be more accurate in hindfoot measurements [7]. This recent imaging technique offers the advantage of a standing position as with weight bearing radiographs but overcomes the disadvantages of the osseous superposition caused by the complex anatomy of the foot and ankle [8–10]. This allows for complete visualization of the hindfoot [11]. Additionally, WBCT software settings can rotate the foot and ankle after the imaging process to acquire a standardized positioning of the hindfoot [7, 8].

Although computed tomography was introduced to orthopedic surgery in the mid-1970s [12], its routine clinical and 3D use only started in the early 1990s with the introduction of the spiral CT, which allowed better insight into complex fracture patterns [13]. Further applications were lacking, which made some authors question the added value of a 3D CT [14]. Reluctance to adopt 3D CTs was evident in foot and ankle literature where most available measurements and reference angels were still performed in 2D [8, 9, 15]. Nevertheless, the orthopedic field's interest in 3D printing and computer-assisted surgery (CAS) has grown in recent years [16, 17]. These tools allow for more precise preoperative planning and intraoperative surgical procedures [18]. However, in order to successfully apply them, a better understand-

Based on Burssens A, Peeters J, Peiffer M, Marien R, Lenaerts T, WBCT ISG, Vandeputte G, Victor J. Reliability and correlation analysis of computed methods to convert conventional 2D radiological hindfoot measurements to a 3D setting using weight bearing CT. *Int J Comp Assisted Radiol Surg* 2018;13(12): 1999–2008 [50].

M. Richter et al., *Weight Bearing Cone Beam Computed Tomography (WBCT) in the Foot and Ankle*, https://doi.org/10.1007/978-3-030-31949-6_10

ing of 3D technology is required. Although the application of these techniques on the skeletal system is generally well understood, their potential use on and subsequent insights from the hindfoot remain unclear; most weight-bearing research of the lower limb has been focused on hip and knee joints [19–21].

The advantage of these methods is that they incorporate each plane according to the region of interest with a high measurement accuracy [19].

Using WBCT, the previously described hindfoot measurements allow for correct foot positioning in the coronal, sagittal, and axial plane, but the actual angles are only obtained from one CT slice in one plane [7, 10, 22, 23].

Although interobserver reliability is high, important spatial data is not used, and the manually drawn angles and foot positioning steps impose additional measurement errors [8].

The aim of this paper is therefore to use computed methods to convert these conventional 2D measurements to a 3D environment. This analytic process will be assessed by rater reliability and regression analysis.

Materials and Methods

Study Population, Design, and Measurement Protocol

Forty-eight patients with clinical and radiological absence of hindfoot pathology were included [24]. The mean age was 39.6 years (SD = 3.2, age range: 19–72 years). The indications for imaging using WBCT were one of the following: minor foot and ankle trauma (e.g., foot and ankle sprain or contusion) with persistent complaints that were negative or nonsignificant for an occult fracture ($n = 31$), the suspicion of osteoarthritis that was undetectable on CT slices ($n = 11$), or a MTP I fusion to assess consolidation ($n = 4$) as shown in Table 10.1.

The contralateral unaffected foot was used for each analysis. The measurements were performed on the images retrieved from the weight bearing pedCAT® cone beam CT, using the incorporated Cubevue® software for the 2D analysis (CurveBeam, Warrington, PA, USA). The 3D analysis was obtained after segmentation of the images using Mimics® 19.0 and analysis using 3-matic® software (Materialise, Leuven, Belgium). The patient records were anonymized and deidentified prior to processing in accordance with the standard data release procedures of the hospital involved in the study. All procedures performed in studies involving human participants were in accordance with the ethical standards of the institutional

Table 10.1 Patient characteristics

Characteristic	Total (N = 48)
Age (±) SD	39.6 ± 13.2 years
Sex (M/F)	28/20
Minor trauma	31
Absence osteoarthritis	11
MTP I fusion	4

and/or national research committee and with the 1964 Helsinki declaration and its later amendments or comparable ethical standards. The Institutional Review Board of AZ Monica approved this study (OG10601102015), and formal consent was not required for this type of study. The following imaging protocol was used: radiation source was set at 4 mAs and 50 kV, with a focus distance of 100 cm, and the beam pointed at the ankle joint. PedCAT used the following settings: tube voltage, 96 kV; tube current, 7.5 mAs; CTDIvol 4.3 mGy; matrix, 160,160,130; pixel size, 0.4 mm; and slice interval, 0.4 mm.

At the department of radiology, patients were asked to stand naturally with both feet parallel to each other, shoulder width apart. Hindfoot measurements were performed in 2D by authors AB and MP. Each measurement was repeated three times. After the set of measurements was complete, the average of these three measurements was used for further analysis. A similar test/retest methodology was performed in other studies concerning hindfoot measurements [3, 5, 8, 25–27]. The hindfoot angle was determined based on the inferior point of the calcaneus (HA2D), as described previously [8]. In brief, the foot was first positioned in line with the collinear axis of the shaft of the second metatarsal, which is considered as the longitudinal axis of the foot in the axial plane (Fig. 10.1). The hindfoot angle was

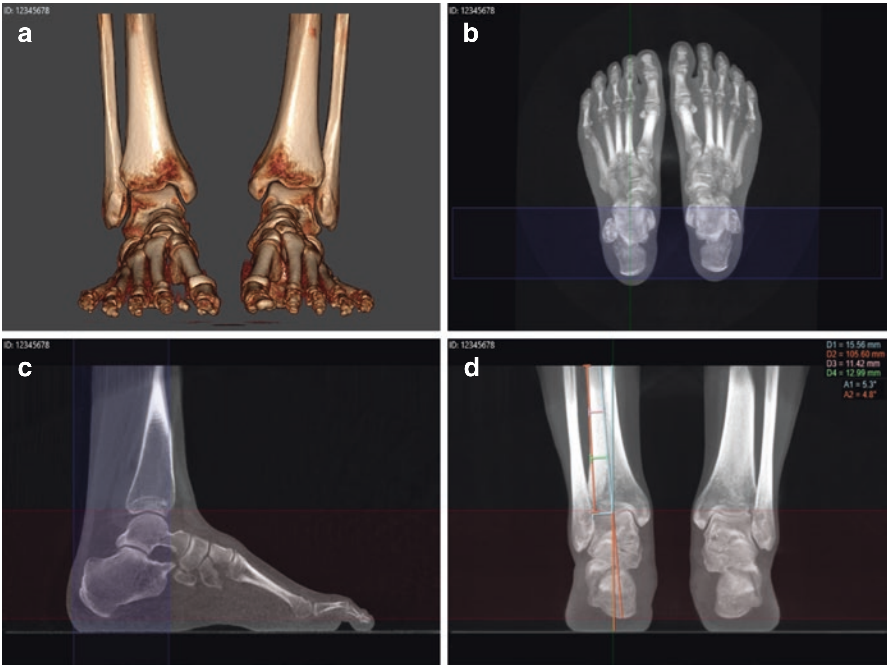

Fig. 10.1 Measuring hindfoot alignment in 2D. (**a**, **b**) Positioning of the foot in line with the axis of the second metatarsal in the axial plane. (**c**, **d**) The hindfoot angle (HA2D) is composed out of the intersection between the anatomical tibia axis (TA2D, blue line) and the talocalcaneal axis (TC2D, orange line). The TC2D connects the inferior point of the calcaneus with the middle of the talar dome

defined as the intersection between the anatomical tibia axis (TA2D) and the talocalcaneal axis (TC2D), which connects the inferior point of the calcaneus and the middle of the upper surface of the talus in the coronal plane (Fig. 10.1c, d).

The varus and valgus alignment of the hindfoot was respectively defined as when the TCA runs medial from the vertical axis and when the TCA runs lateral from the vertical axis, which is often considered as a reference axis [28, 29]. Authors RM and TL determined the 3D hindfoot angle (HA3D) by the use of computer-aided design (CAD) operations (Fig. 10.2a–d).

The anatomical tibia axis (TA3D) was calculated by a best fit centroidal axis along the diaphysis marked above the incisura fibularis (Fig. 10.2a). The talocalcaneal axis (TC3D) was computed by connecting the inferior calcaneus point (ICP) with central talus point (CTP). The ICP was obtained after the calculation of an extrema analysis of the calcaneus (function to determine the most outer point of a structure in the direction of a given axis) (Fig. 10.2b). The CTP was determined by the calculated centroid of the talus (mean position of all the points in a given structure) (Fig. 10.2c). The computed intersection of both the TA3D and the TC3D

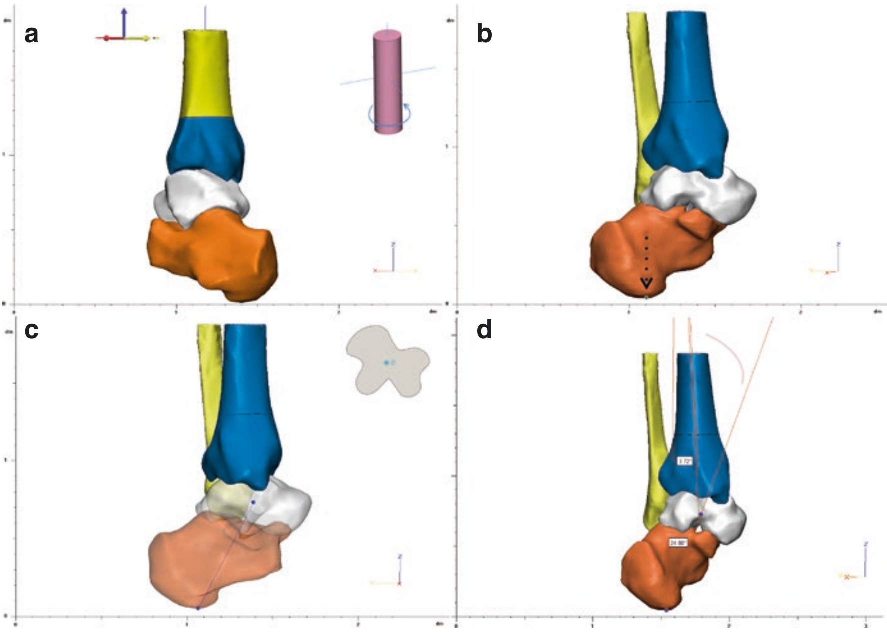

Fig. 10.2 Measuring hindfoot alignment in 3D. (**a**) The anatomical tibia axis (TA3D) was computer calculated as an axis based on the moment of inertia (depicted in the upper right quadrant) through the distal end of the tibia marked above the fibular groove. (**b**) The inferior calcaneus point was calculated by an extrema analysis (a software function to determine the most outer point in the superior-inferior direction) (arrow). (**c**) The center of the talus was calculated as a centroid (depicted in the upper right quadrant) based on the mean position of all points in the talus. The talocalcaneal axis (TC3D) was calculated by connecting the inferior calcaneus point with the centroid of the talus. (**d**) The intersection of both axes became the HA3D

became the HA3D (Fig. 10.2d). The TA and the TC were measured separately in the hindfoot angle when comparing the 2D and the 3D angles in order to emphasize possible inconsistencies attributable to either the tibial or talocalcaneal component.

The talocrural angle (TCr) was used as a radiographic parameter to assess the ankle in the coronal plane [30]. TCr was measured in 2D (TCr2D) as the angle between the intersection of the intermalleolar axis (obtained after connecting the interior point of the medial with the most inferior point of the lateral malleolus) and the horizontal axis of tibial joint line (Fig 10.3a).

In 3D (TCr3D), this measurement is performed in the same manner by the intersecting angle of the intermalleolar axis (the most inferior points of the malleoli were computed using an extrema analysis) and the computed best fitted axis through the horizontal contour of the tibial joint line (Fig. 10.3b).

Characteristics in the tibiotalar joint were measured as the inclination of the tibial joint surface towards the vertical axis perpendicular to the floor (TI2D) and the tilt of the talus towards the vertical axis perpendicular to the floor (TT2D) as described previously (Fig. 10.3c) [8].

The TI3D and TT3D were similarly analyzed by reconstructing the joint surface respective of the tibia and the talus in the coronal plane. This reconstruction allows for the computation of the horizontal axis of both surfaces and the intersection with the vertical axis perpendicular to the floor resulted in the TI3D and TT3D.

In the subtalar joint (STJ), the middle subtalar vertical angle (SVA2D) was determined in the coronal plane according to the method described by Colin et al. [9]. This measurement required the length of the posterior facet of the STJ to be measured in

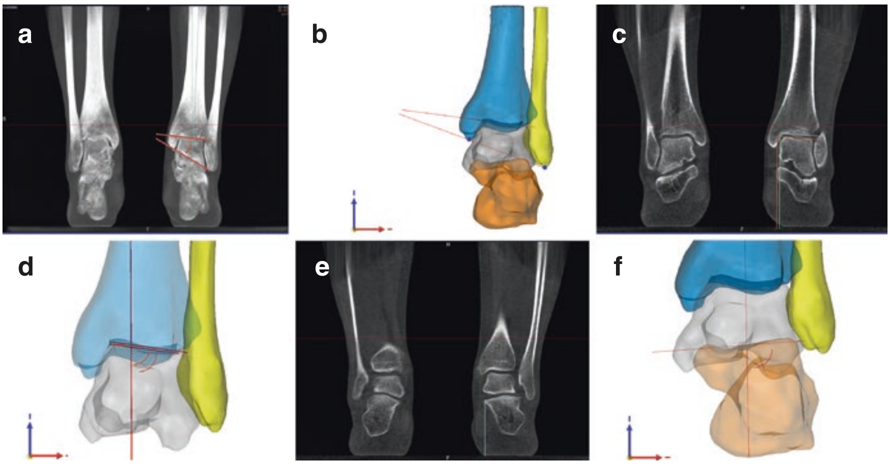

Fig. 10.3 Common ankle and hindfoot measurements. (**a**, **b**) The talocrural angle (TCr) was measured in 2D (TCr2D) by the intersection of the malleolar axis and the tibial joint line. The 3D (TCr3D) was measured as the intersection between the malleolar axis, created by connecting the inferior medial and lateral malleolus through an extremity analysis and the tibial joint line. (**c**) Characteristics in the tibiotalar joint were measured as the tibial inclination (TI2D, upper line) the talar tilt (TT2D, lower line). (**d**) Representation of the TI3D, TT3D. (**e**) Characteristics in the hindfoot were measured as the SVA (SVA 2D). (**f**) Representation of the SVA3D

the sagittal plane. In the midpoint of this distance, the inclination of the STJ surface towards the vertical axis perpendicular to the floor in the coronal plane was determined (Fig. 10.3e). The SVA3D was analyzed similarly to the SVA2D with the same methods as applied in the TI3D and TT3D, which is generalized in Fig. 10.3f and detailed in Fig. 10.4.

By applying goniometric functions built into the software, commonly used measurements from a 2D radiograph can be translated into a 3D angle and its subsequent projection. The general sequence is depicted and explained for the talocrural angle as an example (Fig. 10.4a–d).

The coronal plane in these methods was derived from the Cartesian coordinate system with the inferior calcaneus point as the origin. The *z*-axis was defined as running through the origin perpendicular to the ground floor. The *x*-axis runs through the origin perpendicular to the *z*-axis and lies in the sagittal plane, formed through the center of the second metatarsal head and the origin perpendicular to the ground floor. The *y*-axis goes through the origin, perpendicular to the *x*-axis and *z*-axis (Fig. 10.5e–f).

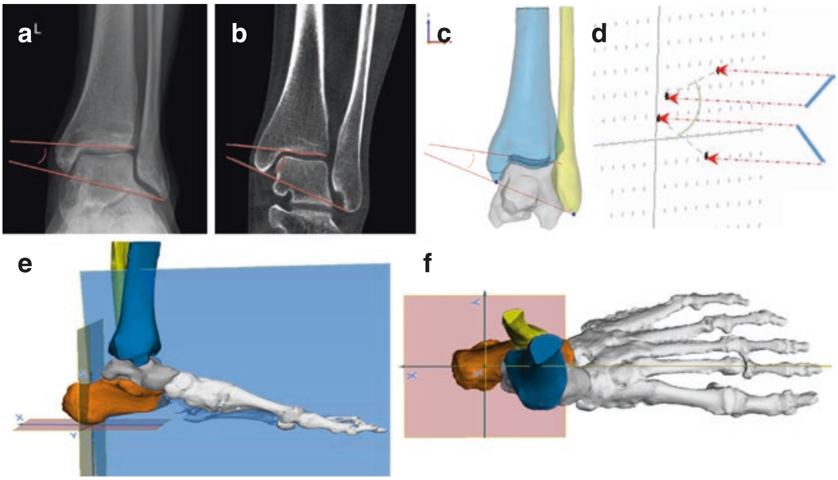

Fig. 10.4 Sequence of translating commonly used 2D measurements to 3D angles. (**a**) Starting as an example with an AP radiograph of the talocrural angle, which was measured as the intersection between the axis connecting both malleoli and the axis parallel to articular surface of the distal tibia in 2D. (**b**) Same measurement in 2D is applied by the use of weight bearing CT after correct rotation. (**c**) Computer-calculated points (blue) to determine the axes and 3D angle. (**d**) Schematic representation of projecting a 3D angle in the coronal (*yz*-plane) through the used software by applying build-in goniometric functions. (**e–f**) Cartesian coordinate system with the origin defined in the inferior point of the calcaneus. The *z*-axis was calculated perpendicular to the floor through the origin. The *x*-axis runs through the origin perpendicular to the *z*-axis and lies in the sagittal plane, formed through the center of the second metatarsal head and the origin perpendicular to the ground floor. The *y*-axis goes through the origin, perpendicular to the *x*-axis and *z*-axis

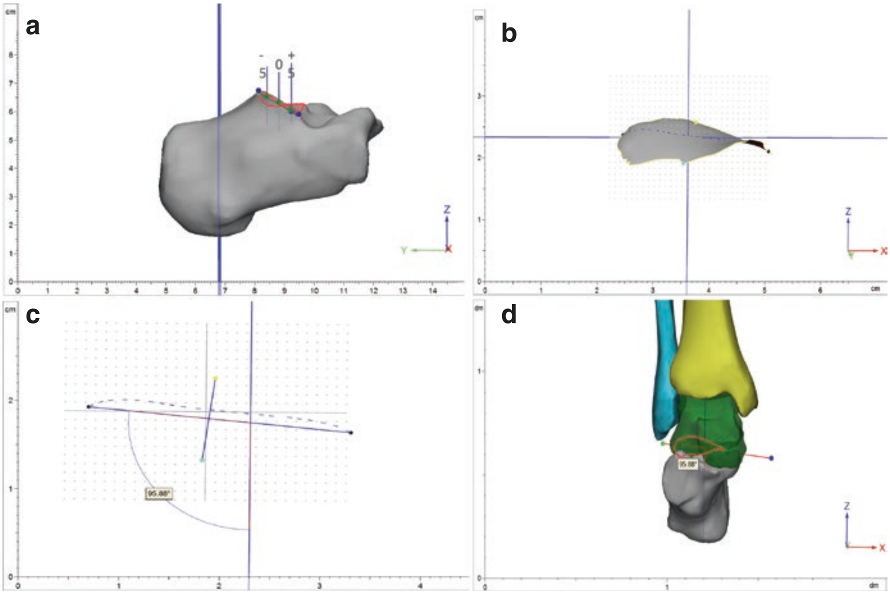

Fig. 10.5 Measurement of the subtalar vertical angle in 3D (SVA_{3D}). (**a**) The surface of the posterior facet of the subtalar joint was marked (red contour). The most posterior and anterior point of the marked surface was calculated in the direction of the AP (*x*-) axis (blue dots). This allowed to determine the length of the posterior facet by a software-operated connection of both points. The midpoint of this distance was calculated and used as an origin to fit a plane parallel to the coronal plane at a distance of −5 mm, 0 mm, and + 5 mm to mimic, respectively, the posterior, middle, and anterior SVA as described by Colin et al. [9]. (**b**) The contour of the posterior facet running in the middle subtalar plane was used to determine the inclination (dashed line) by connecting the calculated most medial with the most lateral point. (**c**) The intersection of this subtalar axis with the vertical (*z*-) axis became the middle SVA. (**d**) Depiction of the middle SVA in a 3D hindfoot configuration

Statistical Analysis

A Kolmogorov-Smirnov normality test was performed to determine if data were normally distributed. A student's t-test and Wilcoxon signed rank test were used for comparison of normally and not normally distributed data (2D vs. 3D hindfoot angles), respectively.

The correlation between the measured 2D and 3D angles was assessed by the Pearson coefficient (r). Linear regression analysis was demonstrated by use of a corresponding scatter plot and calculation of the r^2.

Inter- and intraobserver variability of the obtained measurements were analyzed using the interclass correlation coefficient [16]. Interpretations were as follows: ICC < 0.4, poor; 0.4 < ICC < 0.59, acceptable; 0.6 < ICC < 0.74, good; and ICC > 0.74, excellent [31].

The SPSS (release 20.0.0. standard version, SPSS, Inc., Chicago, IL, USA) statistical package was used to analyze the results. A probability level of $P < 0.05$ was considered significant.

Results

Hindfoot Alignment

The mean HA2D was 0.79° of valgus (SD = 3.2, range 12.7° of valgus–13° of varus), and the HA3D was 8.08° of valgus (SD = 6.5, range 17.2° of valgus–11.3° of varus). There was a statistically significant difference between the HA2D vs. HA3D ($P < 0.001$). There was a good correlation between both angles ($r = 0.72$, $P < 0.001$) (Fig. 10.6). The ICC3D proved to be excellent when compared to the ICC2D, which was good (Table 10.2).

The mean TA2D was 2.7° of varus (SD = 2.1, range 2.5° of valgus–9.1° of varus), and the TA3D was 5.1° of varus (SD = 4.9, range 0.68° of valgus–2.4° of varus). There was a statistically significant difference between the TA2D and TA3D ($P = 0.001$).

There was a good correlation between both angles ($r = 0.77$, $P < 0.001$) (Fig. 10.6b). The ICC2D and ICC3D were both excellent (Table 10.2).

The mean TC2D equaled 0.6° of varus (SD = 2.9, range 9.1° of valgus–12.2° of varus) and showed to be 4.6° of valgus in 3D (SD = 3.7, range 11.34° of valgus–10.71° of varus). There was a statistically significant difference between the TC2D and TC3D ($P < 0.001$). There was a good correlation between both angles ($r = 0.71$, $P < 0.001$) (Fig. 10.6c). The ICC2D and ICC3D were both excellent (Table 10.2).

Ankle and Hindfoot Characteristics

The mean TCr2D and TCr3D were 15.8° (SD = 4.7, range 10.8–23.1°) and 11.8° (SD = 3.4, range 7.2–20.71°), respectively. There was a statistically significant difference between the TCr2D and TCr3D ($P < 0.001$). There was a good correlation between both angles ($r = 0.69$, $P < 0.001$) (Fig. 10.6d). The ICC3D was excellent when compared to the ICC2D, which was good (Table 10.3).

Table 10.2 Mean hindfoot measurements in degrees and concomitant intraclass correlation coefficients

	Hindfoot measurements	SD (±)	ICC_{inter}	ICC_{intra}
HA_{2D}	0.79	3.2	0.73	0.81
TA_{2D}	2.7	2.1	0.76	0.83
TC_{2D}	0.6	2.9	0.85	0.82
HA_{3D}	8.08	6.5	0.91	0.93
TA_{3D}	5.1	4.9	0.86	0.89
TC_{3D}	4.6	3.7	0.99	0.99

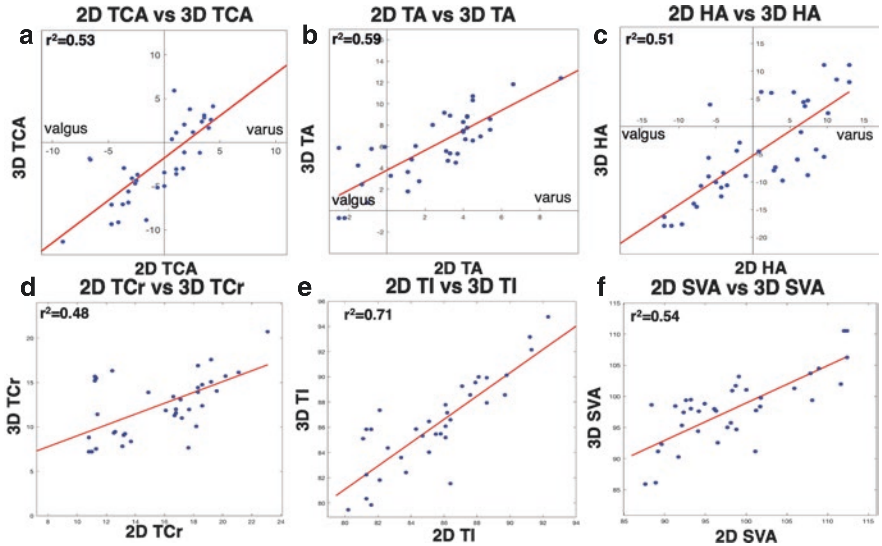

Fig. 10.6 (**a**–**f**) Correlation analysis of the conventional radiographic hindfoot characteristics measured in 2D towards the obtained 3D measurements

Table 10.3 Mean ankle and hindfoot characteristics in degrees and concomitant intraclass correlation coefficients

	Ankle/hindfoot measurements	SD (±)	ICC_{inter}	ICC_{intra}
TCr_{2D}	15.8	4.7	0.69	0.73
TI_{2D}	87.6	3.9	0.81	0.86
TT_{2D}	88.1	3.1	0.83	0.82
SVA_{2D}	96.1	5.7	0.73	0.76
TCr_{3D}	11.8	3.4	0.89	0.91
TI_{3D}	86.6	5.3	0.95	0.93
TT_{3D}	87.2	3.9	0.89	0.94
SVA_{3D}	98.4	8.1	0.81	0.84

The mean TI2D and TI3D were 87.6° (SD = 3.9, range 80.2–94.2°) and 86.6° (SD = 5.3, range 79.46–94.76°), respectively. There was a statistically significant difference between the TI2D and TI3D ($P < 0.001$). There was an excellent correlation between both angles ($r = 0.83$, $P < 0.001$) (Fig. 10.6e). The ICC2D and ICC3D showed both to be excellent (Table 10.3).

The mean TT2D and TT3D were 88.1° (SD = 3.1, range 82.6–96.2°) and 87.2° (SD = 3.9, range 82.9–99.1°), respectively. There was a statistically significant difference between the TT2D and TT3D ($P < 0.001$). There was a good correlation between both angles ($r = 0.79$, $P < 0.001$). The ICC2D and ICC3D showed both to be excellent (Table 10.1).

The mean SVA2D and SVA3D were 96.1° of valgus (SD = 7.2, range 87.6–112.4° of valgus) and 98.45° valgus (SD = 5.6, range 85.9–110.5° of valgus). There was a statistically significant difference between the SVA2D and SVA3D ($P < 0.001$). There was a good correlation between both angles ($r = 0.73$, $P < 0.001$). These angles significantly differed from each other with a ($P < 0.001$). The ICC2D and ICC3D were both excellent (Table 10.1).

Discussion

This study shows a good correlation between the HA2D and the HA3D, indicating that both angles can be used to determine hindfoot alignment. However, the HA3D overcomes the shortcomings encountered by 2D analysis such as the manual foot position according to the longitudinal axis of the second metatarsal, operator-dependent measurements, and projection of the bony hindfoot structures solely in the coronal plane [8]. The latter imposes a loss of important spatial information such as the shape of the calcaneus, which has been demonstrated to contribute to the form or deformity of the hindfoot [32].

In our study, the HA3D was significantly higher than the HA2D. More spatial volume data and variations in the positions of the bony structures, e.g., calcaneal talar rotation, can partially explain these differences [33].

The extent that one measurement method is more accurate than the other remains a subject of debate. Since the HA_{3D} takes into account more data on volume position, it may represent the anatomy more accurately when comparing non-weight bearing with weight bearing hindfoot angles [7].

The main advantage of using the HA3D is its reproducibility, as shown by the excellent to almost perfect intraclass correlation coefficients. High ICC values can be attributed to the computer-aided design operations, which allowed for calculation of the best fitted centroidal axis of the tibia base, the most inferior point of the calcaneus, and the centroid of the talus. Each calculation was repeated according to the same mathematical algorithm, allowing for less user interference compared to other studies [19, 34]. The only user-dependent aspect in determining the hindfoot angle was marking the distal end of the tibia to determine the TA3D. This resulted in a lower ICC when compared to the TC3D. Nevertheless, reliability coefficients of the TA3D were still higher than the TA2D, and reliable landmarks were used based on previous literature [35].

These findings were also observed in other hindfoot and ankle measurements, in which complete computer-calculated angles, such as the talocrural angle, have a higher reliability than angles requiring additional surface analysis such as the TT, TI, and SVA. On the other hand, the talocrural angle showed a lower correlation between 2D and 3D analysis due to the 2D CT measurement difficulties; in a 2D CT, the fibula and the tibia do not lie in the same coronal plane but are angulated 20–30° towards each other [36].

This suggests that obtaining 3D volume data allows for a better multiplanar insight, which is often required in clinical practice during foot and ankle surgery [37].

Another important factor that could influence the obtained measurements is the process of manually segmenting CT slices to obtain volumes. However, these methods have been shown to have a high accuracy in CT, CBCT, and MRI [38–40]. Recent developments even allow fully automatic segmentation of long bones [34, 41].

The limitation of using only the distal part of the tibia in determining the hindfoot alignment could contribute to the higher variation in tibia measurements and is a general limitation of this study. Stufkens et al. [42] confirmed these variations by the marked difference in the medial distal tibia angle (MDTA) measured on whole lower limb radiographs compared to the MDTA in mortise radiographs of the ankle. If the cone beam gantry could scan the entire tibia, more accurate measurements could be obtained as pointed out by Victor et al. [43]. Another method to determine hindfoot alignment overcomes this problem by using the forefoot as a reference based on the tripod index [44, 45]. Recently, Lintz et al. [46] pointed the efficiency out of this 3D biometric tool as part of the TALAS system. For both 3D methods, the radiation dose remains the same and should be taken into account. When compared to plane radiographs, this method is the equivalent of six radiographs for a unilateral PedCAT cone beam CT and 5.6% of the dose from a classic foot and ankle CT [7, 47].

In conclusion, this study shows that 3D measurement methods are more accurate and reproducible than 2D methods. The technique is based on previously described plane radiographs and CT measurements, which makes the interpretation and use for clinical practice straightforward [2, 7, 8]. It should be taken into account that all new 3D measurements cannot be compared to previous measurements and should therefore be firstly evaluated in future radiological and clinical studies, before any strong suggestions and guidelines can be made. The main advantage in clinical practice can be appertained to an improved understanding of complex hindfoot pathology by the provided 3D structural configuration in WBCT. Future research and clinical applications could therefore apply this measurement method in patients with a significant malalignment of the hindfoot. This will provide more preoperative insights into the multiplanar deformity, to facilitate the preoperative surgical planning of the correction, which is currently based on 2D measurements as pointed out by Barg et al. [48] Computer-assisted surgical techniques could incorporate the obtained 3D reference values per-operatively to help corrections of malaligned hindfoot fall within normal angular parameters, as shown by Richter et al. [17]. Postoperative assessment of the achieved correction by the same 3D measurement methods will provide a better quantification and understanding of the surgical intervention.

These findings will prompt more evidence-based surgery and better treatment guidelines. The latter are currently incoherent, reflecting the lack of structural insight into hindfoot pathology [49].

Acknowledgments The authors wish to thank Ir. Karim Chellaoui, as a clinical engineer for his attributive remarks to the study design and thorough review of the statistics.

The linguistic and structural support was provided by Maxwell Weinberg, research assistant at the University of Utah and Hannes Van Wynendaele, MLing of Ugent.

References

1. Cobey JC. Posterior roentgenogram of the foot. Clin Orthop Relat Res. 1976;118:202–7.
2. Saltzman CL, El-Khoury GY. The hindfoot alignment view. Foot Ankle Int. 1995;16(9):572–6.
3. Reilingh ML, Beimers L, Tuijthof GJM, Stufkens SAS, Maas M, van Dijk CN. Measuring hindfoot alignment radiographically: the long axial view is more reliable than the hindfoot alignment view. Skelet Radiol. 2010;39(11):1103–8.
4. Buck FM, Hoffmann A, Mamisch-Saupe N, Espinosa N, Resnick D, Hodler J. Hindfoot alignment measurements: rotation-stability of measurement techniques on hindfoot alignment view and long axial view radiographs. Am J Roentgenol. 2011;197(3):578–82.
5. Barg A, Amendola RL, Henninger HB, Kapron AL, Saltzman CL, Anderson AE. Influence of ankle position and radiographic projection angle on measurement of supramalleolar alignment on the anteroposterior and hindfoot alignment views. Foot Ankle Int. 2011;36(11):1352–61.
6. Ikoma K, Noguchi M, Nagasawa K, Maki M, Kido M, Hara Y, Kubo T. A new radiographic view of the hindfoot. J Foot Ankle Res. 2013;6(1):48.
7. Richter M, Seidl B, Zech S, Hahn S. PedCAT for 3D-imaging in standing position allows for more accurate bone position (angle) measurement than radiographs or CT. Foot Ankle Surg. 2014;20(3):201–7.
8. Burssens A, Peeters J, Buedts K, Victor J, Vandeputte G. Measuring hindfoot alignment in weight bearing CT: a novel clinical relevant measurement method. Foot Ankle Surg. 2011;22(4):233–8.
9. Colin F, Lang TH, Zwicky L, Hintermann B, Knupp M. Subtalar joint configuration on weightbearing CT scan. Foot Ankle Int. 2014;35(10):1057–62. 1071100714540890.
10. Krähenbühl N, Tschuck M, Bolliger L, Hintermann B, Knupp M. Orientation of the subtalar joint measurement and reliability using weightbearing CT scans. Foot Ankle Int. 2016;37(1):109–14.
11. Tuominen EK, Kankare J, Koskinen SK, Mattila KT. Weight-bearing CT imaging of the lower extremity. AJR Am J Roentgenol. 2013;200(1):146–8.
12. O'Connor JF, Cohen J. Computerized tomography (CAT scan, CT scan) in orthopaedic surgery. J Bone Joint Surg Am. 1978;60(8):1096–8.
13. Wicky S, Blaser P, Blanc C, Leyvraz P, Schnyder P, Meuli R. Comparison between standard radiography and spiral CT with 3D reconstruction in the evaluation, classification and management of tibial plateau fractures. Eur Radiol. 2000;10(8):1227–32.
14. te Stroet MA, Holla M, Biert J, van Kampen A. The value of a CT scan compared to plain radiographs for the classification and treatment plan in tibial plateau fractures. Emerg Radiol. 2011;18(4):279–83.
15. Sanders R. Current concepts review-displaced intra-articular fractures of the calcaneus. J Bone Joint Surg. 2000;82(2):225–50.
16. Auricchio F, Marconi S. 3D printing: clinical applications in orthopaedics and traumatology. EFORT Open Rev. 2016;1(5):121–7.
17. Richter M. Computer aided surgery in foot and ankle: applications and perspectives. Int Orthop. 2013;37(9):1737–45.
18. Tack P, Victor J, Gemmel P, Annemans L. 3D-printing techniques in a medical setting: a systematic literature review. Biomed Eng Online. 2016;15(1):115.
19. Jacxsens M, Van Tongel A, Willemot LB, Mueller AM, Valderrabano V, De Wilde L. Accuracy of the glenohumeral subluxation index in nonpathologic shoulders. J Shoulder Elbow Surg. 2015;24(4):541–6.
20. Victor J, Premanathan A. Virtual 3D planning and patient specific surgical guides for osteotomies around the knee. Bone Joint J. 2013;95(11 Supple A):153–8.
21. Audenaert EA, Baelde N, Huysse W, Vigneron L, Pattyn C. Development of a three-dimensional detection method of cam deformities in femoroacetabular impingement. Skelet Radiol. 2011;40(7):921–7.

22. Hirschmann A, Pfirrmann CWA, Klammer G, Espinosa N, Buck FM. Upright cone CT of the hindfoot: comparison of the non-weight-bearing with the upright weight-bearing position. Eur Radiol. 2013;24(3):553–8.
23. de Cesar Netto C, Schon LC, Thawait GK, da Fonseca LF, Chinanuvathana A, Zbijewski WB, Siewerdsen JH, Demehri S. Flexible adult acquired flatfoot deformity: comparison between weight-bearing and non-weight-bearing measurements using cone-beam computed tomography. J Bone Joint Surg. 2017;99(18):e98.
24. Burssens A, Van Herzele E, Buedts K, Leenders T, Clockaerts S, Vandeputte G, Victor J. Weightbearing CT in normal hindfoot alignment – presence of constitutional valgus? Foot Ankle Surg. 2017;23:16.
25. Barg A, Harris MD, Henninger HB, Amendola RL, Saltzman CL, Hintermann B, Anderson AE. Medial distal tibial angle: comparison between weightbearing mortise view and hindfoot alignment view. Foot Ankle Int. 2012;33(8):655–61.
26. Neri T, Barthelemy R, Tourné Y. Radiologic analysis of hindfoot alignment: comparison of Méary, long axial, and hindfoot alignment views. Orthop Traumatol Surg Res. 2017;103(8):1211–6.
27. Dagneaux L, Moroney P, Maestro M. Reliability of hindfoot alignment measurements from standard radiographs using the methods of Meary and Saltzman. Foot Ankle Surg. 2019;25(2):237–41.
28. Iseki Y, Takahashi T, Takeda H, Tsuboi I, Imai H, Mashima N, Watanabe S, Yamamoto H. Defining the load bearing axis of the lower extremity obtained from anterior-posterior digital radiographs of the whole limb in stance. Osteoarthr Cartil. 2009;17(5):586–91.
29. Guichet J-M, Javed A, Russell J, Saleh M. Effect of the foot on the mechanical alignment of the lower limbs. Clin Orthop Relat Res. 2009;415:193–201.
30. Brage ME, Bennett CR, Whitehurst JB, Getty PJ, Toledano A. Observer reliability in ankle radiographic measurements. Foot Ankle Int. 1997;18(6):324–9.
31. Shrout PE, Fleiss JL. Intraclass correlations: uses in assessing rater reliability. Psychol Bull. 1979;86(2):420.
32. Hamel J. Calcaneal Z osteotomy for correction of subtalar hindfoot varus deformity. Oper Orthop Traumatol. 2015;27(4):308.
33. Lundberg A, Svensson O. The axes of rotation of the talocalcaneal and talonavicular joints. Foot. 1993;3(2):65–70.
34. Almeida DF, Ruben RB, Folgado J, Fernandes PR, Audenaert E, Verhegghe B, De Beule M. Fully automatic segmentation of femurs with medullary canal definition in high and in low resolution CT scans. Med Eng Phys. 2016;38(12):1474–80.
35. Chen Y, Qiang M, Zhang K, Li H, Dai H. A reliable radiographic measurement for evaluation of normal distal tibiofibular syndesmosis: a multi-detector computed tomography study in adults. J Foot Ankle Res. 2015;8(1):1.
36. Hansen M, Le L, Wertheimer S, Meyer E, Haut R. Syndesmosis fixation: analysis of shear stress via axial load on 3.5-mm and 4.5-mm quadricortical syndesmotic screws. J Foot Ankle Surg. 2006;45(2):65–9.
37. Quill GE. Reconstruction of multiplanar ankle and hindfoot deformity with intramedullary techniques. Foot Ankle Clin. 2009;14(3):533–47.
38. Van den Broeck J, Vereecke E, Wirix-Speetjens R, Vander Sloten J. Segmentation accuracy of long bones. Med Eng Phys. 2014;36(7):949–53.
39. Al-Rawi B, Hassan B, Vandenberge B, Jacobs R. Accuracy assessment of three-dimensional surface reconstructions of teeth from cone beam computed tomography scans. J Oral Rehabil. 2010;37(5):352–8.
40. Rathnayaka K, Sahama T, Schuetz MA, Schmutz B. Effects of CT image segmentation methods on the accuracy of long bone 3D reconstructions. Med Eng Phys. 2011;33(2):226–33.
41. Ebinger T, Goetz J, Dolan L, Phisitkul P. 3D model analysis of existing CT syndesmosis measurements. Iowa Orthop J. 2013;33:40.

42. Stufkens SA, Barg A, Bolliger L, Stucinskas J, Knupp M, Hintermann B. Measurement of the medial distal tibial angle. Foot Ankle Int. 2011;32(3):288–93.
43. Victor J, Van Doninck D, Labey L, Van Glabbeek F, Parizel P, Bellemans J. A common reference frame for describing rotation of the distal femur. Bone Joint J. 2009;91(5):683–90.
44. Lintz F, Barton T, Millet M, Harries WJ, Hepple S, Winson IG. Ground reaction force calcaneal offset: a new measurement of hindfoot alignment. Foot Ankle Surg. 2012;18(1):9–14.
45. Arunakul M, Amendola A, Gao Y, Goetz JE, Femino JE, Phisitkul P. Tripod index: a new radiographic parameter assessing foot alignment. Foot Ankle Int. 2013;34(10):1411–20.
46. Lintz F, Welck M, Bernasconi A, Thornton J, Cullen NP, Singh D, Goldberg A. 3D biometrics for Hindfoot alignment using weightbearing CT. Foot Ank Int. 2017;38(6):684–9.1071100717690806.
47. Ludlow JB, Ivanovic M. Weightbearing CBCT, MDCT, and 2D imaging dosimetry of the foot and ankle. Int J Diagn Imaging. 2014;1(2):1.
48. Barg A, Saltzman CL. Single-stage supramalleolar osteotomy for coronal plane deformity. Curr Rev Musculoskelet Med. 2014;7(4):277–91.
49. Van Gestel L, Van Bouwel S, Somville J. Surgical treatment of the adult acquired flexible flatfoot. Acta Orthop Belg. 2015;81(2):172–83.
50. Burssens A, Peeters J, Peiffer M, Marien R, Lenaerts T, WBCT ISG, Vandeputte G, Victor J. Reliability and correlation analysis of computed methods to convert conventional 2D radiological hindfoot measurements to a 3D setting using weight bearing CT. Int J Comp Assisted Radiol Surg. 2018;13(12):1999–2008.

Chapter 11
The Hind- and Midfoot Alignment Analyzed After a Medializing Calcaneal Osteotomy Using a 3D Weight Bearing CT

Arne Burssens

Introduction

A medializing calcaneal osteotomy (MCO) is a surgical procedure frequently performed to correct an adult acquired flat foot deformity (AAFD) [1–3]. This condition is characterized by a complex 3D deformity resulting in a loss of the medial longitudinal arch, valgus alignment of the hindfoot, and abduction of the midfoot [4–7]. The initial treatment in mild deformities is conservative (e.g., insoles), but, once progression of the deformity and impairment of functional activities occur, surgery is advised [8]. In case a stage II AAFD, according to Johnson and Strom classification (containing a posterior tibial tendon dysfunction), does not respond to conservative treatment, a MCO is one of the surgical options available depending on the deformity characteristics [9]. The main goal of the procedure is to correct hindfoot alignment (HA) [3]. However, HA is markedly different among patients with stage II AAFD, and thus understanding how a MCO influences hindfoot alignment is essential. Chan et al. [10] have demonstrated a highly positive correlation between the change in the hindfoot moment arm and the amount of millimeters translated during a MCO. Although these findings have improved clinical practices, these measurements are still only performed on 2D radiographs and thus can be improved upon. Because 2D radiographs are a projection of a 3D deformity correction, 2D radiographs are prone to rotational errors and manual measurements. Laquinto et al. [11] addressed the limitations of 2D imaging but only for a 3D-simulated MCO model. Expanding upon this concept, Kido et al. [12] and subsequently Zhang et al. [13] utilized a 3D model in a clinical setting on patients with stage II AFFD. However, surgical corrections could not be assessed, and a CT scan was used to simulate weight bearing; the latter limitation can now be overcome by the use of a weight-

Based on Burssens A, Barg A, van Ovost E, Van Oevelen A, Leenders T, Peiffer M, Bodera I, WBCT ISG, Audenaert E, Victor J. The Hind- and Midfoot Alignment Computed after a Medializing Calcaneal Osteotomy using a 3D Weight bearing CT. *Int J Comp Assisted Radiol Surg* 2019;14(8) 1439–47.

M. Richter et al., *Weight Bearing Cone Beam Computed Tomography (WBCT) in the Foot and Ankle*, https://doi.org/10.1007/978-3-030-31949-6_11

bearing cone beam CT (WBCT) in foot and ankle pathologies [14]. This novel device allows for standing position images at a high resolution and at a relatively low radiation dose [14–17]. The application of a WBCT combined with currently available computed measurement techniques would overcome the aforementioned shortcomings and be for the first time applied in assessing a surgical hindfoot correction in 3D.

Our aim is to analyze the pre- and postoperative hind- and midfoot alignment after a MCO using a WBCT and 3D computed measurement techniques. We hypothesize that there is a linear relationship between the amount of medial translation during a MCO and the correction of both the hind- and midfoot alignment.

Material and Methods

Study Population, Design, and Measurement Protocol

Eighteen consecutive patients with mean age 41.8 years (SD = 17.3, range 19–62 years) were prospectively included between 2015 and 2017 after sustaining a medializing calcaneal osteotomy (MCO) and concomitant inframalleolar procedures (Table 11.1). Surgery was indicated for an adult acquired flat foot stage II ($N = 16$) or posttraumatic valgus deformity ($N = 2$). Exclusion criteria consisted of a tarsal coalition, age younger than 18 years or older than 65 years and concomitant supramalleolar procedures.

A prospective pre-post study design was used: pre- and postoperative weight bearing CT scans were collected before surgery and 12 weeks after surgery. The local Institutional Review Board approved the study (EC15/49/537), and all patients gave informed consent.

A PedCAT® weight bearing cone beam CT was used (CurveBeam, Warrington, PA, USA) containing the following imaging protocol and settings: tube voltage, 96 kV; tube current, 7.5 mAs; CTDIvol 4.3, mGy; matrix, 160,160,130; pixel size, 0.4 mm; and slice interval, 0.4 mm. At the department of radiology, patients were asked to assume a natural stance with both feet parallel to each other at shoulder width apart.

Table 11.1 Patient demographics and concomitant procedures

Characteristic	Total
Age (±) SD	41.8. ± 17.3 years
Sex (M/F)	4/14
TMT 1 fusion	2
Cotton osteotomy	4
Evans osteotomy	1
Gastroc release	11
FDL transfer	9
Spring ligament repair	3
Deltoid ligament reefing	1

In order to perform a 3D analysis, it is required to segment the CT slices based on their outer cortical surfaces. This was applied semiautomatic using the automatic bone segmentation tool in Mimics® 20.0 software (Materialise, Haasrode, Belgium) by manually appointing the cortical contour before Standard Triangulation Language (STL) files could be acquired. These were exported in 3-matic® software (Materialise, Haasrode, Belgium) to compute 3D goniometrical relationships.

A Cartesian coordinate system was acquired: the centroid of the talus was defined as the origin after being projected on the segmented base plate of the WBCT, to represent the ground floor [18]. The *z*-axis was defined as running through the origin and perpendicular to the segmented base plate. The *x*-axis runs through the origin and the projected centroid of the head of the second metatarsal, which simulates the longitudinal axis of the foot. The *Y*-axis was defined as the cross product of the *x*- and *z*-axis. The coronal plane was defined as the *YZ*-plane, the sagittal plane as the *XZ*-plane, and the axial plane as the *XY*-plane (Fig 11.4a–c).

This coordinate system was incorporated in a custom build script, using Matlab® 2016b (The MathWorks, Inc., MA, USA), and aligned pre- and postoperatively, in order to reference the computed angles and distances.

In general, each 3D measurement was determined pre- as well as postoperatively and subsequently projected in the reference plane currently used in clinical practice, to allow comparison and to optimize interpretation of the results.

The landmarks and axes necessary to calculate the following parameters were automatically computed by using the three main functions called "Create point: center of gravity," "Extrema analysis," and "Create line: fit inertia axis" function of the 3-matic® software. These are based on goniometric functions to calculate respectively the centroid of a generated volume, the most outer point of a structure in the direction of a given axis and best fit centroidal axis on a 3D model.

The hindfoot angle (HA) was determined in 3D by the intersection of the anatomical tibia axis (TA_x) and the talocalcaneal axis (TC_x) (Fig. 11.1a), as described previously [19]. The TA_x was computed as the best fitted longitudinal axis of the tibia shaft, manually marked above the incisura fibularis (Fig. 11.1b). Positive values equaled a valgus and negative values a varus hindfoot alignment. The TC_x was obtained after connecting computed centroid of the talus with the computed most inferior point of the calcaneus defined by Saltzman et al. [20] (Fig. 11.1d). Additionally, the TA_x and TC_x were measured separately towards the vertical axis in order to detect spatial changes as a consequence of the MCO.

The rotation of the tibia (TR) was determined by creating an axis (TR_x) connecting the computed most medial point of both the anterior and posterior tubercle using a build in goniometrical software function called (extrema analysis) (Fig. 11.1c, Supplementary Fig. 11.2a, b).

The difference in the axial plane between the pre- and postoperative (TR_x) allowed to determine the rotation of the tibia. Positive values equaled an external rotation and negative values an internal tibia rotation. The translations of the MCO were determined by reconstruction of the osteotomy plane (Fig. 11.2a). This allowed to divide the calcaneus in an anterior and posterior part (Fig. 11.2b). Based on the anterior part, the pre- and postoperative calcaneus could be matched on top of each

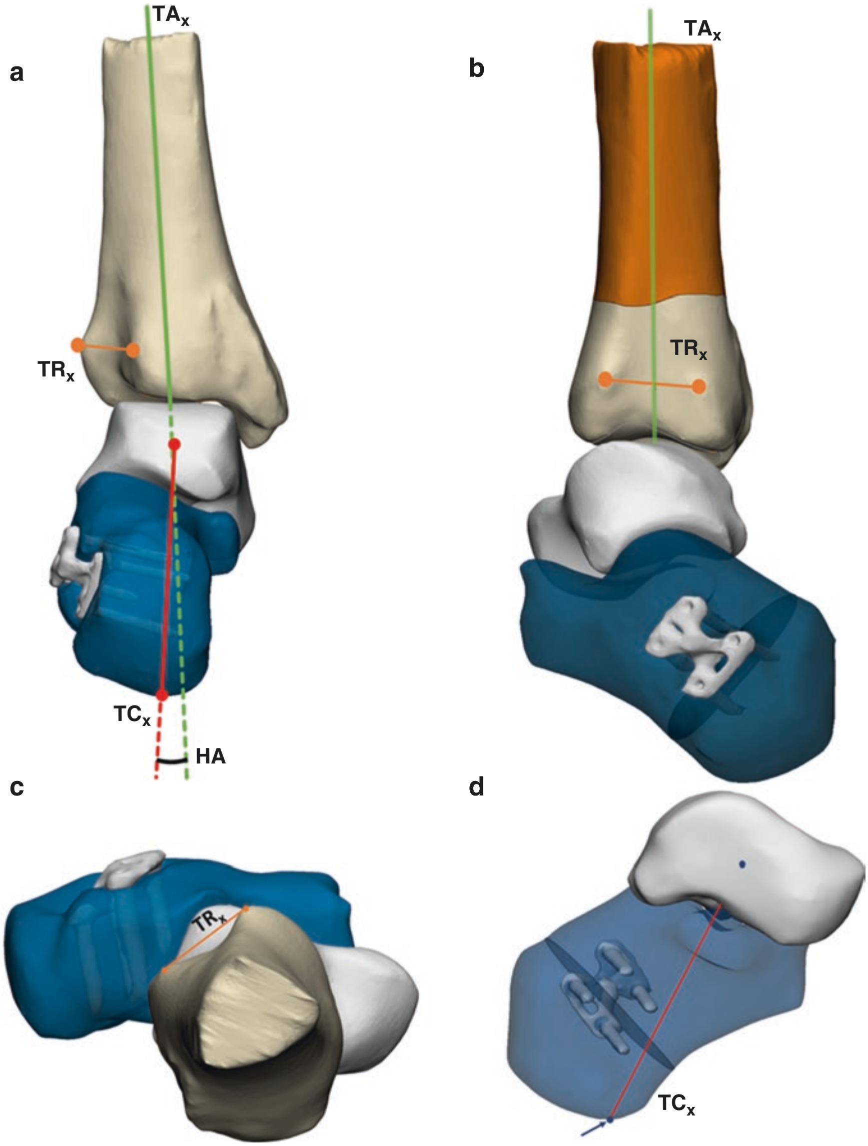

Fig. 11.1 Computed analysis of the hindfoot alignment (HA). (**a**) The (HA) was determined by the intersection of the anatomical tibia axis (TA_x) and the talocalcaneal axis (TC_x). (**b**) The TA_x was computed as the best fitted longitudinal axis above the incisura fibularis of the tibia shaft. (**c**) The TR_x was determined by connecting the computed most medial point of both the anterior and posterior tubercle of the incisura fibularis. (**d**) The TC_x was obtained after connecting the computed most inferior point of the calcaneus with the computed centroid of the talus

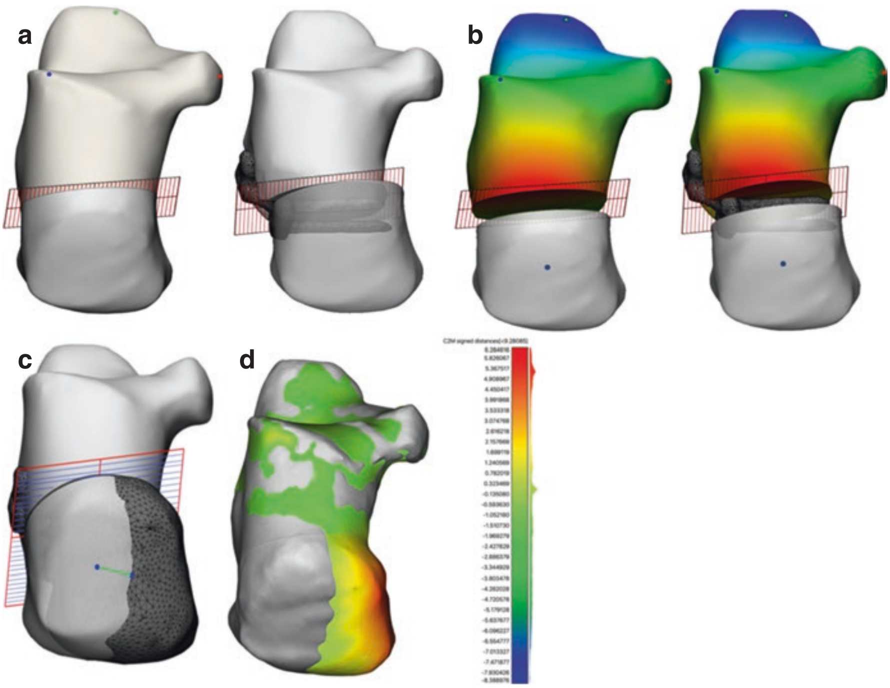

Fig. 11.2 Computing medial translation after a calcaneus osteotomy. (**a**) The osteotomy plane was reconstructed from the postoperative calcaneus. (**b**) Division of the calcaneus into an anterior and posterior part. The centroid of both posterior parts was computed. The anterior parts both preoperative (left) as well as postoperative (right) were fitted on top of each other. (**c**) The computed distance between the centroid of the pre- and postoperative posterior part of the calcaneus allowed for determination of the medial translation of the calcaneus osteotomy. (**d**) A deviation analysis depicting the range of the medial translation

other. The 3D distance between the computed centroid of the pre- and postoperative part of the posterior calcaneus was used to resemble the translation obtained after the MCO (Fig. 11.2c).

An additional deviation analysis was performed using CloudCompare® v 2.0 open source software (CloudCompare, Paris, France) by selecting the preoperative 3D model as a “mesh.” This was automatically used as the reference and the postoperative model as a “cloud.” The latter represented all vertices that form the 3D postoperative model. The distance between these vertices and the reference was determined by the CloudCompare®-software, and this analysis depicted the range of medial translation obtained after a MCO (Fig. 11.2d).

Measurements in the midfoot consisted of the navicular height (NH), navicular rotation (NR), and Méary angle (MA) [21].

The NH was determined as the distance between the computed most inferior point of the navicular and the ground (defined by the baseplate of the WBCT) (Fig. 11.3a). The NR was obtained by creating an axis (NR_x) going from the

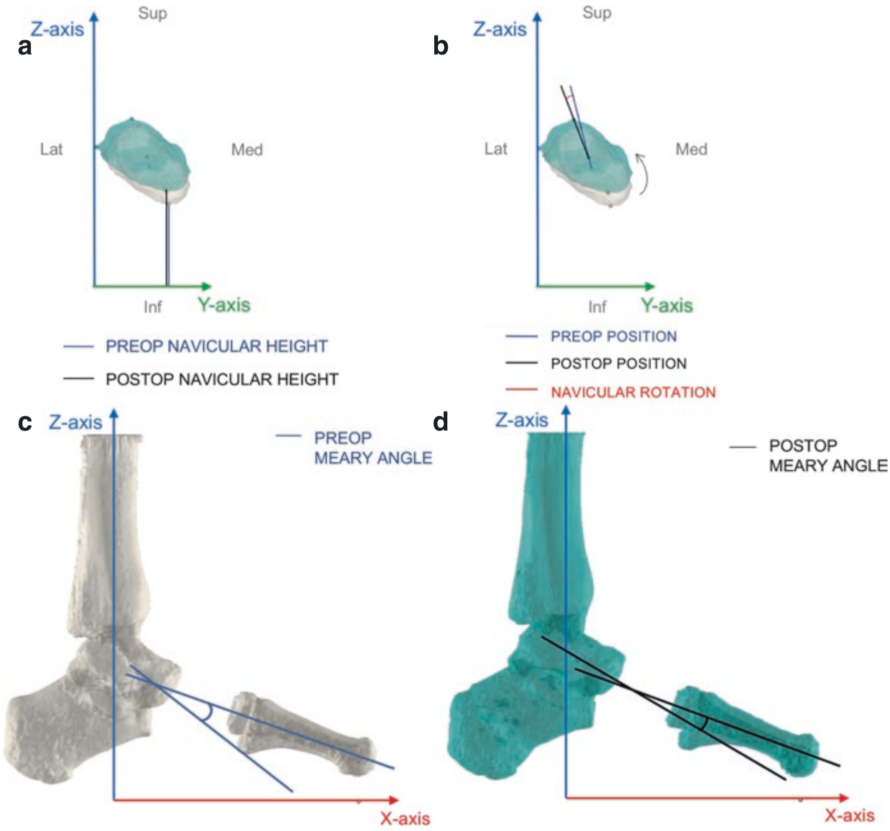

Fig. 11.3 Computed analysis of the midfoot alignment. (**a**) The navicular height (NH) was determined as the distance between the computed most inferior point of the navicular and the base plate (right); (**b**) the navicular rotation (NR) was obtained by creating an axis (NR_x) going from the computed most superior to inferior point of the navicular. The difference in the coronal plane between the pre- and postoperative NR_x helped determine the rotation of the navicular. (**c**) The Méary angle was determined preoperatively as the intersection of the best fitted longitudinal axis from the talar neck TN_x and the metatarsal axis MT_{1x}. (**d**) The same method was applied on the postoperative correction

computed most superior point of the navicular to the centroid of the navicular. The difference in the coronal plane between the pre- and postoperative NR_x allowed to determine the rotation of the navicular (Fig. 11.3b). Positive values equaled an inversion and negative values an eversion of the navicular. The Méary angle (MA) was determined in 3D by the intersection of the talus neck axis (TN_x) and the first metatarsal axis (MT_{1x}). Both axes were defined as a best fit centroidal axis respectively along the manually marked talar neck and computed selection of the first metatarsal (Fig. 11.3c–d). Positive values equaled a planus and negative values a cavus of the MA.

Surgical Procedure

The calcaneus was exposed through a lateral approach. The osteotomy was initiated with an oscillating saw blade 90° to the lateral calcaneal wall and inclined 45° in the sagittal plane according to Myerson et al. [1]. A broad osteotome was used to complete the medial cortex. The amount of medial translation of the calcaneum was determined by the surgeon (TL), based on intraoperative assessment with a neutral heel according to the longitudinal tibia axis. No additional rotation of impaction was performed. The osteotomy was fixated with either a 5 mm, 7.5 mm, or 10 mm calcaneus Step Plate® (Arthrex, Naples, FS, USA) with locking screws or was fixated by the use of two 7 mm cannulated lag screws (Wright Medical, Memphis, TN, USA). Postoperatively, patients were treated consistently with 6–8 weeks of non-weight bearing in a removable boot. This was followed by progression to full weight bearing between weeks 8 and 10, depending on healing.

Statistical Analysis

A Kolmogorov-Smirnov normal distribution test was performed for the hindfoot angle, rotation of the tibia, navicular height and rotation, and Méary angle. These demonstrated to be $P > 0.05$, indicating a normal distribution of the data and the use of further parametric testing. A paired Student's t-test was conducted to compare the means of the preoperative versus the postoperative measurements of both the hindfoot (HA, TAx, TCx, and TRx) and midfoot alignment (NH, NR, and MA).

The correlation between the measured hindfoot/midfoot alignment and amount of medial translation after MCO was assessed by the Pearson coefficient (R). Linear regression analysis was demonstrated by the use of a corresponding scatter plot and calculation of the R^2, when significant.

Inter- and intraobserver variability of the obtained midfoot measurements were analyzed using the interclass correlation coefficient [22]; the reliability of the hindfoot measurements was reported previously to be excellent [19].

Interpretations were as follows: ICC < 0.4, poor; 0.4 < ICC < 0.59, acceptable; 0.6 < ICC < 0.74, good; and ICC > 0.74, excellent [23].

The SPSS (release 22.0.0. standard version, SPSS, Inc., Chicago, IL, USA) statistical package was used to analyze the results. A probability level of $p < 0.05$ was considered significant.

An a priori statistical power analysis was performed using G∗Power (version 3.1.9.2; Dusseldorf University, Dusseldorf, Germany) [24]. Previously reported data regarding regression analysis of the hind- and midfoot alignment were used for sample size estimation [10]. Calculations have shown that a total sample size of $N = 4$ is needed for regression analysis of the hindfoot alignment and $N = 47$ for the midfoot alignment, to reach the respectively calculated effect size of ($f = 0.96$) and ($f = 0.33$) with a power level of 0.80 and a level of significance set at 0.05.

Results

Hindfoot Alignment

Pre- and Postoperative Comparison

A statistically significant difference was obtained in the HA3D, TAX 3D ($p < 0.001$), and TR3D ($p < 0.05$), when comparing pre- towards postoperative hindfoot measurements (Table. 11.2).

The intra- and interclass correlation coefficients were excellent both pre- and postoperatively (Table 11.4). The mean 3D translation obtained by the calcaneal osteotomy during surgery was 8.3 mm (SD = 4.2).

Regression Analysis

The Pearson coefficient showed a significant ($R = 0.926$, $p < 0.001$) correlation between the amount of medial calcaneal translation and the calculated change in HA3D angle. Linear regression analysis demonstrated a significant relationship ($R^2 = 0.84$, $p < 0.001$). The estimated change in hindfoot angle was expected to increase with 2.15° for every mm of MCO performed. The hindfoot angle could be predicted from the amount of MCO by the following equation (Fig. 11.4d): Change in hindfoot angle (degrees) = 2.15 (degrees/mm)· Amount of MCO (mm) − 3.39 3.2

Midfoot Alignment

Pre- and Postoperative Comparison

A statistically significant difference was obtained in the NH3D, NR3D ($p < 0.001$), and TR3D ($p < 0.05$), when comparing pre- towards postoperative midfoot measurements (Table. 11.3).

The intra- and interclass correlation coefficients were excellent both pre- and postoperatively (Table. 11.4).

Table 11.2 Comparison of pre- and postoperative hindfoot measurements

Hindfoot	Direction[a] preoperative			Postoperative		Change		
parameter	Measurement	Mean	SD	Mean	SD	Mean	95% CI	*p*-value
HA	Valg+/Var−	18.2	6.6	9.3	6.1	8.9	[5.9, 11.8]	<0.001
TA_x	Valg+/Var−	6.8	3.3	5.3	2.7	1.5	[1.7, 3.5]	<0.001
TC_x	Valg+/Var−	11.4	6.4	5.3	6.5	6.1	[4.1, 8.0]	<0.001
TR_x	Valg+/Var−	27.1	4.7	28.8	5.8	1.6	[0.4, 2.9]	0.016

[a]+ and – denote the direction of the measurement, *valg* valgus, *var* varus

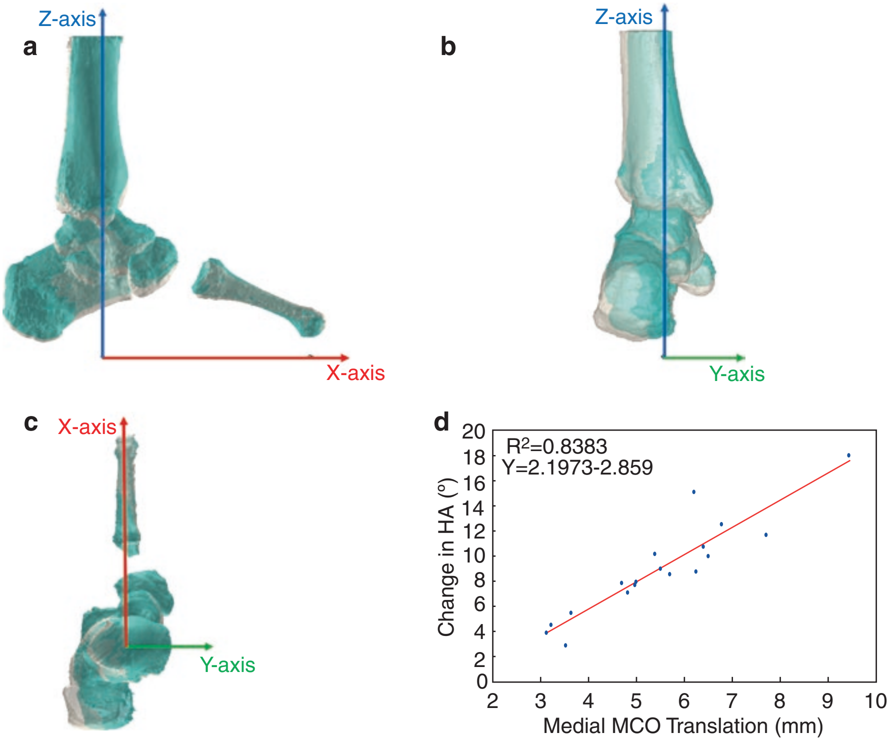

Fig. 11.4 Overview of the Cartesian coordinate system and linear regression analysis. (**a**) The centroid of the talus was defined as the origin after being projected onto the segmented base plate. (**b**) The *z*-axis was defined as running through the origin and perpendicular to the segmented base plate. (**c**) The *x*-axis runs through the origin and the projected centroid of the head of the second metatarsal, simulating the longitudinal axis of the foot. The *Y*-axis was defined as the cross product of the *x*- and *z*-axis. The coronal plane was defined as the *YZ*-plane, the sagittal plane as the *XZ*-plane, and the axial plane as the *XY*-plane. (**d**) Change in the hindfoot angle as a function of medical calcaneus translation. The obtained function can be used in clinical practice for preoperative planning

Table 11.3 Comparison of pre- and postoperative midfoot measurement

Midfoot	Direction[a] preoperative			Postoperative		Change		
parameter	Measurement	Mean	SD	Mean	SD	Mean	95% CI	*p*-value
NH	Prox+/Dist−	33.1	7.6	37.1	7.5	3.9	[2.5, 5.2]	<0.001
NR	Inv+/Ev−	16.3	5.1	22.7	6.5	6.4	[4.2, 8.4]	<0.001
MA	Plan+/Cav−	20.2	7.8	15.0	9.3	5.8	[8.4, 2.0]	<0.05

[a]+ and – denote the direction of the measurement; prox, proximal; dist, distal; inv, inversion; ev, eversion; plan, planus; cav, cavus

Table 11.4 Midfoot intra- and interclass correlation coefficients

Midfoot parameter	ICC			
	Preoperative		Postoperative	
	Intra	Inter	Intra	Inter
NH	0.999	0.999	0.999	0.999
NR	0.999	0.975	0.991	0.949
MA	0.849	0.848	0.896	0.868

Regression Analysis

The Pearson coefficient showed a nonsignificant ($p < 0.05$) correlation between the amount of medial calcaneal translation and the calculated change in NH, NR, and Méary angle (RNH = 0.38, $p = 0.16$; RNR = 0.32, $p = 0.24$; RMéary = 0.02, $p = 0.94$).

Discussion

This study shows an effective correction of the hindfoot valgus in an AAFD after a MCO assessed by a 3D weight bearing CT. It appears that the correction is not only situated in the calcaneus but also to a lesser extent in the tibia, resulting in 10% of the achieved HA correction.

Additional changes in the midfoot alignment were detected after a MCO combined with concomitant procedures: these could point a significant radiographic improvement of the navicular height/rotation and Méary angle.

These novel findings can be attributed to the application of 3D weight bearing and computed assessment of both the hindfoot and the midfoot correction, overcoming the previously encountered superposition and manual measurement methods on 2D plane radiographs [25].

The proposed formula, based on the regression analysis of the hindfoot correction, can be used when performing a 3D preoperative planning of an AAFD, since most of the current planning is based on intraoperative assessment [1, 3].

The obtained findings parallel previous research from Chan et al. [10], demonstrating a higher linear relationship between the amount of medial translation during a calcaneal osteotomy and the hindfoot correction when compared to the midfoot. This was also pointed out in other clinical and computed studies assessing changes in the midfoot alignment, which tended to be less pronounced compared to the hindfoot alignment after an MCO [1, 11]. The detected rotation of the navicular was consistent with previous reports demonstrating a higher eversion of the navicular, ranging from 2.3° to 6.2°, when flat foot deformity was more pronounced [12, 13]. These studies applied a similar measurement method but demonstrated shortcomings using a simulated weight bearing CT, which were overcome by a weight bearing CT in the present study.

The obtained results question the generally accepted osteotomy rule of 1 mm translation causing 1° of correction in knee and foot deformities [26, 27]. This could be attributed towards the 3D measurements containing more spatial data but was previously already shown in other studies containing 2D measurements in deformity corrections [10, 28].

We acknowledge that our study has several important limitations. Firstly, the study group consists of a low case number and is heterogeneous. The sample size calculation demonstrated to be sufficient towards regression analysis of the hindfoot alignment, but not for the midfoot alignment. In addition, midfoot measurements should be interpreted with respect to the performed concomitant procedures such as a FDL transfer, cotton osteotomy, or TMT fusion. The relative contribution of each procedure is difficult to analyze due to the size of the cohort and variation in full activity of an FHL transfer [29]. However, the described computed method could measure postoperative changes in the midfoot alignment, which were not detectible using previous imaging techniques [10].

Two patients were included with a posttraumatic valgus deformity of the calcaneus, containing a different pathoanatomy compared to an AAFD stage II. Despite this difference, a medializing calcaneus osteotomy is indicated as one of the treatment options in these posttraumatic deformities, and data concerning the radiographic outcome are limited [30], advocating the use of the applied measurement method. Moreover, the current preoperative planning is based on the classification of Stephens which uses a non-weight bearing CT, possibly underestimating the deformity during stance [31].

Second, all patients received a medial translation of the calcaneus, although other displacements during the osteotomy were avoided and small rotational changes could not be ruled out. Thirdly, not all radiographic measurement parameters of an AAFD were obtained pre- and postoperatively, but the most relevant ones for clinical practice were used [21]. Finally, the obtained results could have been influenced by the absence of scales or devices used to assess quantitatively if the patient was bearing full weight during the scanning process. However, postoperative scans were obtained at 3 months after surgical corrections, in order to avoid limitations in full weight bearing caused by antalgic reasons.

In conclusion, this study proposes a clinically relevant 3D method to compare the preoperative with the postoperative hind- and midfoot alignment after a MCO. In addition, a formula is provided to determine the required amount of medial translation during a calcaneus osteotomy to obtain the desired hindfoot correction and to prevent an overcorrection.

Future research can be aimed at validating this formula in clinical practice using prospective studies in cohorts stratified according to the concomitant procedure accompanying the MCO. These should incorporate patient-reported outcome scores (PROMS) to assess which amount of hindfoot correction is most beneficial for the patient [32, 33]. Furthermore, technical improvements such as built-in pressure sensors would allow to quantify and standardize the amount of weight applied on the foot, as currently been used to perform pedography in a weight bearing CT [34].

Additional 3D measurements can be aimed at the orientation of the osteotomy to determine which plane is the most optimal biomechanically as was already assessed in 2D by Reilingh et al. [35]. These data could be implemented to develop patient-specific guides as well as protocols for a computer-assisted surgical correction [36, 37].

References

1. Myerson MS, Badekas A, Schon LC. Treatment of stage II posterior tibial tendon deficiency with flexor digitorum longus tendon transfer and calcaneal osteotomy. Foot Ankle Int. 2004;25(7):445–50.
2. Yontar NS, Ogut T, Guven MF, Botanlioglu H, Kaynak G, Can A. Surgical treatment results for flexible flatfoot in adolescents. Acta Orthop Traumatol Turc. 2016;50(6):655–9.
3. Zaw H, Calder JDF. Operative management options for symptomatic flexible adult acquired flatfoot deformity: a review. Knee Surg Sports Traumatol Arthrosc. 2010;18(2):135–42.
4. McCormack AP, Ching RP, Sangeorzan BJ. Biomechanics of procedures used in adult flatfoot deformity. Foot Ankle Clin. 2001;6(1):15–23.
5. Alley MC, Shakked R, Rosenbaum AJ. Adult-acquired flatfoot deformity. JBJS Rev. 5(8):e7–e72017;5(8):e7–e.
6. Haddad SL, Myerson MS, Younger A, Anderson RB, Davis WH, Manoli A. Adult acquired flatfoot deformity. Los Angeles: SAGE Publications Sage CA; 2011.
7. Blackman AJ, Blevins JJ, Sangeorzan BJ, Ledoux WR. Cadaveric flatfoot model: ligament attenuation and Achilles tendon overpull. J Orthop Res. 2009;27(12):1547–54.
8. Wade M, Li Y-C, Wahl GM. Effect of therapeutic insoles on the medial longitudinal arch in patients with flatfoot deformity: a three-dimensional loading computed tomography study. Clin Biomech. 2013;13(2):83–96.
9. Ling SK-K, Lui TH. Posterior tibial tendon dysfunction: an overview. Open Orthop J. 2017;11(Suppl-4, M12):714–23.
10. Chan JY, Williams BR, Nair P, Young E, Sofka C, Deland JT, et al. The contribution of medializing calcaneal osteotomy on hindfoot alignment in the reconstruction of the stage II adult acquired flatfoot deformity. Foot Ankle Int. 2013;34(2):159–66.
11. Iaquinto JM, Wayne JS. Effects of surgical correction for the treatment of adult acquired flatfoot deformity: a computational investigation. J Orthop Res. 2011;29(7):1047–54.
12. Kido M, Ikoma K, Imai K, Maki M, Takatori R, Tokunaga D, et al. Load response of the tarsal bones in patients with flatfoot deformity: in vivo 3D study. Foot Ankle Int. 2011;32(11):1017–22.
13. Zhang Y, Xu J, Wang X, Huang J, Zhang C, Chen L, et al. An in vivo study of hindfoot 3D kinetics in stage II posterior tibial tendon dysfunction (PTTD) flatfoot based on weight-bearing CT scan. Bone Joint Res. 2013;2(12):255–63.
14. Barg A, Bailey T, Richter M, Netto C, Lintz F, Burssens A, et al. Weightbearing computed tomography of the foot and ankle: emerging technology topical review. Foot Ankle Int. 2018;39(3):376–86.
15. Lintz F, Cesar Netto CD, Barg A, Burssens A, Richter M, Group WBCIS. Weight-bearing cone beam CT scans in the foot and ankle. EFORT Open Rev. 2018;3(5):278–86.
16. Roemer W, Dufour AB, Gensure RH, Hannan MT, Hannan T, Dufour AB, et al. Flatfeet are associated with knee pain and cartilage damage in older adults. Arthritis Care Res. 2012;63:7.
17. de Cesar Netto C, Schon LC, Thawait GK, da Fonseca LF, Chinanuvathana A, Zbijewski WB, et al. Flexible adult acquired flatfoot deformity: comparison between weight-bearing and non-weight-bearing measurements using cone-beam computed tomography. J Bone Joint Surg Am. 2017;99(18):e98.

18. Kuo C-C, Lu H-L, Lu T-W, Lin C-C, Leardini A, Kuo M-Y, et al. Effects of positioning on radiographic measurements of ankle morphology: a computerized tomography-based simulation study. Biomed Eng Online. 2013;12(1):131.
19. Burssens A, Peeters J, Peiffer M, Marien R, Lenaerts T, ISG W, et al. Reliability and correlation analysis of computed methods to convert conventional 2D radiological hindfoot measurements to a 3D setting using weightbearing CT. Int J Comput Assist Radiol Surg. 2018;13(12):1999–2008.
20. Saltzman CL, El-Khoury GY. The hindfoot alignment view. Foot Ankle Int. 1995;16(9):572–6.
21. Younger AS, Sawatzky B, Dryden P. Radiographic assessment of adult flatfoot. Foot Ankle Int. 2005;26(10):820–5.
22. Auricchio F, Marconi S. 3D printing: clinical applications in orthopaedics and traumatology. EFORT Open Rev. 2016;1(5):121–7.
23. Shrout PE, Fleiss JL. Intraclass correlations: uses in assessing rater reliability. Psychol Bull. 1979;86(2):420.
24. Faul F, Erdfelder E, Buchner A, Lang A-G. Statistical power analyses using G∗ power 3.1: tests for correlation and regression analyses. Behav Res Methods. 2009;41(4):1149–60.
25. Richter M, Seidl B, Zech S, Hahn S. PedCAT for 3D-imaging in standing position allows for more accurate bone position (angle) measurement than radiographs or CT. Foot Ankle Surg. 2014;20(3):201–7.
26. Baig M, Baig U, Tariq A, Din R. A prospective study of distal metatarsal chevron osteotomies with K-wire fixations to treat hallux valgus deformities. Cureus. 2017;9(9):e1704.
27. Todd M, Lalliss S, DeBerardino T. A simplified technique for high tibial osteotomy with early radiographic follow-up results. Tech Knee Surg. 2008;7(3):172–7.
28. Amis AA. Biomechanics of high tibial osteotomy. Knee Surg Sports Traumatol Arthrosc. 2013;21(1):197–205.
29. Spratley EM, Arnold JM, Owen JR, Glezos CD, Adelaar RS, Wayne JS. Plantar forces in flexor hallucis longus versus flexor digitorum longus transfer in adult acquired flatfoot deformity. Foot Ankle Int. 2013;34(9):1286–93.
30. Nickisch F, Anderson RB. Post–calcaneus fracture reconstruction. Foot Ankle Int. 2006;11(1):85–103.
31. Stephens HM, Sanders R. Calcaneal malunions: results of a prognostic computed tomography classification system. Foot Ankle Int. 1996;17(7):395–401.
32. Conti MS, Ellis SJ, Chan JY, Do HT, Deland JT. Optimal position of the heel following reconstruction of the stage II adult-acquired flatfoot deformity. Foot Ankle Int. 2015;36(8):919–27.
33. Cöster MC, Bremander A, Rosengren BE, Magnusson H, Carlsson Å, Karlsson MK. Validity, reliability, and responsiveness of the Self-reported Foot and Ankle Score (SEFAS) in forefoot, hindfoot, and ankle disorders. Acta Orthop. 2014;85(2):187–94.
34. Richter M, Lintz F, Zech S, Meissner SA. Combination of PedCAT weightbearing CT with pedography assessment of the relationship between anatomy-based foot center and force/pressure-based center of gravity. Foot Ankle Int. 2018;39(3):361–8.
35. Reilingh M, Tuijthof G, Van Dijk C, Blankevoort L. The influence of foot geometry on the calcaneal osteotomy angle based on two-dimensional static force analyses. Arch Orthop Trauma Surg. 2011;131(11):1491–7.
36. Ma B, Kunz M, Gammon B, Ellis RE, Pichora DR. A laboratory comparison of computer navigation and individualized guides for distal radius osteotomy. Int J Comput Assist Radiol Surg. 2014;9(4):713–24.
37. Wei M, Chen J, Guo Y, Sun H. The computer-aided parallel external fixator for complex lower limb deformity correction. Int J Comput Assist Radiol Surg. 2017;12(12):2107–17.

Chapter 12
Is Load Application Necessary when Using Computed Tomography Scans to Diagnose Syndesmotic Injuries? A Cadaver Study

Alexej Barg

Introduction

Injury to the distal tibiofibular syndesmosis is common and appears in up to 20% of patients with an ankle sprain or ankle fracture [1–3]. If not treated appropriately, long-lasting disabilities like chronic pain, instability, and ankle joint osteoarthritis may occur [2, 4, 5]. Injury can occur to any of the four main components of the distal tibiofibular syndesmosis: the anterior inferior tibiofibular ligament (AITFL), interosseous membrane (IOM), posterior inferior tibiofibular ligament (PITFL), and transverse tibiofibular ligament (TTFL) [2, 3, 6]. Additionally, a deltoid ligament injury is also frequently present in patients with syndesmotic injury [7].

Conventional (weight-bearing) radiographs (anteroposterior and mortise view) (Fig. 12.1), CT scans (Fig. 12.2), and magnetic resonance imaging (MRI) (Fig. 12.3) are widely used for assessment of the distal tibiofibular syndesmosis [3].

While pronounced injuries can be reliably assessed using conventional radiographs, the diagnosis of incomplete injuries, especially in the absence of a fracture (e.g., high ankle sprain), is difficult [8–11]. In addition, measurements on conventional radiographs do not reliably reflect the injury pattern, which limits the general utility of conventional radiographs in assessing the distal tibiofibular syndesmosis [12]. Correlating findings in magnetic resonance imaging (MRI) with patient complaints can prove challenging [3]. Therefore, an accurate imaging modality to assess patients with incomplete injuries to the distal tibiofibular syndesmosis is desirable.

With the introduction of weight-bearing CT scans, detailed assessment of foot and ankle disorders under load-bearing conditions became possible [13–15].

Based on Krähenbühl N, Bailey TL, Weinberg MW, Davidson NP, Hintermann B, Presson AP, Allen CM, Henninger HB, Saltzman CL, Barg A. Is load application necessary when using computed tomography scans to diagnose syndesmotic injuries? A cadaver study. *Foot Ankle Surg*, 2019 Feb 18 [epub ahead of print]; and Krähenbühl N, Weinberg MW, Davidson NP, Mills MK, Hintermann B, Saltzman CL, Barg A. Imaging in syndesmotic injury: a systematic literature review. *Skeletal Radiol*, 2018; 47(5): 631–48

M. Richter et al., *Weight Bearing Cone Beam Computed Tomography (WBCT) in the Foot and Ankle*, https://doi.org/10.1007/978-3-030-31949-6_12

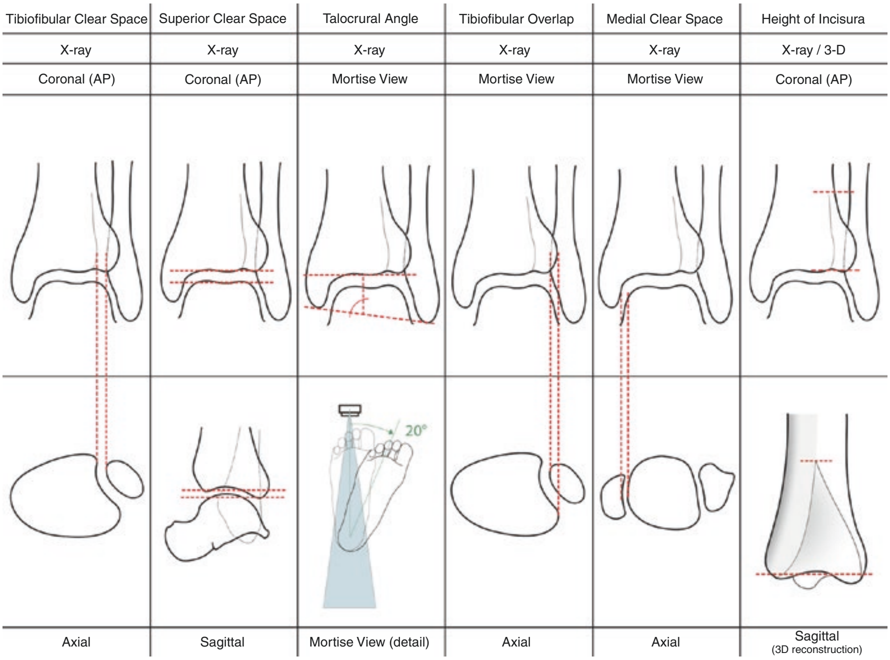

Fig. 12.1 Frequently used measurement methods to assess the distal tibiofibular syndesmosis using plain radiographs [3]

However, the impact of load on two-dimensional (2D) measurements performed on axial CT images to assess the integrity of the distal tibiofibular syndesmosis is debated [16, 17]. The purpose of this cadaver study was to assess the influence of weight on the assessment of incomplete and more complete syndesmotic injuries using 2D measurements on axial CT images. We hypothesized that weight would significantly impact on the assessment of both incomplete and more complete injuries to the distal tibiofibular syndesmosis.

Methods

Data Source

Seven pairs of male cadavers (tibia plateau to toe-tip) were included (mean age 62 ± 7 [range 52–70] years; mean weight 84.9 ± 15.3 [range 65.8–104.8] kg; mean body mass index (BMI) 26.8 ± 5.0 [range 19.7–32.5] kg/m^2). Inclusion criteria were 20–70 years of age and a BMI of less than 35 kg/m^2. Exclusion criteria were a history of any foot and ankle injuries or a history of surgery of the foot and ankle.

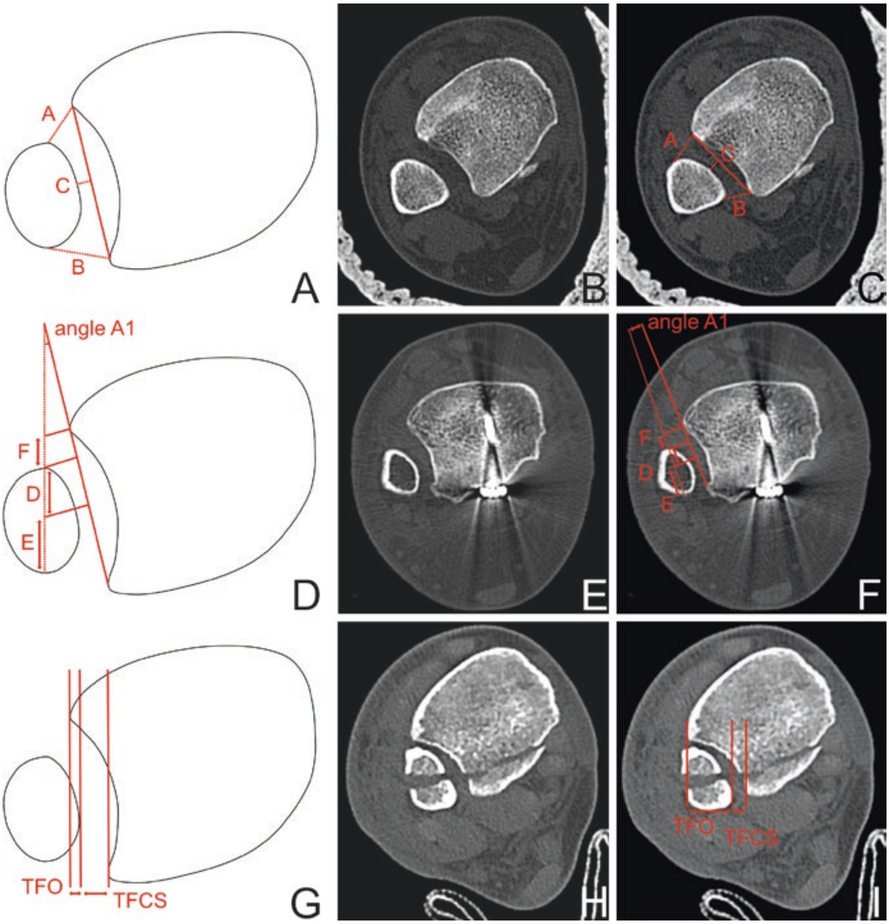

Fig. 12.2 Frequently used measurement methods to assess the distal tibiofibular syndesmosis using computed tomography (CT) scans. Measurements were performed 1 cm above the distal tibial plafond. (**a**) Measurement of the tibiofibular width anterior (**a**), middle (**c**), and posterior (**b**). (**b**) A 35-year-old patient with an acute syndesmotic instability following a high fibular and posterior malleolar fracture. The syndesmotic injury was not addressed on the primary surgery. (**c**) Measurement of the tibiofibular width. (**d**) Measurement of the anteroposterior translation (**d**–**f**) and the rotation (angle A1) of the distal fibula. (**e**) A 47-year-old patient with an acute syndesmotic injury following a high fibular fracture and small posterior malleolar avulsion. (**f**) Measurement of the anteroposterior translation and rotation of the distal fibula. (**g**) Measurement of the tibiofibular clear space (TFCS) and tibiofibular overlap (TFO). (**h**) A 37-year-old patient with an acute syndesmotic injury following a high fibular fracture. (**i**) Measurement of the TFCS and TFO. Radiologists and orthopedic surgeons should be aware that a distal fracture of the fibula and/or an additional tibia fracture influence the measurements. It is important to mention that the rotation of the ankle also influences the measurements [3]

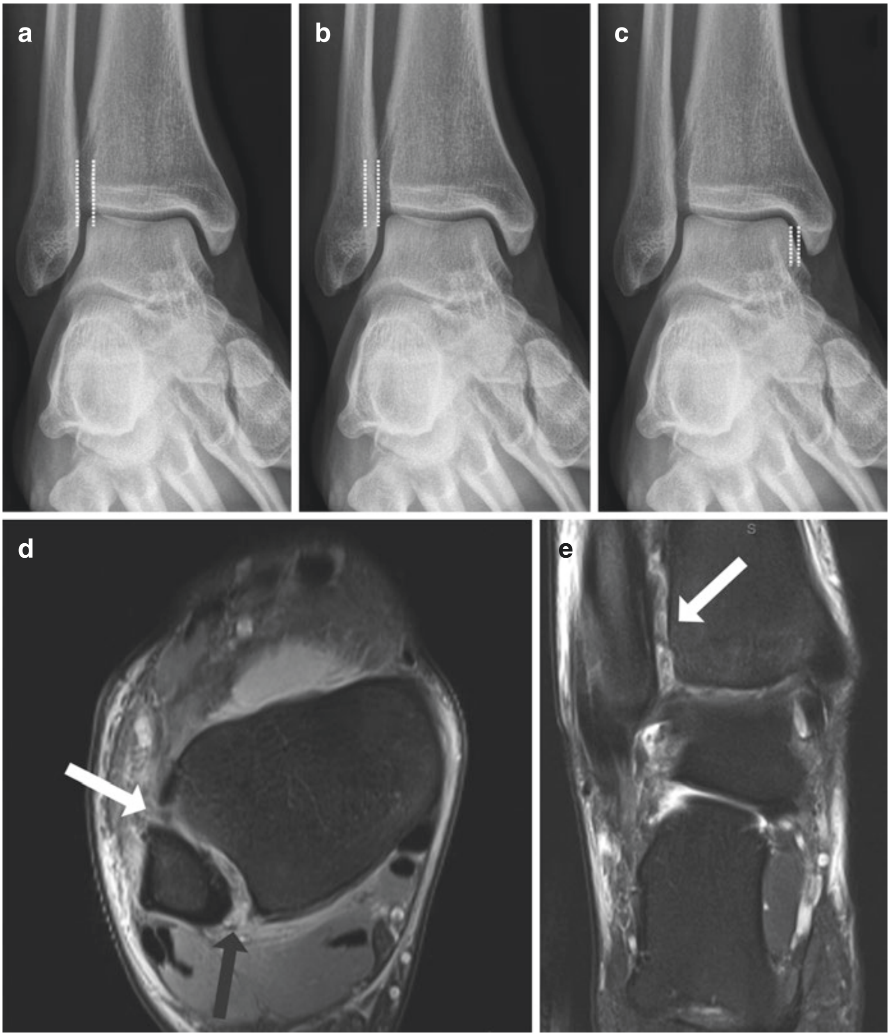

Fig. 12.3 Example of a 37-year-old man with an acute isolated syndesmotic injury. The conventional radiographs (mortise view) cannot predict reliably the syndesmotic injury. (**a**) Normal tibiofibular clear space (TFCS). (**b**) Normal tibiofibular overlap (TFO). (**c**) Normal medial clear space (MCS). (**d**) Axial magnet resonance imaging (MRI) proton density with fat saturation demonstrates full-thickness tear of both the anterior (white arrow) and posterior (grey arrow) tibiofibular ligaments. (**e**) Coronal T2 fat-saturated MRI image shows heterogeneity and increased signal of the syndesmotic ligaments (arrow), consistent with syndesmotic injury [3]

Experimental Setting

Each specimen was thawed for 24 hours at room temperature before any experiments were performed [18]. A radiolucent frame held the specimens in a plantigrade position (Fig. 12.4). The cadaver was fixed with an Ilizarov apparatus that fit into the frame. Four 1.5 mm Kirschner-wires (K-wires) were drilled through the tibia for fixation to the frame. The K-wires were tightened using a dynamometric wire tensioner (Smith & Nephew). The hindfoot was fixed using two 1.5 mm K-wires drilled through the calcaneus, and two-part resin (Bondo®, 3 M) stabilized the soft tissue envelope below the level of the syndesmotic ligaments. Non-weight-bearing and weight-bearing CT scans were collected (PedCAT, CurveBeam LLC, Warrington, USA, medium view, 0.3 mm slice thickness, 0.3 mm slice interval, kVp 120, mAs 22.62).

First, intact ankles (native) were scanned. Second, one specimen from each pair underwent AITFL transection (Condition 1A), while the contralateral underwent deltoid transection (Condition 1B). Third, the lesions were reversed on the same specimens, and the remaining intact deltoid ligament or AITFL was transected in each ankle (Condition 2). Finally, the interosseous membrane (IOM) was transected

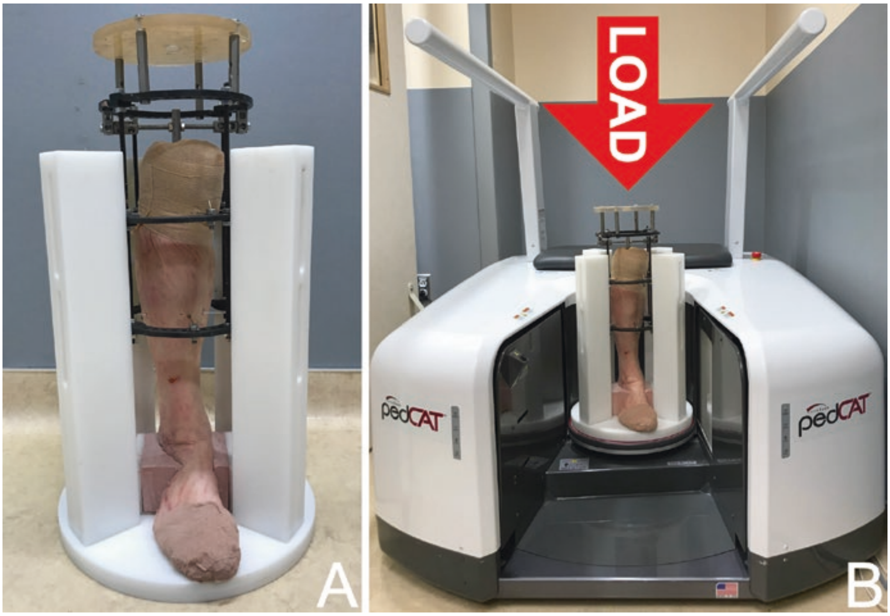

Fig. 12.4 Experimental setting. (**a**) The foot was fixed in an Ilizarov frame, which fit into a radiolucent frame that held the foot in a plantigrade position. The hindfoot was fixed with two Kirschner-wires (K-wires) and a two-part resin (Bondo®, 3 M). (**b**) The frame was put into a weight-bearing computed tomography (CT) scanner for data collection. Load was applied to the plate mounted on top of the Ilizarov frame [1]

in all ankles (Condition 3). Conditions 1A and 1B were considered to mimic incomplete injuries, while Conditions 2 and 3 were considered to mimic more complete injuries. For each condition, non-weight-bearing, half-bodyweight (42.5 kg), and full-bodyweight (85 kg) CT scans were taken. Loading levels were determined from the average of specimen donor anthropometrics. Preconditioning of the specimen was performed by statically loading the frame with 42.5 kg and 85 kg for 2 minutes each before the experiments were performed.

Measurements for interobserver agreement calculation were done by a fellowship-trained orthopedic surgeon and a research analyst. For calculation of the intraobserver agreement, measurements were performed two times with an interval of 3 weeks by a fellowship-trained orthopedic surgeon. Each observer completed a computer-based training before measurements were performed.

Imaging and Measurements

Axial CT images 1 cm above the medial edge of the distal tibial plafond were reconstructed (CurveBeam LLC, Warrington, USA, Version 3.2.1.0) and used for the following measurements: distance between the most anterior point of the tibial incisura and the nearest most anterior point of the fibula (ATFD), distance between the most anterior point of the fibula and a line perpendicular to the most anterior point of the tibial incisura (AFT), distance between the most anterior point of the fibula and a line perpendicular to the connection of the most anterior and posterior point of the tibial incisura (MFT), and distance from the same perpendicular line to the most posterior point of the fibula (PFT, Fig. 12.5) [16, 17, 19]. In addition, the angle between the fibular axis (the line between the most anterior and posterior edge of the fibula) and the line between the anterior and posterior edge of the tibial incisura were measured (Angle 1) [19]. Furthermore, the tibiofibular overlap (TFO, defined as the maximum overlap between the lateral tibia and medial fibula) and the tibiofibular clear space (TFCS, defined as the distance from the lateral border of the posterior tibial tubercle to the medial border of the fibula) were measured on the same axial images [20]. On the level of the talar dome (axial images), the angle between the fibula and medial malleolus (Angle 2) was measured [19].

Statistical Analysis

Intraclass correlation (ICC) was used to quantify the agreement of measurements between and within observers. Estimates and 95% confidence intervals (CI) were calculated for each type of measurement. Interobserver agreement was modeled with a two-way random effect model of absolute agreement with a single measure-

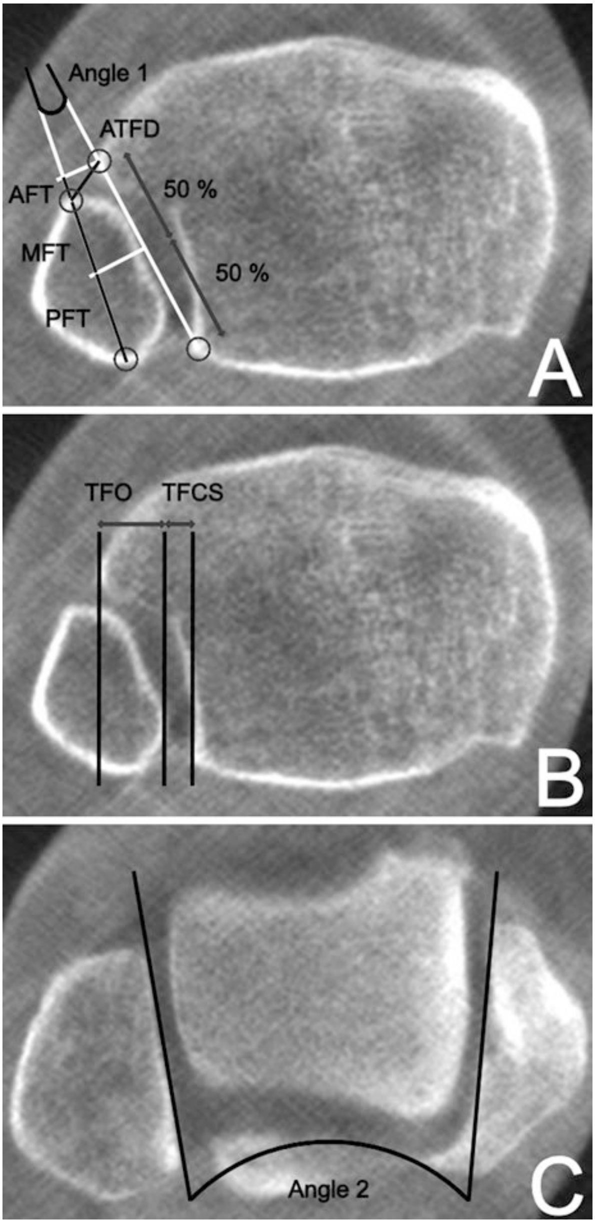

Fig. 12.5 Measurements using computed tomography (CT) scans. (**a**) Axial image 1 cm above of the tibial plafond. The anterior tibiofibular distance (ATFD) represents the distance between the most anterior point of the tibial incisura and the most anterior point of the fibula. The anterior fibular translation (AFT) is defined as the distance between the most anterior point of the fibula and a perpendicular line to the anterior edge of the tibial incisura. The middle fibular translation (MFT) is defined as the distance between the most anterior point of the fibula and a line perpendicular to the connection of the most anterior and posterior point of the tibial incisura. The posterior fibular translation (PFT) represents the distance between the most posterior point of the fibula and the same perpendicular line. Angle 1 represents the angle between a line drawn between the most anterior and posterior point of the tibial incisura and the axis of the fibula. (**b**) Tibiofibular clear space (TFCS) and tibiofibular overlap (TFO) measured 1 cm above the tibial plafond. (**c**) Angle 2 measured between the fibula and the medial malleolus at the level of the tibial dome [1]

ment per observation. Intraobserver agreement was modeled with a two-way mixed effect model of consistency with a single measurement per observation. Agreement was rated as excellent with an ICC >0.75; good with an ICC = 0.61–0.75; fair with an ICC = 0.4–0.6; and poor with an ICC <0.4 [16].

Linear mixed effect models were fit for responses. Cadaver, treated as a random effect, and foot, (left or right) treated as a fixed effect, were included in all models in addition to the variables presented lateral in the tables. Models were fit for subsets of the data (with given weight or condition constant) and estimates and 95% CI are given for differing levels of condition or weight. Confidence intervals were calculated using a Tukey adjustment for multiple comparisons within each model. Significance was determined based on a P-value of less than 0.05 after the Tukey adjustment. All calculations were done in R 3.4.1, specifically using package psych and ImerTest.

Results

Inter- and intraobserver agreement differed between measurements (Table 12.1). Excellent agreement was evident for the TFCS and TFO (intraobserver agreement, 0.79 and 0.94). Poor agreement was evident for Angle 1 (interobserver, 0.39). The agreement of the other measurements (inter- and intraobserver) was either rated as fair or good and ranged from 0.44 to 0.71. Load application had no significant influence on almost every measurement across all conditions (e.g., without subdividing into different conditions; Table 12.2). Divided into the tested conditions, only the ATFD or TFO could identify more complete injuries (Condition 3) from native ankles (Tables 12.3 and 12.4). No significant differences were evident between single AITFL and deltoid ligament transection for the ATFD and TFO. No significant differences were observed within each condition between non-, half-, and full-weight-bearing when using the ATFD or TFO (Tables 12.5 and 12.6).

Table 12.1 Agreement of computed tomography scans assessed by intraclass correlation (ICC) [1]

	Interobserver: ICC(2,1) *Estimate (95% CI)*	Level of agreement	Intraobserver: ICC(3,1) *Estimate (95% CI)*	Level of agreement
Angle 1	0.39 (0.12, 0.60)	Poor	0.51 (0.27, 0.69)	Fair
Angle 2	0.44 (−0.08, 0.74)	Fair	0.67 (0.48, 0.80)	Good
ATFD	0.54 (0.30, 0.71)	Fair	0.58 (0.35, 0.74)	Fair
AFT	0.65 (0.45, 0.79)	Good	0.61* (0.39, 0.76)	Good
MFT	0.65 (0.45, 0.79)	Good	0.71* (0.53, 0.82)	Good
PFT	0.53 (0.29, 0.70)	Fair	0.54 (0.30, 0.71)	Fair
TFCS	0.61 (0.74, 0.97)	Good	0.79 (0.89, 0.97)	Excellent
TFO	0.57 (0.53, 0.98)	Fair	0.94 (0.97, 0.99)	Excellent

CT computed tomography, *CI* confidence interval, *ATFD* anterior tibiofibular distance, *AFT* anterior fibular translation, *MFT* middle fibular translation, *PFT* posterior fibular translation, *TFCS* tibiofibular clear space, *TFO* tibiofibular overlap

*Significant difference (*P*-value <0.05)

Table 12.2 Influence of load on computed tomography measurements across all tested conditions (difference between weight application in millimeters [mm]) [1]

			Estimate (95% CI)	
		Mean (SD; mm)	Non-weight-bearing	Half-bodyweight
Angle 1	Non-weight-bearing	*−13.3 (5.8)*	–	–
	Half-bodyweight	*−13.4 (5.3)*	0.0 (−1.8, 1.8)	–
	Full-bodyweight	*−13.8 (5.4)*	−0.5 (−2.2, 1.3)	−0.4 (−2.2, 1.4)
Angle 2	Non-weight-bearing	*10.3 (7.5)*	–	–
	Half-bodyweight	*10.8 (7.9)*	0.5 (−0.8, 1.8)	–
	Full-bodyweight	*11.1 (7.4)*	0.8 (−0.5, 2.1)	0.3 (−1.0, 1.6)
ATFD	Non-weight-bearing	*4.6 (1.0)*	–	–
	Half-bodyweight	*4.7 (1.3)*	0.1 (−0.4, 0.5)	–
	Full-bodyweight	*4.5 (1.0)*	−0.1 (−0.5, 0.3)	−0.2 (−0.6, 0.3)
AFT	Non-weight-bearing	*2.3 (1.6)*	–	–
	Half-bodyweight	*2.1 (1.5)*	−0.1 (−0.6, 0.3)	–
	Full-bodyweight	*1.0 (1.5)*	−0.3 (−0.7, 0.2)	−0.2 (−0.6, 0.3)
MFT	Non-weight-bearing	*9.3 (1.5)*	–	–
	Half-bodyweight	*9.4 (1.4)*	0.1 (−0.3, 0.6)	–
	Full-bodyweight	*9.7 (1.4)*	0.4 (−0.1, 0.8)	0.3 (−0.2, 0.7)
PFT	Non-Weight-bearing	*8.1 (1.2)*	–	–
	Half-bodyweight	*7.9 (1.1)*	−0.1 (−0.5, 0.3)	–
	Full-bodyweight	*7.6 (1.1)*	**−0.4* (0.8, −0.0)**	−0.3 (−0.7, 0.1)
TFCS	Non-Weight-bearing	*4.5 (1.6)*	–	–
	Half-bodyweight	*4.7 (1.5)*	0.2 (−0.2, 0.5)	–
	Full-bodyweight	*4.7 (1.5)*	0.1 (−0.3, 0.5)	−0.1 (−0.4, 0.3)
TFO	Non-Weight-bearing	*6.2 (1.5)*	–	–
	Half-bodyweight	*6.1 (1.5)*	−0.1 (−0.7, 0.4)	–
	Full-bodyweight	*6.2 (1.4)*	0.0 (−0.5, 0.5)	0.1 (−0.4, 0.7)

SD standard deviation, *CT* computed tomography, *CI* confidence interval, *ATFD* anterior tibiofibular distance, *AFT* anterior fibular translation, *MFT* middle fibular translation, *PFT* posterior fibular translation, *TFCS* tibiofibular clear space, *TFO* tibiofibular overlap
*Significant difference (*P*-value <0.05)

Discussion

A cadaver study testing the impact of weight on assessment of syndesmotic injuries using axial CT images was performed. The three most relevant findings were the following: (1) weight did not improve the ability of most 2D measurements to diagnose syndesmotic injuries; (2) only more complete injuries could be identified using weight-bearing CT scans; and (3) discrete AITFL and deltoid ligament injuries could not be distinguished.

Multiple studies investigating the utility of weight-bearing radiographs or non-weight-bearing CT scans in the diagnoses of injuries to the distal tibiofibular syndesmosis have been published [8–10, 12, 21, 22]. In contrast, only two studies assessed the impact of load on the assessment of the distal tibiofibular syndesmosis

Table 12.3 Influence of ligament resection on anterior tibiofibular distance (computed tomography; difference between each condition in millimeters [mm]) [1]

ATFD		*Mean (SD; mm)*	Estimate (95% CI) Native	Condition 1A	Condition 1B	Condition 2
Non-weight-bearing	Native	*4.0 (0.9)*	–	–	–	–
	Condition 1A	*4.5 (0.7)*	0.5 (−0.5, 1.5)	–	–	–
	Condition 1B	*4.4 (0.6)*	0.4 (−0.6, 1.4)	−0.1 (−1.2, 1.0)	–	–
	Condition 2	*4.5 (0.9)*	0.5 (−0.3, 1.3)	0.0 (−1.0, 1.0)	0.1 (−0.9, 1.1)	–
	Condition 3	*5.4 (1.0)*	**1.4* (0.6, 2.2)**	0.9 (−0.1, 1.9)	**1.0* (0.0, 2.0)**	**0.9* (0.1, 1.7)**
Half-bodyweight	Native	*3.8 (1.0)*	–	–	–	–
	Condition 1A	*4.8 (1.2)*	1.0 (−0.2, 2.2)	–	–	–
	Condition 1B	*4.1 (1.0)*	0.4 (−0.8, 1.5)	−0.7 (−2.0, 0.7)	–	–
	Condition 2	*4.7 (0.9)*	0.93 (−0.02, 1.88)	−0.1 (−1.2, 1.1)	0.6 (−0.6, 1.7)	–
	Condition 3	*5.7 (1.4)*	**1.9* (1.0, 2.9)**	0.9 (−0.3, 2.1)	**1.6* (0.4, 2.7)**	**1.0* (0.0, 1.9)**
Full-bodyweight	Native	*4.0 (0.9)*	–	–	–	–
	Condition 1A	*4.6 (1.0)*	0.5 (−0.4, 1.5)	–	–	–
	Condition 1B	*3.9 (0.9)*	−0.1 (−1.1, 0.8)	−0.7 (−1.7, 0.4)	–	–
	Condition 2	*4.6 (0.9)*	0.6 (−0.1, 1.3)	0.1 (−0.9,1.0)	0.7 (−0.2, 1.6)	–
	Condition 3	*5.1 (1.0)*	**1.1* (0.3, 1.8)**	0.5 (−0.4, 1.4)	**1.2* (0.3, 2.1)**	0.5 (−0.3, 1.2)

CT computed tomography, *SD* standard deviation, *CI* confidence interval, *ATFD* anterior tibiofibular distance

*Significant difference (P-value <0.05)

when using CT scans [16, 17]. Shakoor et al. did not find any significant differences when load was applied for most measurements (asymptomatic ankles included), while Malhotra et al. found that the fibula rotates posterolateral under weight-bearing conditions [16, 17]. Of note, Malhotra et al. did use different CT scanners for weight-bearing and non-weight-bearing imaging [17]. Also, the included cohort was not uniform (e.g., ankles with different pathologies) [17]. This may impact on the assessment of the distal tibiofibular syndesmosis when using axial CT images as 2D measurements are dependent on the position of the ankle joint (e.g., rotation and plantar flexion/dorsal extension) [23, 24]. The present cadaver study supports the findings by Shakoor et al. and showed no differences between 2D measurements with and without load application.

Although loading may not be crucial, weight-bearing CT scans have several advantages over other imaging options: first, the position of the foot can be standardized using weight-bearing CT scans, allowing imaging with the foot in a plantigrade position in the same relative rotation to the body and/or scanner. Second, some weight-bearing CT scans also allow both feet to be scanned at the same time. As the anatomy of the tibial incisura varies between individuals, a left-right comparison can highlight certain injuries and abnormalities that would otherwise go unnoticed [25–29].

The inter- and intraobserver agreement between measurements differed in the present study. Defining anatomical landmarks on axial CT images can be difficult.

Table 12.4 Influence of ligament resection on tibiofibular overlap measurements (computed tomography; difference between each condition in millimeters [mm]) [1]

TFO		*Mean (SD; mm)*	Estimate (95% CI)			
			Native	Condition 1A	Condition 1B	Condition 2
Non-weight-bearing	Native	*6.8 (1.6)*	–	–	–	–
	Condition 1A	*5.9 (1.2)*	−0.9 (−2.4, 0.6)	–	–	–
	Condition 1B	*6.7 (1.4)*	−0.1 (−1.6, 1.4)	0.8 (−1.0, 2.6)	–	–
	Condition 2	*6.3 (1.7)*	−0.5 (−1.8, 0.7)	0.4 (−1.2, 1.9)	−0.4 (−1.9, 1.1)	–
	Condition 3	*5.5 (1.3)*	**−1.3* (−2.5, −0.0)**	−0.4 (−1.9, 1.2)	−1.2 (−2.7, 0.4)	−0.7 (−2.0, 0.5)
Half-bodyweight	Native	*6.7 (1.6)*	–	–	–	–
	Condition 1A	*6.0 (1.6)*	−0.7 (−2.0, 0.7)	–	–	–
	Condition 1B	*6.6 (1.2)*	−0.1 (−1.5, 1.2)	0.5 (−1.0, 2.1)	–	–
	Condition 2	*6.0 (1.5)*	−0.7 (−1.8, 0.4)	−0.1 (−1.4, 1.3)	−0.6 (−1.0, 0.8)	–
	Condition 3	*5.4 (1.9)*	**−1.3* (−2.4, −0.2)**	−0.6 (−1.0, 0.7)	−1.2 (−2.5, 0.2)	−0.6 (−1.7, 0.6)
Full-bodyweight	Native	*6.9 (1.5)*	–	–	–	–
	Condition 1A	*6.1 (1.0)*	−0.8 (−2.2, 0.6)	–	–	–
	Condition 1B	*6.9 (1.4)*	−0.0 (−1.4, 1.4)	0.8 (−0.8, 2.4)	–	–
	Condition 2	*6.0 (1.1)*	−0.9 (−2.1, 0.2)	−0.09 (−1.5, 1.3)	−0.9 (−2.3, 0.5)	–
	Condition 3	*5.4 (1.3)*	**−1.5* (−2.6, −0.4)**	−0.7 (−2.1, 0.7)	**−1.5* (−2.9, −0.1)**	−0.6 (−1.7, 0.6)

CT computed tomography, *SD* standard deviation, *CI* confidence interval, *TFO* tibiofibular overlap
*Significant difference (*P*-value <0.05)

The anatomy of the fibula and the incisura of the tibia differ between individuals, and edges can either be round or sharp (Fig. 12.6) [22, 25–28]. This may be the reason why Angle 1 and Angle 2 showed the lowest agreement compared to the other measurements: four anatomic landmarks had to be defined for each of these two measurements while most other measurement only required two. Also, interobserver agreement was lower compared to intraobserver agreement for every measurement. As measurements were performed by a fellowship orthopedic surgeon and a research analyst less experienced in imaging analysis, our results suggest that the agreement of 2D measurements are dependent on the experience of the observer.

Table 12.5 Influence of weight on anterior tibiofibular distance (computed tomography; difference between weight application in millimeters [mm]) [1]

ATFD		*Mean (SD; mm)*	Estimate (95% CI) Non-weight-bearing	Half-bodyweight
Native	Non-weight-bearing	*4.0 (0.9)*	–	–
	Half-bodyweight	*3.8 (1.0)*	−0.3 (−0.8, 0.3)	–
	Full-bodyweight	*4.0 (0.9)*	0.0 (−0.5, 0.5)	0.3 (−0.3, 0.8)
Condition 1A	Non-weight-bearing	*4.5 (0.8)*	–	–
	Half-bodyweight	*4.8 (1.2)*	0.3 (−0.3, 0.9)	–
	Full-bodyweight	*4.6 (1.0)*	0.1 (−0.5, 0.7)	−0.2 (−0.8, 0.4)
Condition 1B	Non-weight-bearing	*4.4 (0.6)*	–	–
	Half-bodyweight	*4.1 (0.9)*	−0.2 (−1.0, 0.5)	–
	Full-bodyweight	*3.9 (0.9)*	−0.5 (−1.3, 0.3)	−0.3 (−1.0, 0.5)
Condition 2	Non-weight-bearing	*4.5 (0.9)*	–	–
	Half-bodyweight	*4.7 (0.9)*	0.2 (−0.5, 0.9)	–
	Full-bodyweight	*4.6 (0.9)*	0.1 (−0.6, 0.8)	−0.1 (−0.8, 0.6)
Condition 3	Non-weight-bearing	*5.4 (1.0)*	–	–
	Half-bodyweight	*5.7 (1.4)*	0.3 (−0.6, 1.2)	–
	Full-bodyweight	*5.1 (1.0)*	−0.3 (−1.2, 0.6)	−0.6 (−1.5, 0.3)

CT computer tomography, *SD* standard deviation, *CI* confidence interval, *ATFD* anterior tibiofibular distance
*Significant difference (*P*-value <0.05)

Table 12.6 Influence of weight on tibiofibular overlap measurements (computed tomography; difference between weight application in millimeters [mm]) [1]

TFO		*Mean (SD; mm)*	Estimate (95% CI) Non-weight-bearing	Half-bodyweight
Native	Non-weight-bearing	*6.8 (1.6)*	–	–
	Half-bodyweight	*6.7 (1.6)*	−0.1 (−1.2, 1.0)	–
	Full-bodyweight	*6.9 (1.5)*	0.1 (−1.0, 1.3)	0.2 (−0.9, 1.3)
Condition 1A	Non-weight-bearing	*5.9 (1.2)*	–	–
	Half-bodyweight	*6.0 (1.6)*	0.1 (−0.4, 0.7)	–
	Full-bodyweight	*6.1 (1.0)*	0.2 (−0.3, 0.7)	0.0 (−0.5, 0.6)
Condition 1B	Non-weight-bearing	*6.7 (1.4)*	–	–
	Half-bodyweight	*6.6 (1.2)*	−0.1 (−0.7, 0.4)	–
	Full-bodyweight	*6.9 (1.4)*	0.2 (−0.3, 0.8)	0.3 (−0.2, 0.9)
Condition 2	Non-weight-bearing	*6.3 (1.7)*	–	–
	Half-bodyweight	*6.0 (1.5)*	−0.3 (−1.2, 0.6)	–
	Full-bodyweight	*6.0 (1.1)*	−0.3 (−1.2, 0.6)	0.0 (−0.9, 0.9)
Condition 3	Non-weight-bearing	*5.5 (1.3)*	–	–
	Half-bodyweight	*5.4 (1.2)*	−0.1 (−1.0, 0.8)	–
	Full-bodyweight	*5.4 (1.3)*	−0.1 (1.0, 0.8)	0.0 (−0.9, 0.9)

CT computed tomography, *SD* standard deviation, *CI* confidence interval, *TFO* tibiofibular overlap
*Significant difference (*P*-value <0.05)

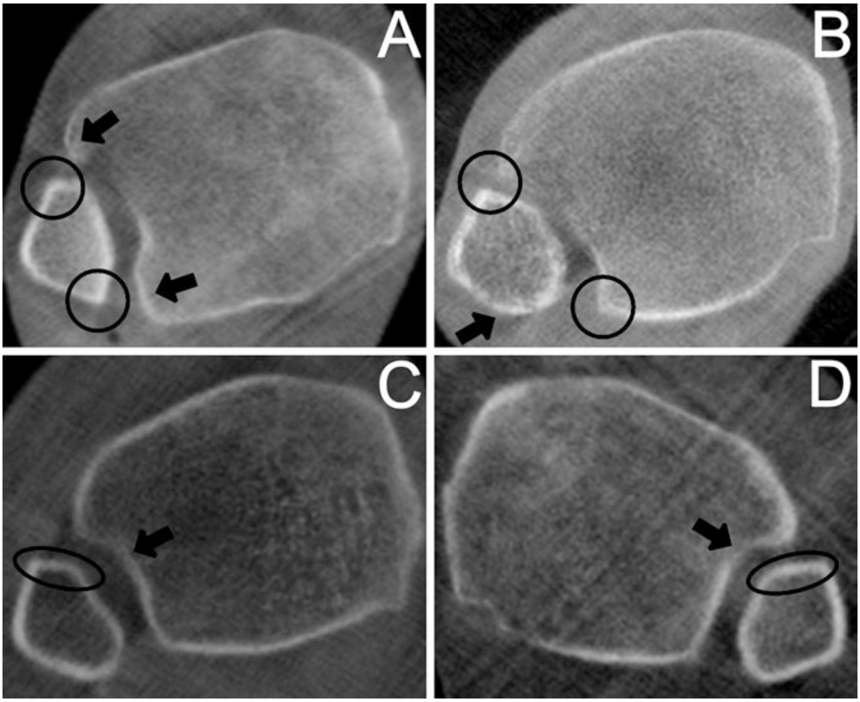

Fig. 12.6 Axial CT images of three different cadavers 1 cm above of the medial edge of the distal tibial plafond. (**a**) Sharp edges are evident anterior and posterior of the fibula (circles), allowing accurate identification of the anteroposterior axis. The tibial incisura shows round anterior and posterior edges (arrows), making a reliable identification of the anterior and posterior margins difficult. (**b**) The anterior and posterior edges of the tibial incisura and the anterior edge of the fibula are well defined (circles), while the posterior edge of the fibula shows a rounded shape and is therefore difficult to identify (arrow). Such findings may negatively impact on the agreement of two-dimensional (2D) measurements on the level of the distal tibiofibular syndesmosis. (**c**) The native weight-bearing right ankle shows a different morphology on the level of the tibiofibular syndesmosis (anterior part of the fibula, circle; tibial incisura, arrow) compared to the (**d**) corresponding left side under the same conditions (anterior part of the fibula, circle; tibial incisura, arrow) [1]

A more experienced observer (e.g., fellowship-trained orthopedic surgeon) can perform 2D measurement on the level of the distal tibiofibular syndesmosis more accurately compared to a less experienced observer.

Our study has several limitations. First, the continuous loading and unloading for each experimental condition may provoke relaxation of soft tissues, impacting measurements. Second, freezing and thawing of tissue may further negatively impact the soft tissue condition. Also, some donors may have been inactive before time of death, which would negatively impact bone quality and, potentially, radiographic measurements. Third, resection of ligaments in cadavers can be done precisely. In a posttraumatic condition, different ligaments of the distal talo-fibular syndesmosis are variably torn or ruptured. Over time, scar tissue may also form. Such complex injuries cannot be simulated accurately using cadaver models.

To conclude, load application does not impact on the ability of weight-bearing CT scans to diagnose incomplete and also more complete syndesmotic injuries in a cadaver model. Nevertheless, the ability to reliably position the foot during imaging is an advantage of weight-bearing CT technology over other imaging options.

References

1. Krähenbühl N, Bailey TL, Weinberg MW, Davidson NP, Hintermann B, Presson AP, Allen CM, Henninger HB, Saltzman CL, Barg A. Is load application necessary when using computed tomography scans to diagnose syndesmotic injuries? A cadaver study. Foot Ankle Surg. 2019. Feb 18, epub ahead of print.
2. Rammelt S, Obruba P. An update on the evaluation and treatment of syndesmotic injuries. Eur J Trauma Emerg Surg. 2015;41(6):601–14.
3. Krähenbühl N, Weinberg MW, Davidson NP, Mills MK, Hintermann B, Saltzman CL, Barg A. Imaging in syndesmotic injury: a systematic literature review. Skelet Radiol. 2018;47(5):631–48.
4. Hunt KJ, Goeb Y, Behn AW, Criswell B, Chou L. Ankle joint contact loads and displacement with progressive syndesmotic injury. Foot Ankle Int. 2015;36(9):1095–103.
5. LaMothe J, Baxter JR, Gilbert S, Murphy CI, Karnovsky SC, Drakos MC. Effect of complete syndesmotic disruption and deltoid injuries and different reduction methods on ankle joint contact mechanics. Foot Ankle Int. 2017;38(6):694–700.
6. Golano P, Vega J, de Leeuw PA, Malagelada F, Manzanares MC, Gotzens V, van Dijk CN. Anatomy of the ankle ligaments: a pictorial essay. Knee Surg Sports Traumatol Arthrosc. 2010;18(5):557–69.
7. Jeong MS, Choi YS, Kim YJ, Kim JS, Young KW, Jung YY. Deltoid ligament in acute ankle injury: MR imaging analysis. Skelet Radiol. 2014;43(5):655–63.
8. Feller R, Borenstein T, Fantry AJ, Kellum RB, Machan JT, Nickisch F, Blankenhorn B. Arthroscopic quantification of syndesmotic instability in a cadaveric model. Arthroscopy. 2017;33(2):436–44.
9. Schoennagel BP, Karul M, Avanesov M, Bannas P, Gold G, Grossterlinden LG, Rupprecht M, Adam G, Yamamura J. Isolated syndesmotic injury in acute ankle trauma: comparison of plain film radiography with 3T MRI. Eur J Radiol. 2014;83(10):1856–61.
10. Hermans JJ, Wentink N, Beumer A, Hop WC, Heijboer MP, Moonen AF, Ginai AZ. Correlation between radiological assessment of acute ankle fractures and syndesmotic injury on MRI. Skelet Radiol. 2012;41(7):787–801.
11. Krähenbühl N, Weinberg MW, Hintermann B, Haller JM, Saltzman CL, Barg A. Surgical outcome in chronic syndesmotic injury: a systematic literature review. Foot Ankle Surg. 2018. epub ahead of print.
12. Nielson JH, Gardner MJ, Peterson MG, Sallis JG, Potter HG, Helfet DL, Lorich DG. Radiographic measurements do not predict syndesmotic injury in ankle fractures: an MRI study. Clin Orthop Relat Res. 2005;436:216–21.
13. Barg A, Bailey T, Richter M, de Cesar Netto C, Lintz F, Burssens A, Phisitkul P, Hanrahan CJ, Saltzman CL. Weightbearing computed tomography of the foot and ankle: emerging technology topical review. Foot Ankle Int. 2018;39(3):376–86.
14. Lintz F, de Cesar Netto C, Barg A, Burssens A, Richter M, Weight Bearing CTISG. Weightbearing cone beam CT scans in the foot and ankle. EFORT Open Rev. 2018;3(5):278–86.

15. Richter M, Seidl B, Zech S, Hahn S. PedCAT for 3D-imaging in standing position allows for more accurate bone position (angle) measurement than radiographs or CT. Foot Ankle Surg. 2014;20(3):201–7.
16. Shakoor D, Osgood GM, Brehler M, Zbijewski WB, de Cesar Netto C, Shafiq B, Orapin J, Thawait GK, Shon LC, Demehri S. Cone-beam CT measurements of distal tibio-fibular syndesmosis in asymptomatic uninjured ankles: does weight-bearing matter? Skelet Radiol. 2019;48(4):583–94.
17. Malhotra K, Welck M, Cullen N, Singh D, Goldberg AJ. The effects of weight bearing on the distal tibiofibular syndesmosis: a study comparing weight bearing-CT with conventional CT. Foot Ankle Surg. 2018. epub ahead of print.
18. Barg A, Amendola RL, Henninger HB, Kapron AL, Saltzman CL, Anderson AE. Influence of ankle position and radiographic projection angle on measurement of supramalleolar alignment on the anteroposterior and hindfoot alignment views. Foot Ankle Int. 2015;36(11):1352–61.
19. Nault ML, Hebert-Davies J, Laflamme GY, Leduc S. CT scan assessment of the syndesmosis: a new reproducible method. J Orthop Trauma. 2013;27(11):638–41.
20. Dikos GD, Heisler J, Choplin RH, Weber TG. Normal tibiofibular relationships at the syndesmosis on axial CT imaging. J Orthop Trauma. 2012;26(7):433–8.
21. Malhotra G, Cameron J, Toolan BC. Diagnosing chronic diastasis of the syndesmosis: a novel measurement using computed tomography. Foot Ankle Int. 2014;35(5):483–8.
22. Yeung TW, Chan CY, Chan WC, Yeung YN, Yuen MK. Can pre-operative axial CT imaging predict syndesmosis instability in patients sustaining ankle fractures? Seven years' experience in a tertiary trauma center. Skelet Radiol. 2015;44(6):823–9.
23. Nault ML, Marien M, Hebert-Davies J, Laflamme GY, Pelsser V, Rouleau DM, Gosselin-Papadopoulos N, Leduc S. MRI quantification of the impact of ankle position on syndesmosis anatomy. Foot Ankle Int. 2017;38(2):215–9.
24. Pneumaticos SG, Noble PC, Chatziioannou SN, Trevino SG. The effects of rotation on radiographic evaluation of the tibiofibular syndesmosis. Foot Ankle Int. 2002;23(2):107–11.
25. Mukhopadhyay S, Metcalfe A, Guha AR, Mohanty K, Hemmadi S, Lyons K, O'Doherty D. Malreduction of syndesmosis–are we considering the anatomical variation? Injury. 2011;42(10):1073–6.
26. Cherney SM, Spraggs-Hughes AG, McAndrew CM, Ricci WM, Gardner MJ. Incisura morphology as a risk factor for syndesmotic malreduction. Foot Ankle Int. 2016;37(7):748–54.
27. Lilyquist M, Shaw A, Latz K, Bogener J, Wentz B. Cadaveric analysis of the distal tibiofibular syndesmosis. Foot Ankle Int. 2016;37(8):882–90.
28. Elgafy H, Semaan HB, Blessinger B, Wassef A, Ebraheim NA. Computed tomography of normal distal tibiofibular syndesmosis. Skelet Radiol. 2010;39(6):559–64.
29. Burssens A, Vermue H, Barg A, Krahenbuhl N, Victor J, Buedts K. Templating of syndesmotic ankle lesions by use of 3D analysis in weightbearing and nonweightbearing CT. Foot Ankle Int. 2018;39(12):1487–96.

Chapter 13
Use of Weight Bearing Computed Tomography in Subtalar Joint Instability: A Cadaver Study

Alexej Barg

Introduction

Chronic hindfoot instability is a frequent problem that is evident in up to 33% of patients with a history of ankle sprains [1]. Hindfoot instability often includes the ankle joint but can also affect the subtalar joint [2–4]. While ankle joint instability can be diagnosed clinically, an accurate assessment of the subtalar joint remains elusive [2, 3, 5]. To provide an adequate treatment for patients with post-traumatic hindfoot instability, a meaningful assessment of the subtalar joint is desirable [2].

Two ligaments are the primary stabilizers of the subtalar joint: the interosseous talocalcaneal ligament (ITCL) and the calcaneofibular ligament (CFL) [6–9]. Other ligaments providing subtalar joint stability include the cervical ligament, lateral talocalcaneal ligament, and deltoid ligament [6–8, 10, 11]. Recent cadaver studies showed that the CFL is potentially the most important stabilizer of the subtalar joint when subjected to inversion and external rotation stress [7, 8]. As the CFL crosses both the ankle and subtalar joint, the stability of both joints is affected after injury. In contrast, the ITCL only provides stability to the subtalar joint [10].

Variation in injury patterns and its complex anatomy make diagnosing subtalar joint instability particularly challenging [2, 12]. Long-lasting instability of the lateral ligament complex results in degenerative changes and chronic hindfoot pain [2, 12–14]. The impact of subtalar joint instability on this development remains unclear [15]. This emphasizes the relevance of a radiographic diagnosis, currently performed by several two-dimensional (2D) measurements including tibiotalar tilt (TT), anterior talar translation (ATT), and subtalar tilt (STT) [2, 4, 16–21]. However, these measurements are limited in their ability to identify subtalar joint instability when using stress radiographs [2, 4].

Based on Krähenbühl N, Burssens A, Davidson NP, Allen CM, Henninger HB, Saltzman CL, Barg A (2019) Can weight bearing computed tomography scans be used to diagnose subtalar joint instability? A cadaver study. *J Orthop Res*, 2019 Jul 19 [epub ahead of print]; and Krähenbühl N, Weinberg MW, Davidson NP, Mills MK, Hintermann B, Saltzman CL, Barg A (2018) Currently used imaging options cannot accurately predict subtalar joint instability. *Knee Surg Sports Traumatol Arthrosc*, 2018 Oct 26 [epub ahead of print]

M. Richter et al., *Weight Bearing Cone Beam Computed Tomography (WBCT) in the Foot and Ankle*, https://doi.org/10.1007/978-3-030-31949-6_13

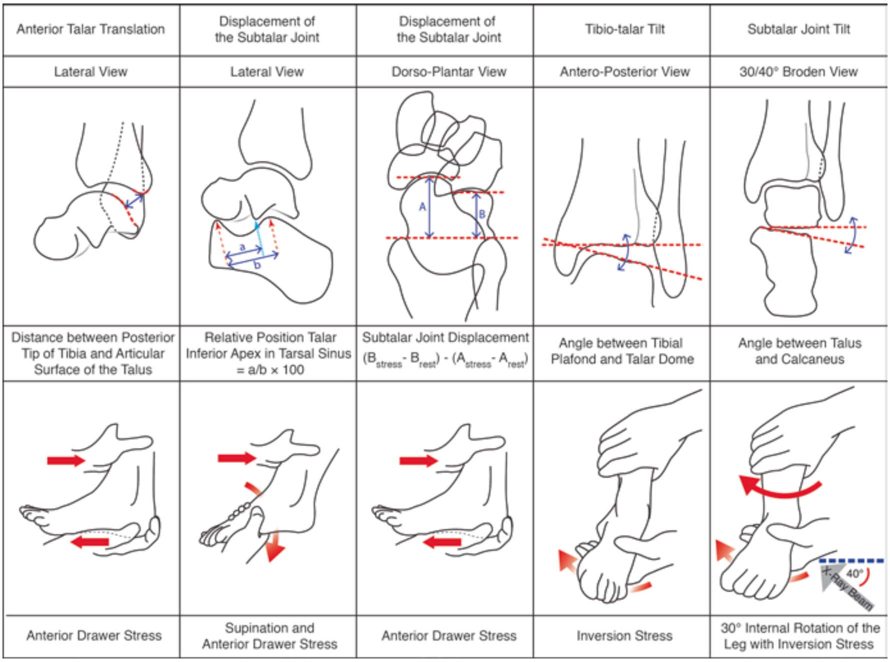

Fig. 13.1 Frequently used measurement methods in conventional radiographs and clinical examination of subtalar joint instability [2]

Our previous review demonstrated that currently used imaging options cannot accurately predict subtalar joint instability [2]. In addition, most of the included studies (imaging and operative) did not differ between ankle and subtalar joint instability. Studies investigating imaging options for chronic subtalar joint instability frequently measured the tilt of the tibiotalar or the talocalcaneal joint on AP stress views of the ankle joint or the anterior translation of the talus in the lateral stress view (Fig. 13.1) [2].

While conventional radiographs are limited in assessing the subtalar joint, weight bearing computed tomography (CT) scans have demonstrated emerging diagnostic applications as they offer an accurate representation of hindfoot joint alignment under weight bearing conditions [22–25]. However, the clinical use of this imaging modality to diagnose subtalar joint instability has yet to be investigated. We hypothesized that isolated subtalar joint instability can accurately be diagnosed when using weight bearing CT scans in a cadaver model.

Methods

Data Source and Specimens

Seven pairs of fresh frozen male cadavers (tibial plateau to toe-tip) were included (mean age 63 ± 5 [range 54–69] years; mean weight 77.2 ± 6.9 [range 68.7–90.7] kg; mean BMI 24.1 ± 1.3 [range 22.2–25.7] kg/m^2). Inclusion criteria were 20 to

70 years of age and a body mass index (BMI) of less than 35 kg/m^2. Only male cadavers were included to ensure a homogeneous cohort. Exclusion criteria were a history of foot and ankle injuries or previous foot and ankle surgery.

Experimental Setting

Each specimen was thawed for 24 hours at room temperature before experimentation [26]. A radiolucent polyoxymethylene (Delrin™) frame held the specimens in a plantigrade position. The frame consisted of a base plate and four pillars located laterally to the foot (Fig. 13.2). To ensure consistent positioning, the cadaver was fixed with an Ilizarov apparatus that fit into the frame (Fig. 13.1). Four 1.5 mm Kirschner wires (K-wires) were drilled through the tibia for fixation to the Ilizarov apparatus. K-wires were tightened using a Dynamometric Wire Tensioner (Smith & Nephew). The hindfoot was fixed using six 1.5 mm K-wires drilled through the calcaneus (Fig. 13.2).

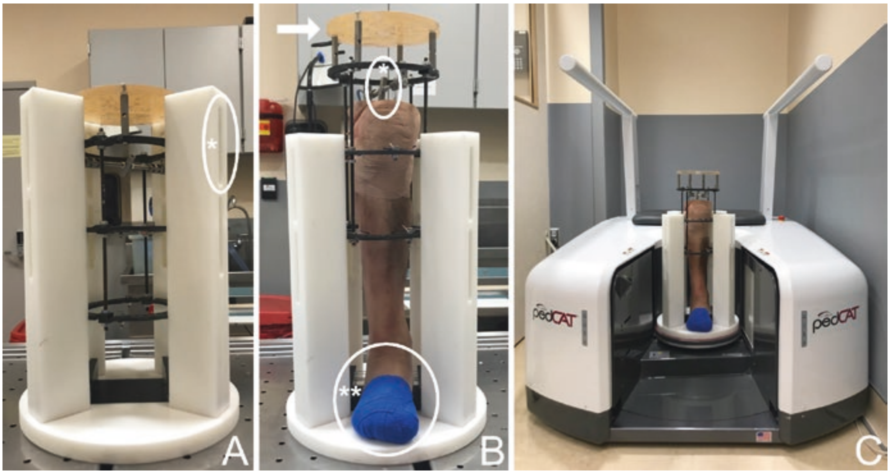

Fig. 13.2 Experimental setting. (**a**) The radiolucent frame (polyoxymethylene, an engineering thermoplastic providing high stiffness, low friction, and dimensional stability – Delrin™) used to hold the Ilizarov apparatus consisted of a base plate and four pillars located lateral to the foot. This allowed the Ilizarov apparatus to rotate in a concentric cylinder when torque was applied. While torque was manually applied, the Ilizarov apparatus was rigidly fixed to the frame through four slots (∗), each accepting a clamp that fastened to the ring in order to maintain the torque over time. (**b**) The tibia was fixed into an Ilizarov apparatus that fits into the frame. A post (∗) was centrally positioned at the proximal end of the Ilizarov to accept a torque wrench. The distal end of the post was placed in the line of the axis of the tibial shaft (at the level of the tibial plateau). Two Kirschner wires (K-wires) were placed on the level of the proximal ring through the tibia (from anteromedial to posterolateral and from medial to lateral). The same fixation holes at the Ilizarov apparatus were used when possible for each experiment. Then, the K-wires on the distal ring were placed similar. Loads were placed on a proximal plate fixed to the Ilizarov apparatus (arrow). The hindfoot was fixed using six 1.5 mm K-wires drilled through the calcaneus using a standardized hole pattern in the side of the retaining box (∗∗). If the tibia was fixed properly to the Ilizarov apparatus, the position of the heel was typically flush to the bottom of the frame. (**c**) The frame fit into the computed tomography (CT) scanner [1]

First, intact ankles (Native) were scanned (pedCAT, CurveBeam LLC, Warrington, USA, medium view, 0.3 mm slice thickness, 0.3 mm slice interval, kVp 120, mAs 22.62, Fig. 13.2). Second, one specimen from each pair underwent ITCL transection, while the contralateral underwent CFL transection (Fig. 13.3). Third, the lesions were reversed on the same specimens, and the remaining ITCL or CFL was transected (Fig. 13.3). Finally, the deltoid ligament (superficial and deep) was

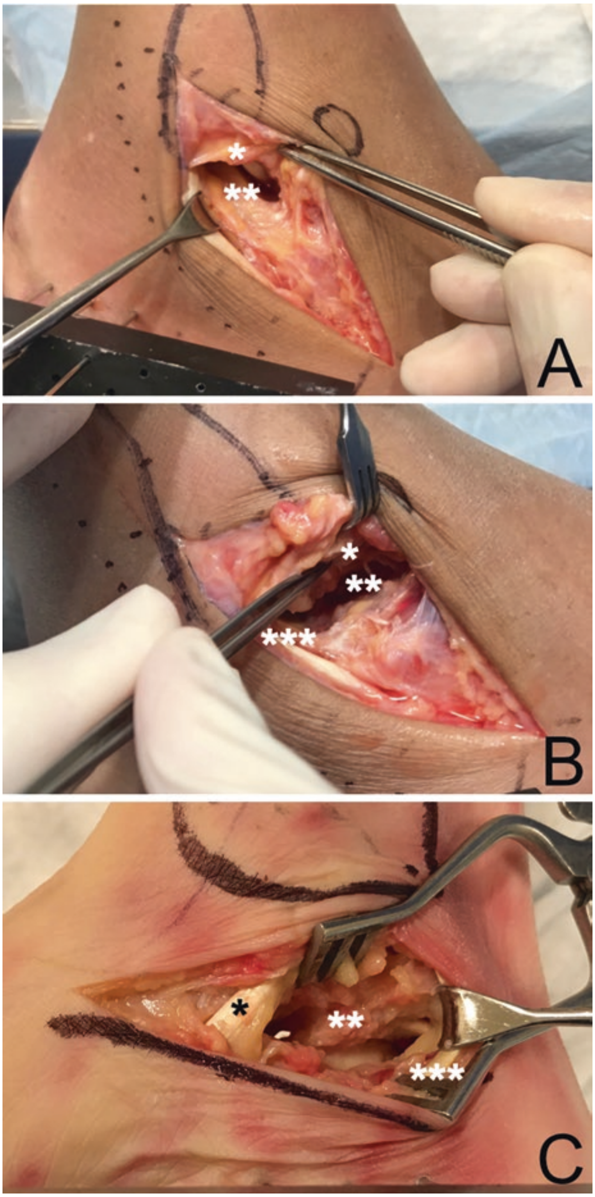

Fig. 13.3 Transection of the ligaments providing stability to the subtalar joint. (**a**) Transected calcaneofibular ligament (CFL, ∗); posterior facet of the subtalar joint (∗∗). (**b**) Additional transection of the interosseous calcaneofibular ligament (ITCL); talus (∗); sinus tarsi showing the transected ITCL (∗∗); posterior facet of the subtalar joint (∗∗∗). A lamina spreader was used to ensure good visualization of the sinus tarsi (including the medial aspect). (**c**) Transection of the deltoid ligament; tibialis posterior tendon (∗); transected deltoid ligament (∗∗); flexor digitorum longus tendon (∗∗∗) [1]

transected in all ankles (Fig. 13.3). While transection of either the ITCL or CFL mimic incomplete injuries, transection of both or all three ligaments mimic more complete injuries.

Non-weight bearing and weight bearing (85 kg; determined from the average of specimen donor anthropometrics) CT scans with and without application of 10 Newton meter (Nm) internal torque applied at the Ilizarov apparatus (corresponding to external torque of the foot and ankle) were collected [27]. Ten Nm torque was chosen for consistency with cadaver studies testing the stability of the distal tibial syndesmosis [27, 28]. Preconditioning of the specimen was performed by consistent loading of the frame with 42.5 kg and 85 kg for 2 minutes each before experimentation.

Imaging and Measurements

Digitally reconstructed radiographs (DRRs) were automatically created using the CT scan dataset (CurveBeam LLC, Warrington, USA). The anteroposterior (AP) view of the ankle joint was generated perpendicular to a line connecting the center of the calcaneus (midway between the medial and lateral process of the tuber calcanei) and the second metatarsal base on a dorsoplantar (DP) view [29]. By virtually externally rotating the foot 90 degrees, a lateral view was generated. Additionally, a 30/40-degree Broden view was reconstructed (30 degrees internal rotation and 40 degrees upward tilt of the foot) [19]. The TT and ATT were measured on the AP and the lateral view, while the STT was assessed on the 30/40-degree Broden view [2, 4, 19–21]. TT and ATT measurements were performed to additionally evaluate the effect of ligament transection (CFL and deltoid ligament) on ankle joint congruency.

Single CT images underwent a similar reconstruction. The same longitudinal axis of the foot used to reconstruct DRRs was created. Based on the longitudinal axis, a sagittal plane was reconstructed. On this plane, the ATT was measured (Fig. 13.4). The TT was measured on a plane perpendicular to the sagittal plane

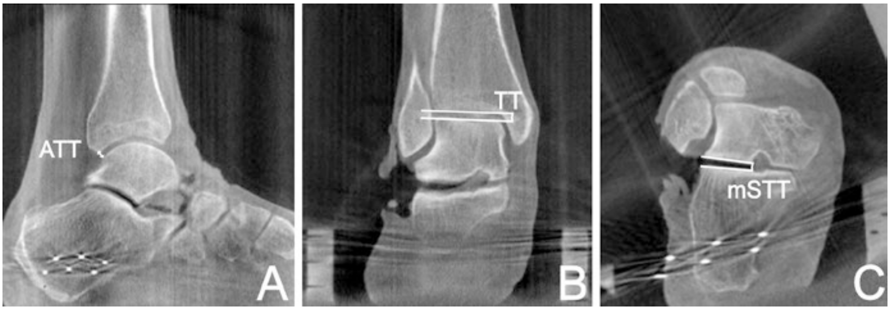

Fig. 13.4 Measurements performed on single computed tomography (CT) images (discrete calcaneofibular ligament [CFL] dissection). (**a**) Lateral view showing the measurement of the anterior talar translation (ATT). (**b**) Anteroposterior (AP) view showing the measurement of the tibiotalar tilt (TT). (**c**) 30/40-degree Broden view (middle plain) showing the measurement of the subtalar tilt (STT) [1]

(Fig. 13.4). The Broden view was reconstructed out of the AP view by 30° internal rotation and 40° upward tilting of the foot to measure the STT (Fig. 13.4). Because of the screw-shaped anatomy of the posterior facet of the subtalar joint, three different planes were reconstructed: a middle plane reflecting the middle of the posterior facet (defined on the initially reconstructed sagittal plane by identifying the anterior and posterior border of the articular surface of the posterior facet of the calcaneus), an anterior plane (5 mm anterior to the middle plane), and a posterior plane (5 mm posterior to the middle plane) [29, 30]. A similar reconstruction was used in previous studies investigating the configuration of the subtalar joint [29, 30].

Statistical Analysis

Intraclass correlation (ICC) was used to quantify the agreement of measurements between and within observers. Estimates and 95% confidence intervals (CI) were calculated for each type of measurement within each view. Interobserver agreement was modeled with a two-way random effect model of absolute agreement with a single measurement per observation. Intraobserver agreement was modeled with a two-way mixed effect model of consistency with a single measurement per observation. Agreement was rated as very good with an ICC > 0.80; good with an ICC = 0.61–0.80; moderate with an ICC = 0.41–0.60; fair with an ICC = 0.21–0.40; and poor with an ICC < 0.20 [31]. Measurements for interobserver agreement calculation were done by a fellowship trained orthopedic surgeon and a research analyst. For calculation of the intraobserver agreement, measurements were performed two times with an interval of 3 weeks by a fellowship trained orthopedic surgeon.

Linear mixed effect models were fit for responses. Within DRR and CT measurements, separate models were fit for each measurement (TT, ATT, and STT) and, for DRR measurements, within each view. Cadaver, a random effect, foot (left or right), and a fixed effect were included in all models in addition to the variables presented. Models were fit for subsets of the data, and estimates and 95% CI were given for differences in measurements in different levels of a specific variable. For each model, only the differences in response that were associated with either different load application, different torques, or different conditions were calculated; the data was subset by the other two variables, and they remained constant within each model. The first set of models compared the differences in response for full versus non-weight bearing with no torque applied (condition constant within each model). The second set compared the differences in response to 10 Nm versus 0 Nm of torque applied with full weight bearing load (condition constant within each model). The last set compared the differences between Conditions 1 through 3 and the native ankles, with full weight bearing load (torque constant within each model). Coefficients and 95% confidence intervals were reported, and statistical significance (marked by an asterisk in all tables and graphs) was determined based on a *P* value less than 0.05. All calculations were done in R 3.4.1, specifically using packages psych and lmerTest.

Results

Digitally Reconstructed Radiographs

Inter- and intraobserver agreement for measurements made on DRRs were rated as fair for the TT, good for the ATT (interobserver agreement), very good for the intraobserver agreement of the ATT, and very good for both the inter- and intraobserver agreement for the STT (Table 13.1). Load application (without torque) had no influence on the majority of measurements independent of the tested condition (Table 13.2).

Table 13.1 Reliability of digitally reconstructed radiographs measurements assessed by intraclass correlation (ICC) [1]

Measurement	Interobserver: ICC(2,1) estimate (95% CI)	Intraobserver: ICC(3,1) estimate (95% CI)
TT	0.22	0.29
	(−0.07, 0.50)	(−0.06, 0.58)
ATT	0.75*	0.88*
	(0.55, 0.87)	(0.78, 0.94)
STT	0.88*	0.97*
	(0.70, 0.95)	(0.93, 0.98)

DRR digitally reconstructed radiograph, *CI* confidence interval, *TT* talar tilt, *ATT* anterior talar translation, *STT* subtalar tilt
*Indicates ICC ≥ 0.61

Table 13.2 Mean difference for each condition with and without load application (no torque) [1]

		Native	Condition 1A	Condition 1B	Condition 2	Condition 3
		Estimate (95% CI)				
DRR	TT (degrees)	0.03	−0.18	−0.18	**−0.25***	**−0.20***
		(−0.13, 0.19)	(−0.54, 0.17)	(−0.36, 0.00)	**(−0.42, −0.08)**	**(−0.37, −0.03)**
	ATT (mm)	**−0.23***	−0.16	−0.03	**−0.19***	−0.11
		(−0.38, −0.08)	(−0.32, 0.00)	(−0.26, 0.20)	**(−0.37, 0.00)**	(−0.30, 0.08)
	STT (degrees)	0.01	0.10	−0.08	−0.15	0.08
		(−0.44, 0.47)	(−0.31, 0.51)	(−0.32, 0.16)	(−0.50, 0.20)	(−0.20, 0.36)
CT	TT (degrees)	−0.03	**−0.22***	−0.04	−0.16	−0.08
		(−0.17, 0.11)	**(−0.40, −0.04)**	(−0.23, 0.15)	(−0.41, 0.10)	(−0.23, 0.08)
	ATT (mm)	−0.17	−0.07	0.03	−0.18	−0.09
		(−0.45, 0.11)	(−0.94, 0.80)	(−0.43, 0.49)	(−0.58, 0.22)	(−0.44, 0.26)
	aSTT (degrees)	−0.02	−0.12	−0.04	−0.08	−0.06
		(−0.24, 0.21)	(−0.26, 0.03)	(−0.21, 0.13)	(−0.30, 0.14)	(−0.20, 0.08)
	mSTT (degrees)	0.11	0.12	−0.04	0.05	−0.01
		(−0.07, 0.28)	(−0.05, 0.28)	(−0.26, 0.18)	(−0.10, 0.21)	(−0.20, 0.19)
	pSTT (degrees)	0.17	−0.04	0.14	0.07	0.05
		(−0.29, 0.63)	(−0.72, 0.63)	(−0.22, 0.49)	(−0.31, 0.46)	(−0.32, 0.42)

DRR digitally reconstructed radiograph, *CT* computed tomography, *TT* talar tilt, *ATT* anterior talar translation, *STT* subtalar tilt, *a* “anterior” plane, *m* “middle” plane, *p* “posterior” plane
*Indicates statistical significance ($P < 0.05$)

Table 13.3 Mean difference for each condition with and without torque application (no load) [1]

		Native	Condition 1A	Condition 1B	Condition 2	Condition 3
		Estimate (95% CI)				
DRR	TT (degrees)	**0.72***	**0.40***	**0.54***	**0.83***	**0.32***
		(0.24, 1.21)	**(0.07, 0.74)**	**(0.22, 0.85)**	**(0.46, 1.20)**	**(0.15, 0.49)**
	ATT (mm)	**1.46***	0.20	**2.03***	**2.92***	**0.23***
		(0.54, 2.39)	(−0.02, 0.42)	**(1.44, 2.61)**	**(1.94, 3.91)**	**(0.04, 0.43)**
	STT (degrees)	**2.67***	0.10	**3.06***	**3.99***	0.11
		(0.96, 4.38)	(−0.31, 0.51)	**(1.98, 4.14)**	**(2.47, 5.51)**	(−0.27, 0.50)
CT	TT (degrees)	**1.76***	0.12	**2.58***	**3.46***	**0.32***
		(1.05, 2.48)	(−0.12, 0.36)	**(1.91, 3.24)**	**(2.44, 4.48)**	**(0.15, 0.49)**
	ATT (mm)	**2.96***	0.81	**3.74***	**4.64***	**0.86***
		(1.27, 4.64)	(−0.02, 1.65)	**(2.54, 4.93)**	**(2.89, 6.38)**	**(0.45, 1.28)**
	aSTT (degrees)	0.63	**0.36***	**0.83***	**1.10***	**0.37***
		(−0.05, 1.30)	**(0.01, 0.71)**	**(0.46, 1.20)**	**(0.46, 1.73)**	**(0.10, 0.64)**
	mSTT (degrees)	**1.79***	**0.21***	**2.12***	**3.01***	0.18
		(0.83, 2.74)	**(0.07, 0.35)**	**(1.55, 2.68)**	**(2.22, 3.80)**	(−0.10, 0.46)
	pSTT (degrees)	**2.63***	0.33	**3.04***	**3.45***	0.26
		(0.53, 4.73)	(−0.10, 0.76)	**(2.06, 4.02)**	**(2.03, 4.87)**	(−0.14, 0.65)

DRR digitally reconstructed radiograph, *CT* computed tomography, *TT* talar tilt, *ATT* anterior talar translation, *STT* subtalar tilt, *a* “anterior” plane, *m* “middle” plane, *p* “posterior” plane
*Indicates statistical significance ($P < 0.05$)

Torque application (without load) showed a significant impact on almost every measurement within each condition with the exception of a discrete ITCL transection (Table 13.3). If torque and axial load were applied, significant differences were evident for native ankles compared to the no axial load condition as well for discrete CFL transection and a combined ITCL and CFL transection, but not after discrete transection of the ITFL or after a combined transection of the ITFL, CFL, and deltoid ligament (Table 13.4). The TT was not a useful predictor to identify incomplete or more complete injuries when compared to native ankles (including torque, independent of load application). The ATT was useful to predict a combined ITCL and CFL transection when torque (without load) was applied (Fig. 13.5). The STT was useful for identifying discrete injury to the ITCL or a combined ITCL, CFL, and deltoid ligament injury (no weight bearing, torque conditions) when compared to native ankles.

Computed Tomography Scans

Inter-and intraobserver agreement for measurements performed on single CT scans images were rated as moderate and fair, respectively, for the TT (Table 13.5). The ATT was rated as good for interobserver and very good for intraobserver agreement. The other measurements showed very good agreement. Load and torque application had a similar effect on measurements compared to DRRs. Load application (without torque) had no impact on measurements, independent of the tested condition (Table 13.2). Torque application (without load) showed a significant impact within each condition on almost every measurement except for STT measurements following discrete ITCL and combined ITCL, CFL, and deltoid ligament transection (Table 13.3). If torque and weight were applied, significant differences were evident within native ankles, discrete CFL transection, and combined ITCL and CFL transection, but not after discrete transection of the ITFL or after transection of the ITFL, CFL, and deltoid ligament (Table 13.4). The TT predicted a discrete injury to the ITCL, a combined ITCL and CFL injury, or a combined injury to the ITCL, CFL, and deltoid ligament (including torque, no load application, Fig. 13.6). The ATT was not a useful predictor for any of the tested conditions when compared to native ankles (including torque, independent if load was applied, Fig. 13.6). The mSTT was useful to identify a discrete injury to the ITCL, a combined ITCL and CFL, or a combined ITCL, CFL, and deltoid ligament injury (no weight bearing, torque conditions, Fig. 13.7) when compared to native ankles.

Table 13.4 Mean difference for each condition with and without torque application (load applied) [1]

		Native	Condition 1A	Condition 1B	Condition 2	Condition 3
		Estimate (95% CI; mm)				
DRR	TT (degrees)	**0.25***	0.25	0.24	**0.31***	**0.30***
		(0.08, 0.42)	(−0.17, 0.66)	(0.00, 0.48)	**(0.04, 0.59)**	**(0.10, 0.51)**
	ATT (mm)	**0.53***	**0.19***	**0.43***	**1.06***	0.05
		(0.28, 0.78)	**(0.02, 0.35)**	**(0.12, 0.74)**	**(0.45, 1.68)**	(−0.14, 0.24)
	STT (degrees)	**0.74***	0.34	**0.93***	**1.47***	0.31
		(0.18, 1.31)	(−0.36, 1.05)	**(0.44, 1.42)**	**(0.42, 2.52)**	(−0.04, 0.66)
CT	TT (degrees)	0.19	0.13	**0.77***	**1.41***	0.09
		(−0.13, 0.50)	(−0.01, 0.26)	**(0.45, 1.10)**	**(0.57, 2.25)**	(−0.08, 0.26)
	ATT (mm)	0.61	0.07	**1.44***	**2.16***	0.23
		(−0.02, 1.25)	(−0.53, 0.67)	**(0.82, 2.05)**	**(0.58, 3.74)**	(−0.28, 0.74)
	aSTT (degrees)	**−0.33***	0.02	−0.08	0.23	−0.07
		(−0.62, −0.04)	(−0.27, 0.31)	(−0.32, 0.16)	(−0.13, 0.60)	(−0.25, 0.12)
	mSTT (degrees)	0.18	0.10	**0.39***	**0.97***	0.06
		(−0.07, 0.43)	(−0.12, 0.32)	**(0.07, 0.71)**	**(0.34, 1.60)**	(−0.10, 0.22)
	pSTT (degrees)	0.17	0.24	0.52	**1.14***	0.17
		(−0.36, 0.71)	(−0.28, 0.77)	(−0.03, 1.07)	**(0.06, 2.21)**	(−0.20, 0.54)

DRR digitally reconstructed radiograph, *CT* computed tomography, *TT* talar tilt, *ATT* anterior talar translation, *STT* subtalar tilt, *a* "anterior" plane, *m* "middle" plane, *p* "posterior" plane
*Indicates statistical significance ($P < 0.05$)

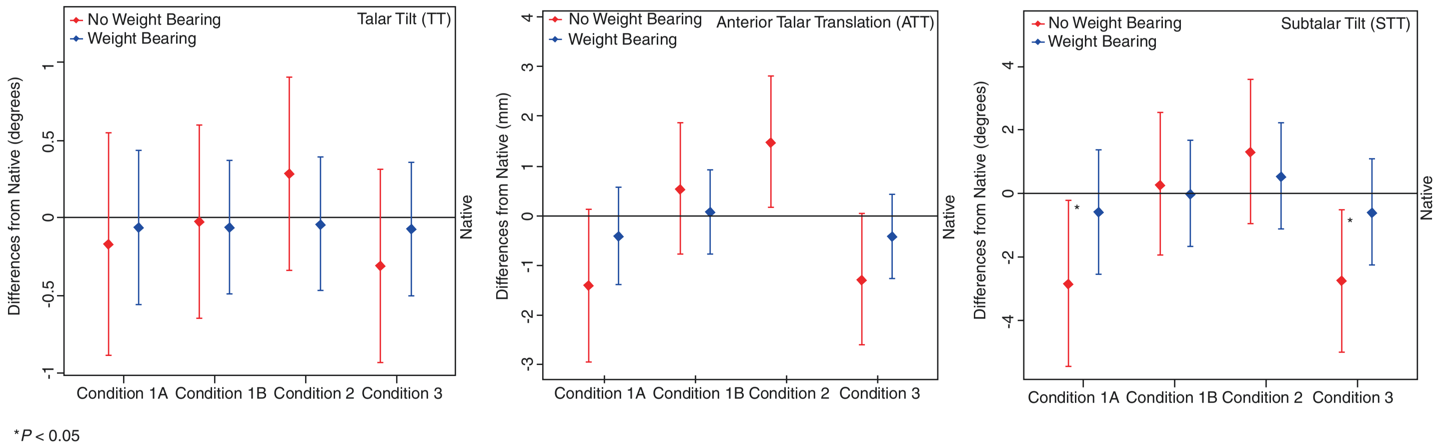

Fig. 13.5 Measurements in different test conditions using digitally reconstructed radiographs (DRRs). The talar tilt (TT) was not a useful predictor to identify an injury to the ligaments stabilizing the subtalar joint, while the anterior talar translation (ATT) identified cadavers with a combined transection of the interosseous talocalcaneal ligament (ITCL) and calcaneofibular ligament (CFL) (no weight, torque applied, ∗). The subtalar tilt (STT) was able to identify cadavers with an isolated transection of the ITFL and transection of the ITCL, CFL, and deltoid ligament (DL; no weight, torque applied, ∗) [1]

Table 13.5 Reliability of CT measurements (AP view) assessed by intraclass correlation ICC [1]

Measurement	Interobserver: ICC(2,1) Estimate (95% CI)	Intraobserver: ICC(3,1) Estimate (95% CI)
TT	0.56	0.25
	(0.14, 0.79)	(−0.11, 0.54)
ATT	0.75∗	0.83∗
	(0.55, 0.87)	(0.67, 0.91)
aSTT	0.94∗	0.98∗
	(0.71, 0.98)	(0.97, 0.99)
mSTT	0.92∗	0.95∗
	(0.84, 0.96)	(0.89, 0.97)
pSTT	0.92∗	0.98∗
	(0.68, 0.97)	(0.96, 0.99)

CT computed tomography, *CI* confidence interval, *TT* talar tilt, *ATT* anterior talar translation, *STT* subtalar tilt, *a* “anterior” plane, *m* “middle” plane, *p* “posterior” plane
∗Indicates ICC ≥ 0.61

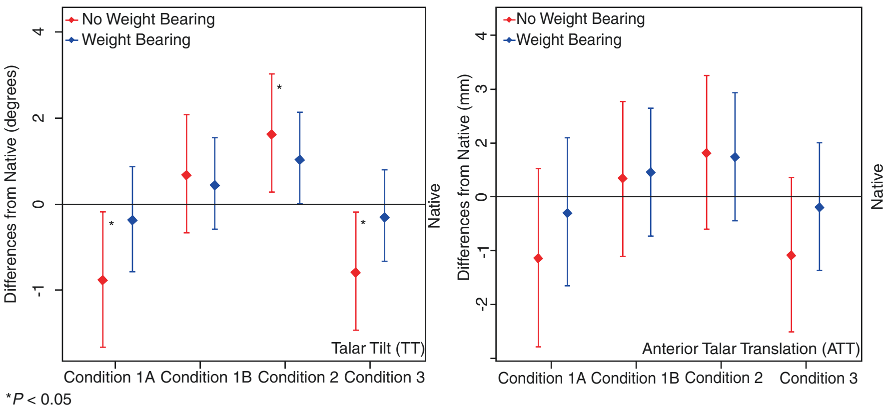

Fig. 13.6 Measurements in different test conditions using single weight bearing computed tomography (CT) images. The talar tilt (TT) was a useful predictor to identify an isolated injury to the interosseous talocalcaneal ligament (ITCL), combined ITCL and calcaneofibular ligament (CFL) injury, and an additional injury to the deltoid ligament (DL; no weight, torque applied, ∗). The anterior talar translation (ATT) was not a useful predictor for subtalar joint instability [1]

Discussion

This cadaver study investigated whether weight bearing CT scans can be used to diagnose subtalar joint instability. The three most relevant findings were (I) Torque is crucial when using weight bearing CT scans to diagnose subtalar joint instability; (II) axial load application decreases the observers’ ability to diagnose instability to the subtalar joint when using 2D measurements on DRRs or single CT images; and (III) radiographic measurements at the level of the subtalar joint are more reliable predictors for subtalar joint instability than measurements at the ankle joint level.

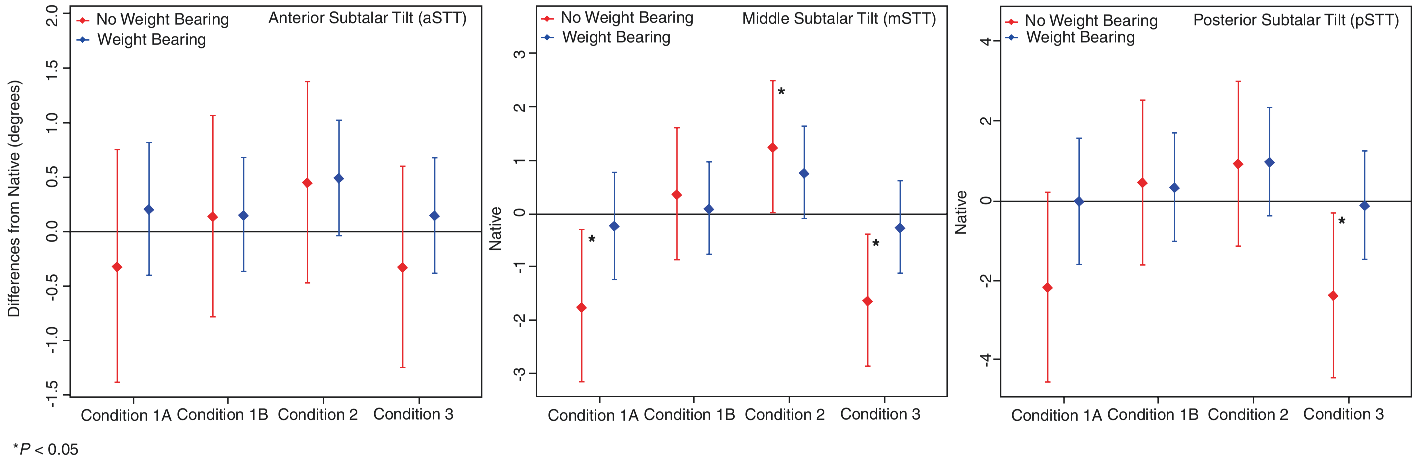

Fig. 13.7 Measurements in different test conditions using single weight bearing computed tomography (CT) images. When using the subtalar tilt (STT), the middle plain of the posterior facet of the subtalar joint was the most useful plain for identification of injuries to the ligaments providing stability to the subtalar joint. The STT was able to identify cadavers with an isolated transection of the talocalcaneal ligament (ITCL), combined transection of the ITCL and calcaneo-fibular ligament (CFL), and cadavers with an additional deltoid ligament (DL) injury (no weight, torque applied, ∗) [1]

Axial loading showed no impact on most 2D measurements performed on either DRRs or single CT images. Axial load alone may not allow the talocalcaneal joint to subluxate after transection of the ligamentous stabilizers, likely due to mechanical constraint from engagement of articular congruity. In contrast, torque application was helpful for exposing subtalar joint instability when using weight bearing CT scans. Radiographic measurements at the subtalar joint level in the coronal plane showed significant differences when torque was applied. Interestingly, the lateral opening of the subtalar joint (assessed by STT) decreased compared to native ankles when only the ITCL was transected. Medial opening of the subtalar joint occurs after releasing the ITCL, leading to more parallel calcaneal and talar joint surfaces when applying torque. This finding agrees with earlier anatomic studies, which showed that the bulk of the ITCL fibers is located at the anteromedial aspect of the sinus tarsi [6, 9].

In contrast, the CFL prevented extensive lateral opening of the subtalar joint compared to native ankles when torque was applied. In the case of a combined ITCL and CFL transection, lateral opening increased. The deltoid ligament appears to act as a pivot point when torque is applied in a combined ITCL and CFL injury. Indeed, removal of the deltoid by additional transection led to a medial opening of the subtalar joint (including torque), decreasing STT measurements relative to native ankles (i.e., more parallel joint surfaces). This may explain why torque had minimal impact on STT measurements after discrete ITCL or combined ITCL, CFL, and deltoid ligament transection. Generally, the difference in measurements between the tested conditions was rather small. Although statistically significant, it is questionable if such minute differences impact decision-making in daily practice. Of note, stress application only included internal torque to the tibia. Stress distribution on the ligamentous stabilizers of the subtalar joint differ between internal or external torque to the tibia. Therefore, our experimental setting is limited to identifying the most important ligamentous stabilizer of the subtalar joint.

Although axial load application negatively impacts the assessment of subtalar joint instability, weight bearing CT scans standardize the positioning of the foot during imaging. Little is known about the influence of the position of the ankle joint (e.g., dorsal-extension, plantar-flexion) on the investigated radiographic measurements. Additionally, weight bearing CTs allow for reliable reconstruction of various views (e.g., Broden view, lateral view, etc.). This is not the case for conventional radiographs or fluoroscopy. Also, weight bearing CTs allow reconstruction of DRRs and single CT images at the same time, minimizing radiation. Capturing both modalities is especially important in foot and ankle surgery as corrective osteotomies and arthrodesis are common procedures. Therefore, the possibility to simultaneously assess the alignment reliably (e.g., using DRRs) and analyze joint surfaces (e.g., using single CT images) may be beneficial.

The agreement of measurements varied between DRRs and single CT scans. Generally, the TT should not be performed on DRRs or single CT images because of insufficient inter- and intraobserver agreement. The poor reliability for TT measurements may explain why an isolated ITCL transection significantly impacted measurements. The agreement of ATT measurements was slightly higher compared to TT measurements, especially if assessed by an experienced observer. In contrast, measurements at the level of the subtalar joint are reliably performed on DRRs and single CT images, independent of the experience of the observer (very good inter- and intraobserver agreement). STT measurements performed on the middle plane of the subtalar joint (30/40-degree Broden view, single CT images) have shown to be the best predictors for subtalar joint instability in this study. Of note, studies have shown that the projected shape (convex vs. flat vs. concave) and configuration (varus vs. valgus) of the posterior facet of the subtalar joint on DRRs are highly dependent on ankle rotation [24, 32]. In addition, studies using weight bearing CT scans have shown that shape and configuration also differ between individuals [33]. Consequently, minimal errors during reconstruction may impact 2D measurements. Also, the individual osseous shape and configuration may impact intrinsic stability of the subtalar joint.

This study has several limitations. First, patients may have more complex injuries including tears of multiple ligaments and tendons on the lateral and/ or medial side of the subtalar joint. Also, scar tissue may have formed over time. These complex injuries are difficult to mimic using a cadaver model but may impact radiographic measurements. Second, only injury to the most important ligaments providing stability to the subtalar joint was simulated. Transection of less important ligaments (e.g., cervical ligament, extensor retinaculum) or partial ligaments (e.g., tibiocalcaneal portion of the superficial deltoid) may influence radiographic measurements. Third, experimental fixation of the calcaneus using K-wires cannot be performed on living patients. Noninvasive heel clamps and forefoot straps may be more appropriate. If the calcaneus cannot be properly fixed, shifting of the foot and base plate may be possible when torque is applied without load. This may negatively impact the radiographic measurements used in this study because the subtalar joint cannot subluxate when the calcaneus is not properly fixed. In addition, our experimental setting limited antero-posterior/mediolateral translation at the level of the subtalar joint. This potentially impacted measurements performed under weight bearing conditions. Fourth, only 2D measurements have been assessed. Although the used measurements reflect the most commonly performed measurements in daily practice, three-dimensional (3D) measurements may be more accurate for assessment of such a complex joint.

To conclude, weight application negatively impacts the assessment of subtalar joint instability, while torque application exposes instability. Future clinical studies to identify subtalar joint instability using weight bearing CT technology may face substantial technical challenges in assessment of hindfoot instability if the loading conditions are not carefully titrated.

References

1. Krähenbühl N, Burssens A, Davidson NP, Allen CM, Henninger HB, Saltzman CL, Barg A. Can weight bearing computed tomography scans be used to diagnose subtalar joint instability? A cadaver study. J Orthop Res. 2019, epub ahead of print.
2. Krähenbühl N, Weinberg MW, Davidson NP, Mills MK, Hintermann B, Saltzman CL, Barg A. Currently used imaging options cannot accurately predict subtalar joint instability. Knee Surg Sports Traumatol Arthrosc. 2018;27(9):2818–30, epub ahead of print.

3. Tourne Y, Besse JL, Mabit C, Sofcot. Chronic ankle instability. Which tests to assess the lesions? Which therapeutic options? Orthop Traumatol Surg Res. 2010;96(4):433–46.
4. Lee BH, Choi KH, Seo DY, Choi SM, Kim GL. Diagnostic validity of alternative manual stress radiographic technique detecting subtalar instability with concomitant ankle instability. Knee Surg Sports Traumatol Arthrosc. 2016;24(4):1029–39.
5. Choisne J, Hoch MC, Bawab S, Alexander I, Ringleb SI. The effects of a semi-rigid ankle brace on a simulated isolated subtalar joint instability. J Orthop Res. 2013;31(12):1869–75.
6. Harper MC. The lateral ligamentous support of the subtalar joint. Foot Ankle. 1991;11(6):354–8.
7. Weindel S, Schmidt R, Rammelt S, Claes L, v Campe A, Rein S. Subtalar instability: a biomechanical cadaver study. Arch Orthop Trauma Surg. 2010;130(3):313–9.
8. Pellegrini MJ, Glisson RR, Wurm M, Ousema PH, Romash MM, Nunley JA 2nd, Easley ME. Systematic quantification of stabilizing effects of subtalar joint soft-tissue constraints in a novel cadaveric model. J Bone Joint Surg Am. 2016;98(10):842–8.
9. Jotoku T, Kinoshita M, Okuda R, Abe M. Anatomy of ligamentous structures in the tarsal sinus and canal. Foot Ankle Int. 2006;27(7):533–8.
10. Ringleb SI, Dhakal A, Anderson CD, Bawab S, Paranjape R. Effects of lateral ligament sectioning on the stability of the ankle and subtalar joint. J Orthop Res. 2011;29(10):1459–64.
11. Crim JR, Beals TC, Nickisch F, Schannen A, Saltzman CL. Deltoid ligament abnormalities in chronic lateral ankle instability. Foot Ankle Int. 2011;32(9):873–8.
12. Barg A, Weinberg MW, Burssens A, Saltzman CL, Krähenbühl N. Subtalar instability: diagnosis and treatment. Fuss Sprungg. 2018;4(4):253–63.
13. Hintermann B, Knupp M, Barg A. Peritalar instability. Foot Ankle Int. 2012;33(5):450–4.
14. Valderrabano V, Hintermann B, Horisberger M, Fung TS. Ligamentous posttraumatic ankle osteoarthritis. Am J Sports Med. 2006;34(4):612–20.
15. Krähenbühl N, Horn-Lang T, Hintermann B, Knupp M. The subtalar joint: a complex mechanism. EFORT Open Rev. 2017;2(7):309–16.
16. Heilman AE, Braly WG, Bishop JO, Noble PC, Tullos HS. An anatomic study of subtalar instability. Foot Ankle. 1990;10(4):224–8.
17. Harper MC. Stress radiographs in the diagnosis of lateral instability of the ankle and hindfoot. Foot Ankle. 1992;13(8):435–8.
18. Kato T. The diagnosis and treatment of instability of the subtalar joint. J Bone Joint Surg Br. 1995;77(3):400–6.
19. Louwerens JW, Ginai AZ, van Linge B, Snijders CJ. Stress radiography of the talocrural and subtalar joints. Foot Ankle Int. 1995;16(3):148–55.
20. van Hellemondt FJ, Louwerens JW, Sijbrandij ES, van Gils AP. Stress radiography and stress examination of the talocrural and subtalar joint on helical computed tomography. Foot Ankle Int. 1997;18(8):482–8.
21. Sijbrandij ES, van Gils AP, van Hellemondt FJ, Louwerens JW, de Lange EE. Assessing the subtalar joint: the Broden view revisited. Foot Ankle Int. 2001;22(4):329–34.
22. Barg A, Bailey T, Richter M, de Cesar Netto C, Lintz F, Burssens A, Phisitkul P, Hanrahan CJ, Saltzman CL. Weightbearing computed tomography of the foot and ankle: emerging technology topical review. Foot Ankle Int. 2018;39(3):376–86.
23. Lintz F, de Cesar Netto C, Barg A, Burssens A, Richter M, Weight Bearing CT International Study Group. Weight-bearing cone beam CT scans in the foot and ankle. EFORT Open Rev. 2018;3(5):278–86.
24. Krähenbühl N, Lenz AL, Lisonbee R, Deforth M, Zwicky L, Hintermann B, Saltzman CL, Anderson AE, Barg A. Imaging of the subtalar joint: a novel approach to an old problem. J Orthop Res. 2019;37(4):921–6.
25. Kleipool RP, Dahmen J, Vuurberg G, Oostra RJ, Blankevoort L, Knupp M, Stufkens SAS. Study on the three-dimensional orientation of the posterior facet of the subtalar joint using simulated weight-bearing CT. J Orthop Res. 2019;37(1):197–204.
26. Barg A, Amendola RL, Henninger HB, Kapron AL, Saltzman CL, Anderson AE. Influence of ankle position and radiographic projection angle on measurement of supramalleolar alignment on the anteroposterior and hindfoot alignment views. Foot Ankle Int. 2015;36(11):1352–61.

27. Clanton TO, Williams BT, Backus JD, Dornan GJ, Liechti DJ, Whitlow SR, Saroki AJ, Turnbull TL, LaPrade RF. Biomechanical analysis of the individual ligament contributions to syndesmotic stability. Foot Ankle Int. 2017;38(1):66–75.
28. Krähenbühl N, Bailey TL, Weinberg MW, Davidson NP, Hintermann B, Presson AP, Allen CM, Henninger HB, Saltzman CL, Barg A. Impact of torque on assessment of syndesmotic injuries using weightbearing computed tomography scans. Foot Ankle Int. 2019;40(6):710–9.
29. Krähenbühl N, Siegler L, Deforth M, Zwicky L, Hintermann B, Knupp M. Subtalar joint alignment in ankle osteoarthritis. Foot Ankle Surg. 2019;25(2):143–9.
30. Krähenbühl N, Tschuck M, Bolliger L, Hintermann B, Knupp M. Orientation of the subtalar joint: measurement and reliability using weightbearing CT scans. Foot Ankle Int. 2016;37(1):109–14.
31. Yeung TW, Chan CY, Chan WC, Yeung YN, Yuen MK. Can pre-operative axial CT imaging predict syndesmosis instability in patients sustaining ankle fractures? Seven years' experience in a tertiary trauma center. Skelet Radiol. 2015;44(6):823–9.
32. Lenz AL, Krähenbühl N, Howell K, Lisonbee R, Hintermann B, Saltzman CL, Barg A. Influence of the ankle position and X-ray beam angulation on the projection of the posterior facet of the subtalar joint. Skelet Radiol. 2019;48(10):1581–9, epub ahead of print.
33. Colin F, Horn Lang T, Zwicky L, Hintermann B, Knupp M. Subtalar joint configuration on weightbearing CT scan. Foot Ankle Int. 2014;35(10):1057–62.

Chapter 14
Is Torque Application Necessary When Using Computed Tomography Scans to Diagnose Syndesmotic Injuries? A Cadaver Study

Alexej Barg

Introduction

Accurate identification of distal tibiofibular syndesmosis injuries is difficult, especially in the absence of frank bony diastasis [1–4]. Literature suggests that missed injuries may lead to chronic pain and early degeneration of tibiotalar articulation [5, 6]. Currently, the initial diagnosis of syndesmotic disruption is based off several radiographic parameters [2]. Measurement of the medial clear space (MCS), tibiofibular clear space (TFCS), and the tibiofibular overlap (TFO) on external stress ankle radiography has high specificity yet low sensitivity [2, 7]. Magnetic resonance imaging (MRI) has also been shown to aid in diagnosis; however, this non-weight bearing modality fails to illustrate the dynamic relationship between the tibia and fibula when load and torque are applied to the ankle [2, 8–10].

The anatomical relationship within the distal tibiofibular syndesmosis is highly complex and relies on four main ligaments to maintain congruity: the anterior-inferior tibiofibular ligament (AITFL), interosseous membrane (IOM), posterior inferior tibiofibular ligament (PITFL), and transverse tibiofibular ligament (TTFL) [11]. Additionally, medial ankle support via the deltoid ligament is thought to play a pivotal role [12]. The entire complex is subject to acute and chronic structural changes from repeated stresses seen during daily ambulation or secondary to acute injury [13]. An appropriate understanding of how these structures interact and react under stress is essential to our understanding of pathology.

First described in 1998, cone beam computed tomography (CT) utilization has steadily increased since its introduction in the orthopedic literature in 2013 [14, 15]. Weight bearing CT offers a precise representation of bony architecture under physiologic loads as well as the resultant change in biomechanics incurred during injury [16]. The purpose of this cadaver study was to assess whether weight bearing CT scans

Based on Krähenbühl N, Bailey TL, Presson AP, Allen CM, Henninger HB, Saltzman CL, Barg A. Torque application helps to diagnose incomplete syndesmotic injuries using weight-bearing computed tomography images. *Skeletal Radiol* 2019; 48(9): 1367–76.

M. Richter et al., *Weight Bearing Cone Beam Computed Tomography (WBCT) in the Foot and Ankle*, https://doi.org/10.1007/978-3-030-31949-6_14

can be used to identify subtle and also more severe injuries to the distal tibiofibular syndesmosis using three commonly used measurement options.

Methods

Data Source

Ten different male cadavers (tibia plateau to toe-tip; seven left, three right) were included (mean age 63 ± 9 [range 47–70] years; mean weight 83.1 ± 13.5 [range 63.5–104.8] kg; mean BMI 26.3 ± 3.8 [range 20.1–32.3] kg/m^2). The cadavers have been provided by United Tissue Network (Norman, OK, USA), and Science Care (Phoenix, AZ, USA). Inclusion criteria were 20–70 years of age and a body mass index (BMI) of less than 35 kg/m^2. To ensure a homogeneous cohort, only male cadavers were included. Exclusion criteria were a history of any foot and ankle injuries or a history of surgery of the foot and ankle.

Experiments

Before any experiments were performed, each specimen was thawed for at least 24 hours at room temperature [17]. A radiolucent frame consisting of a base plate and four pillars located on the lateral sides of the foot was created to hold the specimens in a plantigrade position (Fig. 14.1). Each cadaver was fixed with an Ilizarov apparatus (using four 1.5 mm Kirschner wires [K-wires] drilled through the tibia) that fit into the frame. Tightening of the K-wires was done using a dynamometric wire tensioner (Smith & Nephew). The hindfoot was fixed using two 1.5 mm K-wires drilled through the calcaneus. In addition, a two-part resin (Bondo®, 3 M) was used to stabilize the hindfoot.

Intact ankles (native) were scanned first. Then, each ankle underwent AITFL transection (Condition 1). The deltoid ligament was transected next (Condition 2), followed by the IOM (Condition 3), and the PITFL (Condition 4). Transection of the deltoid ligament included the tibio-navicular and tibio-spring ligament. Then, the tibiocalcaneal ligament was transected. Finally, the anterior and posterior parts of the deep deltoid ligament were transected under visual control. While Conditions 1 and 2 mimic incomplete injuries, Conditions 3 and 4 mimic more complete injuries to the distal tibiofibular syndesmosis.

Weight bearing (85 kg; determined from the average specimen weight) CT scans with and without application of 10 Newton meter (Nm) internal rotation torque applied at the Ilizarov apparatus (corresponding to external torque of the foot and ankle) were performed (PedCAT, CurveBeam LLC, Warrington, USA, medium view, 0.3 mm slice thickness, 0.3 mm slice interval, kVp 120, mAs 22.62) [13].

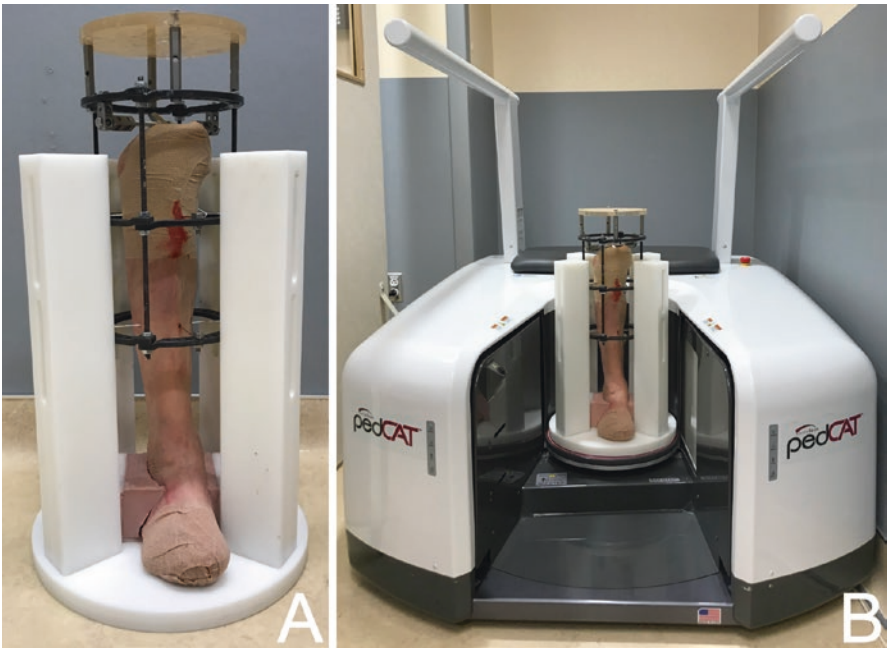

Fig. 14.1 Experimental setting. (**a**) Frame used to hold the cadaver in a plantigrade position. An Ilizarov apparatus was used for fixation of the tibia. (**b**) The frame fits into the weight bearing CT scanner. Load and torque can be applied following dissection of the distal tibiofibular syndesmosis [1]

Before the experiments were performed, preconditioning of the specimens was done by loading the frame with 42.5 kg and 85 kg for 2 minutes each.

Imaging and Measurements

Digitally reconstructed radiographs (DRRs) were reconstructed automatically using the CT scan dataset (CurveBeam LLC, Warrington, USA, Version 3.2.1.0). Previous research showed that measurements on DRRs were comparable to conventional radiographs [16]. As conventional radiographs are still the standard imaging modality to assess syndesmotic injuries, this approach provides additional information regarding the impact of torque on measurements when using conventional radiographs. The anteroposterior (AP) view of the ankle joint was generated perpendicular to a longitudinal axis of the foot [18, 19]. The mortise view was generated by virtually internally rotating the foot until a symmetrical widening of the medial and lateral gutters were visible [20]. As torque impacts talar rotation, it is difficult to reconstruct a mortise view under torque conditions [21]. Therefore, the same degree of internal rotation in native conditions was used for reconstruction of a mortise view from an AP view in the same specimens while under torque loading. The TFCS and the TFO were measured 1 cm above and the MCS 1 cm below the medial edge of the distal tibial plafond on both AP and mortise views (Fig. 14.2) [22, 23].

CT scans 1 cm above the medial edge of the distal tibial plafond (axial images) were reconstructed at the highest point of the distal tibial plafond on the sagittal view and used for measurements of the TFO and the TFCS (Fig. 14.2) [24]. CT scans 1 cm below the medial edge of the distal tibial plafond (axial images) were

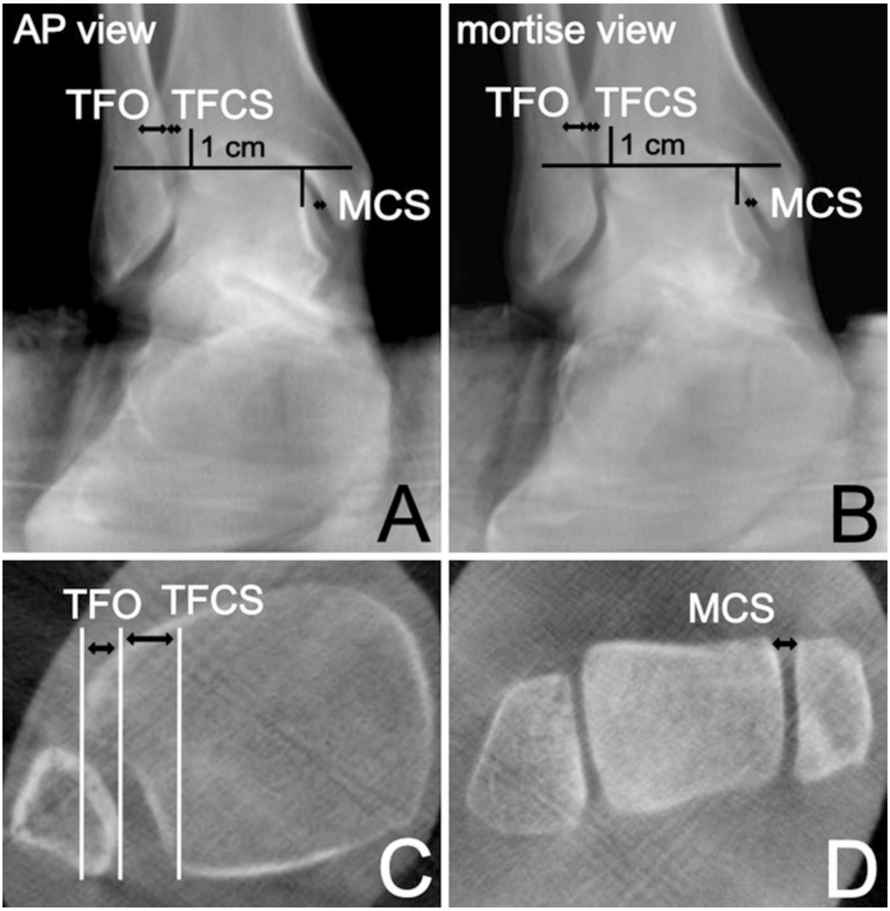

Fig. 14.2 Measurements performed and digitally reconstructed radiographs (DRRs) and single computed tomography (CT) images. (**a**) Anteroposterior (AP) view showing the medial clear space (MCS), tibiofibular clear space (TFCS), and tibiofibular overlap (TFO). (**b**) Mortise view of the same cadaver showing symmetrical widening of the ankle mortise. (**c**) Single CT image 1 cm above of the ankle joint showing the TFCS and TFO. (**d**) Single CT image 1 cm below of the ankle joint showing the MCS measured at the most anterior part of the joint between the medial malleolus und the talus [1]

additionally reconstructed. Those images were used for measurement of the MCS (Fig. 14.2). The MCS was defined as the distance between the most anterior articular surface of the medial malleolus to the talus.

Statistical Analysis

Intraclass correlation coefficients (ICC) were used to quantify the agreement of measurements between and within observers. Estimates and 95% confidence intervals (CI) were calculated for each type of measurement within each view. Interobserver agreement was modeled with a two-way random effect model of absolute agreement with a single measurement per observation, defined as ICC. Intraobserver agreement was modeled with a two-way mixed effect model of consistency with a single measurement per observation, defined as ICC. Agreement was rated as very good (ICC > 0.80), good (ICC = 0.61–0.80), moderate (ICC = 0.41–0.60), fair (ICC = 0.21–0.40), and poor (ICC < 0.20) [25]. Measurements for interobserver agreement calculation were done by a physician and a research analyst. For calculation of the intraobserver agreement, measurements were performed two times with an interval of 3 weeks by a physician.

Linear mixed effect models were fit for responses. Within DRR and CT measurements, separate models were fit for each measurement (MCS, TFO, and TFCS) and, for DRR measurements, within each view. Cadaver, a random effect, and foot (left or right), a fixed effect, were included in all models in addition to the variables presented. Models were fit for subsets of the data and estimates, and 95% CI were given for differences in measurements in different levels of a specific variable. For each of the models, only the differences in response that were associated with either different torques or different conditions were calculated; the data was subset by the other two variables, and they remained constant within each model. The first set of models compared the differences in response for 10 Nm versus 0 Nm of torque applied with full weight bearing load (condition constant within each model). The second set of models compare the differences in response between Conditions 1 through 4 and the native ankles, with full weight bearing load (torque constant within each model). Coefficients and 95% confidence intervals were reported, and statistical significance (marked by an asterisk in all tables and graphs) was determined based on a P-value of less than 0.05.

Pearson's correlation was used to assess the relationship between DRR—AP view only—and CT scan. Correlation was graded as very strong (>0.80), strong (0.60–0.80), moderate (0.40–0.60), weak (0.20–0.40), and very weak (<0.20). For each measurement, values were paired by cadaver, foot, condition, and torque, and the correlation estimated between the pairs was computed. Confidence intervals were constructed using the Fisher transformation. All calculations were done in R 3.4.1, specifically using packages psych and lmerTest.

Results

Digitally Reconstructed Radiographs

The average internal rotation to reconstruct a mortise view out of an AP view was 9.9 ± 1.4 (range 8.0–13.9) degrees. Inter- and intraobserver agreement for measurements made on DRRs were rated as very good/good for the MCS and TFO (Table 14.1). TFCS measurements were rated as moderate for interobserver and very good (AP view)/good (mortise view) for intraobserver reliability. Torque significantly impacted MCS measurements if any of the four ligaments was transected, but not on native ankles (Table 14.2). The TFCS significantly decreased for native ankles (AP and mortise view) and additionally for Condition 1 (mortise view) if torque was applied. A significant increase of the TFCS was evident for Condition 4 (mortise view, including torque). TFO measurements on native ankles and on each condition significantly decreased if torque was applied. The AITFL and deltoid ligament had to be transected to detect a significant difference for the MCS on the AP and mortise view compared to native ankles (including torque, Fig. 14.3). For the

Table 14.1 Reliability of digitally reconstructed radiographs (DRR) and computed tomography (CT) measurements assessed by intraclass correlation coefficient (ICC) [1]

		Interobserver: ICC(2,1) Estimate (95% CI)	Intraobserver: ICC(3,1) Estimate (95% CI)
AP (DRR)	MCS	0.75	0.93
		(0.51, 0.87)	(0.87, 0.96)
	TFCS	**0.59**∗	0.88
		(0.35, 0.76)	(0.79, 0.94)
	TFO	0.95	0.99
		(0.88, 0.98)	(0.97, 0.99)
Mortise (DRR)	MCS	0.87	0.95
		(0.77, 0.93)	(0.91, 0.98)
	TFCS	**0.55**∗	0.70
		(0.29, 0.73)	(0.50, 0.83)
	TFO	0.92	0.97
		(0.77, 0.97)	(0.94, 0.98)
CT scan	MCS	0.94	0.95
		(0.89, 0.97)	(0.92, 0.98)
	TFCS	0.93	0.94
		(0.74, 0.97)	(0.89, 0.97)
	TFO	0.92	0.99
		(0.53, 0.98)	(0.97, 0.99)

DRR digitally reconstructed radiograph, *AP* anteroposterior, *CT* computed tomography, *MCS* medial clear space, *TFCS* tibiofibular clear space, *TFO* tibiofibular overlap, *CI* confidence interval, *ICC* intraclass correlation coefficient
∗Indicates ICC < 0.61

Table 14.2 Influence of torque application on measurements (weight bearing). The table shows mean differences for each stage of dissection with and without torque application [1]

			Native	Condition 1	Condition 2	Condition 3	Condition 4
			Estimate (95% CI; mm)				
DRR	MCS	AP	0.01	**0.34**	**0.40**	**1.14**	**1.56**
			(−0.21, 0.23)	**(0.08, 0.60)***	**(0.02, 0.78)***	**(0.39, 1.88)***	**(1.02, 2.11)***
		Mortise	−0.07	**0.50**	**0.92**	**1.62**	**1.90**
			(−0.33, 0.18)	**(0.16, 0.83)***	**(0.55, 1.28)***	**(0.94, 2.29)***	**(0.93, 2.87)***
	TFCS	AP	**−0.77**	**−0.44**	−0.29	0.14	0.31
			(−1.22, −0.32)*	**(−0.75, −0.12)***	(−0.81, 0.24)	(−0.69, 0.96)	(−0.54, 1.17)
		Mortise	**−0.53**	0.17	0.29	0.48	**1.43**
			(−0.93, −0.13)*	(−0.41, 0.74)	(−0.30, 0.87)	(−0.45, 1.41)	**(0.47, 2.38)***
	TFO	AP	**−2.89**	**−3.38**	**−3.92**	**−4.63**	**−3.93**
			(−3.60, −2.18)*	**(−4.50, −2.25)***	**(−4.69, −3.15)***	**(−5.54, −3.71)***	**(−5.42, −2.44)***
		Mortise	**−2.44**	**−2.96**	**−3.12**	**−2.64**	**−2.50**
			(−3.15, −1.74)*	**(−3.88, −2.03)***	**(−3.92, −2.32)***	**(−3.39, −1.89)***	**(−3.45, −1.55)***
CT scan	MCS		**1.22**	**1.51**	**1.78**	**2.81**	**3.35**
			(0.62, 1.81)*	**(1.18, 1.84)***	**(1.27, 2.28)***	**(1.37, 4.26)***	**(1.77, 4.92)***
	TFCS		**−1.07**	**−0.90**	**−0.94**	−0.04	1.29
			(−1.50, −0.65)*	**(−1.41, −0.40)***	**(−1.55, −0.33)***	(−1.29, 1.20)	(−0.13, 2.71)
	TFO		**−2.98**	**−3.63**	**−3.84**	**−4.46**	**−4.49**
			(−3.51, −2.45)*	**(−4.57, −2.69)***	**(−4.85, −2.82)***	**(−5.68, −3.24)***	**(−6.33, −2.65)***

DRR digitally reconstructed radiograph, *CT* computed tomography, *AP* anteroposterior, *MCS* medial clear space, *TFCS* tibiofibular clear space, *TFO* tibiofibular overlap, *CI* confidence interval
*Indicates statistical significance ($P < 0.05$)

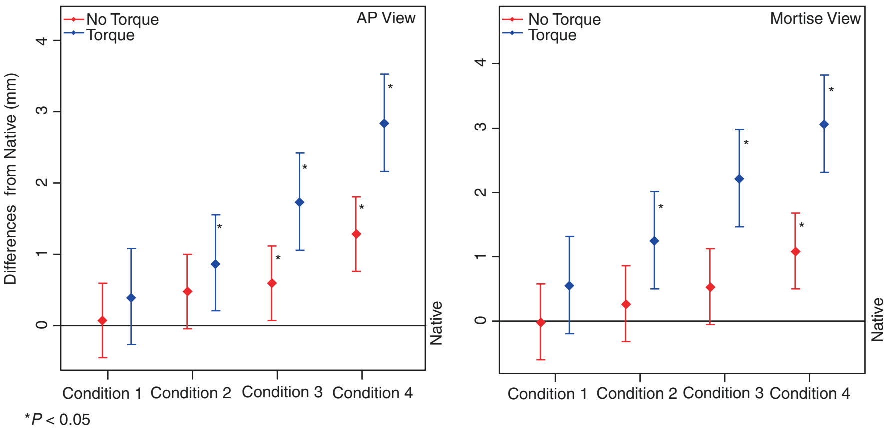

Fig. 14.3 Differences of the medial clear space (MCS) between each tested condition and intact ankles (native) assessed on the anteroposterior (AP) and mortise view (digitally reconstructed radiographs [DRRs]). Using torque, the anterior inferior tibiofibular ligament (AITFL) as well as the deltoid ligament must be transected to detect a significant difference (AP and mortise view) [1]

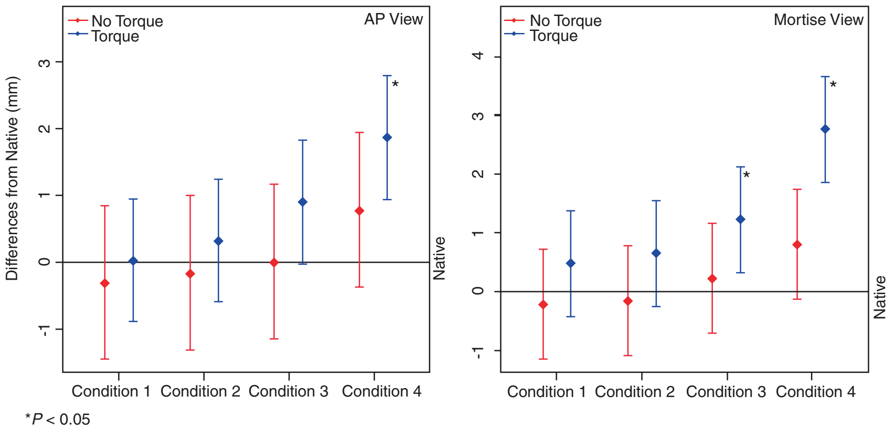

Fig. 14.4 Differences of the tibiofibular clear space (TFCS) between each tested condition and intact ankles (native) assessed on the anteroposterior (AP) and mortise view (digitally reconstructed radiographs [DRRs]). Using torque, the anterior inferior talo-fibular ligament (AITFL), deltoid ligament as well as the interosseous membrane (IOM) must be transected to create a significant difference compared to intact ankles (mortise view) [1]

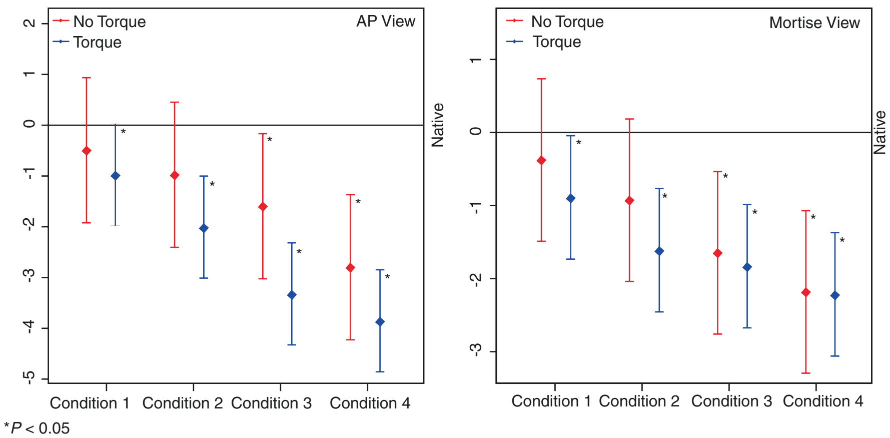

Fig. 14.5 Differences of the tibiofibular overlap (TFO) between each tested condition and intact ankles (native) assessed on the anteroposterior (AP) and mortise view (digitally reconstructed radiographs). Isolated anterior inferior tibiofibular ligament (AITFL) transection significantly differed from intact ankles on the AP and mortise view [1]

TFCS, only fully dissected ankles (Condition 4) significantly differed from native ankles (both views, including torque). Using the mortise view, Condition 3 additionally differed significantly from native ankles when the TFCS was measured (including torque, Fig. 14.4). For the TFO, isolated AITFL release significantly differed from native ankles if torque was applied (Fig. 14.5).

Weight Bearing CT Scans

Inter- and intraobserver agreement for CT measurements were very good for each assessed parameter (Table 14.1). Torque significantly impacted MCS measurements in native ankles and in each condition (Table 14.2). The TFCS significantly decreased in native ankles, for Condition 1, and for Condition 2 when torque was applied. TFO measurements on native ankles and on each tested condition were significantly impacted by torque application. The AITFL and deltoid ligament had to be transected to detect a significant difference for the MCS compared to native ankles if torque was applied (Fig. 14.6). The TFCS was only helpful in differentiating an intact from a disrupted syndesmosis after complete release of the AITF, deltoid ligament, and IOM (including torque application). Isolated AITFL transection was recognized by a significant change in TFO values when torque was applied. Correlation between DRR and CT measurements was best for the TFO (very strong), followed by the MCS (very strong) and TFCS (strong, Table 14.3).

Discussion

A cadaver study examining the utility of weight bearing CT scans to assess incomplete and more complete syndesmotic injuries on DRRs and axial CT images was performed. The three most relevant findings were (1) torque application helps to identify incomplete syndesmotic injuries; (2) the TFO was the most useful predictor for incomplete syndesmotic injuries; and (3) the MCS and TFCS predict more complete injuries.

The reliability of DRR measurements for MCS and TFO on DRRs were comparable with published data for conventional radiographs [22, 26]. These two measurements can reliably be determined on conventional radiographs and DRRs. A similar result was evident for MCS and TFO measurements on axial CT images [24, 27]. The reliability for TFCS measurements on DRRs was slightly lower compared to published data for conventional radiographs [22]. The resolution of DRRs is slightly lower compared to conventional radiographs, wherefore the identification of the anteromedial border of the distal tibial incisura was less precise on DRRs than on conventional radiographs, perhaps explaining the difference between the reliability for the TFCS measured on DRRs compared to published measurements on conventional radiographs [22]. However, TFCS measurements could reliably be performed on axial CT images. Consequently, the TFCS should be assessed on axial CT scans rather than on DRRs.

The impact of torque on measurements describing the distal tibiofibular syndesmosis has already been investigated in healthy volunteers, but the influence on measurement in cases of a syndesmotic injury is not yet fully understood [28]. Torque application helps to reveal incomplete syndesmotic injuries in this study. Without application of torque, only severe injuries could be identified. Recent research

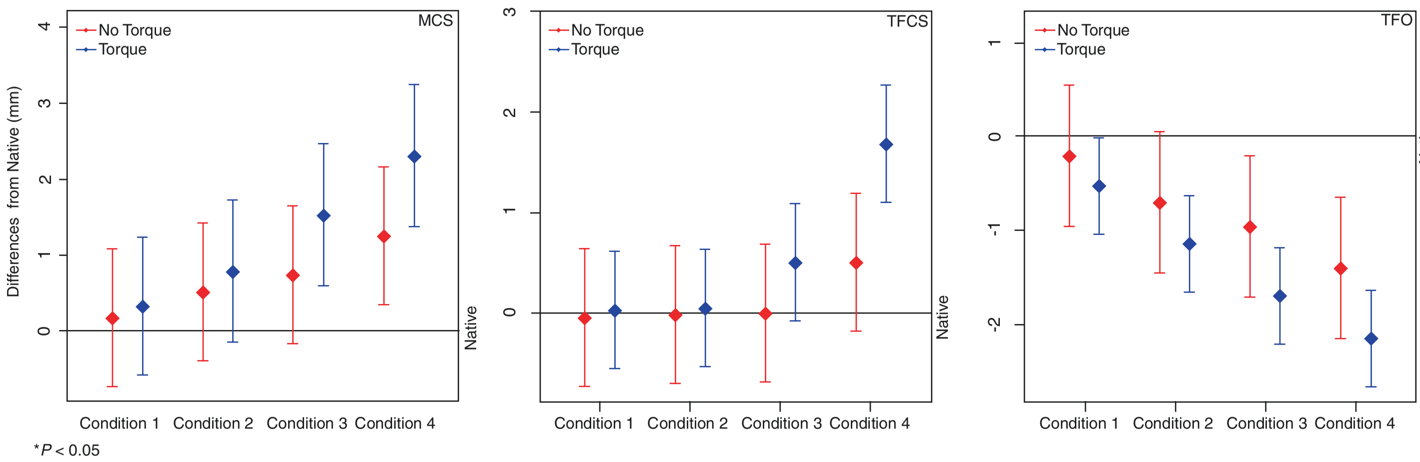

Fig. 14.6 Difference of the medial clear space (MCS), tibiofibular clear space (TFCS), and tibiofibular overlap (TFO) between each tested condition and intact ankles (native) assessed on axial computed tomography (CT) images (weight bearing condition). Results were similar to measurements done on digitally reconstructed radiographs (DRRs). Using torque, the anterior inferior talo-fibular ligament (AITFL) and deltoid ligament must be transected to create a significant difference of the MCS compared to intact ankles. For the TFCS, the interosseous membrane (IOM) must be additionally transected, while for the TFO, isolated AITFL ligament transection significantly differed from intact ankles [1]

Table 14.3 Correlation between DRR (AP View) and CT measurements. Pearson's correlation with confidence intervals computed using the Fisher transformation [1]

Measurement	Estimate (95% CI)
MCS	0.83
	(0.78, 0.87)
TFCS	0.80
	(0.75, 0.85)
TFO	0.93
	(0.91, 0.95)

DRR digitally reconstructed radiographs, *CT* computed tomography, *AP* anteroposterior, *MCS* medial clear space, *TFCS* tibiofibular clear space, *TFO* tibiofibular overlap, *CI* confidence interval

showed that measurements describing the distal tibiofibular syndesmosis are highly dependent on the position of the ankle joint (e.g., rotation of the foot, dorsal extension/plantar flexion of the ankle joint) [29, 30]. A standardized position of the ankle when imaging is performed is therefore crucial for a meaningful interpretation of any measurements. Using weight bearing CT scans, torque application can be done with the foot in a plantigrade position (e.g., in standing position). This may be an advantage to other imaging modalities, where the rotation of the foot cannot be adjusted after imaging is performed (conventional radiograph) or the foot is in a non-weight bearing condition (non-weight bearing CT scan, MRI).

The TFO outperformed the other measurements to detect incomplete syndesmotic injuries. Including torque, single ligament injuries (AITFL transection) could be differentiated from native ankles. This finding was independent of the imaging modality: DRRs as well as single axial CT images showed the same result. This is different than recent research where the TFO could not detect isolated AITF injuries when using stress fluoroscopy [31]. This result may be explained by the standardized setting used in this study: reconstruction of DRRs and axial CT images was done precisely to ensure no differences in rotation. MCS measurements were only useful in conditions where the deltoid ligament was additionally transected (DRRs and single CT images). Therefore, the MCS may be useful to identify patients with an additional deltoid ligament injury. The TFCS, however, was only useful to predict more complete syndesmotic injuries including the posterior syndesmotic ligaments. Interestingly, torque decreased TFCS measurement except if the PITFL was dissected for most conditions. An intact PITFL may not allow the fibula to displace posteriorly if torque is applied. Therefore, TFCS measurements may be used to identify patients with an additional injury to the posterior part of the distal tibiofibular syndesmosis.

Interestingly, the correlation between measurements done on DRRs and on axial CT images was very strong for the MCS and TFO and strong for the TFCS. Given the fact that the reliability of measurements was comparable for DRRs and axial CT images when using the MCS and TFO, those two measurements can either be assessed on DRRs (weight bearing) and axial CT images (weight bearing). The TFCS, however, should only be assessed on axial CT images rather than on DRRs as the reliability is lower on DRRs.

Our study has several limitations. A cadaver model was used to assess the impact of torque on the assessment of syndesmotic injuries. In vivo, fixation of the calcaneus using K-wires is not feasible. The utility of applying torque to patient use will require further experimentation and innovation. However, the amount of torque applied in this study (10 Nm) is relatively small and should be well tolerated. A second limitation is the precise transection of ligaments when using cadaver model to mimic syndesmotic injuries. In a posttraumatic condition, different ligaments of the distal talo-fibular syndesmosis are variably torn and healed. Such complex injuries cannot be simulated accurately using cadaver models. Finally, several different measurement options using either conventional radiographs or CT scans are available. This study only investigated three commonly used measurements. Other measurements may be better predictors for injuries to the distal tibiofibular syndesmosis.

To conclude, the application of torque helps when using weight bearing CT scans to identify incomplete syndesmotic injuries (cadaver model). The TFO is a better predictor for incomplete syndesmotic injuries, while the MCS and TFCS can be used for more complete lesions.

References

1. Krähenbühl N, Bailey TL, Presson AP, Allen CM, Henninger HB, Saltzman CL, Barg A. Torque application helps to diagnose incomplete syndesmotic injuries using weight-bearing computed tomography images. Skelet Radiol. 2019;48(9):1367–76.
2. Krähenbühl N, Weinberg MW, Davidson NP, Mills MK, Hintermann B, Saltzman CL, Barg A. Imaging in syndesmotic injury: a systematic literature review. Skelet Radiol. 2018;47(5):631–48.
3. Rammelt S, Obruba P. An update on the evaluation and treatment of syndesmotic injuries. Eur J Trauma Emerg Surg. 2015;41(6):601–14.
4. Nussbaum ED, Hosea TM, Sieler SD, Incremona BR, Kessler DE. Prospective evaluation of syndesmotic ankle sprains without diastasis. Am J Sports Med. 2001;29(1):31–5.
5. Krähenbühl N, Weinberg MW, Hintermann B, Haller JM, Saltzman CL, Barg A. Surgical outcome in chronic syndesmotic injury: a systematic literature review. Foot Ankle Surg. 2018, epub ahead of print.
6. Waterman BR, Belmont PJ Jr, Cameron KL, Svoboda SJ, Alitz CJ, Owens BD. Risk factors for syndesmotic and medial ankle sprain: role of sex, sport, and level of competition. Am J Sports Med. 2011;39(5):992–8.
7. Pakarinen H, Flinkkila T, Ohtonen P, Hyvonen P, Lakovaara M, Leppilahti J, Ristiniemi J. Intraoperative assessment of the stability of the distal tibiofibular joint in supination-external rotation injuries of the ankle: sensitivity, specificity, and reliability of two clinical tests. J Bone Joint Surg Am. 2011;93(22):2057–61.
8. Roemer FW, Jomaah N, Niu J, Almusa E, Roger B, D'Hooghe P, Geertsema C, Tol JL, Khan K. Ligamentous injuries and the risk of associated tissue damage in acute ankle sprains in athletes: a cross-sectional MRI study. Am J Sports Med. 2014;42(7):1549–57.
9. Hermans JJ, Wentink N, Beumer A, Hop WC, Heijboer MP, Moonen AF, Ginai AZ. Correlation between radiological assessment of acute ankle fractures and syndesmotic injury on MRI. Skelet Radiol. 2012;41(7):787–801.

10. Schoennagel BP, Karul M, Avanesov M, Bannas P, Gold G, Grossterlinden LG, Rupprecht M, Adam G, Yamamura J. Isolated syndesmotic injury in acute ankle trauma: comparison of plain film radiography with 3T MRI. Eur J Radiol. 2014;83(10):1856–61.
11. Golano P, Vega J, de Leeuw PA, Malagelada F, Manzanares MC, Gotzens V, van Dijk CN. Anatomy of the ankle ligaments: a pictorial essay. Knee Surg Sports Traumatol Arthrosc. 2010;18(5):557–69.
12. Jeong MS, Choi YS, Kim YJ, Kim JS, Young KW, Jung YY. Deltoid ligament in acute ankle injury: MR imaging analysis. Skelet Radiol. 2014;43(5):655–63.
13. Clanton TO, Williams BT, Backus JD, Dornan GJ, Liechti DJ, Whitlow SR, Saroki AJ, Turnbull TL, LaPrade RF. Biomechanical analysis of the individual ligament contributions to syndesmotic stability. Foot Ankle Int. 2017;38(1):66–75.
14. Tuominen EK, Kankare J, Koskinen SK, Mattila KT. Weight-bearing CT imaging of the lower extremity. AJR Am J Roentgenol. 2013;200(1):146–8.
15. Mozzo P, Procacci C, Tacconi A, Martini PT, Andreis IA. A new volumetric CT machine for dental imaging based on the cone-beam technique: preliminary results. Eur Radiol. 1998;8(9):1558–64.
16. Barg A, Bailey T, Richter M, de Cesar Netto C, Lintz F, Burssens A, Phisitkul P, Hanrahan CJ, Saltzman CL. Weightbearing computed tomography of the foot and ankle: emerging technology topical review. Foot Ankle Int. 2018;39(3):376–86.
17. Barg A, Amendola RL, Henninger HB, Kapron AL, Saltzman CL, Anderson AE. Influence of ankle position and radiographic projection angle on measurement of supramalleolar alignment on the anteroposterior and hindfoot alignment views. Foot Ankle Int. 2015;36(11):1352–61.
18. Krähenbühl N, Siegler L, Deforth M, Zwicky L, Hintermann B, Knupp M. Subtalar joint alignment in ankle osteoarthritis. Foot Ankle Surg. 2019;25(2):143–9.
19. Krähenbühl N, Tschuck M, Bolliger L, Hintermann B, Knupp M. Orientation of the subtalar joint: measurement and reliability using weightbearing CT scans. Foot Ankle Int. 2016;37(1):109–14.
20. Takao M, Ochi M, Naito K, Iwata A, Uchio Y, Oae K, Kono T, Kawasaki K. Computed tomographic evaluation of the position of the leg for mortise radiographs. Foot Ankle Int. 2001;22(10):828–31.
21. Lepojarvi S, Niinimaki J, Pakarinen H, Koskela L, Leskela HV. Rotational dynamics of the talus in a normal tibiotalar joint as shown by weight-bearing computed tomography. J Bone Joint Surg Am. 2016;98(7):568–75.
22. Shah AS, Kadakia AR, Tan GJ, Karadsheh MS, Wolter TD, Sabb B. Radiographic evaluation of the normal distal tibiofibular syndesmosis. Foot Ankle Int. 2012;33(10):870–6.
23. Grass R, Rammelt S, Biewener A, Zwipp H. Peroneus longus ligamentoplasty for chronic instability of the distal tibiofibular syndesmosis. Foot Ankle Int. 2003;24(5):392–7.
24. Dikos GD, Heisler J, Choplin RH, Weber TG. Normal tibiofibular relationships at the syndesmosis on axial CT imaging. J Orthop Trauma. 2012;26(7):433–8.
25. Yeung TW, Chan CY, Chan WC, Yeung YN, Yuen MK. Can pre-operative axial CT imaging predict syndesmosis instability in patients sustaining ankle fractures? Seven years' experience in a tertiary trauma center. Skelet Radiol. 2015;44(6):823–9.
26. Brage ME, Bennett CR, Whitehurst JB, Getty PJ, Toledano A. Observer reliability in ankle radiographic measurements. Foot Ankle Int. 1997;18(6):324–9.
27. Shakoor D, Osgood GM, Brehler M, Zbijewski WB, de Cesar Netto C, Shafiq B, Orapin J, Thawait GK, Shon LC, Demehri S. Cone-beam CT measurements of distal tibio-fibular syndesmosis in asymptomatic uninjured ankles: does weight-bearing matter? Skelet Radiol. 2019;48(4):583–94.
28. Lepojarvi S, Niinimaki J, Pakarinen H, Leskela HV. Rotational dynamics of the normal distal tibiofibular joint with weight-bearing computed tomography. Foot Ankle Int. 2016;37(6):627–35.
29. Pneumaticos SG, Noble PC, Chatziioannou SN, Trevino SG. The effects of rotation on radiographic evaluation of the tibiofibular syndesmosis. Foot Ankle Int. 2002;23(2):107–1.

30. Nault ML, Marien M, Hebert-Davies J, Laflamme GY, Pelsser V, Rouleau DM, Gosselin-Papadopoulos N, Leduc S. MRI quantification of the impact of ankle position on syndesmosis anatomy. Foot Ankle Int. 2017;38(2):215–9.
31. Feller R, Borenstein T, Fantry AJ, Kellum RB, Machan JT, Nickisch F, Blankenhorn B. Arthroscopic quantification of syndesmotic instability in a cadaveric model. Arthroscopy. 2017;33(2):436–44.

Chapter 15
Flexible Adult-Acquired Flatfoot Deformity: Comparison Between Weight Bearing and Non-weight Bearing Measurements Using Cone Beam Computed Tomography

Cesar de Cesar Netto

Introduction

Initially described as a consequence of isolated dysfunction of the posterior tibialis tendon [1–3], adult-acquired flatfoot deformity (AAFD) is a common and complex disorder characterized by a diverse combination of deformities. It can differ in severity and location along the entire medial longitudinal arch of the foot and is associated with failure of multiple soft tissue structures [4], including the talonavicular joint capsule, deltoid ligament [5], and other arch support ligaments, with the spring ligament being the most important [6–8]. Deficiency of these structures can occur before or after posterior tibialis tendon failure [9]. The resultant deformity is a combination of flattening, plantar, and medial migration of the talar head and foot abduction at the talonavicular joint, midfoot joint displacement, and hindfoot valgus [10].

Staging of AAFD is based on clinical and radiographic assessment. Four stages of disease progression have been described [4, 11–13], with the first 2 stages representing flexible deformities. Weight bearing (WB) plain radiographs are the standard imaging modality, and different measurements have been described as tools for assessing the deformity [14–17]. The use of WB computed tomography (CT) is rapidly expanding and may allow a more detailed understanding of this complex, three-dimensional (3D) deformity [18–25] that has been challenging to characterize using two-dimensional (2D) plain radiographs.

We recently showed that WB 3D extremity cone beam computed tomography (CBCT) outperforms multidetector computed tomography (MDCT) in image evaluation of the foot and ankle, with less radiation exposure [26]. We also found that CBCT scans were better for evaluating bone anatomy, with good interobserver reliability [27].

Based on de Cesar Netto C, Schon LC, Thawait GK, da Fonseca LF, Chinanuvathana A, Zbijewski WB, Siewerdsen JH, Demehri S. Flexible adult acquired flatfoot deformity: Comparison Between Weightbearing and Nonweightbearing Measurements Using Cone Beam Computed Tomography. *J Bone Joint Surg Am*. 2017 Sep 20;99(18):e98. doi: 10.2106/JBJS.16.01366.

M. Richter et al., *Weight Bearing Cone Beam Computed Tomography (WBCT) in the Foot and Ankle*, https://doi.org/10.1007/978-3-030-31949-6_15

The purpose of this study was to test the hypothesis that, compared with non-weight bearing (NWB) measurements, measurements performed on WB CBCT images can better demonstrate AAFD.

Materials and Methods

Institutional review board approval was obtained for this dual-center study, which complied with the Declaration of Helsinki and the Health Insurance Portability and Accountability Act (HIPAA). Written informed consent was obtained from all participants.

Study Design

We prospectively recruited consecutive patients in our tertiary hospital clinic from September 2014 through June 2016. We used the following inclusion criteria: clinical diagnosis of symptomatic flexible AAFD; age 18 years or older; ability to communicate effectively with clinical study personnel; ability to stand or sit still, unassisted, for at least 40 seconds; and availability of comparative imaging study (CT scan, magnetic resonance imaging scan, or radiograph) performed for a clinical purpose within the past 3 months. We excluded pregnant patients and those with major medical or psychiatric illness that could prevent completion of the procedure. Screened, enrolled, and included patients are presented in a CONSORT diagram (Fig. 15.1).

Subjects

Twenty patients (14 right feet, 6 left feet) were included in the study. The cohort consisted of 12 men and 8 women, with a mean age of 52 years (range, 20–88) and a mean body mass index value of 30 (range, 19–46).

CBCT Imaging Technique

All CT studies were performed on a CBCT extremity scanner (generation II, Carestream Health Inc., Rochester, NY) [27]. Participants underwent two consecutive scans of the symptomatic foot: one NWB scan (sitting position with knee extended, ankle joint in neutral position, and foot placed plantigrade over a foam surface in the CBCT gantry) and one WB scan (physiological upright WB position). For the WB position, the scan was performed with the participant standing with feet

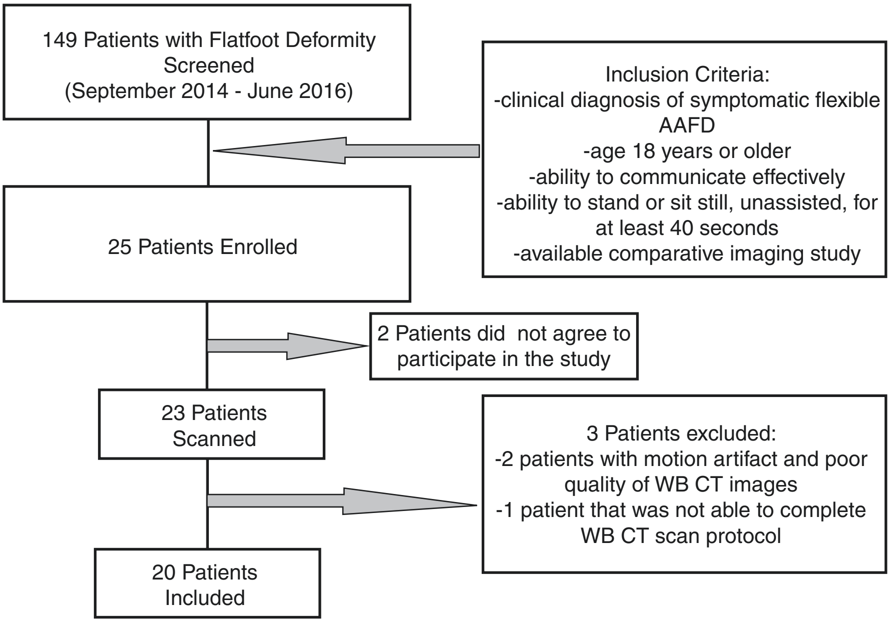

Fig. 15.1 CONSORT diagram of screened, enrolled, and included patients. AAFD, adult-acquired flatfoot deformity

approximately at shoulder width and distributing body weight evenly between both legs. The nominal scan protocol was based on previous technical assessment [26, 27]. We applied 90 kVp and 72 mAs (6 mA and 20 msec for each frame, 600 frame acquisition) for all scans to optimize contrast-to-noise ratio per unit of dose within the limits of our CT system power. Conversion factors for size-specific dose estimates were 1.4 for the foot and ankle (8 cm diameter); therefore, the size-specific dose estimate for CBCT ankle imaging was estimated to be 12 mGy.

The weighted CT dose index for CBCT ankle acquisition has been estimated to be 15 mGy using a Farmer chamber in a stack of three 16 cm CT dose index phantoms [27]. The CBCT image data were reconstructed using a "bone" algorithm using iterative reconstruction with scatter correction to images with $0.5 \times 0.5 \times 0.5$ mm^3 isotropic voxels.

Measurements

The raw 3D data were converted to sagittal, coronal, and axial image slices that were transferred digitally into dedicated software (Vue PACS; Carestream Health, Inc.; Rochester, NY) for computer-based measurements. Image annotations were removed, and each study was assigned a unique and random number. After completion of a mentored training protocol with five AAFD cases in which the observers learned how to use the software and how to perform the measurements, two fellowship-trained foot and ankle surgeons and one fellowship-trained radiologist performed the measurements in an independent, random, and blinded fashion. One of the observers (surgeon) performed a second set of measurements for intraobserver reliability assessment 1 month after the first assessment was completed (to reduce memory bias). WB and NWB images were compared with respect to averaged values of measurements analogous to AAFD radiographic parameters [17, 21] on the axial, sagittal, and coronal views.

Axial Plane Measurements

The axial plane was defined as parallel to the horizontal platform, with the horizontal edge of the images aligned to the axis of the first metatarsal. Two axial parameters were assessed (Fig. 15.2). The first was the talus-first metatarsal angle, which is formed by the intersection of two lines representing the axis of the first metatarsal and the axis of the talus [17]. Values were considered positive when the angle had a medial vertex, indicating relative increased forefoot abduction. The second was the talonavicular coverage angle, as described by Sangeorzan et al. [28].

Coronal Plane Measurements

The coronal plane was defined as perpendicular to the horizontal platform, with the horizontal edge of the images aligned to a line perpendicular to the ankle bimalleolar axis. Nine coronal parameters were assessed (Figs. 15.3 and 15.4). The first was the forefoot arch angle, as described by Ferri et al. [22]. Positive values represented

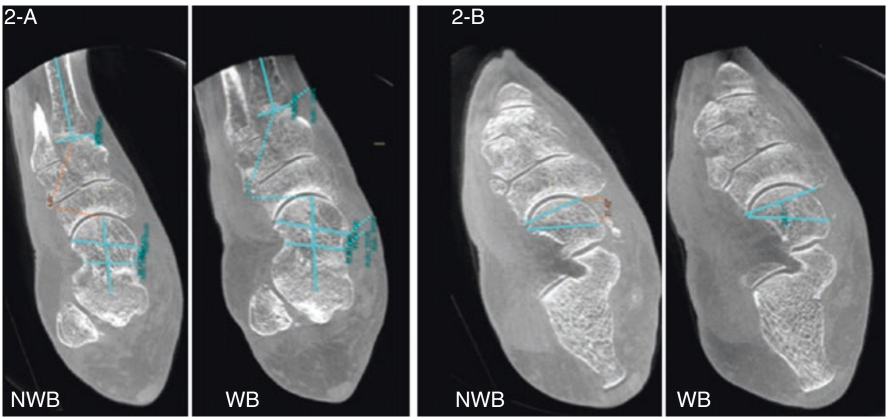

Fig. 15.2 Measurements on the axial plane in the same patient. Non-weight bearing (NWB) and weight bearing (WB) images: (**a**) talus-first metatarsal angle; (**b**) talonavicular coverage angle

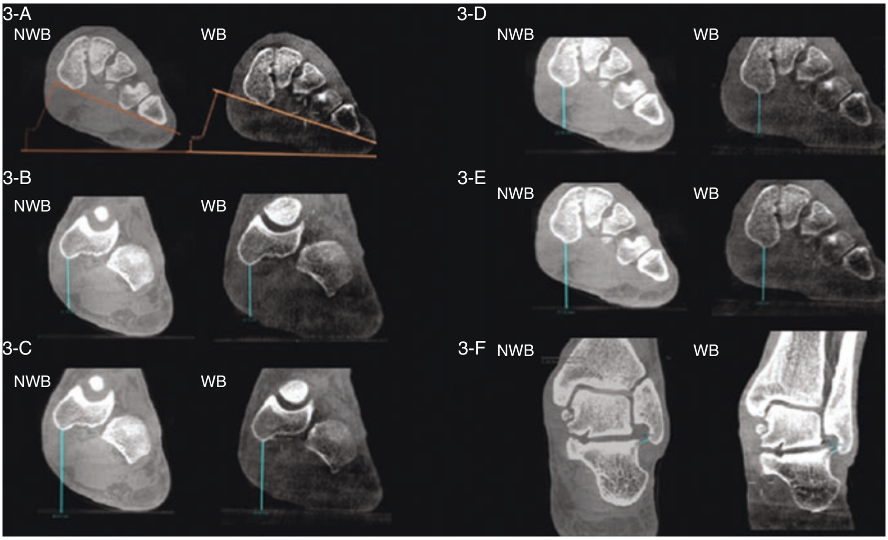

Fig. 15.3 Measurements on the coronal plane in the same patient. Non-weight bearing (NWB) and weight bearing (WB) images: (**a**) forefoot arch angle; (**b**) navicular to skin distance; (**c**) navicular to floor distance; (**d**) medial cuneiform to skin distance; (**e**) medial cuneiform to floor distance; (**f**) calcaneofibular distance

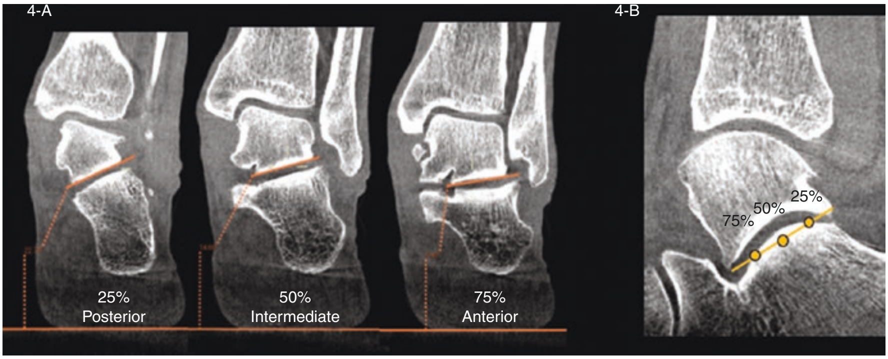

Fig. 15.4 Subtalar horizontal angle measurements in the same patient. Weight bearing images: (**a**) coronal plane, subtalar horizontal angle at 25% (posterior), 50% (intermediate), and 75% (anterior); (**b**) sagittal plane, demarcation of points where the coronal plane images were used for subtalar horizontal angle evaluation at 25%, 50%, and 75% of the longitudinal length of the subtalar joint

a relative higher positioning of the medial cuneiform to the fifth metatarsal. The second was the navicular to skin distance, also as described by Ferri et al. [22]. The third was the navicular to floor distance, measured from the most inferior aspect of the navicular to the floor line. The fourth was the medial cuneiform to skin distance, measured from the most inferior aspect of the medial cuneiform to the plantar skin.

The fifth was the medial cuneiform to floor distance, measured from the most inferior aspect of the medial cuneiform to the floor line. The sixth was the calcaneofibular distance, which was the shortest distance between the distal fibula and the lateral/superior surface of the calcaneus [20, 21, 23]. The seventh was the subtalar horizontal angle, which was the angle between the posterior facet of the talus and the floor (horizontal line) measured at 25% (posterior aspect), 50% (midpoint), and 75% (anterior aspect) of the posterior subtalar joint length [19, 25, 29, 30]. Positive values represented valgus alignment of the joint.

Sagittal Plane Measurements

The sagittal plane was defined as perpendicular to the horizontal platform with the horizontal edge of the images aligned to the axis of the second metatarsal. Eight sagittal parameters were evaluated (Fig. 15.5). The first was the talus-first metatarsal angle, which was formed by the intersection of the axis of the first metatarsal and the axis of the talus [17]. Values were considered positive when the angle had a plantar vertex. The second was the navicular to skin distance, measured from the most inferior aspect of the navicular to the plantar skin surface. The third was the navicular to floor distance, measured from the most inferior aspect of the navicular to the floor line. The fourth was the cuboid to skin distance, measured from the most

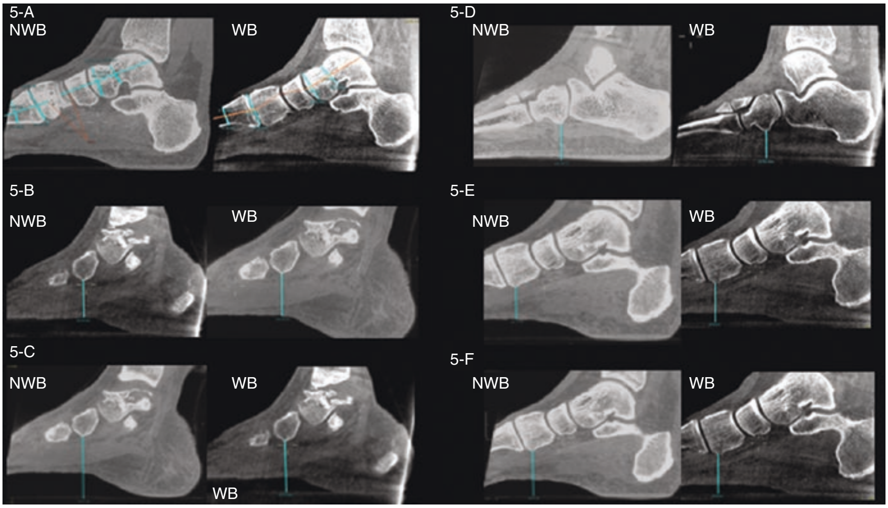

Fig. 15.5 Measurements on the sagittal plane in the same patient. Non-weight bearing (NWB) and weight bearing (WB) images: (**a**) talus-first metatarsal angle; (**b**) navicular to skin distance; (**c**) navicular to floor distance; (**d**) cuboid to floor distance; (**e**) medial cuneiform to skin distance; (**f**) medial cuneiform to floor distance

inferior aspect of the cuboid to the plantar skin surface. The fifth was the cuboid to floor distance, measured from the most inferior aspect of the cuboid to the floor line [21]. The sixth was the medial cuneiform to skin distance, measured from the most inferior aspect of the medial cuneiform to the plantar skin surface. The seventh was the medial cuneiform to floor distance, measured from the most inferior aspect of the medial cuneiform to the floor line [31–33]. The eighth was the calcaneal inclination angle, which was the intersection of the floor line and a line connecting the most inferior point of the calcaneal tuberosity and the undersurface edge of the anterior process of the calcaneus [34].

Statistical Analysis

Data from each type of measurement were evaluated for normality by the Shapiro-Wilk test. The intraobserver reliability (one observer) was calculated using the Pearson's or Spearman's correlation test and 95% confidence intervals. Interobserver reliability was assessed using intraclass correlation coefficients (ICCs) and 95% confidence intervals for each measurement in each image type, considering the amount by which bias and interaction factors can reduce the ICC. Correlations of 0.81–1.00 were considered almost perfect, 0.61–0.80 were considered substantial, 0.41–0.60 were considered moderate, 0.21–0.40 were considered fair, and <0.20 were considered slight agreement [35, 36]. Measurements performed on WB and NWB images were compared using paired Student's t-tests or Wilcoxon rank-sum tests. $P < 0.05$ was considered significant.

Source of Funding

This work was based on an industrial grant from Carestream, Inc., which provide monetary incentive to subjects who undergo CBCT examinations. The decision to recruit the proper subjects who meet the criteria was based on clinical presentation and decided by the orthopedic surgeon.

Results

We found substantial to almost perfect intraobserver (Table 15.1) and interobserver reliability (Table 15.2). We found significant differences in the mean value of almost all measurements performed when comparing WB and NWB images of patients with flexible AAFD (Tables 15.3 and 15.4). The only exception was the calcaneal inclination angle ($P = 0.1446$).

Table 15.1 Intraobserver reliability of CT-based measurements of adult-acquired flatfoot deformity in 20 patients

Measurement by view	NWB images		WB images	
	Pearson's *r*/ Spearman's r_s	95% CI	Pearson's *r*/Spearman's r_s	95% CI
Axial view				
Talonavicular coverage angle	0.94	0.85, 0.98	0.88	0.72, 0.95
Talus-first metatarsal angle	0.88	0.71, 0.95	0.89	0.75, 0.96
Coronal view				
Medial cuneiform to floor distance	0.99	0.96, 0.99	0.99	0.99, 1.00
Navicular to floor distance	0.98	0.94, 0.99	0.99	0.99, 1.00
Forefoot arch angle	0.98	0.96, 0.99	0.99	0.97, 0.99
Medial cuneiform to skin distance	0.98	0.94, 0.99	0.99	0.98, 1.00
Navicular to skin distance	0.96	0.90, 0.98	0.99	0.98, 1.00
Calcaneofibular distance	0.96	0.90, 0.98	0.93	0.82, 0.97
Subtalar horizontal angle, 50%	0.75	0.46, 0.89	0.92	0.80, 0.97
Subtalar horizontal angle, 75%	0.74	0.44, 0.89	0.90	0.75, 0.96
Subtalar horizontal angle, 25%	0.73	0.43, 0.89	0.88	0.71, 0.95
Sagittal view				
Medial cuneiform to floor distance	0.99	0.97, 1.00	0.96	0.89, 0.98
Cuboid to floor distance	0.95	0.86, 0.98	0.96	0.90, 0.99
Navicular to floor distance	0.95	0.87, 0.98	0.95	0.87, 0.98
Cuboid to skin distance	0.93	0.83, 0.97	0.96	0.89, 0.98
Medial cuneiform to skin distance	0.91	0.78, 0.97	0.98	0.96, 0.99
Calcaneal inclination angle	0.88	0.71, 0.95	0.95	0.87, 0.98
Navicular to skin distance	0.84	0.64, 0.94	0.92	0.81, 0.97
Talus-first metatarsal angle	0.77	0.49, 0.90	0.72	0.41, 0.88

CI confidence interval, *CT* computed tomography, *NWB* non-weightbearing, *WB* weightbearing

Table 15.2 Interobserver reliability of CT-based measurements of adult-acquired flatfoot deformity in 20 patients

Measurement by view	NWB images		WB images	
	ICC	classification[a]	ICC	classification[a]
Axial view				
Talonavicular coverage angle	0.55	Moderate	0.39	Fair
Talus-first metatarsal angle	0.49	Moderate	0.54	Moderate
Coronal view				
Calcaneofibular distance	0.90	Almost perfect	0.85	Almost perfect
Forefoot arch angle	0.95	Almost perfect	0.96	Almost perfect
Medial cuneiform to floor distance	0.99	Almost perfect	0.99	Almost perfect
Medial cuneiform to skin distance	0.95	Almost perfect	0.96	Almost perfect
Navicular to floor distance	0.94	Almost perfect	0.99	Almost perfect
Navicular to skin distance	0.89	Almost perfect	0.97	Almost perfect
Subtalar horizontal angle, 25%	0.62	Substantial	0.68	Substantial

Table 15.2 (continued)

Measurement by view	NWB images		WB images	
	ICC	classification[a]	ICC	classification[a]
Subtalar horizontal angle, 75%	0.60	Moderate	0.64	Substantial
Subtalar horizontal angle, 50%	0.59	Moderate	0.62	Substantial
Sagittal view				
Calcaneal inclination angle	0.79	Substantial	0.75	Substantial
Cuboid to floor distance	0.96	Almost perfect	0.94	Almost perfect
Cuboid to skin distance	0.95	Almost perfect	0.96	Almost perfect
Medial cuneiform to floor distance	0.76	Substantial	0.96	Almost perfect
Medial cuneiform to skin distance	0.77	Substantial	0.97	Almost perfect
Navicular to floor distance	0.96	Almost perfect	0.96	Almost perfect
Navicular to skin distance	0.88	Almost perfect	0.83	Almost perfect
Talus-first metatarsal angle	0.65	Substantial	0.39	Fair

CT computed tomography, *ICC* intraclass correlation coefficient, *NWB* non-weightbearing, *WB* weightbearing
[a]ICC agreement was classified as follows: 0.81–0.99, almost perfect; 0.61–0.80, substantial; 0.41–0.60, moderate; 0.21–0.40, fair; and <0.20, slight

Table 15.3 CT-based measurements in 20 patients with adult-acquired flatfoot deformity

Measurement by view	NWB images		WB images	
	Mean	95% CI	Mean	95% CI
Axial view				
Talus-first metatarsal angle (°)	13	10, 15	20	17, 23
Talonavicular coverage angle (°)	21	18, 24	30	27, 34
Coronal view				
Calcaneofibular distance (mm)	6.0	5.5, 6.5	5.0	4.5, 5.5
Medial cuneiform to skin distance (mm)	20	19, 21	16	15, 17
Navicular to skin distance (mm)	25	24, 26	19	17, 20
Medial cuneiform to floor distance (mm)	29	28, 31	18	17, 19
Navicular to floor distance (mm)	38	36, 40	23	22, 25
Subtalar horizontal angle, 25% (°)	23	22, 24	25	24, 27
Subtalar horizontal angle, 50% (°)	15	14, 16	18	16, 20
Subtalar horizontal angle, 75% (°)	9.8	8.3, 11	13	11, 15
Forefoot arch angle (°)	13	12, 15	3.0	1.4, 4.6
Sagittal view				
Cuboid to skin distance (mm)	20	19, 21	16	15, 17
Cuboid to floor distance (mm)	22	21, 23	17	16, 18
Medial cuneiform to skin distance (mm)	20	19, 22	16	15, 17
Medial cuneiform to floor distance (mm)	29	27, 31	18	17, 19
Navicular to skin distance (mm)	26	25, 28	19	18, 21
Navicular to floor distance (mm)	38	36, 40	23	22, 25
Calcaneal inclination angle (°)	16	15, 17	15	14, 16
Talus-first metatarsal angle (°)	14	13, 16	24	22, 26

CI confidence interval, *CT* computed tomography, *NWB* non-weightbearing, *WB* weightbearing

Table 15.4 Differences between weightbearing and non-weightbearing CT-based measurements of adult-acquired flatfoot deformity in 20 patients

Measurement by view	Difference of the means	95% CI	*P*
Axial view			
Talus-first metatarsal angle (°)	7.2	3.6, 11	<0.0001
Talonavicular coverage angle (°)	9.1	4.4, 14	0.0002
Coronal view			
Medial cuneiform to skin distance (mm)	−4.5	−5.9, −3.1	<0.0001
Navicular to skin distance (mm)	−6.2	−8.1, −4.3	<0.0001
Medial cuneiform to floor distance (mm)	−11	−13, −9.1	<0.0001
Navicular to floor distance (mm)	−15	−18, −12	<0.0001
Forefoot arch angle (°)	−10	−13, −8.0	<0.0001
Calcaneofibular distance (mm)	−1.0	−1.7, −0.3	0.0035
Subtalar horizontal angle, 50% (°)	3.0	0.8, 5.2	0.0070
Subtalar horizontal angle, 75% (°)	3.5	0.9, 6.1	0.0070
Subtalar horizontal angle, 25% (°)	2.2	0.2, 4.2	0.0310
Sagittal view			
Cuboid to skin distance (mm)	−4.1	−5.4, −2.8	<0.0001
Cuboid to floor distance (mm)	−5.3	−6.8, −3.8	<0.0001
Medial cuneiform to skin distance (mm)	−4.8	−6.3, −3.3	<0.0001
Medial cuneiform to floor distance (mm)	−11	−13, −8.7	<0.0001
Navicular to skin distance (mm)	−7.2	−9.6, −4.8	<0.0001
Navicular to floor distance (mm)	−15	−17, −12	<0.0001
Talus-first metatarsal angle (°)	9.8	7.2, 12	<0.0001
Calcaneal inclination angle (°)	−1.1	−2.6, 0.4	0.1446

CI confidence interval, *CT* computed tomography

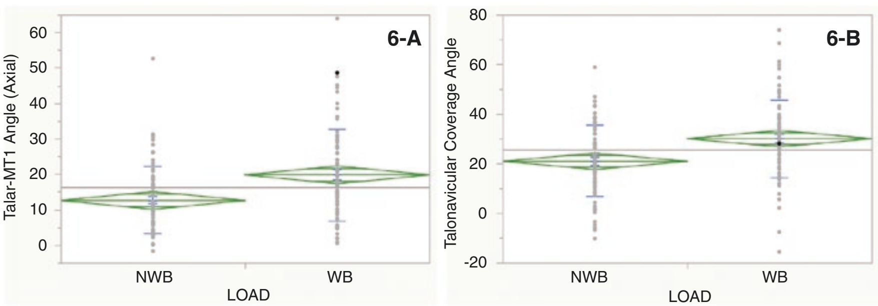

Fig. 15.6 Graphic plots of mean values for non-weight bearing (NWB) and weight bearing (WB) measurements in the axial plane: (**a**) talus-first metatarsal angle; (**b**) talonavicular coverage angle

In the axial plane (Fig. 15.6), WB measurements demonstrated a significant mean increase in forefoot abduction, with increased talus-first metatarsal angle (7.2°, 95% CI: 3.6–11°) and talonavicular coverage angle (9.1°, 95% CI: 4.4–14°).

In the coronal plane (Fig. 15.7), WB measurements showed increased collapse of the longitudinal and transverse arches of the foot and increased hindfoot valgus alignment with decreased mean forefoot arch angle (11°, 95% CI: 8.0–13°); decreased navicular to skin distance (6.2 mm, 95% CI: 4.3–8.1 mm); decreased navicular to floor distance (15 mm, 95% CI: 12–18 mm); decreased medial cuneiform to skin distance (4.5 mm, 95% CI: 3.1–5.9 mm); decreased medial cuneiform to floor distance (11 mm, 95% CI: 9.1–13 mm); decreased calcaneofibular distance (1.0 mm, 95% CI: 0.3–1.7 mm); and increased subtalar horizontal angles at posterior position (2.2°, 95% CI: 0.2–4.2°), middle position (3.0°, 95% CI: 0.8–5.2°), and anterior position (3.5°, 95% CI: 0.9–6.1°) of the subtalar joint.

In the sagittal plane (Fig. 15.8), WB images demonstrated increased collapse of the longitudinal arch of the foot, with increased mean talus-first metatarsal angle (9.8°, 95% CI: 7.2–12°), decreased navicular to skin distance (7.2 mm, 95% CI: 4.8–9.6 mm), decreased navicular to floor distance (15 mm, 95% CI: 12–17 mm), decreased cuboid to skin distance (4.1 mm, 95% CI: 2.8–5.4 mm), decreased cuboid to floor distance (5.3 mm, 95% CI:I 3.8–6.8 mm), decreased medial cuneiform to skin distance (4.8 mm, 95% CI: 3.3–6.3 mm), and decreased cuneiform to floor distance (10.9 mm, 95% CI: 8.7–13 mm).

Discussion

To our knowledge, this is the first prospective study to use CBCT images to compare the effect of standing WB on measurements traditionally used in the staging of AAFD. Although conventional WB radiograph measurements for AAFD have been validated in multiple studies [17, 32, 37], the literature is sparse regarding the role of the WB CT in the assessment of patients with this deformity, with most studies inducing simulated WB [18, 38–40].

The age and BMI of patients in our study population were similar to those in populations with AAFD, who are typically older and have a higher rate of obesity than the general population [41]. However, the most common cause of AAFD is posterior tibial tendon dysfunction, which is more common in woman than in men [42]. Despite this, 60% of our patients were men.

We found overall substantial to almost perfect intraobserver and interobserver reliabilities for the parameters evaluated, with results slightly favoring WB images over NWB images. This may be attributable to the fact that the real floor line was definable in the WB images, which was not the case in the NWB images, in which the "floor line" was represented by the upper surface of the foam where the foot rested during image acquisition. We believe this may have contributed to the variability in measurements. In addition, reliability was higher in measurements that involved the use of distances compared with angle determinations. As expected, the addition of a second line to build an angle was also added to the intraobserver and interobserver variability.

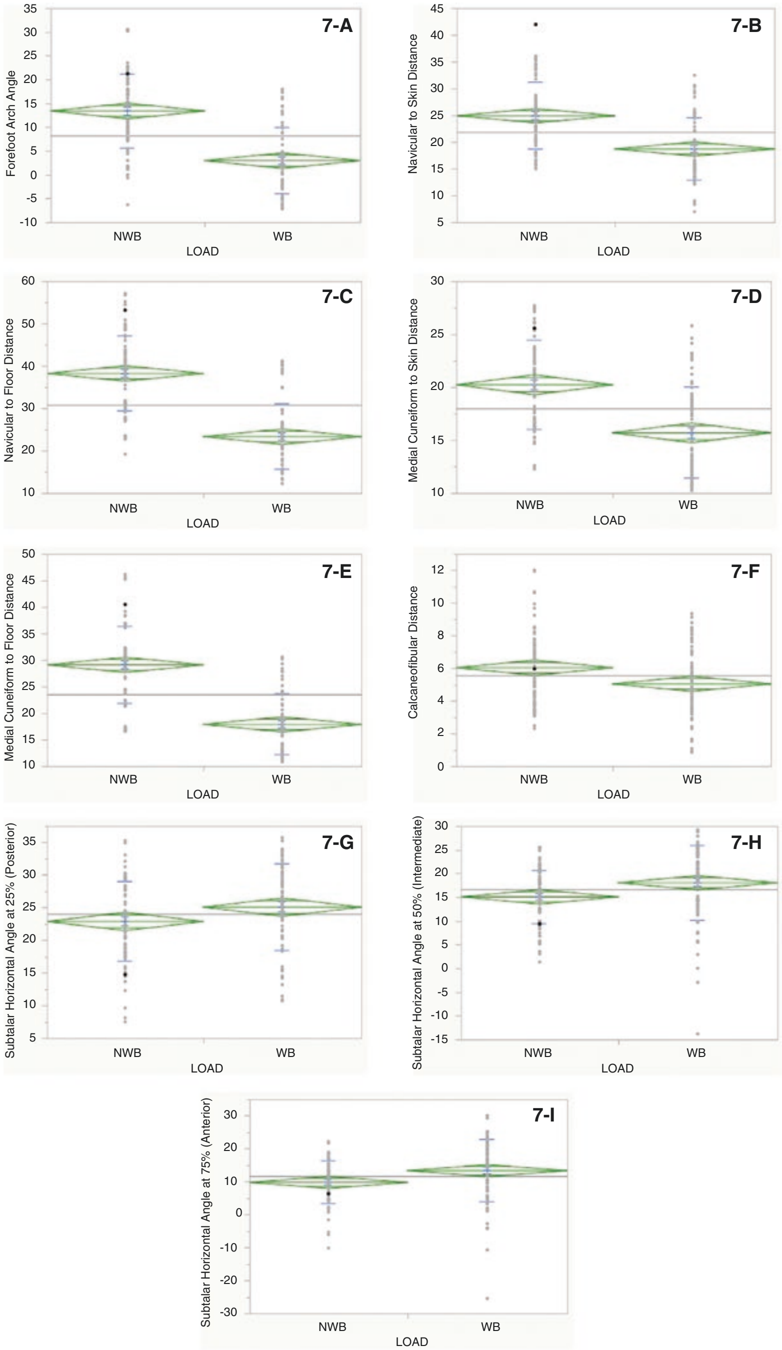

Fig. 15.7 Graphic plots of mean values for non-weight bearing (NWB) and weight bearing (WB) measurements in the coronal plane: (**a**) forefoot arch angle; (**b**) navicular to skin distance; (**c**) navicular to floor distance; (**d**) medial cuneiform to skin distance; (**e**) medial cuneiform to floor distance; (**f**) calcaneofibular distance; (**g**) subtalar horizontal angle at 25%, (**h**) subtalar horizontal angle at 50%; (**i**) subtalar horizontal angle at 75%

The measurements performed in the axial plane demonstrated lower reliability compared with other planes. This may be attributable to the 3D component of the deformity and increased complexity in finding a plane that contained both bone structures used to build the measurement. Subtle modifications in the axial plane were frequently required to include both landmark osseous structures in the same image.

In contrast to prior studies [17, 21, 43, 44], we found relative low interobserver reliability for the talus-first metatarsal angle in both sagittal and axial planes. This represents an important negative finding because the sagittal talus-first metatarsal angle, or Meary's angle, is considered an important index of arch collapse and one of the best measurements available to grade AAFD [17]. This finding may be because, as in the axial plane, it was difficult to find a perfect sagittal plane that included talus and first metatarsal in the same image.

Similar to the work by Ferri et al. [22] that demonstrated the value of simulated WB CT in the evaluation of osseous collapse and deformity in patients with pes planus, our study showed that CBCT is also capable of demonstrating worsening of AAFD during physiological WB scan acquisition. When compared with NWB images, WB CBCT images showed significantly increased deformity for almost all parameters evaluated. In the axial view, the talus-first metatarsal angle and talonavicular coverage angle progressed by 57% and 43%, respectively, reflecting the increased abduction of the forefoot under WB.

In the coronal plane, measurements representing increased arch collapse were significantly more pronounced in WB images compared with NWB images. There was a 78% decrease in the forefoot arch angle; 25% and 39% decreases in navicular to skin and navicular to floor distances, respectively; and 22% and 38% decreases in medial cuneiform to skin and to floor distances, respectively. Similar results were found for hindfoot valgus deformity parameters, including a 16% decrease in the calcaneofibular distance and 9%, 19%, and 36% increases in the subtalar horizontal angle at posterior, middle, and anterior positions, respectively.

Regarding the subtalar horizontal angle, we found similar results to those of prior studies [19, 25, 30], with a tendency to progression of valgus alignment from anterior to posterior. This tendency was found in both NWB and WB images (Fig. 15.9).

In the sagittal plane, measurements representing arch collapse were significantly more pronounced in the WB images compared with NWB images, with an increase of 69% in the talus-first metatarsal angle; decreases of 27% and 38% in the navicular to skin and navicular to floor distances, respectively; decreases of 20% and 23% in the cuboid to skin and cuboid to floor distances, respectively; and decreases of 23% and 37% in the medial cuneiform to skin and medial cuneiform to floor distances, respectively. The only measurement that was not significantly different between WB and NWB images was the calcaneal inclination angle, although it was 7% less in the WB images.

This study has several limitations. First, we did not compare WB and NWB CBCT measurements in asymptomatic control subjects. These measurements may vary between WB and NWB scan acquisitions, even in asymptomatic patients without flatfoot deformity. Second, we had a relatively small sample size. However,

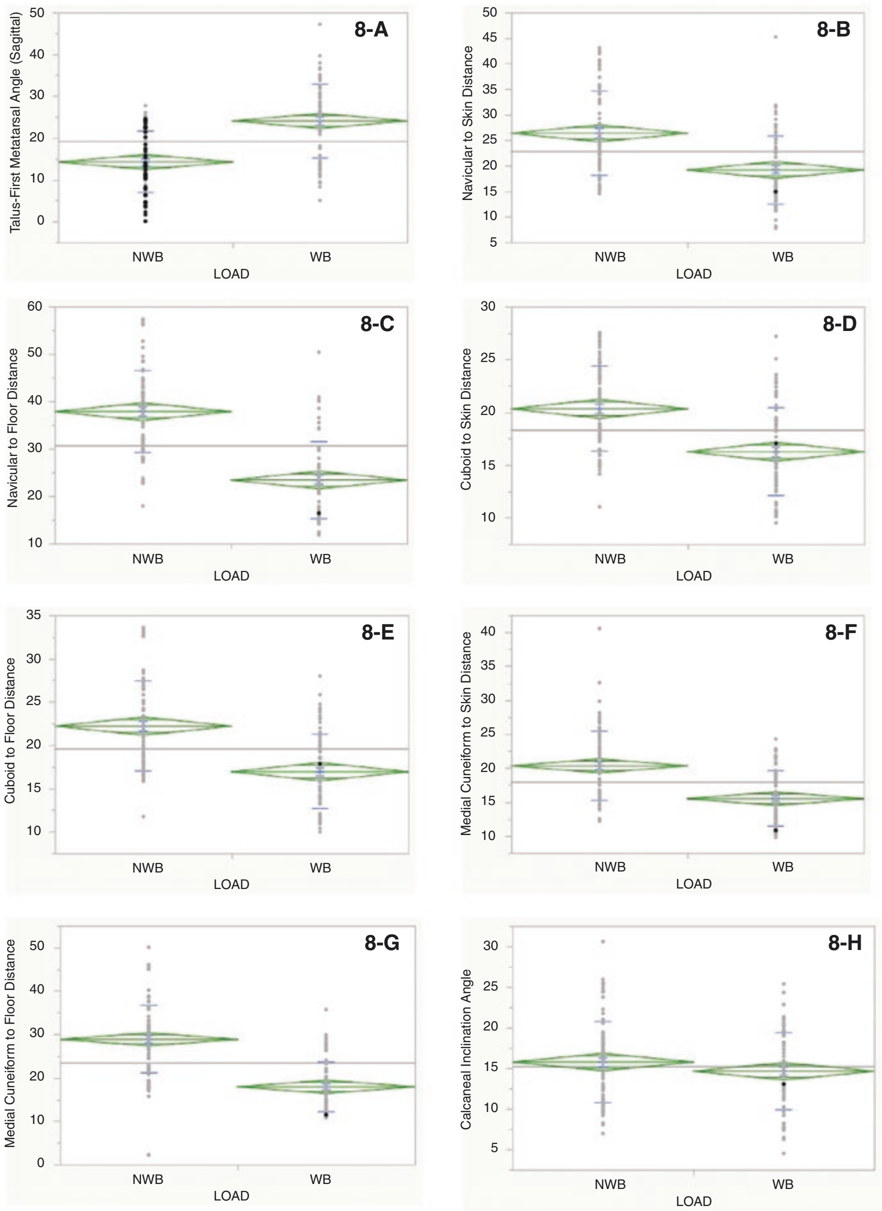

Fig. 15.8 Graphic plots of mean values for non-weight bearing (NWB) and weight bearing (WB) measurements in the sagittal plane: (**a**) talus-first metatarsal angle; (**b**) navicular to skin distance; (**c**) navicular to floor distance; (**d**) cuboid to skin distance; (**e**) cuboid to floor distance; (**f**) medial cuneiform to skin distance; (**g**) medial cuneiform to floor distance; (**h**) calcaneal inclination angle

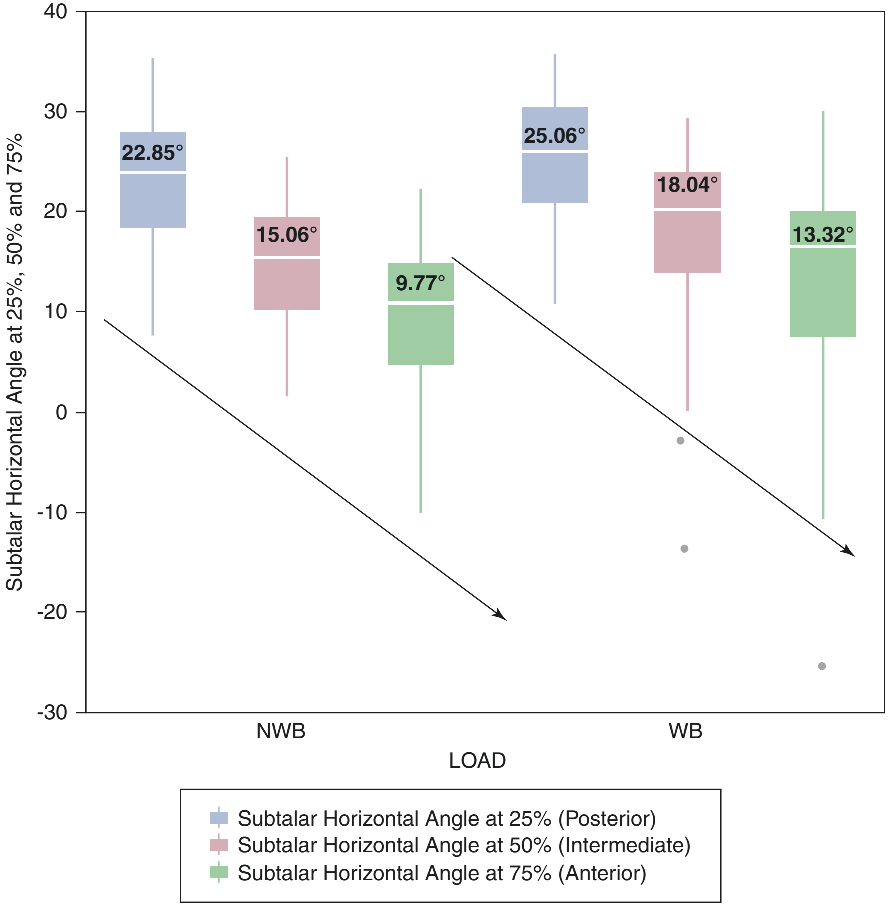

Fig. 15.9 Graphic plots demonstrating mean values for subtalar horizontal angle measurements at 25% (posterior), 50% (intermediate), and 75% (anterior) of the longitudinal length of the subtalar joint in non-weight bearing (NWB) and weight bearing (WB) images

significant results suggest adequate power to demonstrate the effect size that can support our conclusions. Third, we could not visualize the whole length of the first metatarsal, especially its distal aspect. This was a limitation in the image acquisition of the CBCT extremity scanner used in the study. This impediment greatly influenced the low reliability for all measurements that involved the assessment of the first metatarsal axis. Fourth, some of the differences in the measurements when comparing NWB and WB images, even in the presence of statistical significance, might not be clinically important. These differences could be caused by measurement error. Another important limitation is that no sample size calculation was performed prospectively. However, even our relatively small sample allowed us to detect differences of at least 10% of the mean value for 17 of 19 measurements when comparing NWB and WB images [45].

In conclusion, measurements analogous to traditional AAFD radiographic measurements are obtainable using high-resolution 3D CBCT imaging, which enables reliable assessment during physiological upright WB. In patients with AAFD, measurements demonstrating increased severity of the disease were more pronounced in the WB images compared with NWB images. Future studies are needed to evaluate the role of WB 3D CBCT in routine clinical practice, its diagnostic and therapeutic role, and its ability to assess correction of the deformity after surgical treatment. Additionally, improvements in software tools that could facilitate the choice of the correct image plane to be used for each of the measurements, allowance of a true 3D measurement, and a more precise guideline definition of individual axes for each foot and ankle bone are important next steps for future research.

References

1. de Cesar Netto C, Schon LC, Thawait GK, da Fonseca LF, Chinanuvathana A, Zbijewski WB, Siewerdsen JH, Demehri S. Flexible adult acquired flatfoot deformity: comparison between weight-bearing and non-weight-bearing measurements using cone-beam computed tomography. J Bone Joint Surg Am. 2017;99(18):e98. https://doi.org/10.2106/JBJS.16.01366.
2. Johnson KA. Tibialis posterior tendon rupture. Clin Orthop. 1983;177:140–7.
3. Mann RA, Thompson FM. Rupture of the posterior tibial tendon causing flat foot. Surgical treatment. J Bone Joint Surg Am. 1985;67:556–61.
4. Johnson KA, Strom DE. Tibialis posterior tendon dysfunction. Clin Orthop. 1989;239:196–206.
5. Gazdag AR, Cracchiolo A III. Rupture of the posterior tibial tendon. Evaluation of injury of the spring ligament and clinical assessment of tendon transfer and ligament repair. J Bone Joint Surg Am. 1997;79:675–81.
6. Deland JT. Adult-acquired flatfoot deformity. J Am Acad Orthop Surg. 2008;16:399–406.
7. Niki H, Ching RP, Kiser P, Sangeorzan BJ. The effect of posterior tibial tendon dysfunction on hindfoot kinematics. Foot Ankle Int. 2001;22:292–300.
8. Shibuya N, Ramanujam CL, Garcia GM. Association of tibialis posterior tendon pathology with other radiographic findings in the foot: a case-control study. J Foot Ankle Surg. 2008;47:546–53.
9. Deland JT, de Asla RJ, Sung IH, Ernberg LA, Potter HG. Posterior tibial tendon insufficiency: which ligaments are involved? Foot Ankle Int. 2005;26:427–35.
10. Mosier SM, Pomeroy G, Manoli A 2nd. Pathoanatomy and etiology of posterior tibial tendon dysfunction. Clin Orthop. 1999;365:12–22.
11. Deland JT, Page A, Sung IH, O'Malley MJ, Inda D, Choung S. Posterior tibial tendon insufficiency results at different stages. HSS J. 2006;2:157–60.
12. Myerson MS. Adult acquired flatfoot deformity: treatment of dysfunction of the posterior tibial tendon. Instr Course Lect. 1997;46:393–405.
13. Vora AM, Tien TR, Parks BG, Schon LC. Correction of moderate and severe acquired flexible flatfoot with medializing calcaneal osteotomy and flexor digitorum longus transfer. J Bone Joint Surg Am. 2006;88:1726–34.
14. Coughlin MJ, Mann RA, Saltzman CL. Surgery of the foot and ankle. Philadelphia: Mosby Elsevier; 2007.
15. Montagne J, Chevrot A, Galmiche JM. Atlas of foot radiology. New York: Masson Publishing USA, Inc; 1981.
16. Perry MD, Mont MA, Einhorn TA, Waller JD. The validity of measurements made on standard foot orthoroentgenograms. Foot Ankle Int. 1992;13:502–7.

17. Younger AS, Sawatzky B, Dryden P. Radiographic assessment of adult flatfoot. Foot Ankle Int. 2005;26:820–5.
18. Ananthakrisnan D, Ching R, Tencer A, Hansen ST Jr, Sangeorzan BJ. Subluxation of the talocalcaneal joint in adults who have symptomatic flatfoot. J Bone Joint Surg Am. 1999;81:1147–54.
19. Apostle KL, Coleman NW, Sangeorzan BJ. Subtalar joint axis in patients with symptomatic peritalar subluxation compared to normal controls. Foot Ankle Int. 2014;35:1153–8.
20. Ellis SJ. Peritalar symposium: determining the talus orientation and deformity of planovalgus feet using weightbearing multiplanar axial imaging. Foot Ankle Int. 2012;33:444–9.
21. Ellis SJ, Deyer T, Williams BR, Yu JC, Lehto S, Maderazo A, Pavlov H, Deland JT. Assessment of lateral hindfoot pain in acquired flatfoot deformity using weightbearing multiplanar imaging. Foot Ankle Int. 2010;31:361–71.
22. Ferri M, Scharfenberger AV, Goplen G, Daniels TR, Pearce D. Weightbearing CT scan of severe flexible pes planus deformities. Foot Ankle Int. 2008;29:199–204.
23. Haleem AM, Pavlov H, Bogner E, Sofka C, Deland JT, Ellis SJ. Comparison of deformity with respect to the talus in patients with posterior tibial tendon dysfunction and controls using multiplanar weight-bearing imaging or conventional radiography. J Bone Joint Surg Am. 2014;96:e63.
24. Kido M, Ikoma K, Imai K, Tokunaga D, Inoue N, Kubo T. Load response of the medial longitudinal arch in patients with flatfoot deformity: in vivo 3D study. Clin Biomech (Bristol, Avon). 2013;28:568–73.
25. Probasco W, Haleem AM, Yu J, Sangeorzan BJ, Deland JT, Ellis SJ. Assessment of coronal plane subtalar joint alignment in peritalar subluxation via weight-bearing multiplanar imaging. Foot Ankle Int. 2015;36:302–9.
26. Carrino JA, Al Muhit A, Zbijewski W, Thawait GK, Stayman JW, Packard N, Senn R, Yang D, Foos DH, Yorkston J, Siewerdsen JH. Dedicated cone-beam CT system for extremity imaging. Radiology. 2014;270:816–24.
27. Demehri S, Muhit A, Zbijewski W, Stayman JW, Yorkston J, Packard N, Senn R, Yang D, Foos D, Thawait GK, Fayad LM, Chhabra A, Carrino JA, Siewerdsen JH. Assessment of image quality in soft tissue and bone visualization tasks for a dedicated extremity cone-beam CT system. Eur Radiol. 2015;25:1742–51.
28. Sangeorzan BJ, Mosca V, Hansen ST Jr. Effect of calcaneal lengthening on relationships among the hindfoot, midfoot, and forefoot. Foot Ankle Int. 1993;14:136–41.
29. Cody EA, Williamson ER, Burket JC, Deland JT, Ellis SJ. Correlation of talar anatomy and subtalar joint alignment on weightbearing computed tomography with radiographic flatfoot parameters. Foot Ankle Int. 2016;37:874–81.
30. Colin F, Horn Lang T, Zwicky L, Hintermann B, Knupp M. Subtalar joint configuration on weightbearing CT scan. Foot Ankle Int. 2014;35:1057–62.
31. Arangio GA, Wasser T, Rogman A. Radiographic comparison of standing medial cuneiform arch height in adults with and without acquired flatfoot deformity. Foot Ankle Int. 2006;27:636–8.
32. Chadha H, Pomeroy G, Manoli A 2nd. Radiologic signs of unilateral pes planus. Foot Ankle Int. 1997;18:603–4.
33. Iossi M, Johnson JE, McCormick JJ, Klein SE. Short-term radiographic analysis of operative correction of adult acquired flatfoot deformity. Foot Ankle Int. 2013;34:781–91.
34. Coughlin MJ, Kaz A. Correlation of Harris mats, physical exam, pictures, and radiographic measurements in adult flatfoot deformity. Foot Ankle Int. 2009;30:604–12.
35. Landis JR, Koch GG. The measurement of observer agreement for categorical data. Biometrics. 1977;33:159–74.
36. Meyers CR. Measurement in physical education. 2nd ed. New York: Ronald Press Company; 1974.
37. Saltzman CL, Brandser EA, Berbaum KS, DeGnore L, Holmes JR, Katcherian DA, Teasdall RD, Alexander IJ. Reliability of standard foot radiographic measurements. Foot Ankle Int. 1994;15:661–5.

38. Greisberg J, Hansen ST Jr, Sangeorzan B. Deformity and degeneration in the hindfoot and midfoot joints of the adult acquired flatfoot. Foot Ankle Int. 2003;24:530–4.
39. Kido M, Ikoma K, Imai K, Maki M, Takatori R, Tokunaga D, Inoue N, Kubo T. Load response of the tarsal bones in patients with flatfoot deformity: in vivo 3D study. Foot Ankle Int. 2011;32:1017–22.
40. Malicky ES, Crary JL, Houghton MJ, Agel J, Hansen ST Jr, Sangeorzan BJ. Talocalcaneal and subfibular impingement in symptomatic flatfoot in adults. J Bone Joint Surg Am. 2002;84-a:2005–9.
41. Bare AA, Haddad SL. Tenosynovitis of the posterior tibial tendon. Foot Ankle Clin. 2001;6:37–66.
42. Kohls-Gatzoulis J, Woods B, Angel JC, Singh D. The prevalence of symptomatic posterior tibialis tendon dysfunction in women over the age of 40 in England. Foot Ankle Surg. 2009;15:75–81.
43. Arunakul M, Amendola A, Gao Y, Goetz JE, Femino JE, Phisitkul P. Tripod index: a new radiographic parameter assessing foot alignment. Foot Ankle Int. 2013;34:1411–20.
44. Sensiba PR, Coffey MJ, Williams NE, Mariscalco M, Laughlin RT. Inter- and intraobserver reliability in the radiographic evaluation of adult flatfoot deformity. Foot Ankle Int. 2010;31:141–5.
45. Eng J. Sample size estimation: a glimpse beyond simple formulas. Radiology. 2004;230:606–12.

Chapter 16
Hindfoot Alignment of Adult-Acquired Flatfoot Deformity: A Comparison of Clinical Assessment and Weight Bearing Cone Beam CT Examinations

Cesar de Cesar Netto

Introduction

Adult-acquired flatfoot deformity (AFFD) represents a progressive and complex structural deformity of foot [1, 2]. Although posterior tibial tendon (PTT) dysfunction has historically been recognized as the principal culprit leading to collapse of the medial longitudinal arch (MLA) [3], further soft tissue insufficiency and underlying bony deformities have been implicated in the development of AFFD [4, 5]. Equinus contracture, spring ligament, interosseous and deltoid ligament attenuation, as well as an increased innate valgus angulation of the subtalar joint can predispose to and eventually lead to subtalar joint eversion and subsequent hindfoot valgus [4, 6].

Currently, a set of measurements based on clinical and radiographic examinations are employed to evaluate hindfoot alignment [7]. Although these measurements have been extensively described, substantial disagreement remains in clinical judgment and radiographic measures to define an accurate method for the evaluation of hindfoot alignment [8, 9]. Clinical assessment including visual evaluation and Harris mat footprint and quantitative measures such as valgus index have been defined; however they have shown to be highly unreliable due to significant interobserver variation even among experienced orthopedic surgeons [7, 8, 10].

Furthermore, radiographic assessment of hindfoot alignment is quite cumbersome. The two-dimensional nature of plain radiographs limits their accuracy, and optimal evaluation of hindfoot alignment is hampered by complex anatomy of subtalar joint [5, 11]. Besides, lack of standardized methods to evaluate the alignment is another source of disagreement [9]. Previous cohorts used distinct set of reference points as well as different hindfoot specific views including long axial view [12–14].

Based on de Cesar Netto C, Shakoor D, Roberts L, Chinanuvathana A, Mousavian A, Lintz F, Schon LC, Demehri S, Weightbearing CT International Study Group. Hindfoot Alignment of Adult Acquired Flatfoot Deformity: A Comparison of Clinical Assessment and Weightbearing Cone Beam CT Examinations. *Foot Ankle Surg*. 2018 Nov 5. pii: S1268-7731(18)30301-1. doi: https://doi.org/10.1016/j.fas.2018.10.008. [Epub ahead of print]

M. Richter et al., *Weight Bearing Cone Beam Computed Tomography (WBCT) in the Foot and Ankle*, https://doi.org/10.1007/978-3-030-31949-6_16

Some studies used angular measurements, while others employed linear measurements. Prior reports have also indicated that malpositioning during image acquisition, inconsistent angulation, or superimposition could generate considerable measurement errors [7, 15]. Therefore, radiographic measures of hindfoot alignment are associated with major fundamental flaws due to several anatomical and observer-related bias.

Cross-sectional imaging modalities including computed tomography (CT) provide enhanced, detailed visualization of hindfoot with simultaneous demonstration of different structures; however, they are only able to provide images obtained with the patient supine [16, 17]. Additionally, in patients with AFFD, hindfoot instability has been observed when a weight bearing condition is applied [18]. Therefore, due to the major impact of loading on hindfoot alignment, it is crucial to assess suspected cases in the standing position [19]. Recent developments in CT scan design have contributed to the advent of cone beam computed tomography (CBCT). This novel technique allows imaging of lower extremity in a normal upright weight bearing state. Initial studies reported excellent image quality with sufficient contrast resolution to visualize soft tissue and bone exceeding conventional radiography and multiple detector computed tomography (MDCT) [20, 21].

Considering the ability of WB CBCT to demonstrate three-dimensional deformities in a standing physiologic setup with an enhanced visualization of bony landmarks and soft tissue structures, the application of this modality in patients with AFFD has recently been demonstrated to accurately reflect the effect of body weight in this dynamic deformity [22]. Measurements used in the staging and evaluation of the deformity were also reported to be repeatable and reliable when performed not only by experts [22] but also by in-training medical personnel [23]. Also recently, significant correlation between clinical and conventional radiographic hindfoot alignment was demonstrated in patients with flexible AAFD, but the radiographic measurements of hindfoot valgus were found to be significantly more pronounced valgus alignment than the standardized clinical evaluation [23]. Thus, in this study, we intended to compare clinical assessment of hindfoot valgus alignment with different possible hindfoot alignment measurements performed on WB CBCT images, in patients with AAFD. Our hypothesis was that measurements would correlate but different degrees of valgus alignment would be found, depending on the anatomical landmarks used.

Materials and Methods

Study Design

This dual-center IRB-approved prospective study complied with the Health Insurance Portability and Accountability Act (HIPAA) and the Declaration of Helsinki. Informed consent was signed by all study participants.

Subjects

In the two involved tertiary hospital clinics, consecutive patients with clinical diagnosis of symptomatic flexible AAFD from October 2014 till June 2016 were recruited. We excluded patients who were younger than 18 years old, were not able to communicate efficiently with clinical study personnel, or were not able to stand still independently for at least 40 seconds. Individuals with the inability to bear weight and a rigid deformity or those who had standard contraindications for standard CT scans including pregnancy or those with serious medical or psychiatric issues were also not enrolled in this prospective study.

Coronal plane clinical hindfoot alignment of all study participants was measured in the physiologic WB position by the most experienced of the senior authors (LCS). Patients were instructed to stand in a comfortable and natural stance position, and the medial border of each foot was positioned over two parallel lines that were drawn into the floor, controlling for rotational misalignment. The measurement obtained here, named clinical hindfoot alignment angle (CHAA) (Fig. 16.1a), was similar to the standing tibiocalcaneal angle (STCA) and was based on clinical expertise of the senior author and evaluation of anatomical surface landmarks [8, 23].

Following clinical examination, all patients underwent WB CBCT examinations.

CBCT Imaging Technique

All CT studies were conducted using a CBCT extremity scanner (Generation II, Carestream Health Inc., Rochester, NY). All imaging studies were performed under physiological upright WB position with the patients standing with their feet almost at shoulder width, distributing body weight evenly between their both legs. We employed the same scan protocol that was described in prior studies [22, 24, 25].

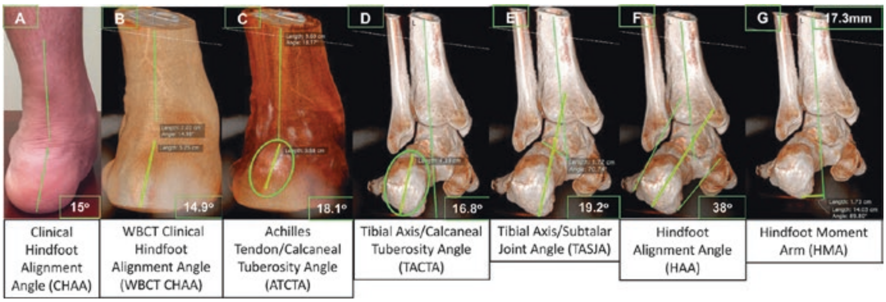

Fig. 16.1 Example of measurements performed: (**a**) Clinical hindfoot alignment angle (CHAA); (**b**) weight bearing computed tomography clinical hindfoot alignment angle (WBCT CHAA); (**c**) Achilles tendon/calcaneal tuberosity angle (ATCTA); (**d**) tibial axis/calcaneal tuberosity angle (TACTA); (**e**) tibial axis/subtalar joint angle (TASJA); (**f**) hindfoot alignment angle (HAA); (**g**) hindfoot moment arm (HMA)

WB CBCT Measurements

To develop computer-based measurements, the raw 3D data were used to generate and create axial, coronal, and sagittal image slices and were digitally transferred into our dedicated software (Vue PACS, Carestream Health, Inc., Rochester, NY). Image annotations were deleted, and a unique random number was allocated to each imaging study.

Following a mentored training protocol entailing five AAFD cases, three fellowship trained foot and ankle surgeons applied different hindfoot alignment measurements independently using the dedicated software. All observers were blinded, and the order of images was randomized. One month following the first assessment, a second set of measurements for intraobserver reliability was performed by one of the observers. The measurements were performed on the clinical reconstructed 3D images. Rotational position control was assured with the use of images where the medial aspect of the heel and the most medial aspect of forefoot and the medial eminence of the first metatarsal were in line with each other. The images used were also tangential to the floor.

The first measurement performed aimed to mimic the clinical hindfoot alignment evaluation and was named WBCT clinical hindfoot alignment angle (WBCT CHAA). It was obtained on 3D images where the windowing was set to maintain the surface anatomical landmarks, including the skin (Fig. 16.1b).

The second measurement was performed in an image with the same positioning, but the windowing was changed, removing the skin and subcutaneous, but keeping some of the overlying soft tissue structures including the Achilles tendon. That image also allowed a better evaluation of the calcaneal tuberosity, used as a bony anatomical landmark. The angle measured was formed by the longitudinal axis of the Achilles tendon and the longitudinal axis of the calcaneal tuberosity and was named Achilles tendon/calcaneal tuberosity angle (ATCTA) (Fig. 16.1c). To adequately assess the alignment of the calcaneal tuberosity, we used similar technique drawing ellipses as described by Johnson et al. [13].

The last four measurements were performed in images with the same positioning, however with different windowing that removed all the soft tissue structures, maintaining only the bony anatomy. The third measurement obtained was the tibial axis/calcaneal tuberosity angle (TACTA), which was formed by the intersection of axes of calcaneal tuberosity and the tibia (Fig. 16.1d). The fourth measurement was the tibial axis/subtalar joint angle (TASJA) formed by the intersection of tibial axis and the line connecting midpoint of the posterior facet of the subtalar joint and most inferior point of the calcaneal tuberosity (Fig. 16.1e). The fifth measurement was the hindfoot alignment angle (HAA), as described by Williamson et al. [26] (Fig. 16.1f), and the sixth measurement was the hindfoot moment arm (HMA) (Fig. 16.1g), as described by Saltzman et al. [12].

Positive values were considered valgus alignment.

Statistical Analysis

Data analysis was performed with JMP Pro version 12.2.0 (SAS Institute, Marlow-Buckinghamshire, UK). We used Shapiro-Wilk W test to evaluate the normal distribution of each set of measurements. The intraobserver and interobserver reliability was assessed by intraclass correlation coefficient (ICCs). Correlations between 0.81 and 1 were regarded almost perfect, 0.61–0.8 were considered as considered as substantial, 0.41–0.6 were considered as moderate, 0.21–0.4 were regarded as fair, 0.1–0.2 were considered as slight agreement, and less than 0.1 were regarded as poor agreement [22, 27]. Measurements obtained from clinical examination and WB CBCT images were compared by one-way ANOVA and paired Student's t-tests or the Wilcoxon rank-sum tests and nonparametric comparison for each pair by the Wilcoxon method. We used a linear regression model to evaluate the relation between values of hindfoot moment arm and measurements obtained from clinical examinations as well as WB CBCT images. *P*-values of less than .05 were considered significant.

Results

Twenty patients (12 men and 8 women) with mean age of 52.2 (range, 20–88) years old and mean body mass index value of 30.35 (range, 19–46) kg/m^2 were included in this cohort.

We observed almost perfect intraobserver agreement for all WB CBCT 3D measurements, with ICC ranging from 0.87 to 0.97. Interobserver agreement, measured by ICC, ranged from 0.51 to 0.88. A summary of the agreements is presented in Table 16.1.

A summary with the mean values and 95% confidence interval (CI) for all hindfoot valgus measures performed on the 3D WB CBCT images is outlined in

Table 16.1 Intra- and interobserver reliability for three-dimensional (3D) weightbearing (WB) cone-beam computed tomography (CBCT) hindfoot valgus measures

		Intraobserver agreement		Interobserver agreement	
		ICC	Classification	ICC	Classification
Soft tissue windowing level	WBCT clinical hindfoot alignment angle (WBCT CHAA)	0.94	Almost perfect	0.51	Moderate
	Achilles tendon/calcaneal tuberosity angle (ATCTA)	0.93	Almost perfect	0.76	Substantial
Bone windowing level	Tibial axis/calcaneal tuberosity angle (TACTA)	0.87	Almost perfect	0.63	Substantial
	Tibial axis/subtalar joint angle (TASJA)	0.90	Almost perfect	0.80	Substantial
	Hindfoot alignment angle (HAA)	0.88	Almost perfect	0.73	Substantial
	Hindfoot moment arm (HMA)	0.97	Almost perfect	0.88	Almost perfect

Abbreviations: *ICC* intraclass correlation coefficient

Table 16.2, and a graphical plot demonstrating the mean values of each measurement is shown in Fig. 16.2.

The hindfoot alignment measurements were found to significantly differ ($p < 0.0001$), and the paired comparison is detailed in Table 16.3. The mean clinical

Table 16.2 Summary of three-dimensional (3D) weightbearing (WB) cone beam computed tomography (CBCT) hindfoot valgus measures

		3D WB CBCT hindfoot alignment			
		Mean value	Standard error of the mean	Lower 95% CI	Upper 95% CI
Soft tissue windowing level	WBCT clinical hindfoot alignment angle (WBCT CHAA)	9.9°	0.53	8.9°	11.0°
	Achilles tendon/calcaneal tuberosity angle (ATCTA)	3.2°	0.95	1.3°	5.0°
Bone windowing level	Tibial axis/calcaneal tuberosity angle (TACTA)	6.1°	0.86	4.3°	7.8°
	Tibial axis/subtalar joint angle (TASJA)	7.0°	0.88	5.3°	8.8°
	Hindfoot alignment angle (HAA)	22.8°	1.22	20.4°	25.3°
	Hindfoot moment arm (HMA)	15.1 mm	0.88	13.4 mm	16.9 mm

Abbreviations: *CI* confidence interval

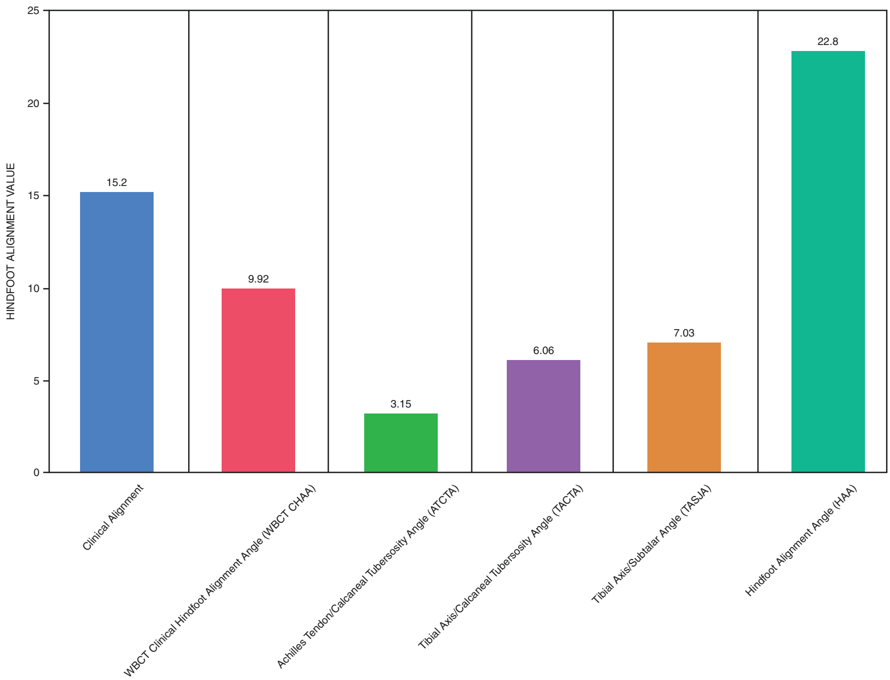

Fig. 16.2 Graphical plots representing mean values for the different measurements of hindfoot alignment

Table 16.3 Paired *T*-test comparison of clinical and WB CBCT hindfoot alignment measurements

Measurement 1	Measurement 2	Mean difference	Standard error of the difference	Lower 95% confidence interval	Upper 95% confidence interval	*P*-value
Hindfoot alignment angle (HAA)	Achilles tendon/calcaneal tuberosity angle (ATCTA)	19.69817	1.299332	17.1417	22.25467	<0.0001*
Hindfoot alignment angle (HAA)	Tibial axis/calcaneal tuberosity angle (TACTA)	16.79217	1.299332	14.2357	19.34867	<0.0001*
Hindfoot alignment angle (HAA)	Tibial axis/subtalar joint angle (TASJA)	15.81867	1.299332	13.2622	18.37517	<0.0001*
Hindfoot alignment angle (HAA)	WBCT clinical hindfoot alignment angle (WBCT CHAA)	12.92817	1.299332	10.3717	15.48467	<0.0001*
Clinical alignment	Achilles tendon/calcaneal tuberosity angle (ATCTA)	11.99967	1.837534	8.3842	15.61510	<0.0001*
Clinical alignment	Tibial axis/calcaneal tuberosity angle (TACTA)	9.09367	1.837534	5.4782	12.70910	<0.0001*
Clinical alignment	Tibial axis/subtalar joint angle (TASJA)	8.12017	1.837534	4.5047	11.73560	<0.0001*
Hindfoot alignment angle (HAA)	Clinical alignment	7.69850	1.837534	4.0831	11.31393	<0.0001*
WBCT clinical hindfoot alignment angle (WBCT CHAA)	Achilles tendon/calcaneal tuberosity angle (ATCTA)	6.77000	1.299332	4.2135	9.32650	<0.0001*
Clinical alignment	WBCT clinical hindfoot alignment angle (WBCT CHAA)	5.22967	1.837534	1.6142	8.84510	0.0047*
Tibial axis/subtalar joint angle (TASJA)	Achilles tendon/calcaneal tuberosity angle (ATCTA)	3.87950	1.299332	1.3230	6.43600	0.0031*
WBCT clinical hindfoot alignment angle (WBCT CHAA)	Tibial axis/calcaneal tuberosity angle (TACTA)	3.86400	1.299332	1.3075	6.42050	0.0032*
Tibial axis/calcaneal tuberosity angle (TACTA)	Achilles tendon/calcaneal tuberosity angle (ATCTA)	2.90600	1.299332	0.3495	5.46250	0.0260*
WBCT clinical hindfoot alignment angle (WBCT CHAA)	Tibial axis/subtalar joint angle (TASJA)	2.89050	1.299332	0.3340	5.44700	0.0268*
Tibial axis/subtalar joint angle (TASJA)	Tibial axis/calcaneal tuberosity angle (TACTA)	0.97350	1.299332	−1.5830	3.53000	0.4543

* statistically significant difference ($p < 0.05$)

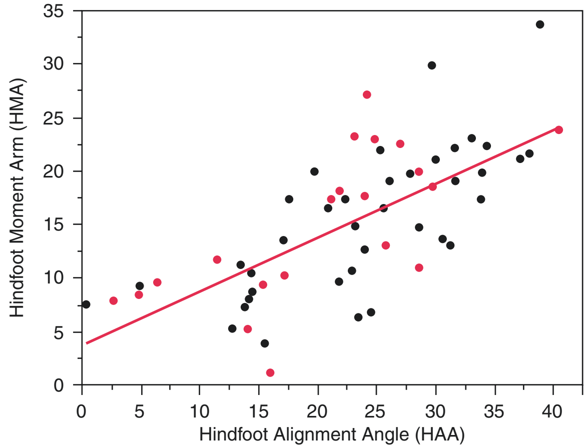

	Estimate	Standard Error	T-Ratio	P-value
Intercept	3.5540918	1.676834	2.12	0.0383*
Hindfoot Alignment Angle (HAA)	0.5066449	0.067921	7.46	<.0001*

Fig. 16.3 Graphical plotting and detailed results for linear regression model comparing hindfoot moment arm (HMA) and hindfoot alignment angle (HAA) measurements. Estimate values for intercept and HAA, standard error, T-ratio and *P*-values

hindfoot alignment angle was 15.2 (95% CI, 11.5–18.8)°. It was found to demonstrate significantly increased valgus alignment when compared to the WBCT CHAA (mean difference, 5.23°, $p = 0.0047$), ATCTA (mean difference, 12.00°, $p < 0.0001$), TACTA (mean difference, 9.10°, $p < 0.0001$), and TASJA (mean difference, 8.12°, $p < 0.0001$). However, it was found to be significantly decreased when compared to the hindfoot valgus alignment measured by the HAA (mean difference, −7.70°, $p < 0.0001$).

The mean of HMA was 15.1 (95% CI, 13.4–16.9) mm. The hindfoot moment arm was correlated significantly with the HAA ($p < 0.0001$), increasing by 0.51 mm for every degree increase in the HAA (Adjusted $R^2 = 0.48$) (Fig. 16.3). The HMA was also correlated significantly with the clinical hindfoot alignment angle ($p = 0.0087$), increasing by 0.53 mm for every degree increase in the clinical alignment angle (adjusted $R^2 = 0.29$) (Fig. 16.4).

Discussion

To the authors' knowledge, this is the first study to compare the evaluation of clinical and 3D WB CBCT hindfoot alignment in patients with AAFD. We found the different WB CBCT measurement modalities performed in this study to be repeat-

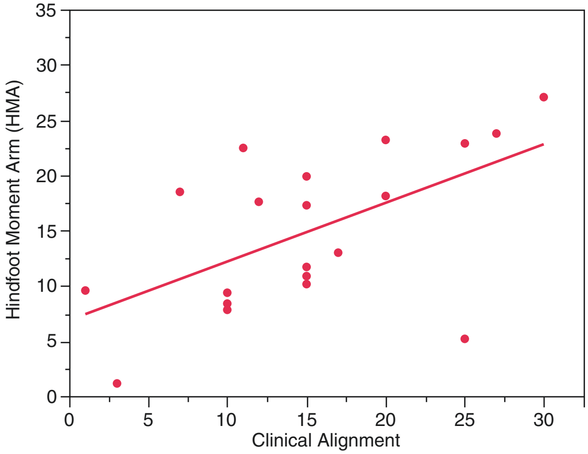

	Estimate	Standard Error	T-Ratio	P-value
Intercept	6.9155843	3.032914	2.28	0.0350*
Clinical Alignment	0.5277502	0.179387	2.94	0.0087*

Fig. 16.4 Graphical plotting and detailed results for linear regression model comparing hindfoot moment arm (HMA) and clinical alignment measurements. Estimate values for intercept and HAA, standard error, T-ratio and *P*-values

able and reliable, but to significantly differ from each other and from the clinical evaluation of hindfoot valgus alignment. Our findings demonstrated that the valgus hindfoot alignment in patients with AAFD is significantly influenced by the anatomical landmarks used to define the angular measurement. We also found that the clinical assessment of hindfoot valgus by an experienced observer was significantly different from the HAA measured in WB CBCT images, demonstrating underestimation of the hindfoot valgus by the clinical evaluation, similar to reported data for conventional radiographs [23].

The proper assessment of hindfoot alignment and valgus deviation is paramount in the diagnosis and staging of AAFD [28–31]. Various studies have looked at defining an accurate way of clinically assessing hindfoot alignment [8, 32–36], and the ability to correct the hindfoot valgus deformity intraoperatively, bringing the heel into a clinically neutral positioning, has been shown to correlate with significant improvement in clinical outcomes [37]. Accurate radiographic definition of hindfoot valgus is also important, and both hindfoot alignment and long axis views have been utilized as radiographic incidences in the assessment of WB hindfoot alignment [7, 12, 13, 38]. These radiographic views and the multiple anatomical landmarks and angles reported in the literature aim to accurately demonstrate the true bone alignment and the relationship between the axis of the tibia and the axis of the calcaneus [7, 12–14, 38–42]. Superposition and enlargement of structures as well as inadequate alignment of the foot and ankle during image acquisition have been shown to significantly hinder the evaluation of bone alignment [42–44]. The ability of standardized clinical assessment in predicting radiographic bone hindfoot alignment in patients with stage II AAFD was recently reported in the literature [23]. This study demonstrated that even though significant correlation was found between clinical and radiographic alignments, clinical assessment underestimated the radiographic valgus alignment of about 10–15°, when measured by the HAA [23].

The use of WB CBCT scans in the assessment of foot and ankle pathologies has recently begun increasing [45]. Important benefits in the assessment of 3D bone relationship and bone alignment in patients with AAFD have been demonstrated in the literature [15, 22, 23, 46–48], with low radiation dosage, extraordinary spatial resolution, and fast imaging acquisition time [49, 50].

Burssens et al. studied the use of WB CBCT in the assessment of hindfoot alignment [15]. They have shown that this imaging modality allows adequate assessment in patients with valgus and varus deformities, revealing significant differences in the measurements depending on the anatomical landmarks and angular measurements used. Even though different hindfoot alignment angles were used in our study, we also found that the measurements change significantly depending on the anatomical landmarks used. One important difference to be noted is that Burssens et al. discovered that the clinical alignment measured in WB CBCT, with the image windowing maintaining the skin and surface landmarks, demonstrated increased valgus alignment when compared to bone measurements. Similar to prior results reported in the literature using conventional radiographs [23], our study determined completely opposite results when using the HAA as described by Williamson et al. [26]. We found the HAA to demonstrate significantly increased valgus when compared to both real and WB CBCT clinical hindfoot alignment evaluation, with mean differences of approximately 13 and 8°, respectively. It is our understanding that the HAA represents the best bone measurement of hindfoot alignment, using more reliable landmarks and considering the 3D format of the calcaneus including its lateral wall and the sustentaculum tali. It is the first time the use of the HAA is reported in WB CBCT images, and we found it to be reliably performed.

Our study was also the first to evaluate the HMA, as described by Saltzman and el-Khoury [12], using 3D WB CBCT images, demonstrating almost perfect intra- and interobserver reliability. Similar to prior results in the literature [26], we found the HMA to significantly correlate with both HAA and clinical hindfoot alignment evaluation, increasing approximately 0.5 mm for every degree increase in both hindfoot alignment angulations. The amount of HMA increase found for every degree of HAA differs from the value described by Williamson et al. [26]. The authors reported in their study increases of approximately 0.8 mm for every degree increase in the HAA measured in conventional radiographs. The difference in the values could be potentially explained by a more adequate evaluation of the real 3D hindfoot alignment using WB CBCT images, when compared to conventional radiographs. Unfortunately, no certain affirmation can be made regarding this. It is important to emphasize that an adequate evaluation and a positive and significantly correlation between hindfoot alignment and HMA are important, so surgeons can predict the amount of medial slide that is needed intraoperatively when performing a calcaneal osteotomy in the treatment of patients with AAFD [37, 51].

There are some limitations of the current study to be considered. Firstly, the sample population included was relatively small, and no power analysis was performed. The statistically significant differences in the measurements found nevertheless demonstrate adequate sample size to achieve the objectives of our study. Also, the present study did not compare the differences in clinical and WB CBCT hindfoot alignment measures in control patients. It would be important to investigate in the near future if similar measurement differences would be present in patients with normal hindfoot alignment. Another important fact is that even when controlling for rotational misalignment during the clinical and WB CBCT assessment of patients, some inconsistency and error due to positioning can still exist when performing the measurements.

In conclusion, our study provides evidence that the use of 3D WB CBCT imaging can potentially help us to more adequately understand AAFD. Further to this, it can help us determine which anatomical landmarks should be used to correctly assess the true valgus hindfoot alignment in patients with this disease. We found the different WB CBCT measurements observed to be reliable and repeatable and to significantly differ from the clinical hindfoot alignment.

References

1. de Cesar Netto C, Shakoor D, Roberts L, Chinanuvathana A, Mousavian A, Lintz F, Schon LC, Demehri S, Weight Bearing CTISG. Hindfoot alignment of adult acquired flatfoot deformity: A comparison of clinical assessment and weightbearing cone beam CT examinations. Foot Ankle Surg. 2018. pii: S1268-7731(18)30301-1. https://doi.org/10.1016/j.fas.2018.10.008. [Epub ahead of print].
2. Greisberg J, Hansen ST, Sangeorzan B. Deformity and degeneration in the hindfoot and midfoot joints of the adult acquired flatfoot. Foot Ankle Int. 2003;24:530–4.
3. Giza E, Cush G, Schon LC. The flexible flatfoot in the adult. Foot Ankle Clin. 2007;12:251–71, vi.
4. Vulcano E, Deland JT, Ellis SJ. Approach and treatment of the adult acquired flatfoot deformity. Curr Rev Musculoskelet Med. 2013;6:294–303.
5. Cody EA, Williamson ER, Burket JC, Deland JT, Ellis SJ. Correlation of talar anatomy and subtalar joint alignment on weightbearing computed tomography with radiographic flatfoot parameters. Foot Ankle Int. 2016;37(8):874–81. https://doi.org/10.1177/1071100716646629.
6. Ozan F, Doğar F, Gençer K, Koyuncu Ş, Vatansever F, Duygulu F, Altay T. Symptomatic flexible flatfoot in adults: subtalar arthroereisis. Ther Clin Risk Manag. 2015;11:1597.
7. Buck FM, Hoffmann A, Mamisch-Saupe N, Espinosa N, Resnick D, Hodler J. Hindfoot alignment measurements: rotation-stability of measurement techniques on hindfoot alignment view and long axial view radiographs. AJR Am J Roentgenol. 2011;197:578–82.
8. Haight HJ, Dahm DL, Smith J, Krause DA. Measuring standing hindfoot alignment: reliability of goniometric and visual measurements. Arch Phys Med Rehabil. 2005;86:571–5.
9. Coughlin MJ, Kaz A. Correlation of Harris mats, physical exam, pictures, and radiographic measurements in adult flatfoot deformity. Foot Ankle Int. 2009;30:604–12.
10. Menz H. Clinical hindfoot measurement: a critical review of the literature. Foot. 1995;5:57–64.
11. Hirschmann A, Pfirrmann CW, Klammer G, Espinosa N, Buck FM. Upright cone CT of the hindfoot: comparison of the non-weight-bearing with the upright weight-bearing position. Eur Radiol. 2014;24:553–8.

12. Saltzman CL, el-Khoury GY. The hindfoot alignment view. Foot Ankle Int. 1995;16:572–6.
13. Johnson JE, Lamdan R, Granberry WF, Harris GF, Carrera GF. Hindfoot coronal alignment: a modified radiographic method. Foot Ankle Int. 1999;20:818–25.
14. Reilingh ML, Beimers L, Tuijthof GJ, Stufkens SA, Maas M, van Dijk CN. Measuring hindfoot alignment radiographically: the long axial view is more reliable than the hindfoot alignment view. Skelet Radiol. 2010;39:1103–8.
15. Burssens A, Peeters J, Buedts K, Victor J, Vandeputte G. Measuring hindfoot alignment in weight bearing CT: a novel clinical relevant measurement method. Foot Ankle Surg. 2016;22:233–8.
16. Seltzer SE, Weissman BN, Braunstein EM, Adams DF, Thomas WH. Computed tomography of the hindfoot. J Comput Assist Tomogr. 1984;8:488–97.
17. Van Bergeyk AB, Younger A, Carson B. CT analysis of hindfoot alignment in chronic lateral ankle instability. Foot Ankle Int. 2002;23:37–42.
18. Kido M, Ikoma K, Imai K, Tokunaga D, Inoue N, Kubo T. Load response of the medial longitudinal arch in patients with flatfoot deformity: in vivo 3D study. Clin Biomech. 2013;28:568–73.
19. Haleem AM, Pavlov H, Bogner E, Sofka C, Deland JT, Ellis SJ. Comparison of deformity with respect to the talus in patients with posterior tibial tendon dysfunction and controls using multiplanar weight-bearing imaging or conventional radiography. J Bone Joint Surg Am. 2014;96:e63.
20. Tuominen EK, Kankare J, Koskinen SK, Mattila KT. Weight-bearing CT imaging of the lower extremity. Am J Roentgenol. 2013;200:146–8.
21. Thawait GK, Demehri S, AlMuhit A, Zbijweski W, Yorkston J, Del Grande F, Zikria B, Carrino JA, Siewerdsen JH. Extremity cone-beam CT for evaluation of medial tibiofemoral osteoarthritis: initial experience in imaging of the weight-bearing and non-weight-bearing knee. Eur J Radiol. 2015;84:2564–70.
22. de Cesar Netto C, Schon LC, Thawait GK, da Fonseca LF, Chinanuvathana A, Zbijewski WB, Siewerdsen JH, Demehri S. Flexible adult acquired flatfoot deformity: comparison between weight-bearing and non-weight-bearing measurements using cone-beam computed tomography. J Bone Joint Surg Am. 2017;99(18):e98. https://doi.org/10.2106/JBJS.16.01366.
23. de Cesar Netto C, Kunas GC, Soukup D, Marinescu A, Ellis SJ. Correlation of clinical evaluation and radiographic hindfoot alignment in stage II adult-acquired flatfoot deformity. Foot Ankle Int. 2018;39(7):771–9. https://doi.org/10.1177/1071100718762113.
24. Carrino JA, Al Muhit A, Zbijewski W, Thawait GK, Stayman JW, Packard N, Senn R, Yang D, Foos DH, Yorkston J. Dedicated cone-beam CT system for extremity imaging. Radiology. 2013;270:816–24.
25. Demehri S, Muhit A, Zbijewski W, Stayman J, Yorkston J, Packard N, Senn R, Yang D, Foos D, Thawait G. Assessment of image quality in soft tissue and bone visualization tasks for a dedicated extremity cone-beam CT system. Eur Radiol. 2015;25:1742–51.
26. Williamson ER, Chan JY, Burket JC, Deland JT, Ellis SJ. New radiographic parameter assessing hindfoot alignment in stage II adult-acquired flatfoot deformity. Foot Ankle Int. 2015;36:417–23.
27. Landis JR, Koch GG. The measurement of observer agreement for categorical data. Biometrics. 1977;33:159–74.
28. Bluman EM, Myerson MS. Stage IV posterior tibial tendon rupture. Foot Ankle Clin. 2007;12:341–62, viii.
29. Johnson KA. Tibialis posterior tendon rupture. Clin Orthop Relat Res. 1983;177:140–7.
30. Johnson KA, Strom DE. Tibialis posterior tendon dysfunction. Clin Orthop Relat Res. 1989;239:196–206.
31. Myerson MS. Adult acquired flatfoot deformity: treatment of dysfunction of the posterior tibial tendon. Instr Course Lect. 1997;46:393–405.
32. Grumbine NA, Santoro JP. The tendo Achillis as it relates to rearfoot position. A new classification for evaluation of calcaneal stance position. Clin Podiatr Med Surg. 1990;7:203–16.
33. Keenan AM, Bach TM. Clinicians' assessment of the hindfoot: a study of reliability. Foot Ankle Int. 2006;27:451–60.

34. Lamm BM, Mendicino RW, Catanzariti AR, Hillstrom HJ. Static rearfoot alignment: a comparison of clinical and radiographic measures. J Am Podiatr Med Assoc. 2005;95:26–33.
35. Smith-Oricchio K, Harris BA. Interrater reliability of subtalar neutral, calcaneal inversion and eversion. J Orthop Sports Phys Ther. 1990;12:10–5.
36. Slullitel G, Álvarez V, Lopez V, Calvi JP, Calvo AB. How accurate is clinical evaluation in hindfoot coronal alignment? Foot Ankle Orthopaedics. 2017;2(4) https://doi.org/10.1177/2473011417731563.
37. Conti MS, Ellis SJ, Chan JY, Do HT, Deland JT. Optimal position of the heel following reconstruction of the stage II adult-acquired flatfoot deformity. Foot Ankle Int. 2015;36:919–27.
38. Mendicino RW, Catanzariti AR, John S, Child B, Lamm BM. Long leg calcaneal axial and hindfoot alignment radiographic views for frontal plane assessment. J Am Podiatr Med Assoc. 2008;98:75–8.
39. Arangio G, Rogman A, Reed JF 3rd. Hindfoot alignment valgus moment arm increases in adult flatfoot with Achilles tendon contracture. Foot Ankle Int. 2009;30:1078–82.
40. Sutter R, Pfirrmann CW, Espinosa N, Buck FM. Three-dimensional hindfoot alignment measurements based on biplanar radiographs: comparison with standard radiographic measurements. Skelet Radiol. 2013;42:493–8.
41. Tuijthof GJ, Herder JL, Scholten PE, van Dijk CN, Pistecky PV. Measuring alignment of the hindfoot. J Biomech Eng. 2004;126:357–62.
42. Willauer P, Sangeorzan BJ, Whittaker EC, Shofer JB, Ledoux WR. The sensitivity of standard radiographic foot measures to misalignment. Foot Ankle Int. 2014;35:1334–40.
43. Baverel L, Brilhault J, Odri G, Boissard M, Lintz F. Influence of lower limb rotation on hindfoot alignment using a conventional two-dimensional radiographic technique. Foot Ankle Surg. 2017;23:44–9.
44. Saltzman CL, Brandser EA, Berbaum KS, DeGnore L, Holmes JR, Katcherian DA, Teasdall RD, Alexander IJ. Reliability of standard foot radiographic measurements. Foot Ankle Int. 1994;15:661–5.
45. Barg A, Bailey T, Richter M, Netto C, Lintz F, Burssens A, Phisitkul P, Hanrahan CJ, Saltzman CL. Weightbearing computed tomography of the foot and ankle: emerging technology topical review. Foot Ankle Int. 2017;39(3):376–86. https://doi.org/10.1177/1071100717740330.
46. Richter M, Lintz F, Zech S, Meissner SA. Combination of PedCAT weightbearing CT with pedography assessment of the relationship between anatomy-based foot center and force/pressure-based center of gravity. Foot Ankle Int. 2017;39(3):361–8. https://doi.org/10.1177/1071100717744206.
47. Richter M, Seidl B, Zech S, Hahn S. PedCAT for 3D-imaging in standing position allows for more accurate bone position (angle) measurement than radiographs or CT. Foot Ankle Surg. 2014;20:201–7.
48. Lintz F, Welck M, Bernasconi A, Thornton J, Cullen NP, Singh D, Goldberg A. 3D biometrics for hindfoot alignment using weightbearing CT. Foot Ankle Int. 2017;38:684–9.
49. Carrino JA, Al Muhit A, Zbijewski W, Thawait GK, Stayman JW, Packard N, Senn R, Yang D, Foos DH, Yorkston J, Siewerdsen JH. Dedicated cone-beam CT system for extremity imaging. Radiology. 2014;270:816–24.
50. Tuominen EK, Kankare J, Koskinen SK, Mattila KT. Weight-bearing CT imaging of the lower extremity. AJR Am J Roentgenol. 2013;200:146–8.
51. Chan JY, Williams BR, Nair P, Young E, Sofka C, Deland JT, Ellis SJ. The contribution of medializing calcaneal osteotomy on hindfoot alignment in the reconstruction of the stage II adult acquired flatfoot deformity. Foot Ankle Int. 2013;34:159–66.

Chapter 17
Influence of Investigator Experience on Reliability of Adult-Acquired Flatfoot Deformity Measurements Using Weight Bearing Computed Tomography

Cesar de Cesar Netto

Introduction

Adult-acquired flatfoot deformity (AAFD) is a complex, three-dimensional foot deformity involving failure of several static and dynamic biomechanical stabilizers [1, 2]. Loss of the medial longitudinal arch, hindfoot valgus, and mid-/forefoot abduction are the main components of the deformity [3]. The posterior tibialis tendon (PTT) is the primary dynamic stabilizer of the medial longitudinal arch, and its dysfunction is commonly associated with AAFD [4]. Some authors consider AAFD a consequence of PTT dysfunction [5, 6]. Body weight is distributed abnormally on static stabilizers, including the spring ligament, deltoid complex, and sinus tarsi ligaments. Failure of these secondary structures leads to AAFD progression [7]. Other authors consider the bony deformity as primary and PTT and other soft tissue failures as consequences [8–10].

Given the heterogeneous and complex pathophysiology of AAFD, staging systems have been developed to characterize its biomechanical derangement and optimize its treatment [5, 6, 11]. These staging systems use patients' symptoms, physical examinations, and imaging measurements obtained from conventional weight bearing radiographs [11]. Operative and non-operative treatment guidelines have been recommended for each stage, and treatment is tailored according to the severity and stage of AAFD [12]. In the initial and flexible stages, deformity is altered with load; therefore, weight bearing radiographs have been used widely to evaluate and determine AAFD stage [13]. Because of the three-dimensional (3D) and complex relationships of small osseous structures of the foot, accurate assessment of subtle changes during weight bearing is challenging using two-dimensional (2D)

Based on de Cesar Netto C, Shakoor D, Dein EJ, Zhang H, Thawait GK, Richter M, Ficke JR, Schon LC, Weightbearing CT International Study Group, Demehri S. Hindfoot Alignment of Adult Acquired Flatfoot Deformity: A Comparison of Clinical Assessment and Weight bearing Cone Beam CT Examinations. *Foot Ankle Surg*. 2018 Mar 12. pii: S1268-7731(18)30058-4. doi: https://doi.org/10.1016/j.fas.2018.03.001. [Epub ahead of print]

M. Richter et al., *Weight Bearing Cone Beam Computed Tomography (WBCT) in the Foot and Ankle*, https://doi.org/10.1007/978-3-030-31949-6_17

conventional radiographs [8, 14, 15] and usually requires a high level of clinical experience [11].

Weight bearing computed tomography (WBCT) is an emerging imaging modality that provides high-resolution 3D images and enables detailed assessment of tarsal bones during weight bearing [16, 17]. WBCT may improve precision and accuracy of the characterization of AAFD. A recent study demonstrated the superior capability of WBCT to show the collapse in flexible AAFD compared with non-weight bearing WBCT and reported considerable reliability of measurements when performed by experts [14, 17]. The objective of our study was to evaluate the intra- and interobserver reliability of AAFD measurements taken by investigators with different levels of clinical experience using WBCT images.

Material and Methods

This study complied with the Health Insurance Portability and Accountability Act and the Declaration of Helsinki. All aspects of the study were approved by our institutional review board, and written informed consent was obtained from all participants.

Study Design

In this prospective, dual-institution study, we recruited consecutive patients in our tertiary hospital clinics from September 2014 through June 2016. We included patients aged 18 years or older with a diagnosis of symptomatic, flexible AAFD. We excluded patients who were unable to stand independently for at least 40 seconds, those incapable of communicating effectively with clinical study personnel, and those with contraindications for standard CT scans.

Subjects

Nineteen patients (13 right feet, 6 left feet) were included in our study. The study group consisted of 11 men and 8 women, with a mean body mass index of 31 (range, 19–46) and a mean age of 52 (range, 20–88) years.

WBCT Imaging Technique

Imaging studies were conducted on a cone beam WBCT extremity scanner (generation II, Carestream Health Inc., Rochester, NY). Participants were scanned in a physiological upright weight bearing position, standing with their feet at shoulder width and distributing their body weight equally between both lower extremities. We applied a protocol similar to that used in previous technical assessments [16–18]. The contrast-to-noise ratio per unit of dose within the boundaries of the CT was enhanced by 90 kVp and 72 mA (6 mA and 20 msec for each frame, 600 frame acquisition). The size-specific dose estimate for WBCT ankle imaging was calculated to be approximately12 mGy.

A Farmer chamber in a stack of three 16 cm CT dose index phantoms was used to calculate the weighted CT dose index and was found to be approximately 15 mGy [12]. Images of 0.5 mm^3 isotropic voxels were reconstructed using a bone algorithm.

Measurements

The raw 3D data were used to generate axial, sagittal, and coronal image slices that were transferred digitally into Vue PACS software (Carestream Health, Inc., Rochester, NY) for computer-based measurements. Image annotations were eliminated, and a unique, random number was assigned to each study. The investigators consisted of a board-certified foot and ankle surgeon, an orthopedic surgery resident, and a medical student. Each investigator completed a training protocol with five AAFD patients who were not included in the study. After the protocol, each observer performed the measurements twice, independently and blindly, using a dedicated software. The training protocol included a standardized assessment of the full dataset of images; however, the final choice of which image to use to perform each measurement was made freely and independently by each observer. The second set of measurements was performed 30 days after the first assessment. Investigators were blinded to the patient's identification and other measurements, and the order of the patient images was randomized.

Axial Plane Measurements

The axial plane was defined as parallel to the horizontal plane, represented by the platform where the patient was standing, with the horizontal boundary of the images aligned to the axis of the first metatarsal bone. Two axial measurements were defined: the talonavicular coverage angle (Fig. 17.1a) [17, 19] and the talus-first metatarsal angle (Fig. 17.1b) [20].

Coronal Plane Measurements

The coronal plane was defined as perpendicular to the horizontal plane, with the horizontal margins of the images perpendicularly aligned to the bimalleolar ankle axis. Nine coronal measurements were defined. The first three measurements involved the

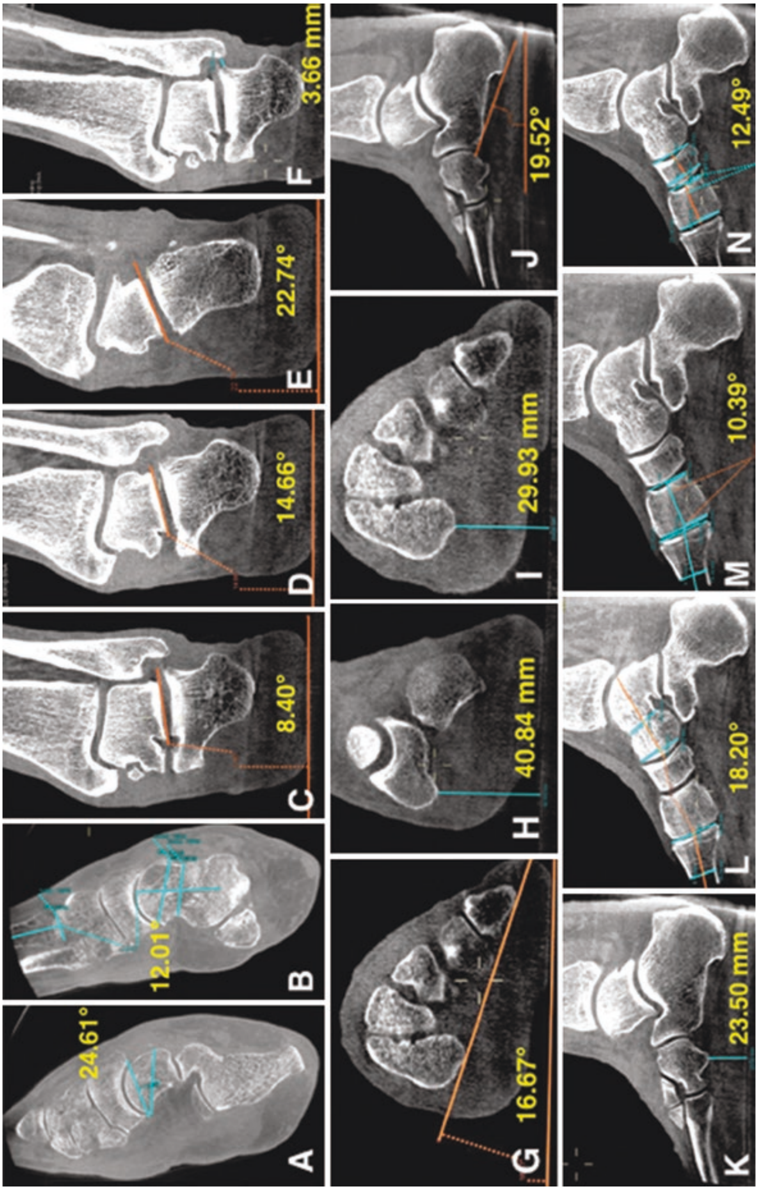

Fig. 17.1 Examples of measurements performed by 3 readers in 19 patients with adult-acquired flatfoot deformity using weight bearing computed tomography. (**a**) Talonavicular coverage angle. (**b**) Talus-first metatarsal angle (axial plane). (**c**) Subtalar horizontal angle, 75% (posterior). (**d**) Subtalar horizontal angle, 50% (midpoint). (**e**) Subtalar horizontal angle, 25% (anterior). (**f**) Calcaneal-fibular distance. (**g**) Forefoot arch angle. (**h**) Navicular to floor distance. (**i**) Medial cuneiform to floor distance. (**j**) Calcaneal inclination angle. (**k**) Cuboid to floor distance. (**l**) Talus-first metatarsal angle (sagittal plane). (**m**) Medial cuneiform-first metatarsal angle. (**n**) Navicular-medial cuneiform angle

subtalar horizontal angle, which comprises the angle formed by the intersection of the horizontal line of the floor and the tangent line to the posterior facet of the talus. The angle was measured at three levels: 75%, anterior aspect (Fig. 17.1c); 50%, midpoint (Fig. 17.1d); and 25%, posterior aspect (Fig. 17.1e) of the posterior subtalar joint length. Positive values signified valgus alignment of the subtalar joint. The fourth measurement was the calcaneal-fibular distance, which was obtained by measuring the shortest distance between the superior or lateral surface of the calcaneus and the distal part of the fibula (Fig. 17.1f). The fifth measurement was the forefoot arch angle (Fig. 17.1g) [21]. A positive value showed a relative lower positioning of the fifth metatarsal to the medial cuneiform. The sixth measurement was the navicular to skin distance [21]. The seventh measurement was the navicular to floor distance (Fig. 17.1h). The eighth measurement was the medial cuneiform to skin distance. The ninth measurement was the medial cuneiform to floor distance (Fig. 17.1i).

Sagittal Plane Measurements

The sagittal plane was defined as perpendicular to the axial and coronal planes. The second metatarsal axis was used to determine the horizontal border of the images. Ten sagittal measurements were assessed. The first was calcaneal inclination angle (Fig. 17.1j) [22]. The second and third measurements were the navicular to floor and navicular to skin distances. The fourth and fifth measurements were the cuboid to floor (Fig. 17.1k) and to cuboid to skin distances [23]. The sixth and seventh measurements were the medial cuneiform to floor and medial cuneiform to skin distances [24–26]. The eighth measurement was the talus-first metatarsal angle (Fig. 17.1l). The ninth measurement was the medial cuneiform-first metatarsal angle, which was formed by the intersection of the axes of the first metatarsal and medial cuneiform (Fig. 17.1m). The tenth measurement was the navicular-medial cuneiform angle, which was also created by the intersection of the axes of the navicular and medial cuneiform (Fig. 17.1n) [23].

The axis of short bones (i.e., navicular, medial cuneiform) was defined as a line connecting the midpoint of their proximal and distal articular surfaces. Because of a limitation in the field of view of the WBCT scan used in the study, the distal aspect of the first metatarsal could not be visualized, hindering the assessment of the true axis of the first metatarsal bone. An alternative standardized definition of the axis was used, represented by a line connecting the midpoint of the proximal articular surface and the midpoint of the width of the proximal third of the first metatarsal shaft.

Statistical Analysis

We used the Shapiro-Wilk test to assess normality of the data distribution for each measurement. The intraobserver reliability of each measurement was determined using the Pearson or Spearman correlation test, depending on the normality of the data. Intraclass correlation coefficients (ICCs) were used to assess interobserver reliability. The extent to which bias and interaction factors can decrease the ICC was also considered. Correlations were categorized as excellent, >0.74; good, 0.60–0.74; fair, 0.40–0.59; and poor, <0.40 [23, 27]. We also compared the means of each measurement among the three readers using one-way ANOVA when the data distribution was normal. For non-normally distributed data, we used Kruskal-Wallis analysis. P values of less than 0.05 were considered significant.

Results

Intraobserver Reliability

Intraobserver reliability for each of the three readers is listed in Table 17.1. All measurements showed significant intraobserver reliability ($P < 0.05$). Averaged values showed excellent intraobserver reliability for the board-certified foot and ankle surgeon ($r = 0.87$), orthopedic resident ($r = 0.86$), and medical student ($r = 0.81$).

Medial cuneiform-first metatarsal angle (sagittal plane), navicular-medial cuneiform angle (sagittal plane), and talus-first metatarsal angle (coronal plane) showed the weakest reliability among all measurements.

Interobserver Reliability

Interobserver reliability for each measurement is reported in Table 17.2. Good to excellent interobserver reliability was observed for most of the measurements performed. Talus-first metatarsal angle (in both axial and sagittal planes), talonavicular coverage angle (axial plane), navicular-medial cuneiform angle (sagittal plane), and medial cuneiform-first metatarsal angle (sagittal plane) had the weakest results, with only poor to fair reliability.

Plots of interobserver reliability are presented for measurements in the axial and coronal planes (Fig. 17.2) and in the sagittal plane (Fig. 17.3).

Measurement Differences

Mean values, confidence intervals, and comparisons of each measurement among the three investigators are reported in Table 17.3. Of the 21 measurements, we observed significant differences among the investigators in only 2 measurements: the medial cuneiform-first metatarsal angle ($P = 0.003$) and navicular-medial cuneiform angle ($P = 0.001$). In the post hoc group comparison, the medial cuneiform-first metatarsal angle measurements were different between the board-certified foot

Table 17.1 Intraobserver reliability of measurements of adult-acquired flatfoot deformity in 19 patients using weight bearing computed tomography

Measurement by view	Board-certified foot and ankle surgeon		Orthopedic surgery resident		Medical student	
	Pearson/ Spearman *r*	*P*	Pearson/ Spearman *r*	*P*	Pearson/ Spearman *r*	*P*
Axial view						
Talonavicular coverage angle	0.72	0.003	0.70	0.005	0.55	0.023
Talus-first metatarsal angle	0.65	0.005	0.63	0.008	0.43	0.031
Coronal view						
Subtalar horizontal angle, 25%	0.91	<0.001	0.91	<0.001	0.87	<0.001
Subtalar horizontal angle, 50%	0.93	<0.001	0.88	<0.001	0.87	<0.001
Subtalar horizontal angle, 75%	0.88	<0.001	0.85	<0.001	0.85	<0.001
Forefoot arch angle	0.99	<0.001	0.97	<0.001	0.94	<0.001
Navicular to skin distance	0.99	<0.001	0.97	<0.001	0.96	<0.001
Navicular to floor distance	0.98	<0.001	0.99	<0.001	0.96	<0.001
Calcaneal-fibular distance	0.92	<0.001	0.93	<0.001	0.88	<0.001
Medial cuneiform to skin distance	0.99	<0.001	0.98	<0.001	0.96	<0.001
Medial cuneiform to floor distance	0.99	<0.001	0.98	<0.001	0.98	<0.001
Sagittal view						
Calcaneal inclination angle	0.95	<0.001	0.96	<0.001	0.85	<0.001
Navicular to floor distance	0.94	<0.001	0.96	<0.001	0.92	<0.001
Navicular to skin distance	0.92	<0.001	0.91	<0.001	0.88	<0.001
Cuboid to floor distance	0.96	<0.001	0.96	<0.001	0.90	<0.001
Cuboid to skin distance	0.95	<0.001	0.94	<0.001	0.90	<0.001
Medial cuneiform to floor distance	0.96	<0.001	0.95	<0.001	0.91	<0.001
Medial cuneiform to skin distance	0.98	<0.001	0.95	<0.001	0.90	<0.001
Talus-first metatarsal angle	0.73	0.004	0.74	0.003	0.70	0.004
Medial cuneiform-first metatarsal angle	0.41	0.032	0.33	0.040	0.33	0.034

(continued)

Table 17.1 (continued)

Measurement by view	Board-certified foot and ankle surgeon		Orthopedic surgery resident		Medical student	
	Pearson/ Spearman *r*	*P*	Pearson/ Spearman *r*	*P*	Pearson/ Spearman *r*	*P*
Navicular-medial cuneiform angle	0.55	0.025	0.58	0.020	0.49	0.028
Averaged value	0.87		0.86		0.81	

Correlations were categorized as perfect agreement, 0.81–1.0; substantial, 0.61–0.80; moderate, 0.41–0.60; fair, 0.21–0.40; slight, 0.10–0.20; and poor, less than 0.10

Table 17.2 Interobserver reliability of measurements of adult-acquired flatfoot deformity in 19 patients using weight bearing computed tomography. Correlations were categorized as excellent, >0.74; good, 0.60–0.74; fair, 0.40–0.59; and poor, <0.40

Measurement by view	Intraclass correlation	Classification
Axial view		
Talonavicular coverage angle	0.56	Fair
Talus-first metatarsal angle	0.53	Fair
Coronal view		
Subtalar horizontal angle, 25%	0.68	Good
Subtalar horizontal angle, 50%	0.74	Good
Subtalar horizontal angle, 75%	0.76	Excellent
Forefoot arch angle	0.98	Excellent
Navicular to skin distance	0.98	Excellent
Navicular to floor distance	0.99	Excellent
Calcaneal-fibular distance	0.76	Excellent
Medial cuneiform to skin distance	0.98	Excellent
Medial cuneiform to floor distance	0.98	Excellent
Sagittal view		
Calcaneal inclination angle	0.76	Excellent
Navicular to floor distance	0.96	Excellent
Navicular to skin distance	0.90	Excellent
Cuboid to floor distance	0.95	Excellent
Cuboid to skin distance	0.96	Excellent
Medial cuneiform to floor distance	0.94	Excellent
Medial cuneiform to skin distance	0.98	Excellent
Talus-first metatarsal angle	0.42	Fair
Medial cuneiform-first metatarsal angle	0.21	Poor
Navicular-medial cuneiform angle	0.37	Poor
Averaged value	0.78	Excellent

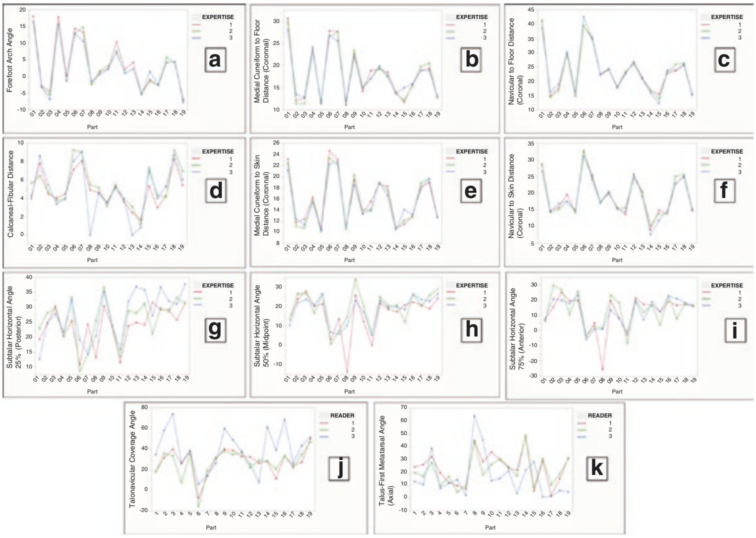

Fig. 17.2 Plots of interobserver agreement for measurements in the coronal and axial planes. Reader 1, board-certified foot and ankle surgeon; reader 2, orthopedic surgery resident; and reader 3, medical student. (**a**) Forefoot arch angle (coronal plane). (**b**) Medial cuneiform to floor distance (coronal plane). (**c**) Navicular to floor distance (coronal plane). (**d**) Calcaneal-fibular distance (coronal plane). (**e**) Medial cuneiform to skin distance (coronal plane). (**f**) Navicular to skin distance (coronal plane). (**g**) Subtalar horizontal angle, 25% (posterior). (**h**) Subtalar horizontal angle, 50% (midpoint). (**i**) Subtalar horizontal angle, 75% (anterior). (**j**) Talonavicular coverage angle (axial plane). (**k**) Talus-first metatarsal angle (axial plane)

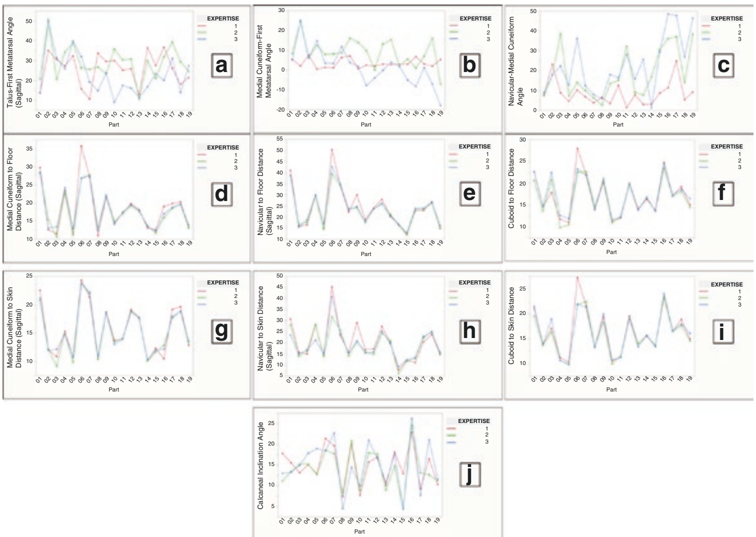

Fig. 17.3 Plots of interobserver agreement for measurements in the sagittal plane. Reader 1, board-certified foot and ankle surgeon; reader 2, orthopedic surgery resident; and reader 3, medical student. (**a**) Talus-first metatarsal angle. (**b**) Medial cuneiform-first metatarsal angle. (**c**) Navicular-medial cuneiform angle. (**d**) Medial cuneiform to floor distance. (**e**) Navicular to floor distance. (**f**) Cuboid to floor distance. (**g**) Medial cuneiform to skin distance. (**h**) Navicular to skin distance. (**i**) Cuboid to skin distance. (**j**) Calcaneal inclination angle

Table 17.3 Measurements in 19 patients with adult-acquired flatfoot deformity performed by three investigators of varying expertise using weight bearing computed tomography

	Board-certified foot and ankle surgeon		Orthopedic resident		Medical student		
Measurement by view	Mean	95% CI	Mean	95% CI	Mean	95% CI	*P*
Axial view							
Talonavicular coverage angle, degrees	27.9	20.7, 35.1	26.8	19.4, 33.9	39.2	32.0, 46.4	.032[d]
Talus-first metatarsal angle, degrees	23.1	16.7, 29.6	21.4	15.0, 27.8	16.7	10.3, 23.1	0.111
Coronal view							
Subtalar horizontal angle 25%, degrees	23.8	20.5, 27.2	25.7	22.3, 29.1	27.2	23.8, 30.6	0.376
Subtalar horizontal angle 50%, degrees	16.4	12.3, 20.4	19.5	15.4, 23.5	18.4	14.4, 22.5	0.626
Subtalar horizontal angle 75%, degrees	11.9	6.95, 16.8	13.2	8.26, 18.1	12.7	7.82, 17.6	0.971
Forefoot arch angle, degrees	3.49	0.08, 6.91	2.91	−0.51, 6.32	2.61	−0.81, 6.02	0.935
Navicular to skin distance, mm	19.1	16.4, 21.9	19.1	16.4, 21.9	18.7	16.0, 21.5	0.993
Navicular to floor distance, mm	23.5	19.7, 27.2	23.5	19.8, 27.3	23.6	19.9, 27.4	0.988
Calcaneal-fibular distance, mm	4.86	3.80, 5.91	5.34	4.29, 6.41	4.83	3.77, 5.88	0.739
Medial cuneiform to skin distance, mm	15.9	13.9, 17.9	15.6	13.6, 17.7	15.5	13.5, 17.6	0.980
Medial cuneiform to floor distance, mm	18.0	15.4, 20.7	17.9	15.2, 20.5	17.9	15.3, 20.6	0.938
Sagittal view							
Calcaneal inclination angle, degrees	14.9	12.5, 17.3	14.0	11.6, 16.4	15.0	12.6, 17.3	0.818
Navicular to floor distance, mm	24.3	20.3, 28.2	23.3	19.3, 27.3	23.8	19.9, 27.8	0.954
Navicular to skin distance, mm	20.4	16.9, 23.9	19.0	15.5, 22.5	19.3	15.8, 22.8	0.952
Cuboid to floor distance, mm	17.2	15.1, 19.3	16.7	14.6, 18.7	17.3	15.2, 19.4	0.908
Cuboid to skin distance, mm	16.5	14.5, 18.5	15.9	13.9, 17.9	16.2	14.2, 18.3	0.967
Medial cuneiform to floor distance, mm	18.5	15.8, 21.3	17.9	15.1, 20.6	18.1	15.4, 20.9	0.984
Medial cuneiform to skin distance, mm	15.5	13.5, 17.5	15.2	13.2, 17.3	15.4	13.4, 17.5	0.945
Talus-first metatarsal angle, degrees	25.7	21.5, 29.9	29.0	24.8, 33.2	23.0	18.8, 27.2	0.127

(continued)

Table 17.3 (continued)

Measurement by view	Board-certified foot and ankle surgeon		Orthopedic resident		Medical student		
	Mean	95% CI	Mean	95% CI	Mean	95% CI	*P*
Medial cuneiform-first metatarsal angle, degrees	3.39	0.19, 6.58	8.83	5.63, 12.0	1.61	−1.58, 4.81	.003[a, c]
Navicular-medial cuneiform angle, degrees	8.48	3.19, 13.8	18.6	13.3, 23.9	22.5	17.2, 27.8	.001[a, b]

CI confidence interval
[a]Significant difference between surgeon and resident ($P < 0.05$)
[b]Significant difference between surgeon and medical student ($P < 0.05$)
[c]Significant difference between resident and medical student ($P < 0.05$)
[d]Difference not confirmed in the post hoc group comparison

and ankle surgeon and the orthopedic resident ($P = 0.003$) and between the orthopedic resident and the medical student ($P = 0.005$). Navicular-medial cuneiform angle readings were different between the board-certified foot and ankle surgeon and the orthopedic resident ($P = 0.0005$) and between the board-certified foot and ankle surgeon and the medical student ($P = 0.005$). We also found significant differences among the investigators for the talonavicular coverage angle measurements ($P = 0.032$). However, in the post hoc group comparison, that difference was not confirmed.

Discussion

To our knowledge, this is the first study to evaluate the reliability of traditional measurements of AAFD using high-resolution 3D WBCT by investigators of different levels of clinical experience. Our results show that, after training, most of the evaluated measurements can be performed reliably by a medical student, an orthopedic resident, and a board-certified foot and ankle surgeon.

There has been a growing trend among foot and ankle surgeons to use WBCT in the assessment of patients with AAFD [13, 21, 23, 28–32]. This imaging modality improves our understanding of this complex 3D deformity and overcomes challenges associated with the 2D biometrics of conventional radiographs [33]. Multiple radiographic measurements have been described to assist in the staging and operative treatment algorithm for AAFD, and their intra- and interobserver reliabilities have been reported [20]. Younger et al. [20] found the talus-first metatarsal angle in the lateral view (sagittal plane) to be the most consistently accurate measurement to differentiate AAFD patients from controls, with high intraobserver ($r = 0.75$) and interobserver reliability ($r = 0.83$). They also measured cuboid to floor and medial cuneiform to floor distances in the sagittal plane, with fair intraobserver reliability ($r = 0.40$ and $r = 0.51$, respectively) and excellent interobserver reliability ($r = 0.96$

and 0.90, respectively); calcaneal inclination angle, with good intraobserver reliability ($r = 0.60$) and fair interobserver reliability ($r = 0.54$); talus-first metatarsal angle in the anteroposterior view (axial plane), with excellent intra- ($r = 0.76$) and interobserver reliability ($r = 0.86$); and the talonavicular coverage angle, with poor intraobserver ($r = 0.01$) and interobserver reliability ($r = 0.30$) [20]. Similarly, Arunakul et al. [34] showed overall excellent intraobserver reliability and good to excellent interobserver reliability between an orthopedic foot and ankle fellow and a biomechanical engineer. The authors measured the intraobserver and interobserver reliability of the talonavicular coverage angle (ICC = 0.93 and 0.85, respectively), the talus-first metatarsal angle in the sagittal plane (ICC = 0.96 and 0.69, respectively), and the calcaneal inclination angle (ICC = 0.95 and 0.98, respectively) [34].

Sensiba et al. [11] were the first to evaluate the reliability of AAFD measurements with readers of different levels of clinical experience (medical student, junior and senior orthopedic residents) using conventional and digital weight bearing radiographs. They found substantial to perfect interobserver reliability for all evaluated measurements. Interobserver reliability was especially high for the medial cuneiform-fifth metatarsal distance in the sagittal plane (0.99), an alternative way of measuring medial column height, and the calcaneal inclination angle (0.95). The authors also found substantial to perfect intraobserver reliability, with overall better results favoring the more experienced residents, with r values ranging from 0.66 to 0.98 for the medical student, 0.77 to 0.98 for the junior resident, and 0.83 to 0.95 for the senior resident [11].

Ellis et al. [23] studied multiple AAFD measurements in patients with flexible deformity using weight bearing multiplanar CT images. They reported good to excellent interobserver reliability between two board-certified radiologists for the readings of the talus-first metatarsal angle in the axial and sagittal planes (0.84 and 0.82, respectively), forefoot arch angle (0.81), and medial cuneiform to floor distance in the sagittal view (0.93). The authors also found fair interobserver reliability for the talonavicular coverage angle (0.53), navicular to skin distance in the coronal plane (0.52), lateral gutter distance in the coronal plane (0.48) (a measurement that is similar to the calcaneal-fibular distance performed in our study), and the navicular-medial cuneiform angle in the sagittal plane (0.51). They concluded that most of the parameters typically assessed with conventional radiographs showed good to excellent ICC values for interobserver reliability when measured using multiplanar CT images. The authors also proposed that the lower reliability in some of the measurements, especially those performed in the coronal plane, could be related to the fact that they are not commonly measured by radiologists. Probasco et al. [32] evaluated the subtalar joint alignment of patients with flexible AAFD and controls using weight bearing multiplanar CT. They found excellent intraobserver (ICC = 0.94) and interobserver reliability (ICC = 0.99) for the subtalar horizontal angle.

A recent study found that measurements analogous to traditional radiographic measurements of AAFD are obtainable using high-resolution WBCT imaging [17]. In that study, using only expert investigators (two board-certified foot and ankle surgeons and one fellowship-trained radiologist), the authors showed increased severity of the deformity in weight bearing images compared with non-weight bearing images. They also found overall excellent intra- and interobserver reliability on weight bearing images ($r = 0.93$ and ICC = 0.81, respectively) [17]. However, the proper approach to obtaining the correct images and performing the measurements in a 3D imaging environment demands training and is extremely time-consuming, which may hinder its routine use in evaluating AAFD patients. We believe it is important to verify the quality and reproducibility of the measurements when performed by less experienced healthcare personnel.

When comparing the readings of 3 investigators of different levels of clinical expertise, we observed significant differences in the mean values for only 2 of 21 measurements performed (medial cuneiform-first metatarsal angle and navicular-medial cuneiform angle). Although it is impossible to determine which investigators made the correct measurements, the readings of the most experienced investigator were the ones that differed from those performed by the least experienced investigators. Similar to prior studies, we also found that measurement of linear distances is more reliable than measurement of angles, demonstrating higher intra- and interobserver reliability [17, 20, 23, 34]. Measuring distances is simpler than measuring angles because angle measurements usually depend on a more complex process of finding particular bone axes. Measurements that involve the evaluation of the axis of the talus are even more difficult to perform reliably, demonstrating the challenges inherent in the complex 3D shape of this bone [17, 18, 20, 23, 34]. The positioning of the line representing the talar axis is technically demanding and seems to be sensitive to slight changes in the plane of the image used to perform a measurement [17].

Our study has several limitations. Although a standardized alternative assessment was used in the definition of the first metatarsal axis, the investigators were unable to see the whole length of the first metatarsal, especially its distal aspect, in sagittal and axial plane images. That represents a limitation in the field of view and imaging acquisition of the WBCT scanner used in the study. This could have influenced the adequate definition of the first metatarsal axis, hindering the measurement of the talus-first metatarsal and medial cuneiform-first metatarsal angles, likely affecting intra- and interobserver reliability. We also had a relatively small number of subjects involved in the study [19], and no power or sample size calculation was performed prospectively. However, our findings of significant intra- and interobserver correlations suggest adequate statistical power.

In conclusion, we found that AAFD measurements can be performed reliably by investigators with different levels of clinical experience using WBCT imaging, demonstrating overall good to excellent intra- and interobserver reliability.

References

1. de Cesar Netto C, Shakoor D, Dein EJ, Zhang H, Thawait GK, Richter M, Ficke JR, Schon LC, Weightbearing CTISG, Demehri S. Influence of investigator experience on reliability of adult acquired flatfoot deformity measurements using weightbearing computed tomography. Foot Ankle Surg. 2019;25(4):495–502. https://doi.org/10.1016/j.fas.2018.03.001. Epub 2018 Mar 12

2. Toullec E. Adult flatfoot. Orthop Traumatol Surg Res. 2015;101:S11–7.
3. Peeters K, Schreuer J, Burg F, Behets C, Van Bouwel S, Dereymaeker G, Sloten JV, Jonkers I. Alterated talar and navicular bone morphology is associated with pes planus deformity: a CT-scan study. J Orthop Res. 2013;31:282–7.
4. Basioni Y, El-Ganainy AR, El-Hawary A. Double calcaneal osteotomy and percutaneous tenoplasty for adequate arch restoration in adult flexible flat foot. Int Orthop. 2011;35:47–51.
5. Johnson KA, Strom DE. Tibialis posterior tendon dysfunction. Clin Orthop Relat Res. 1989;1(239):196–206.
6. Myerson MS. Adult acquired flatfoot deformity. Treatment of dysfunction of the posterior tibial tendon. J Bone Joint Surg Am. 1996;78:780–92.
7. Lin YC, Mhuircheartaigh JN, Lamb J, Kung JW, Yablon CM, Wu JS. Imaging of adult flatfoot: correlation of radiographic measurements with MRI. AJR Am J Roentgenol. 2015;204:354–9.
8. Richter M, Zech S. Lengthening osteotomy of the calcaneus and flexor digitorum longus tendon transfer in flexible flatfoot deformity improves talo-1st metatarsal-index, clinical outcome and pedographic parameter. Foot Ankle Surg. 2013;19:56–61.
9. Deland JT. Adult-acquired flatfoot deformity. J Am Acad Orthop Surg. 2008;16:399–406.
10. Cody EA, Williamson ER, Burket JC, Deland JT, Ellis SJ. Correlation of talar anatomy and subtalar joint alignment on weightbearing computed tomography with radiographic flatfoot parameters. Foot Ankle Int. 2016;37:874–81.
11. Sensiba PR, Coffey MJ, Williams NE, Mariscalco M, Laughlin RT. Inter- and intraobserver reliability in the radiographic evaluation of adult flatfoot deformity. Foot Ankle Int. 2010;31:141–5.
12. American Association of Physicists in Medicine. Comprehensive methodology for the evaluation of radiation does in x-ray computed tomography. AAPM Report No. 111. Available at http://www.aapm.org/pubs/reports/RPT_111.pdf. Accessed on July 28. In. 2017.
13. Kido M, Ikoma K, Imai K, Maki M, Takatori R, Tokunaga D, Inoue N, Kubo T. Load response of the tarsal bones in patients with flatfoot deformity: in vivo 3D study. Foot Ankle Int. 2011;32:1017–22.
14. Richter M, Seidl B, Zech S, Hahn S. PedCAT for 3D-imaging in standing position allows for more accurate bone position (angle) measurement than radiographs or CT. Foot Ankle Surg. 2014;20:201–7.
15. Richter M, Zech S. Arthrorisis with calcaneostop screw in children corrects Talo-1st Metatarsal-Index (TMT-Index). Foot Ankle Surg. 2013;19:91–5.
16. Carrino JA, Al Muhit A, Zbijewski W, Thawait GK, Stayman JW, Packard N, Senn R, Yang D, Foos DH, Yorkston J, Siewerdsen JH. Dedicated cone-beam CT system for extremity imaging. Radiology. 2014;270:816–24.
17. de Cesar Netto C, Schon LC, Thawait GK, da Fonseca LF, Chinanuvathana A, Zbijewski WB, Siewerdsen JH, Demehri S. Flexible adult acquired flatfoot deformity: comparison between weight-bearing and non-weight-bearing measurements using cone-beam computed tomography. J Bone Joint Surg Am. 2017;99(18):e98. https://doi.org/10.2106/JBJS.16.01366.
18. Demehri S, Muhit A, Zbijewski W, Stayman JW, Yorkston J, Packard N, Senn R, Yang D, Foos D, Thawait GK, Fayad LM, Chhabra A, Carrino JA, Siewerdsen JH. Assessment of image quality in soft tissue and bone visualization tasks for a dedicated extremity cone-beam CT system. Eur Radiol. 2015;25:1742–51.
19. Sangeorzan BJ, Mosca V, Hansen ST Jr. Effect of calcaneal lengthening on relationships among the hindfoot, midfoot, and forefoot. Foot Ankle Int. 1993;14:136–41.
20. Younger AS, Sawatzky B, Dryden P. Radiographic assessment of adult flatfoot. Foot Ankle Int. 2005;26:820–5.
21. Ferri M, Scharfenberger AV, Goplen G, Daniels TR, Pearce D. Weightbearing CT scan of severe flexible pes planus deformities. Foot Ankle Int. 2008;29:199–204.
22. Coughlin MJ, Kaz A. Correlation of Harris mats, physical exam, pictures, and radiographic measurements in adult flatfoot deformity. Foot Ankle Int. 2009;30:604–12.
23. Ellis SJ, Deyer T, Williams BR, Yu JC, Lehto S, Maderazo A, Pavlov H, Deland JT. Assessment of lateral hindfoot pain in acquired flatfoot deformity using weightbearing multiplanar imaging. Foot Ankle Int. 2010;31:361–71.

24. Iossi M, Johnson JE, McCormick JJ, Klein SE. Short-term radiographic analysis of operative correction of adult acquired flatfoot deformity. Foot Ankle Int. 2013;34:781–91.
25. Arangio GA, Wasser T, Rogman A. Radiographic comparison of standing medial cuneiform arch height in adults with and without acquired flatfoot deformity. Foot Ankle Int. 2006;27:636–8.
26. Chadha H, Pomeroy G, Manoli A 2nd. Radiologic signs of unilateral pes planus. Foot Ankle Int. 1997;18:603–4.
27. Fleiss JL. Statistical methods for rates and proportions. New York: Wiley, John and Sons, Inc.; 1981.
28. Apostle KL, Coleman NW, Sangeorzan BJ. Subtalar joint axis in patients with symptomatic peritalar subluxation compared to normal controls. Foot Ankle Int. 2014;35:1153–8.
29. Colin F, Horn Lang T, Zwicky L, Hintermann B, Knupp M. Subtalar joint configuration on weightbearing CT scan. Foot Ankle Int. 2014;35:1057–62.
30. Krahenbuhl N, Tschuck M, Bolliger L, Hintermann B, Knupp M. Orientation of the subtalar joint: measurement and reliability using weightbearing CT scans. Foot Ankle Int. 2016;37:109–14.
31. Malicky ES, Crary JL, Houghton MJ, Agel J, Hansen ST Jr, Sangeorzan BJ. Talocalcaneal and subfibular impingement in symptomatic flatfoot in adults. J Bone Joint Surg Am. 2002;84:2005–9.
32. Probasco W, Haleem AM, Yu J, Sangeorzan BJ, Deland JT, Ellis SJ. Assessment of coronal plane subtalar joint alignment in peritalar subluxation via weight-bearing multiplanar imaging. Foot Ankle Int. 2015;36:302–9.
33. Hirschmann A, Pfirrmann CW, Klammer G, Espinosa N, Buck FM. Upright cone CT of the hindfoot: comparison of the non-weight-bearing with the upright weight-bearing position. Eur Radiol. 2014;24:553–8.
34. Arunakul M, Amendola A, Gao Y, Goetz JE, Femino JE, Phisitkul P. Tripod index: a new radiographic parameter assessing foot alignment. Foot Ankle Int. 2013;34:1411–20.

Chapter 18
Results of More Than 11,000 Scans with Weight Bearing CT: Impact on Costs, Radiation Exposure, and Procedure Time

Martinus Richter

Introduction

Weight bearing CT (WBCT) has been proven to more precisely measure bone position than conventional sequencing including systematic weight bearing radiograph series (R) and optional conventional CT without weight bearing (CT) [1–8]. These improvements are attributed to the absence of superimposition and the possibility to account for rotational errors after the image process [6, 9]. Time spent on image acquisition (T) has shown to be lower for WBCT than for R and CT [6]. Radiation dose (RD) for WBCT has also shown to be lower than for CT [6]. The cost-effectiveness of using WBCT clinical settings is questionable. As far as we know, T, RD, and especially cost-effectiveness have not been investigated in a high number of patients so far. The purpose of this study was to assess the potential benefits of using WBCT instead of R and/or CT in a foot and ankle department, regarding RD, T, and cost-effectiveness.

Methods

Study Design

A WBCT device (PedCAT, CurveBeam, Warrington, PA, USA) was put into operation from July 1, 2013, in the first author's foot and ankle department. All patients who obtained WBCT (bilateral scan) and/or CT from July 1, 2013 until March 15, 2019 were included in the study (WBCT group).

Based on Richter M, Lintz F, Cesar de Netto C, Barg A, Burssens A. Results of more than 11,000 scans with Weightbearing CT - Impact on costs, radiation exposure, and procedure time. *Foot Ankle Surg* 2019; pii: S1268-7731(19)30096-7. doi: https://doi.org/10.1016/j.fas.2019.05.019. [epub ahead of print]

M. Richter et al., *Weight Bearing Cone Beam Computed Tomography (WBCT) in the Foot and Ankle*, https://doi.org/10.1007/978-3-030-31949-6_18

Control Group

All patients who obtained radiographs and/or CT from January 1 to December 31, 2012 were included in the control group (R/CT group).

No exclusion criteria for patients were defined (both groups). Initial radiographs in trauma patients and early postoperative (1–4 days) radiographs were excluded from the study (both groups).

Data Acquisition

Age, gender, primary pathology location, and additional CT (bilateral feet and ankles) were registered. Pathology location was differentiated in the ankle, hindfoot, midfoot, forefoot, and multiple other locations based on anatomy as follows: the hindfoot between the ankle and the Chopart joint, the midfoot between the Chopart and Lisfranc joints, and the forefoot distal to the Lisfranc joint. Involvement of the joints were defined relative to the main neighboring location or, when unclear, as multiple location.

Imaging Time (T)

T was calculated based on an analysis of previous studies as follows: R (bilateral feet dorsoplantar and lateral, metatarsal head skyline view), 902 seconds; CT (bilateral feet and ankle), 415 seconds; and WBCT (bilateral), 207 seconds [6].

Radiation Dose (RD)

RD per patient was calculated based on previous phantom measurements as part of obligatory standard periodic quality assurance protocols: R, 1.4 uSv; CT, 25 uSv; and WBCT 4.2 uSv [10].

Cost-Effectiveness

For the analysis of cost-effectiveness, device cost, working time cost of radiology technicians (similar to T), and reimbursement in the local setting were taken into consideration for the WBCT group. The total device cost was calculated at a 200,000 Euro acquisition cost with a 5-year asset depreciation range (40,000 Euro yearly) and an annual 5000 Euro maintenance cost, i.e., 45,000 Euro yearly cost for the WBCT group. No device costs were included for the RCT group since the R and CT devices were already installed. Staff costs were calculated by multiplication of T with 20 Euro per hour (based on local practice fares). The only reimbursement that could be considered was the one generated by privately insured patients or self-payers which corresponded to 15.5/15.1% of WBCT/RCT groups at a rate of 30 Euro for each R series and 300 Euro for each CT/WBCT. Vice versa, no reimbursement was achieved and considered for the study for all other patients (with public insurance). The potential profit was then considered in total and per patient.

Data Analysis/Control Group

All parameters were compared between WBCT and R/CT group.

Statistics

Either a Student's t-test or Chi-square test was used for comparison between groups with normal distributed and binomial data, respectively. *P*-values were considered significant when lower than .05. SPSS (20.0.0, SPSS, Inc., Chicago, IL, USA) was used.

Results

11,009 WBCT scans were obtained from 4987 patients (WBCT group). 4987 (45%) scans were performed before treatment, and 6022 (55%) at follow-up between 3 months and 5 years after operative treatment. 1957 WBCT scans and 10.6 CTs (all before treatment) were obtained on average yearly. The mean age of the scanned patients was 52.4 years (range, 8–92), and 41% were male. Table 18.1 shows the pathology location. The most common single location was forefoot (19.8%). In 2012, 1850 Rs and 254 CTs were obtained from 885 patients (RCT group). The yearly average RD was 4.3 uSv for WBCT group and 4.8 uSv for RCT group (mean difference of 0.5 uSv; a 10% decrease for the WBCT group, $p < 0.01$) (Table 18.2). The mean yearly T was 114 hours in total (3.3 minutes per patient) for the WBCT group and 493 hours in total (16.0 minutes per patient) for the RCT group (mean difference of 379 hours; a 77% decrease for the WBCT group, $p < 0.01$) (Table 18.2). The mean yearly cost-effectiveness was a profit of 43,959/−723 Euros for WBCT/RCT groups, respectively, 50.3/−0.82 Euros per patient (Table 18.2). Consequently, there is an overall profit increase of 44,682 Euros (51.12 Euros per patient).

Table 18.1 Epidemiology and pathology location RCT and WBCT groups

	RCT		WBCT		Test *p*
Age (mean, range)	52.4 (8–92)		53.8 (6–91)		t-test 0.7
Gender (male n, %)	2045 (49%)		779 (42%)		Chi2 0.9
Pathology location	n	%	n	%	
Ankle	603	12.1	104	11.8	Chi2 0.8
Hindfoot	480	10.1	98	11.1	
Midfoot	457	9.2	78	8.8	
Forefoot	987	19.8	182	11.8	
Multiple locations	2423	48.6	423	47.8	

RCT group, group from 2012 with conventional radiographs and optional CT; WBCT group, group from July 1, 2013 until March 12, 2019 with WBCT and additional conventional radiographs and CT

Table 18.2 Imaging data RCT and WBCT groups

Parameter	RCT	WBCT	T-test *p*
Patient number	885	873.6 ± 53	
Radiographs (series, n per year)	1850		
WBCT (n per year)		1957 ± 87	
CT (n per year)	254	10.6 ± 2.4	
Radiation dose per patient (uSv)	4.8 ± 4.3	4.3 ± 1.5	<.01
Time spent radiology technician (hours in total per year)	493	114 ± 14.5	<.01
Time spent radiology technician (minutes.seconds per patient)	15.59 ± 8.04	3.29 ± 2.56	<.01
Private insurance/self-payers (%)	15.1	15.5	
Profit (Euros in total per year)	−723	43,959 ± 6512	<.01
Profit (Euros per patient)	.82	50.3 ± 10.9	<.01

RCT group, group from 2012 with conventional radiographs and optional CT; WBCT group, group from July 1, 2013, until March 12, 2019, with WBCT and additional conventional radiographs and CT. Numbers for WBCT group are average yearly numbers

Discussion

This study confirmed WBCT used as standard of care resulted in lower radiation dosage and procedure time and was financially profitable. In our experience, these benefits offset costs within the first year of introduction, despite a very unfavorable local reimbursement situation; no specific code existed for patients without private insurance or self-payers.

So far, all studies analyzing WBCT focused on bone position measurement accuracy and/or pathology detection, leaving little room to investigate the technical superiority and cost-effectiveness of WBCT relative to R and CT [2–6, 9, 11–58]. Despite these advantages, WBCT has yet to replace R and CT sequences in the standard assessment of foot and ankle patients. Arguments like higher RD in relation to R and device costs have hindered the broader distribution of WBCT [59]. Also, most institutions have already installed R and/or CT devices and are thus reluctant to additionally invest in a WBCT device. To the best of our knowledge, this is the first study to investigate and compare RD as a benefit for the patient and cost-effectiveness as a benefit for the institution of WBCT used as standard of care in a large number of foot and ankle patients. The study's setting was an institution with existing R and CT devices that installed a WBCT device in 2013. After using the device alongside R and CT for a comparative study, WBCT replaced R and CT as the standard imaging in this clinic a few months after installation [6]. Radiographs were limited to early postoperative (1–4 days) imaging for patients without weight bearing, initial, or better preoperative radiographs, and CTs were limited to trauma cases that comprised around 3% in the local setting. Radiographs were indicated for initial assessment and CT when weight bearing was not possible and 3D imaging was indicated (e.g., calcaneal fractures). In the control group (RCT), the imaging for early postoperative and trauma cases was the same. As the indication for initial radiographs in trauma cases and early postoperative radiographs was similar in WBCT and RCT groups, this imaging was excluded from the comparative study. Thus, the CT imaging in the WBCT group as described above was not excluded because it was also considered as 3D imaging (as WBCT). However, with ten CTs on average yearly, the effect of the CT in the WBCT group on the comparison is minimal. In the RCT group, a high rate of CT (29% of all patients) was observed. CT was indicated in addition to radiographs with weight bearing for (complex) deformities or other pathologies in the hindfoot, midfoot, or multiple locations. The high rate for CT is consequently based on the high rate of pathologies in the hindfoot (10%), midfoot (9%), and multiple locations (49%) (Table 18.1).

This study was not focused on the type of pathology, type of treatment, or accuracy/sensitivity/specificity of the imaging. In this study, we found a substantial decrease in R and CT use for the WBCT group as expected. The decrease of CT use from more than 250 per year (RCT group) to 10 per year (WBCT group) influenced the finding of decreased RD for the entire WBCT group. RD for CT (25 uSv) is more than five times higher than for WBCT (4.2 uSv) which overcompensates for the three times higher RD of WBCT relative to R (1.4 uSv). While the RD for WBCT is often argued to be greater, RD is definitively shown to decrease (10%) [60]. Other centers with low usage of CT might not decrease RD by substituting R alone with WBCT. When analyzing cost-effectiveness, the initial cost for device acquisition and the absence of specific reimbursement are usually taken into consideration as the main factors against WBCT device profitability. While purchasing cost does not significantly differ between device types or countries, the reimbursement situation can vary drastically. Our calculation is just one example in a special setting, and the numbers might differ in other countries with different insurance settings. The special situation here was that only patients with private insurance or self-payers (around 15% of all patients in WBCT and RCT groups) were charged at all for the imaging. Privately insured patients pay themselves and get reimbursement from their private insurance, whereas self-payers pay themselves without reimbursement. A higher percentage of self-payers or privately insured would increase the reimbursement more in the WBCT group than in the RCT group, because the reimbursement is higher for WBCT/CT (300 Euros) than for radiographs (30 Euros). The situation has already evolved in many countries, such as the United States, UK, and Belgium, where authorities have recognized the general usefulness and benefits of WBCT for patients and institutions relative to the traditional RCT sequence. We found the 77% decrease in image acquisition time for the WBCT group relative to the RCT group to be the main factor for increased profit. This effect might also differ in other settings. However, cone beam technology (as in WBCT) is currently being developed to scan knees, hands, and elbows. This expanded application may possibly increase indications and usability of WBCT scans in institutions which are not specialized in foot and ankle surgery or with a more restricted flow of patients needing regular CT scans.

Shortcomings of the Study

There are numerous shortcomings of the study. Specific diagnosis for multiple foot and ankle pathologies was not analyzed. The indication for the imaging was not analyzed and could differ in other institutions. Preoperative and follow-up imaging were included in the analysis because these were found to reflect the local situation most appropriately. For both groups, early postoperative radiographs without weight bearing were not registered and included in the further analysis. This could be considered as a shortcoming because not all radiographs were included in the study. However, the indication and frequency for these radiographs did not differ between RCT and WBCT groups and were therefore not included. The same is true for initial radiographs in trauma patients as discussed above. RD was not measured but projected with data from an earlier phantom measurement [10]. For this phantom study, the same WBCT device was used, but R and CT devices differed [10]. Consequently, the real RD might differ in our setting. However, we are not aware of any other comparable study that measured RD in such a large patient series. With later device generations (WBCT, CT, and R), RD might differ. To the best of our understanding, it would be more probable that newer WBCT technology would decrease RD more than the much longer available and further developed R and CT technology. We are aware all authors have a conflict of interest because all authors use WBCT in their institutions and are consultants for one of the device manufacturers and board members of the International WBCT Society. This might cause bias in the data interpretation. However, we want to stress that this conflict of interest did not influence data collection (T, RD, cost/reimbursement) or statistical analysis.

In conclusion, 11,009 WBCT scans for 4987 patients as the prevailing substitution for R and CT over a 5.6-year period at a foot and ankle center resulted in a 10% decreased RD (minus 0.5 uSV on average per patient) as benefit for the patients. Yearly T decreased by 439 hours (77%) in total (12.30 minutes/seconds per patient) as a benefit for patients and institution. Yearly financial profit for imaging increased by more than 44,000 Euros in total (51 Euros per patient) as benefit for the institution.

References

1. Richter M, Lintz F, Cesar de Netto C, Barg A. Results of more than 11,000 scans with weight-bearing CT – impact on costs, radiation exposure, and procedure time. Foot Ankle Surg. 2019; accepted. https://doi.org/10.1016/j.fas.2019.05.019.
2. Burssens A, Peeters J, Peiffer M, Marien R, Lenaerts T, Vandeputte G, Victor J. Reliability and correlation analysis of computed methods to convert conventional 2D radiological hindfoot measurements to a 3D setting using weightbearing CT. Int J Comput Assist Radiol Surg. 2018;13(12):1999–2008.
3. de Cesar Netto C, Shakoor D, Dein EJ, Zhang H, Thawait GK, Richter M, Ficke JR, Schon LC, Demehri S. Influence of investigator experience on reliability of adult acquired flatfoot deformity measurements using weightbearing computed tomography. Foot Ankle Surg. 2019;25(4):495–502. https://doi.org/10.1016/j.fas.2018.03.001.
4. Lintz F, Welck M, Bernasconi A, Thornton J, Cullen NP, Singh D, Goldberg A. 3D biometrics for hindfoot alignment using weightbearing CT. Foot Ankle Int. 2017;38(6):684–9.
5. Zhang JZ, Lintz F, Bernasconi A, Zhang S. 3D biometrics for hindfoot alignment using weight-bearing computed tomography. Foot Ankle Int. 2019;40(6):684–9.
6. Richter M, Seidl B, Zech S, Hahn S. PedCAT for 3D-imaging in standing position allows for more accurate bone position (angle) measurement than radiographs or CT. Foot Ankle Surg. 2014;20:201–7.
7. Richter M, Zech S, Hahn S, Naef I, Merschin D. Combination of pedCAT for 3D imaging in standing position with Pedography shows no statistical correlation of bone position with force/pressure distribution. J Foot Ankle Surg. 2016;55(2):240–6.
8. Richter M, Lintz F, Zech S, Meissner SA. Combination of PedCAT weight bearing CT with pedography shows relationship between anatomy based foot center (FC) and force/pressure based center of gravity (COG). Foot Ankle Int. 2018;39(3):361–8.
9. Barg A, Bailey T, Richter M, de Cesar Netto C, Lintz F, Burssens A, Phisitkul P, Hanrahan CJ, Saltzman CL. Weightbearing computed tomography of the foot and ankle: emerging technology topical review. Foot Ankle Int. 2018;39(3):376–86.
10. Ludlow BW, Ivanovic M. Weightbearing CBCT, MDCT, and 2D imaging dosimetry of the foot and ankle. Int J Diagn Imaging. 2014;1(2):1–9.
11. Welck MJ, Myerson MS. The value of weight-bearing CT scan in the evaluation of subtalar distraction bone block arthrodesis: case report. Foot Ankle Surg. 2015;21(4):e55–9.
12. Tuominen EK, Kankare J, Koskinen SK, Mattila KT. Weight-bearing CT imaging of the lower extremity. AJR Am J Roentgenol. 2013;200(1):146–8.
13. Richter M, Lintz F, Zech S, Meissner SA. Combination of PedCAT weightbearing CT with pedography assessment of the relationship between anatomy-based foot center and force/pressure-based center of gravity. Foot Ankle Int. 2018;39(3):361–8.
14. Lepojarvi S, Niinimaki J, Pakarinen H, Leskela HV. Rotational dynamics of the normal distal tibiofibular joint with weight-bearing computed tomography. Foot Ankle Int. 2016;37(6):627–35.
15. Lepojarvi S, Niinimaki J, Pakarinen H, Koskela L, Leskela HV. Rotational dynamics of the talus in a normal tibiotalar joint as shown by weight-bearing computed tomography. J Bone Joint Surg Am. 2016;98(7):568–75.
16. Lawlor MC, Kluczynski MA, Marzo JM. Weight-bearing cone-beam CT scan assessment of stability of supination external rotation ankle fractures in a cadaver model. Foot Ankle Int. 2018;39(7):850–7.
17. Krahenbuhl N, Tschuck M, Bolliger L, Hintermann B, Knupp M. Orientation of the subtalar joint: measurement and reliability using weightbearing CT scans. Foot Ankle Int. 2016;37(1):109–14.
18. Jeng CL, Rutherford T, Hull MG, Cerrato RA, Campbell JT. Assessment of bony subfibular impingement in flatfoot patients using weight-bearing CT scans. Foot Ankle Int. 2019;40(2):152–8.

19. Hirschmann A, Pfirrmann CW, Klammer G, Espinosa N, Buck FM. Upright cone CT of the hindfoot: comparison of the non-weight-bearing with the upright weight-bearing position. Eur Radiol. 2014;24(3):553–8.
20. Ferri M, Scharfenberger AV, Goplen G, Daniels TR, Pearce D. Weightbearing CT scan of severe flexible pes planus deformities. Foot Ankle Int. 2008;29(2):199–204.
21. de Cesar Netto C, Schon LC, Thawait GK, da Fonseca LF, Chinanuvathana A, Zbijewski WB, Siewerdsen JH, Demehri S. Flexible adult acquired flatfoot deformity: comparison between weight-bearing and non-weight-bearing measurements using cone-beam computed tomography. J Bone Joint Surg Am. 2017;99(18):e98.
22. Collan L, Kankare JA, Mattila K. The biomechanics of the first metatarsal bone in hallux valgus: a preliminary study utilizing a weight bearing extremity CT. Foot Ankle Surg. 2013;19(3):155–61.
23. Colin F, Horn Lang T, Zwicky L, Hintermann B, Knupp M. Subtalar joint configuration on weightbearing CT scan. Foot Ankle Int. 2014;35(10):1057–62.
24. Burssens A, Peeters J, Buedts K, Victor J, Vandeputte G. Measuring hindfoot alignment in weight bearing CT: a novel clinical relevant measurement method. Foot Ankle Surg. 2016;22(4):233–8.
25. An TW, Michalski M, Jansson K, Pfeffer G. Comparison of lateralizing calcaneal osteotomies for varus hindfoot correction. Foot Ankle Int. 2018;39(10):1229–36.
26. Zhang Y, Xu J, Wang X, Huang J, Zhang C, Chen L, Wang C, Ma X. An in vivo study of hindfoot 3D kinetics in stage II posterior tibial tendon dysfunction (PTTD) flatfoot based on weight-bearing CT scan. Bone Joint Res. 2013;2(12):255–63.
27. Yoshioka N, Ikoma K, Kido M, Imai K, Maki M, Arai Y, Fujiwara H, Tokunaga D, Inoue N, Kubo T. Weight-bearing three-dimensional computed tomography analysis of the forefoot in patients with flatfoot deformity. J Orthop Sci. 2016;21(2):154–8.
28. Welck MJ, Singh D, Cullen N, Goldberg A. Evaluation of the 1st metatarso-sesamoid joint using standing CT – the Stanmore classification. Foot Ankle Surg. 2018;24(4):314–9.
29. Thawait GK, Demehri S, AlMuhit A, Zbijweski W, Yorkston J, Del Grande F, Zikria B, Carrino JA, Siewerdsen JH. Extremity cone-beam CT for evaluation of medial tibiofemoral osteoarthritis: initial experience in imaging of the weight-bearing and non-weight-bearing knee. Eur J Radiol. 2015;84(12):2564–70.
30. Segal NA, Nevitt MC, Lynch JA, Niu J, Torner JC, Guermazi A. Diagnostic performance of 3D standing CT imaging for detection of knee osteoarthritis features. Phys Sportsmed. 2015;43(3):213–20.
31. Segal NA, Frick E, Duryea J, Roemer F, Guermazi A, Nevitt MC, Torner JC, Felson DT, Anderson DD. Correlations of medial joint space width on fixed-flexed standing computed tomography and radiographs with cartilage and meniscal morphology on magnetic resonance imaging. Arthritis Care Res. 2016;68(10):1410–6.
32. Segal NA, Frick E, Duryea J, Nevitt MC, Niu J, Torner JC, Felson DT, Anderson DD. Comparison of tibiofemoral joint space width measurements from standing CT and fixed flexion radiography. J Orthop Res. 2017;35(7):1388–95.
33. Segal NA, Bergin J, Kern A, Findlay C, Anderson DD. Test-retest reliability of tibiofemoral joint space width measurements made using a low-dose standing CT scanner. Skelet Radiol. 2017;46(2):217–22.
34. Marzo JM, Kluczynski MA, Clyde C, Anders MJ, Mutty CE, Ritter CA. Weight bearing cone beam CT scan versus gravity stress radiography for analysis of supination external rotation injuries of the ankle. Quant Imaging Med Surg. 2017;7(6):678–84.
35. Marzo J, Kluczynski M, Notino A, Bisson L. Comparison of a novel weightbearing cone beam computed tomography scanner versus a conventional computed tomography scanner for measuring patellar instability. Orthop J Sports Med. 2016;4(12):1–7.
36. Lintz F, de Cesar Netto C, Barg A, Burssens A, Richter M. Weight-bearing cone beam CT scans in the foot and ankle. EFORT Open Rev. 2018;3(5):278–86.

37. Kunas GC, Probasco W, Haleem AM, Burket JC, Williamson ERC, Ellis SJ. Evaluation of peritalar subluxation in adult acquired flatfoot deformity using computed tomography and weightbearing multiplanar imaging. Foot Ankle Surg. 2018;24(6):495–500.
38. Kimura T, Kubota M, Taguchi T, Suzuki N, Hattori A, Marumo K. Evaluation of first-ray mobility in patients with hallux valgus using weight-bearing CT and a 3-D analysis system: a comparison with normal feet. J Bone Joint Surg Am. 2017;99(3):247–55.
39. Kimura T, Kubota M, Suzuki N, Hattori A, Marumo K. Comparison of intercuneiform 1–2 joint mobility between hallux valgus and normal feet using weightbearing computed tomography and 3-dimensional analysis. Foot Ankle Int. 2018;39(3):355–60.
40. Kim JB, Yi Y, Kim JY, Cho JH, Kwon MS, Choi SH, Lee WC. Weight-bearing computed tomography findings in varus ankle osteoarthritis: abnormal internal rotation of the talus in the axial plane. Skelet Radiol. 2017;46(8):1071–80.
41. Hoogervorst P, Working ZM, El Naga AN, Marmor M. In vivo CT analysis of physiological fibular motion at the level of the ankle syndesmosis during plantigrade weightbearing. Foot Ankle Spec. 2018;12(3):233–7. https://doi.org/10.1177/1938640018782602.
42. Godoy-Santos AL, Cesar CN. Weight-bearing computed tomography of the foot and ankle: an update and future directions. Acta Ortopedica Bras. 2018;26(2):135–9.
43. Cody EA, Williamson ER, Burket JC, Deland JT, Ellis SJ. Correlation of talar anatomy and subtalar joint alignment on weightbearing computed tomography with radiographic flatfoot parameters. Foot Ankle Int. 2016;37(8):874–81.
44. Cheung ZB, Myerson MS, Tracey J, Vulcano E. Weightbearing CT scan assessment of foot alignment in patients with hallux Rigidus. Foot Ankle Int. 2018;39(1):67–74.
45. Burssens A, Van Herzele E, Leenders T, Clockaerts S, Buedts K, Vandeputte G, Victor J. Weightbearing CT in normal hindfoot alignment – presence of a constitutional valgus? Foot Ankle Surg. 2018;24(3):213–8.
46. Shakoor D, Osgood GM, Brehler M, Zbijewski WB, de Cesar Netto C, Shafiq B, Orapin J, Thawait GK, Shon LC, Demehri S. Cone-beam CT measurements of distal tibio-fibular syndesmosis in asymptomatic uninjured ankles: does weight-bearing matter? Skelet Radiol. 2019;48(4):583–94.
47. Patel S, Malhotra K, Cullen NP, Singh D, Goldberg AJ, Welck MJ. Defining reference values for the normal tibiofibular syndesmosis in adults using weight-bearing CT. Bone Joint J. 2019;101-b(3):348–52.
48. Osgood GM, Shakoor D, Orapin J, Qin J, Khodarahmi I, Thawait GK, Ficke JR, Schon LC, Demehri S. Reliability of distal tibio-fibular syndesmotic instability measurements using weightbearing and non-weightbearing cone-beam CT. Foot Ankle Surg. 2018; https://doi.org/10.1016/j.fas.2018.10.003.
49. Malhotra K, Welck M, Cullen N, Singh D, Goldberg AJ. The effects of weight bearing on the distal tibiofibular syndesmosis: a study comparing weight bearing-CT with conventional CT. Foot Ankle Surg. 2019;25(4):511–6. https://doi.org/10.1016/j.fas.2018.03.006.
50. Lintz F, de Cesar Netto C, Burssens A, Barg A, Richter M. The value of axial loading three dimensional (3D) CT as a substitute for full weightbearing (standing) 3D CT: comparison of reproducibility according to degree of load. Foot Ankle Surg. 2018;24(6):553–4.
51. Krahenbuhl N, Bailey TL, Weinberg MW, Davidson NP, Hintermann B, Presson AP, Allen CM, Henninger HB, Saltzman CL, Barg A. Impact of torque on assessment of syndesmotic injuries using weightbearing computed tomography scans. Foot Ankle Int. 2019;40(6):710–9. https://doi.org/10.1177/1071100719829720.
52. Krahenbuhl N, Bailey TL, Presson AP, Allen CM, Henninger HB, Saltzman CL, Barg A. Torque application helps to diagnose incomplete syndesmotic injuries using weight-bearing computed tomography images. Skelet Radiol. 2019;48:1367.
53. Kleipool RP, Dahmen J, Vuurberg G, Oostra RJ, Blankevoort L, Knupp M, Stufkens SAS. Study on the three-dimensional orientation of the posterior facet of the subtalar joint using simulated weight-bearing CT. J Orthop Res. 2019;37(1):197–204.

54. Kennelly H, Klaassen K, Heitman D, Youngberg R, Platt SR. Utility of weight-bearing radiographs compared to computed tomography scan for the diagnosis of subtle Lisfranc injuries in the emergency setting. Emerg Med Australas. 2019; https://doi.org/10.1111/1742-6723.13237.
55. Ha AS, Cunningham SX, Leung AS, Favinger JL, Hippe DS. Weightbearing digital tomosynthesis of foot and ankle arthritis: comparison with radiography and simulated weightbearing CT in a prospective study. AJR Am J Roentgenol. 2019;212(1):173–9.
56. de Cesar Netto C, Shakoor D, Roberts L, Chinanuvathana A, Mousavian A, Lintz F, Schon LC, Demehri S. Hindfoot alignment of adult acquired flatfoot deformity: a comparison of clinical assessment and weightbearing cone beam CT examinations. Foot Ankle Surg. 2018; https://doi.org/10.1016/j.fas.2018.10.008.
57. de Cesar Netto C, Bernasconi A, Roberts L, Pontin PA, Lintz F, Saito GH, Roney A, Elliott A, O'Malley M. Foot alignment in symptomatic national basketball association players using weightbearing cone beam computed tomography. Orthop J Sports Med. 2019;7(2):2325967119826081. https://doi.org/10.1177/2325967119826081.
58. Burssens A, Vermue H, Barg A, Krahenbuhl N, Victor J, Buedts K. Templating of syndesmotic ankle lesions by use of 3D analysis in weightbearing and nonweightbearing CT. Foot Ankle Int. 2018;39(12):1487–96.
59. Richter MZS, Hahn S. PedCAT for radiographic 3D-imaging in standing position. Fuss Sprungg. 2015;13:85–102.
60. Kang DH, Kang C, Hwang DS, Song JH, Song SH. The value of axial loading three dimensional (3D) CT as a substitute for full weightbearing (standing) 3D CT: comparison of reproducibility according to degree of load. Foot Ankle Surg. 2019;25(2):215–20.

Part III
Technical Guide to Weight Bearing Cone Beam Computed Tomography

Chapter 19
Technology of Weight Bearing Cone Beam Computed Tomography

Francois Lintz

Introduction

Cone beam is a recent technology, published in 1998 by Mozzo et al. [1]. It first was used in the dental and cranial arena. It took 15 years for the technology to gradually replace panoramic radiographs in the clinical setting and completely in preoperative planning. In orthopedics, the use of cone beam CT (CBCT) was first published in 2011 by Zbijewski et al. [2], and the first mention of weight-bearing was in a 2013 paper by Tuominen et al. [3].

A cone beam is a rotating XR, where the center of rotation is the investigated object, the photon source is at one end of the diameter axis, and the target (a digital silicon detector panel) at the other. The target is continuously projected with the photons which have traversed the object, and the result is an intermingled array of lines and shades called a sinogram (Fig. 19.1), which has to be interpreted using mathematical transforms (the Fournier, which reconstructs multiple simple sinus

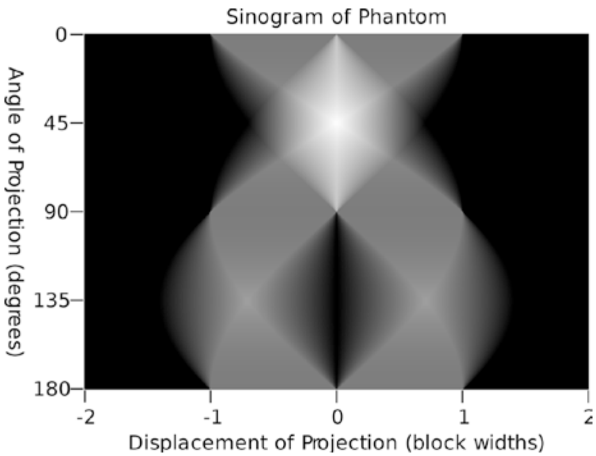

Fig. 19.1 Sinogram

M. Richter et al., *Weight Bearing Cone Beam Computed Tomography (WBCT) in the Foot and Ankle*, https://doi.org/10.1007/978-3-030-31949-6_19

functions from a single complex one) and the Radon, which reconstructs a set of 3D coordinates.

The result is a 3D cylindrical volume or field of view (FOV), which varies in diameter between 10 cm and 40 cm (Fig. 19.2). This is divided into smaller cubes or voxels: the 3D equivalent of 2D pixels. The side of each voxel is usually around 0.3 mm (slab thickness). The resolution depends essentially on the density of receptors on the target panel but also on software and memory capabilities. A typical FOV contains several hundred million voxels. Each voxel has four dimensions including a set of three coordinates (x, y, z) and a value for the radiodensity, given as the Hounsfield unit (HU). For example, the radiodensity of air is −1000 HU.

Acquisition time is typically under a minute. In terms of radiation exposure, 3,9 a CBCT scan with a small, single foot FOV is around 2 Micro Sieverts (mSV) and a large FOV bilateral foot scan around 6 mSV. As a comparison, US daily background exposure is around 8 mSV, 1 mSV for an extremity conventional XR, 2 mSV for a chest XR, and 25 mSV–100 mSV (or typically 70 mSV for an ankle scan) for an extremity CT. In terms of size, a typical machine will weigh around 250 kg and fit in a 1 m Å~1 m footprint (Fig. 19.3).

Fig. 19.2 Typical field of view

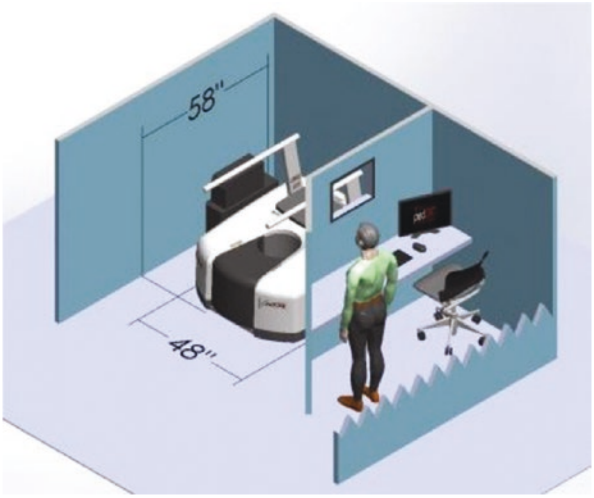

Fig. 19.3 Typical WBCT machine footprint

How It Works

It is a real 3D technology, which reconstructs 3D models from the information contained in stacked up 2D transverse slabs of the anatomy, much like a conventional CT scan. In the case of cone beam CT, however, a fan beam (instead of a linear one) is projected through the anatomy. The result is called a sinogram. This is the continuous projection of the anatomy on the target (a standard flat panel detector) which faces the X-ray source on the other side of the patient's foot and ankle. To decipher this image back to a 3D volume, mathematical algorithms based on the Radon and the Fourier transforms are necessary. Fourier tells us how to distinguish multiple signals piled up together. Radon tells us how to calculate or back-project the coordinates of each pixels and therefore reconstruct the whole volume, slice after slice. However, in cone beam CT, the X-ray source only performs a single revolution around the anatomy, as compared to a conventional CT which spirals around (Fig. 19.4).

The result is that much less radiation dose is required to obtain all the information, and the difference is even more important in the clinical setting. For example, considering a standard knee or a foot and ankle assessment prior to a reconstructive surgical procedure typically requires the 3D non-weight bearing information (provided by conventional CT: 25–70 μSv, equivalent to 25–50 radiographs) which needs to be coupled with the 2D non-weight bearing information (6–8 radiographs including usually bilateral AP, lateral and complementary views). Merging the 3D non-weight bearing and 2D weight bearing information happens in the surgeons' brains and requires experience, and some degree of planning, based on the biased 2D measurements. On the contrary, the radiological cost of WBCT is only of 2 for a small field of view (FOV), typically 15 cm in diameter scanning a single foot to 6 μSv for a large 30 cm FOV scanning bilateral feet. This corresponds approximately

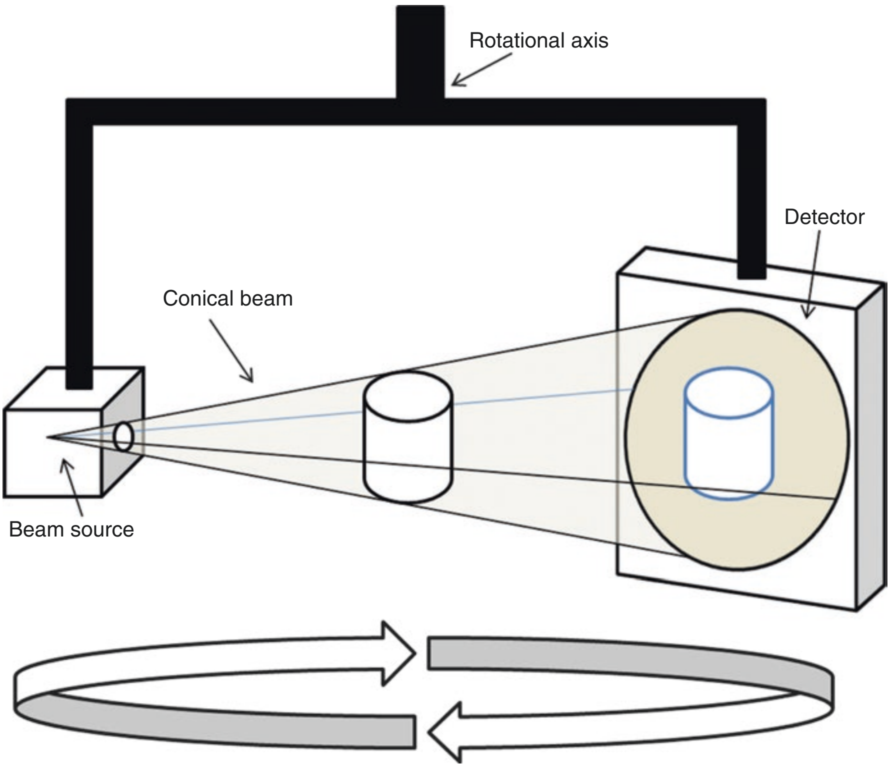

Fig. 19.4 Principles of WBCT cone beam imaging

to half of the daily natural radiation in the United States or equivalent to ten conventional radiographs but achieves to produce a precise virtual 3D weight bearing model of the anatomy of the two lower limbs (Fig. 19.5).

A 3D Environment

Understanding this model, however, requires being familiar with notions related to 3D imaging as opposed to 2D, which is one of the challenges faced when adopting the technology, having been trained for decades in using another. In the 3D environment that contains the foot and ankle virtual clone of the patient's anatomy (the FOV or "field of view"), what used to be a flat picture becomes a volume and pixels become voxels (little cubes of space). The grayscale is defined by Hounsfield's attenuation coefficient (HU for Hounsfield unit) which corresponds to the density of the traversed anatomical tissues compared to air and water (where the value for air is 1 and 1000 for water). Furthermore, where landmark positions were defined in 2D by their relative position to other landmarks through distances and angles which produced the upper mentioned biased measurements, it is now possible to define the position of each voxel relative to an orthogonal referential. So each voxel is now

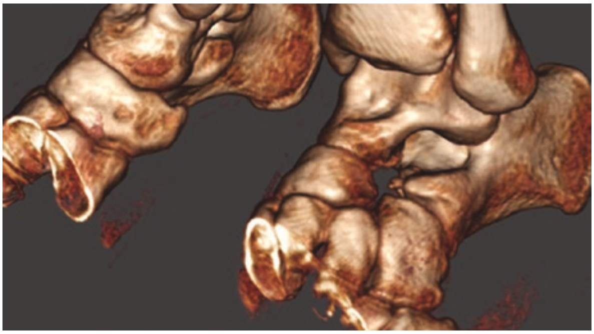

Fig. 19.5 Example of 3D rendering

Fig. 19.6 MPR and 3D rendering windows

defined by its x, y, z coordinates and its HU. In terms of size, the acquisition chamber within a typical bilateral WBCT is 1,000,000 voxels each approximately $0.3 \times 0.3 \times 0.3$ mm in size. A typical foot within this space would be approximately 200,000 voxels. Acquisition time for such a volume is typically under a minute. A typical machine will weigh around 250 kg and fit in a 1 m × 1 m footprint.

DRRs: Digitally Reconstructed Radiographs

Because interacting with a reliable 3D virtual model of the foot and ankle is completely different to interacting with a flat image, new tools have to become available. The amount of information simply is too great for the investigator to process swiftly and efficiently, and computerized help is indispensable. Depending on the industrial provider, the presentation of the 3D model may vary, but generally, an MPR (multiplanar reconstruction) screen is used and divided into four parts, containing one 3D visual (3D rendering) (Fig. 19.6) and three spatial 2D planes (coronal, transverse, and sagittal) allowing plan-by-plan or 3D navigation and measurements.

Fig. 19.7 Example of DRR and IM1-2 angle measurement

Along with this "modern" presentation, most manufacturers allow surgeons to work on digitally reconstructed radiographs or DRRs. Those are artificially flat, 2D conventional radiographs which are reconstructed from the information contained in the 3D volume. In algorithmic terms, this is achieved by increasing the width of a chosen slab (a single "slice" of the volume) in a chosen plane (Fig. 19.7). It seems really uncanny that this technique even exists. Why would someone get rid of all the new information contained in the 3D volume and go back to a 2D format. There are two main reasons to explain this. First, the current generation of specialists has been trained using 2D radiographs, so it will take some time before the acceptance of the newer technology is obtained. In order for the caretaker to quickly grasp the situation, a "snapshot" of some sort is required and for that purpose, until an innovative solution is found, DRRs are interesting since, contrary to the more ancient protocols combining conventional CT and radiographs, they can be obtained without extra radiation dose for the patient, so that the total dose is five times less with the use of WBCT.

Biases of Conventional Radiography

Weight bearing cone beam CT is not a CT "only-nicer-because-it is-weight-bearing". Its main advantage is to produce an accurate 3D model of the weight bearing foot, thereby overcoming most of the biases related to conventional radiography, as mentioned in Chaps. 1, 2, and 3. It is therefore essential to understand what those are.

Three main types of bias are considered:

- Perspective bias, among which:
  - Rotation bias: depending on the incidence angle of the X-ray beam, projected distances, shapes, and angles will vary.

  - Fan effect: depending on the distance from the X-ray source to the object, projected lengths will increase compared to the real length.
- Operator-related bias: this concerns the technical aspects of setting the radiographic apparatus around the patient and the placement of the patient himself. The positioning of the foot opposite to the X-ray source, the height of the source, and its distance is impossible to reproduce exactly from one setup to the other. In practice, patients are always radiographed at least twice for the same event to obtain an anterior-posterior and a lateral view, which is the most minimal acceptable combination in orthopedic imaging. However, they are never radiographed twice to evaluate the reproducibility of the radiographic setup. If this would have been done, the patient, the detector and the radiation source needs to be repositioned. The radiology technician could vary. Considering all these variables, repetitive radiographs might differ and would not be comparable within the same patient or between different patients.
- Superimposition bias: this is related to the projection of a 3D structure in a 2D plane, where multiple planes are piled up into a single plane. This results into areas where contours cannot be distinguished, where edges can be superimposed, which implies a certain amount of guesswork or experience to decipher. This is what the orthopedic foot and ankle surgeons' brains have been trained to do for decades. Now WBCT offers a different kind of challenge, where the potential amount of information provided is too complicated and too long to process within the clinical setting.

References

1. Mozzo P, Procacci C, Tacconi A, Martini PT, Andreis IA. A new volumetric CT machine for dental imaging based on the cone-beam technique: preliminary results. Eur Radiol. 1998;8(9):1558–64.
2. Zbijewski W, De Jean P, Prakash P, Ding Y, Stayman JW, Packard N, Senn R, Yang D, Yorkston J, Machado A, Carrino JA, Siewerdsen JH. A dedicated cone-beam CT system for musculoskeletal extremities imaging: design, optimization, and initial performance characterization. Med Phys. 2011;38(8):4700–13.
3. Tuominen EKJ, Kankare J, Koskinen SK, Mattila KT. Weight-bearing CT imaging of the lower extremity. AJR Am J Roentgenol. 2013;200(1):146–8.

Chapter 20
Weight Bearing Computed Tomography Devices

Arne Burssens

Beginning of Weight Bearing Computed Tomography Devices

The necessity for weight bearing computed tomography (CT) devices has already been demonstrated in the mid-1990s by Greisberg et al. [1]. This pivotal paper reported on the peritalar subluxation occurring in flatfoot deformities using a simulated weight bearing CT device containing a custom-built loading frame with the patient positioned supine. It soon became a stepping stone for other reports to follow, incorporating a similar setup [2, 3]. Despite these important findings, limitations regarding patient positioning, amount of load, and a high radiation dose were inevitable [4]. This advocated the development toward the weight bearing CT devices currently used in clinical practice.

Foot and Ankle Weight Bearing Computed Tomography Devices

The first weight bearing CT devices were available beginning of the 2010s [5–7]. They incorporate cone beam CT technology, which in essence uses a rotating X-ray to obtain the field of view. It was initially popularized in the dental area, but technical improvements caused it to be widely used across the majority of medical disciplines. The main advantages include a low radiation dose, the absence of superimposition, and a high image resolution. One of the first applications of weight bearing musculoskeletal scanning was dedicated to the foot and ankle [8, 9].

Currently, three companies are on the market offering weight bearing CT devices in this area (in alphabetical order): Carestream (Rochester, NY, USA), CurveBeam (Philadelphia, PA, USA) and Planmed (Helsinki, SF, FI). Their physical properties as well as the concomitant landmark studies will be discussed for each device (Figs. 20.1, 20.2, and 20.3).

M. Richter et al., *Weight Bearing Cone Beam Computed Tomography (WBCT) in the Foot and Ankle*, https://doi.org/10.1007/978-3-030-31949-6_20

Fig. 20.1 Onsight 3D Extremity System® (Carestream, Rochester, NY, USA). Physical dimensions of this device are as follows (in transport mode): length, 78.8″; width, 32″; and height, 76″. The gantry can be moved upward and turned 90°. This allows additional non-weight bearing imaging of the lower limb, as well as imaging of the upper extremities: the hand, wrist, and elbow. The first version of this device was described in one of the most early technical reports on musculoskeletal weight bearing CT imaging [10]. The first clinical applications were demonstrated in the alignment of flatfoot deformities [6]. Full technical details can be found on the website: https://www.carestream.com/en/us/medical/products/carestream-onsight-3d-extremity-system

Fig. 20.2 PedCAT® (CurveBeam, Philadelphia, PA, USA). Physical dimensions of this device are as follows: length, 58″; width, 28.5″; and height, 51″. Imaging of the foot and ankle can be performed both during weight bearing, physiological bipedal stance, as well as non-weight bearing while seated. The first study using this device included both technical details as well as clinical applications. In this pivotal report, a comparison was made toward non-weight bearing CT regarding radiation dose and accuracy of measurements commonly used in clinical foot and ankle practice [5]. Full technical details can be found on the website: https://www.curvebeam.com/products/pedcat/

Fig. 20.3 Verity® (Planmed, Helsinki, SF, FI). Physical dimensions of this device are as follows: length, 73″; width, 30″; and height, 66″. The gantry can be moved upward and turned 90°. This allows additional non-weight bearing imaging of the lower limb, as well as imaging of the upper extremities: the hand, wrist, and elbow. In the first study using this device, technical details were analyzed and reported [11]. Clinical examples demonstrated a higher accuracy in detecting ankle and midfoot osteoarthritis [11]. Full technical details can be found on the website: https://www.planmed.com/computed-tomography/

Knee Weight Bearing Computed Tomography Devices

The numerous applications and advantages encountered during weight bearing CT imaging of the foot and ankle raised the interest toward similar investigations at the level of the knee. The same three companies as mentioned above provide weight bearing CT devices to perform knee imaging. Their technical details will be described as well as their reports in clinical practice (Figs. 20.4, 20.5, and 20.6).

The Future of Weight Bearing Computed Tomography Devices

Weight bearing CT imaging is expected to extend towards the hip, allowing a complete analysis of the entire lower limb. This advancement will provide additional data over full leg radiographs, as 3D measurements will be possible. These data will increase our understanding of different types of deformities and their relation toward joint preserving as well as replacing procedures.

Fig. 20.4 Onsight 3D Extremity System® (Carestream, Rochester, NY, USA). Physical dimensions of this device are described above. The gantry can be moved upward to allow weight bearing CT imaging of the knee. It can be turned 90°, in the case non-weight bearing CT imaging is preferred [12]. The first version of this device was described in one of the most early technical reports on musculoskeletal weight bearing CT imaging [10]. The first clinical applications were demonstrated in patients with knee osteoarthritis quantifying joint space with and meniscal extrusion [6]

Fig. 20.5 LineUp® (CurveBeam, Philadelphia, PA, USA). Physical dimensions of this device are as follows: length, 48″; width, 28.5″; and height, 51.3″. Weight bearing CT imaging of the knee is achieved by elevation of the gantry while the patient is in physiological bipedal stance. Non-weight bearing CT imaging is also available but requires the patient to be seated in a chair. The first study using this device included both technical details and clinical applications [13]. In comparison with MRI and X-rays, weight bearing CT imaging was more sensitive and accurate to detect knee osteoarthritis. Full technical details can be found on the website: https://www.curvebeam.com/products/lineup/

Fig. 20.6 Verity® (Planmed, Helsinki, SF, FI). Physical dimensions of this device are described above. The gantry can be moved upward to allow weight bearing CT imaging of the knee. It can be turned 90°, in the case non-weight bearing CT imaging is preferred. In the first study using this device, technical details were analyzed and reported [11]. Clinical examples demonstrated advantages toward metal artifact reduction of prosthetic components and alignment of the knee [11]

Another area that could benefit from weight bearing CT imaging is the axial skeleton, particularly in the case of scoliosis. This 3D deformity is difficult to understand on 2D radiographs and substantially influenced by weight bearing conditions. A full-bodyweight bearing CT is expected to be developed for this process. However, such devices face technical difficulties as the gantry needs to turn horizontally, meaning perpendicularly to the direction of gravity. A future engineering and multidisciplinary approach will be required to succeed in this challenging process.

References

1. Greisberg J, Hansen ST Jr, Sangeorzan B. Deformity and degeneration in the hindfoot and midfoot joints of the adult acquired flatfoot. Foot Ankle Int. 2003;24(7):530–4.
2. Kido M, Ikoma K, Imai K, Maki M, Takatori R, Tokunaga D, et al. Load response of the tarsal bones in patients with flatfoot deformity: in vivo 3D study. Foot Ankle Int. 2011;32(11):1017–22.
3. Zhang Y, Xu J, Wang X, Huang J, Zhang C, Chen L, et al. An in vivo study of hindfoot 3D kinetics in stage II posterior tibial tendon dysfunction (PTTD) flatfoot based on weight-bearing CT scan. Bone Joint Res. 2013;2(12):255–63.
4. Al-Rawi B, Hassan B, Vandenberge B, Jacobs R. Accuracy assessment of three-dimensional surface reconstructions of teeth from cone beam computed tomography scans. J Oral Rehabil. 2010;37(5):352–8.
5. Richter M, Seidl B, Zech S, Hahn S. PedCAT for 3D-imaging in standing position allows for more accurate bone position (angle) measurement than radiographs or CT. Foot Ankle Surg. 2014;20(3):201–7.

6. de Cesar Netto C, Schon LC, Thawait GK, da Fonseca LF, Chinanuvathana A, Zbijewski WB, et al. Flexible adult acquired flatfoot deformity: comparison between weight-bearing and non-weight-bearing measurements using cone-beam computed tomography. J Bone Joint Surg Am. 2017;99(18):e98.
7. Lepojärvi S, Niinimäki J, Pakarinen H, Koskela L, Leskelä H-V. Rotational dynamics of the talus in a normal tibiotalar joint as shown by weight-bearing computed tomography. J Bone Joint Surg Am. 2016;98(7):568–75.
8. Barg A, Bailey T, Richter M, de Cesar Netto C, Lintz F, Burssens A, et al. Weightbearing computed tomography of the foot and ankle: emerging technology topical review. Foot Ankle Int. 2018;39(3):376–86.
9. Lintz F, de Cesar Netto C, Barg A, Burssens A, Richter M, Weight Bearing CT International Study Group. Weight-bearing cone beam CT scans in the foot and ankle. EFORT Open Rev. 2018;3(5):278–86.
10. Zbijewski W, De Jean P, Prakash P, Ding Y, Stayman JW, Packard N, et al. A dedicated cone-beam CT system for musculoskeletal extremities imaging: design, optimization, and initial performance characterization. Med Phys. 2011;38(8):4700–13.
11. Tuominen EK, Kankare J, Koskinen SK, Mattila KT. Weight-bearing CT imaging of the lower extremity. Am J Roentgenol. 2013;200(1):146–8.
12. Thawait GK, Demehri S, AlMuhit A, Zbijweski W, Yorkston J, Del Grande F, et al. Extremity cone-beam CT for evaluation of medial tibiofemoral osteoarthritis: initial experience in imaging of the weight-bearing and non-weight-bearing knee. Eur J Radiol. 2015;84(12):2564–70.
13. Segal NA, Nevitt MC, Lynch JA, Niu J, Torner JC, Guermazi A. Diagnostic performance of 3D standing CT imaging for detection of knee osteoarthritis features. Phys Sportsmed. 2015;43(3):213–20.

Chapter 21
Measurements in Weight Bearing Computed Tomography

Cesar de Cesar Netto

The literature on weight bearing computed tomography (WBCT) measurements in the assessment of complex foot and ankle deformities has been steadily growing during the last 4–5 years [1–4]. The main subjects of interest have been adult-acquired flatfoot deformity [5–12], hindfoot alignment [10, 13–20], alignment of the subtalar joint [5, 10, 11, 21–25], the distal tibiofibular (syndesmotic) joint [26–31], first ray hypermobility [32–34], hallux rigidus (HR) [35], and hallux valgus (HV) [33, 36–40]. A summary of some of the most important measurements reported in the literature is presented in this chapter, along with references to figures and photos in earlier chapters that depict examples of the measurements.

Adult-Acquired Flatfoot Measurements

- Talus-first metatarsal angle [8, 41]: measured in the axial and sagittal planes, by intersection of the lines representing the axis of the first metatarsal and the axis of the talus (Figs. 2.1, 2.2, and 4.3a)
- Talonavicular coverage angle [8, 42]: measured in the axial plane by the relationship between a line connecting, respectively, the medial and lateral edges of the articular surface of the talar head and a line connecting the medial and lateral edges of the articular surface of the navicular at the talonavicular joint (Fig. 15.2)
- Forefoot arch angle [43]: angle between the floor and a line drawn from the inferior aspect of the medial cuneiform to the inferior aspect of the fifth metatarsal (Figs. 2.4 and 15.3)
- Navicular to skin distance [43]: distance between the most inferior point of the navicular to the plantar skin, perpendicular to the floor (Fig. 2.4)
- Navicular to floor distance [8]: distance between the most inferior point of the navicular to the floor (Fig. 2.4)
- Medial cuneiform to skin distance [8]: distance between the most inferior point of the medial cuneiform to the plantar skin, perpendicular to the floor (Fig. 2.4)

M. Richter et al., *Weight Bearing Cone Beam Computed Tomography (WBCT) in the Foot and Ankle*, https://doi.org/10.1007/978-3-030-31949-6_21

- Medial cuneiform to floor distance [8]: distance between the most inferior point of the navicular to the floor (Fig. 2.4)
- Cuboid to skin distance [44]: distance between the most inferior point of the cuboid to the plantar skin, perpendicular to the floor (Fig. 2.4)
- Cuboid to floor distance [9]: distance between the most inferior point of the cuboid to the floor (Fig. 2.4)
- Calcaneofibular distance [6, 44]: measured in the coronal plane by shortest distance between the distal aspect of the fibula and the lateral-superior surface of the calcaneus (Fig. 2.4)
- Calcaneal inclination angle [8, 45]: measured in the sagittal plane by the intersection of the floor line and a line connecting the most inferior point of the calcaneal tuberosity and the bottom surface of the anterior process of the calcaneus (Figs. 2.2, 2.4 and 4.3b)
- Medial cuneiform-first metatarsal angle [9]: measured in the sagittal plane by the intersection of the axes of the first metatarsal and medial cuneiform (Fig. 2.4).
- Navicular-medial cuneiform angle [44]: also measured in the sagittal plane, by the angulation between the lines of the axes of the navicular and medial cuneiform (Fig. 2.4)

Hindfoot Alignment Measurements

- Foot and ankle offset [14, 18, 19]: semiautomatic three-dimensional (3D) offset measurement of the torque acting in the ankle joint as result of body weight and ground reaction forces. It takes into consideration the relationship between the center of gravity of the tripod of the foot and the center of the ankle joint, represented by the apex of the talar dome. Negative measurements indicate that the center of the ankle joint lies laterally to the bisecting line of the foot tripod (varus alignment). Positive values implicate that center of the ankle joint is positioned medially to the bisecting line of the foot tripod (valgus alignment). The 3D coordinates for calculation of FAO are harvested using the multiplanar reconstruction (MPR) images. The first point marked is the most distal voxel of the first metatarsal head, followed by the most distal voxel of the fifth metatarsal head and next the most distal voxel of the calcaneal tuberosity. Finally, the most central and proximal aspect of the talar dome was marked, and the automatic calculation of the FAO is given by a dedicated software (TALAS™, CubeVue™, CurveBeam, LLC, Warrington, PA, USA) (Figs. 5.2b, 5.4a, 5.4c, and 8.1).
- Hindfoot alignment angle (CT, Novel) [13]: measured in the coronal plane, considering the inclination of the tibia (anatomical axis) as well as the inclination of the talus and calcaneum (talocalcaneal angle) (Figs. 2.1, 2.3, 9.1, 9.2, 9.3, 9.4, 10.1, 10.2, 10.3, 10.4, and 10.5). Represented by the sum of talocalcaneal angle with the angle of the anatomical axis of the tibia.
- WBCT clinical hindfoot alignment angle [10]: obtained using 3D reconstruction images where the windowing is set to maintain the surface anatomical

landmarks, including the skin. Represented by the angle formed between a line bisecting of the Achilles tendon and a line bisecting the calcaneal tuberosity/heel (Fig. 9.1).

- Achilles tendon/calcaneal tuberosity angle [10]: obtained using 3D reconstruction images where the windowing is set to remove the skin and subcutaneous tissue but maintaining the overlying soft tissue structures including the Achilles tendon, also allowing a better evaluation of the calcaneal tuberosity. The angle is measured between the lines of the longitudinal axis of the Achilles tendon and the longitudinal axis of the calcaneal tuberosity.
- Tibial axis/calcaneal tuberosity angle [10]: obtained using 3D reconstruction images maintaining only the bony anatomy. Angle was formed by the intersection of axes of calcaneal tuberosity and the tibia.
- Tibial axis/subtalar joint angle [10]: obtained using 3D reconstruction images with the windowing set to remove all the soft tissue structures, maintaining only the bony anatomy. Formed by the intersection of tibial axis and the line connecting midpoint of the posterior facet of the subtalar joint and most inferior point of the calcaneal tuberosity.
- Hindfoot alignment angle (HAA) [10, 46]: also obtained using 3D reconstruction images with the windowing maintaining only the bony anatomy. Defined as the angle between the tibial axis and calcaneal axis lines. The calcaneal axis is determined by the bisecting line of the angle formed by two lines representing the lateral and medial osseous contours of the calcaneus. The line for the lateral osseous contour is drawn between the most lateral aspect of the lateral process on the calcaneal tuberosity and the most superior and lateral discernable aspect of the calcaneus. The line for the medial osseous contour is drawn from the most medial aspect of the medial process of the calcaneal tuberosity to the most inferomedial discernable aspect of the sustentaculum tali.
- Hindfoot moment arm [10, 47]: obtained using 3D reconstruction images maintaining only the bony anatomy. Defined as the distance connecting the most inferior aspect of the calcaneus to the tibial axis line.

Subtalar Joint Alignment Measurements

- Subtalar horizontal angle or inferior talus-horizontal angle (inftal-hor) [5, 8, 24, 25]: measured in the coronal plane, angle between the articular surface of posterior facet of the talus and the floor, measured at three different points in the longitudinal length of the articular facet, 25% (posterior aspect), 50% (midpoint), and 75% (anterior aspect) (Fig. 15.4)
- Subtalar vertical angle [23]: measured in the coronal plane, angle between the articular surface of posterior facet of the talus and a vertical line to the floor
- Inferior talus-superior talus angle (inftal-suptal) [24, 25]: measured in the coronal plane by the angulation between the inferior and superior aspects of the talus, inferiorly at the posterior facet of the subtalar joint

- Inferior talus-superior calcaneal angle (inftal-supcal): measured in the coronal plane by the angulation between the inferior aspect of the talar and superior aspect of the calcaneal articular surfaces at the posterior facet of the subtalar joint
- Subtalar joint subluxation at the posterior facet [43]: measured in the coronal plane at the level of the most posterior aspect of the fibula. Represented by the distance from the lateral margin of the calcaneal articular surface to the lateral margin of the talar articular surface, at the posterior facet of the subtalar joint
- Percentage of uncoverage of the middle facet of the subtalar joint [48]: measured in the coronal plane, at the midpoint of the anterior-to-posterior dimension of the talar middle facet, by the percentage of the talar articular surface of middle facet that is not opposed by the calcaneal articular surface
- Incongruence angle of the middle facet of the subtalar joint [48]: measured in the coronal plane, at the midpoint of the anterior-to-posterior dimension of the talar middle facet. Represented by the angulation between the articular surfaces of the talar and calcaneal middle facets of the subtalar joint

Distal Tibiofibular Syndesmotic Measurements

Measurements are usually performed in the axial plane, at two different levels (10 mm above the tibial plafond and/or 2.5 mm below the talar dome) [27, 31]:

- Anterior tibiofibular distance [31, 49, 50]: shortest distance between the tip of the anterior tibial tubercle and the nearest point on the anterior border of the fibula (Figs. 12.1, 12.2, and 12.5).
- Posterior tibiofibular distance [31, 49, 50]: obtained by measuring the distance between the tip of the posterior tibial tubercle and the nearest point on the medial border of the fibula (Figs. 12.1, 12.2, and 12.5).
- Tibiofibular clear space [31]: the tibial incisura length line is first marked by a line connecting the tips of the anterior and posterior tibial tubercles. Two parallel lines to the line of the incisura are then marked, one tangential to the deepest point of the incisura and the other tangential to the medial border of the fibula. The distance between these two lines represents the tibiofibular clear space (Figs. 12.1, 12.2, and 12.5).
- Syndesmotic diastasis [31, 51]: central points of the tibia and fibula are marked by determining the midpoints of the lines connecting the anterior and posterior borders of each bone. Then, a line is marked connecting the midpoints of both bones. Diastasis measurement is represented by the distance between the medial cortex of the fibula and the lateral cortex of the tibia along the marked line (Figs. 12.1, 12.2, and 12.5).
- Angular measurement of syndesmotic diastasis [31, 52]: angle created between two tangential lines over the bony surface of the anterior and posterior aspects of the distal tibiofibular joint (Figs. 12.1, 12.2, and 12.5).

- DELTAFIB measurement [31, 53]: the tibial incisura length line is first marked by a line connecting the tips of the anterior and posterior tibial tubercles. The DELTAFIB measurement represents the angle between the incisura line and a line connecting the anterior and posterior tubercles of the fibula (Figs. 12.1, 12.2, and 12.5).
- Zwipp rotation [31, 54]: angle formed by the connection of a line across the anterior and posterior tubercles of the fibula and a line tangential line to the most anterior point of the tibia.
- Tang rotation [31, 55]: multiple bisecting lines are marked over tibial surface to determine the summation of these lines as the center of the tibia. Following that, the distances between this central point of the tibia and the most anterior and posterior points of the fibula are measured. The Tang rotation is represented by the ratio between the anterior and posterior distances.
- Phisitkul translation [31, 56]: the tibial incisura length line is first marked by a line connecting the tips of the anterior and posterior tibial tubercles. A perpendicular line to the incisura line is marked at the level of the anterior tibial tubercle. The shortest distance from this perpendicular line to the most anterior point of the distal fibula represents the Phisitkul translation.
- Davidovitch translation [31, 57]: first, a line connecting the widest anteroposterior dimension of fibula is marked. Then, a perpendicular to this line is marked at most anterior point of the distal fibula. A parallel line to this perpendicular line is marked at the level of the anterior tibial tubercle. The distance between these two parallel lines represents the Davidovitch translation.
- Lateral clear space [31, 58]: measured at a level 2.5 mm below the talar dome by the shortest distance between the distal fibula and the talus (Figs. 12.1, 12.2, and 12.5).
- Medial clear space [31, 58]: also measured at a level 2.5 mm below the talar dome, represented by the shortest distance between the medial malleolus and talus (Figs. 12.1, 12.2, and 12.5).

Hallux Valgus Measurements

- Hallux valgus angle [38, 59]: measured either in axial plane images or 3D reconstruction images. Represented by the angle between the axis of the first metatarsal and the proximal phalanx of the first toe.
- Hallux valgus interphalangeal angle [38, 59]: measured either in axial plane images or 3D reconstruction images. It describes the valgus angulation between the axis of the proximal and distal phalanxes of the first toe.
- 1–2 Intermetatarsal angle (IMA) [38, 59]: measured either in axial plane images or 3D reconstruction images. It measures the angulation between the axes of the first and second metatarsals.
- Sesamoid/metatarsal head positioning [40, 60–62]: measured in the coronal plane by the evaluation of the relative positioning between the medial sesamoid and the intersesamoid crista. Sesamoid subluxation could be graded as the pro-

portion of the medial sesamoid that is positioned laterally to the intersesamoid ridge regarding, when considering the total width of the medial sesamoid. A four-stage classification system was reported, where grade 0 represents the situation where the medial sesamoid is positioned entirely medial to the intersesamoid crista, grade 1 when less than half the width of the medial sesamoid is subluxated laterally, grade 2 when more than half the width of the medial sesamoid is subluxated laterally, and grade 3 when the medial sesamoid is entirely lateral to the crista.

- Sesamoid rotation angle (SRA) [37, 59, 63]: measured in the coronal plane, represents the angulation between a line connecting the most plantar aspects of both sesamoid bones and the floor.
- First metatarsal rotation Alpha-Angle [40, 59]: measured in the coronal plane. First, a line is marked connecting the lateral edge of the lateral sesamoid sulcus and the medial edge of the medial sesamoid sulcus of the first metatarsal head. Subsequently, a second line is marked connecting the medial and lateral dorsal corners of the first metatarsal head. A line connecting the midpoints of these both lines is then marked. The alpha-angle is the angle between this line and a perpendicular line to the floor.
- Stanmore classification system [37, 59]: consider the positioning of the sesamoid bones in relation to the intersesamoid crista as well as the amount of sesamoid wear. Degeneration of the metatarsosesamoid joint is graded as (A) normal (joint space higher than 1 mm), (B) reduced (joint space of less than 1 mm), (C) absent (bone on bone), and (D) with bone destruction, as determined by an empty intersesamoid crista). Sesamoid positioning is measured in the four-stage system previously mentioned (0, 1, 2, and 3).

References

1. Barg A, Bailey T, Richter M, de Cesar Netto C, Lintz F, Burssens A, Phisitkul P, Hanrahan CJ, Saltzman CL. Weightbearing computed tomography of the foot and ankle: emerging technology topical review. Foot Ankle Int. 2018;39:376–86.
2. Godoy-Santos AL, Cesar CN, Weight-Bearing Ct International Study G. Weight-Bearing computed tomography of the foot and ankle: an update and future directions. Acta Ortop Bras. 2018;26:135–9.
3. Lintz F, de Cesar Netto C, Barg A, Burssens A, Richter M, Weight Bearing CTISG. Weightbearing cone beam CT scans in the foot and ankle. EFORT Open Rev. 2018;3:278–86.
4. Richter M, Seidl B, Zech S, Hahn S. PedCAT for 3D-imaging in standing position allows for more accurate bone position (angle) measurement than radiographs or CT. Foot Ankle Surg. 2014;20:201–7.
5. Apostle KL, Coleman NW, Sangeorzan BJ. Subtalar joint axis in patients with symptomatic peritalar subluxation compared to normal controls. Foot Ankle Int. 2014;35:1153–8.
6. Haleem AM, Pavlov H, Bogner E, Sofka C, Deland JT, Ellis SJ. Comparison of deformity with respect to the talus in patients with posterior tibial tendon dysfunction and controls using multiplanar weight-bearing imaging or conventional radiography. J Bone Joint Surg Am. 2014;96:e63.

7. Yoshioka N, Ikoma K, Kido M, Imai K, Maki M, Arai Y, Fujiwara H, Tokunaga D, Inoue N, Kubo T. Weight-bearing three-dimensional computed tomography analysis of the forefoot in patients with flatfoot deformity. J Orthop Sci. 2016;21:154–8.
8. de Cesar Netto C, Schon LC, Thawait GK, da Fonseca LF, Chinanuvathana A, Zbijewski WB, Siewerdsen JH, Demehri S. Flexible adult acquired flatfoot deformity: comparison between weight-bearing and non-weight-bearing measurements using cone-beam computed tomography. J Bone Joint Surg Am. 2017;99(18):e98. https://doi.org/10.2106/JBJS.16.01366.
9. de Cesar Netto C, Shakoor D, Dein EJ, Zhang H, Thawait GK, Richter M, Ficke JR, Schon LC, Weightbearing CT International Study Group, Demehri S. Influence of investigator experience on reliability of adult acquired flatfoot deformity measurements using weightbearing computed tomography. Foot Ankle Surg. 2019;25(4):495–502. https://doi.org/10.1016/j.fas.2018.03.001. Epub 2018 Mar 1.2
10. de Cesar Netto C, Shakoor D, Roberts L, Chinanuvathana A, Mousavian A, Lintz F, Schon LC, Demehri S, Weight Bearing CT International Study Group. Hindfoot alignment of adult acquired flatfoot deformity: a comparison of clinical assessment and weightbearing cone beam CT examinations. Foot Ankle Surg. 2018. pii: S1268-7731(18)30301-1. doi: https://doi.org/10.1016/j.fas.2018.10.008. [Epub ahead of print].
11. Kunas GC, Probasco W, Haleem AM, Burket JC, Williamson ERC, Ellis SJ. Evaluation of peritalar subluxation in adult acquired flatfoot deformity using computed tomography and weightbearing multiplanar imaging. Foot Ankle Surg. 2018;24:495–500.
12. Peiffer M, Belvedere C, Clockaerts S, Leenders T, Leardini A, Audenaert E, Victor J, Burssens A, Wbct ISG. Three-dimensional displacement after a medializing calcaneal osteotomy in relation to the osteotomy angle and hindfoot alignment. Foot Ankle Surg. 2018; https://doi.org/10.1016/j.fas.2018.11.015.
13. Burssens A, Peeters J, Buedts K, Victor J, Vandeputte G. Measuring hindfoot alignment in weight bearing CT: a novel clinical relevant measurement method. Foot Ankle Surg. 2016;22:233–8.
14. Lintz F, Welck M, Bernasconi A, Thornton J, Cullen NP, Singh D, Goldberg A. 3D biometrics for hindfoot alignment using weightbearing CT. Foot Ankle Int. 2017;38:684–9.
15. Burssens A, Peeters J, Peiffer M, Marien R, Lenaerts T, WBCT ISG, Vandeputte G, Victor J. Reliability and correlation analysis of computed methods to convert conventional 2D radiological hindfoot measurements to a 3D setting using weightbearing CT. Int J Comput Assist Radiol Surg. 2018;13:1999–2008.
16. Burssens A, Van Herzele E, Leenders T, Clockaerts S, Buedts K, Vandeputte G, Victor J. Weightbearing CT in normal hindfoot alignment – presence of a constitutional valgus? Foot Ankle Surg. 2018;24:213–8.
17. Burssens A, Barg A, van Ovost E, Van Oevelen A, Leenders T, Peiffer M, Bodere I, Weightbearing CTISG, Audenaert E, Victor J. The hind- and midfoot alignment computed after a medializing calcaneal osteotomy using a 3D weightbearing CT. Int J Comput Assist Radiol Surg. 2019;14:1439–47.
18. de Cesar Netto C, Bernasconi A, Roberts L, Pontin PA, Lintz F, Saito GH, Roney A, Elliott A, O'Malley M. Foot alignment in symptomatic national basketball association players using weightbearing cone beam computed tomography. Orthop J Sports Med. 2019;7:2325967119826081. https://doi.org/10.1177/2325967119826081.
19. Zhang JZ, Lintz F, Bernasconi A, Weight Bearing CTISG, Zhang S. 3D biometrics for hindfoot alignment using weightbearing computed tomography. Foot Ankle Int. 2019;40:720–6.
20. Hirschmann A, Pfirrmann CW, Klammer G, Espinosa N, Buck FM. Upright cone CT of the hindfoot: comparison of the non-weight-bearing with the upright weight-bearing position. Eur Radiol. 2014;24:553–8.
21. Ananthakrisnan D, Ching R, Tencer A, Hansen ST Jr, Sangeorzan BJ. Subluxation of the talocalcaneal joint in adults who have symptomatic flatfoot. J Bone Joint Surg Am. 1999;81:1147–54.

22. Malicky ES, Crary JL, Houghton MJ, Agel J, Hansen ST Jr, Sangeorzan BJ. Talocalcaneal and subfibular impingement in symptomatic flatfoot in adults. J Bone Joint Surg Am. 2002;84:2005–9.
23. Colin F, Horn Lang T, Zwicky L, Hintermann B, Knupp M. Subtalar joint configuration on weightbearing CT scan. Foot Ankle Int. 2014;35:1057–62.
24. Probasco W, Haleem AM, Yu J, Sangeorzan BJ, Deland JT, Ellis SJ. Assessment of coronal plane subtalar joint alignment in peritalar subluxation via weight-bearing multiplanar imaging. Foot Ankle Int. 2015;36:302–9.
25. Cody EA, Williamson ER, Burket JC, Deland JT, Ellis SJ. Correlation of talar anatomy and subtalar joint alignment on weightbearing computed tomography with radiographic flatfoot parameters. Foot Ankle Int. 2016;37:874–81.
26. Burssens A, Vermue H, Barg A, Krahenbuhl N, Victor J, Buedts K. Templating of syndesmotic ankle lesions by use of 3D analysis in weightbearing and nonweightbearing CT. Foot Ankle Int. 2018;39:1487–96.
27. Osgood GM, Shakoor D, Orapin J, Qin J, Khodarahmi I, Thawait GK, Ficke JR, Schon LC, Demehri S. Reliability of distal tibio-fibular syndesmotic instability measurements using weightbearing and non-weightbearing cone-beam CT. Foot Ankle Surg. 2018; https://doi.org/10.1016/j.fas.2018.10.003.
28. Krahenbuhl N, Bailey TL, Presson AP, Allen CM, Henninger HB, Saltzman CL, Barg A. Torque application helps to diagnose incomplete syndesmotic injuries using weight-bearing computed tomography images. Skelet Radiol. 2019;48:1367–76.
29. Krahenbuhl N, Bailey TL, Weinberg MW, Davidson NP, Hintermann B, Presson AP, Allen CM, Henninger HB, Saltzman CL, Barg A. Impact of torque on assessment of syndesmotic injuries using weightbearing computed tomography scans. Foot Ankle Int. 2019;40:710–9.
30. Patel S, Malhotra K, Cullen NP, Singh D, Goldberg AJ, Welck MJ. Defining reference values for the normal tibiofibular syndesmosis in adults using weight-bearing CT. Bone Joint J. 2019;101-B:348–52.
31. Shakoor D, Osgood GM, Brehler M, Zbijewski WB, de Cesar Netto C, Shafiq B, Orapin J, Thawait GK, Shon LC, Demehri S. Cone-beam CT measurements of distal tibio-fibular syndesmosis in asymptomatic uninjured ankles: does weight-bearing matter? Skelet Radiol. 2019;48:583–94.
32. Geng X, Wang C, Ma X, Wang X, Huang J, Zhang C, Xu J, Yang J. Mobility of the first metatarsal-cuneiform joint in patients with and without hallux valgus: in vivo three-dimensional analysis using computerized tomography scan. J Orthop Surg Res. 2015;10:140.
33. Kimura T, Kubota M, Taguchi T, Suzuki N, Hattori A, Marumo K. Evaluation of first-ray mobility in patients with hallux valgus using weight-bearing CT and a 3-D analysis system: a comparison with normal feet. J Bone Joint Surg Am. 2017;99:247–55.
34. Kimura T, Kubota M, Suzuki N, Hattori A, Marumo K. Comparison of intercuneiform 1-2 joint mobility between hallux valgus and normal feet using weightbearing computed tomography and 3-dimensional analysis. Foot Ankle Int. 2018;39:355–60.
35. Cheung ZB, Myerson MS, Tracey J, Vulcano E. Weightbearing CT scan assessment of foot alignment in patients with hallux rigidus. Foot Ankle Int. 2018;39:67–74.
36. Welck MJ, Al-Khudairi N. Imaging of hallux valgus: how to approach the deformity. Foot Ankle Clin. 2018;23:183–92.
37. Welck MJ, Singh D, Cullen N, Goldberg A. Evaluation of the 1st metatarso-sesamoid joint using standing CT – the Stanmore classification. Foot Ankle Surg. 2018;24:314–9.
38. Collan L, Kankare JA, Mattila K. The biomechanics of the first metatarsal bone in hallux valgus: a preliminary study utilizing a weight bearing extremity CT. Foot Ankle Surg. 2013;19:155–61.
39. Campbell B, Miller MC, Williams L, Conti SF. Pilot study of a 3-dimensional method for analysis of pronation of the first metatarsal of hallux valgus patients. Foot Ankle Int. 2018;39:1449–56.
40. Kim Y, Kim JS, Young KW, Naraghi R, Cho HK, Lee SY. A new measure of tibial sesamoid position in hallux valgus in relation to the coronal rotation of the first metatarsal in CT scans. Foot Ankle Int. 2015;36:944–52.

41. Younger AS, Sawatzky B, Dryden P. Radiographic assessment of adult flatfoot. Foot Ankle Int. 2005;26:820–5.
42. Sangeorzan BJ, Mosca V, Hansen ST Jr. Effect of calcaneal lengthening on relationships among the hindfoot, midfoot, and forefoot. Foot Ankle. 1993;14:136–41.
43. Ferri M, Scharfenberger AV, Goplen G, Daniels TR, Pearce D. Weightbearing CT scan of severe flexible pes planus deformities. Foot Ankle Int. 2008;29:199–204.
44. Ellis SJ, Deyer T, Williams BR, Yu JC, Lehto S, Maderazo A, Pavlov H, Deland JT. Assessment of lateral hindfoot pain in acquired flatfoot deformity using weightbearing multiplanar imaging. Foot Ankle Int. 2010;31:361–71.
45. Coughlin MJ, Kaz A. Correlation of Harris mats, physical exam, pictures, and radiographic measurements in adult flatfoot deformity. Foot Ankle Int. 2009;30:604–12.
46. Williamson ER, Chan JY, Burket JC, Deland JT, Ellis SJ. New radiographic parameter assessing hindfoot alignment in stage II adult-acquired flatfoot deformity. Foot Ankle Int. 2015;36:417–23.
47. Saltzman CL, el-Khoury GY. The hindfoot alignment view. Foot Ankle Int. 1995;16:572–6.
48. de Cesar Netto C, Godoy-Santos AL, Saito GH, Lintz F, Siegler S, O'Malley M, Deland JT, Ellis SJ. Subluxation of the middle facet of the subtalar joint as a marker of peritalar subluxation in adult acquired flatfoot deformity. A case-control study. J Bone Joint Surg Am. 2019. In Press
49. Gardner MJ, Demetrakopoulos D, Briggs SM, Helfet DL, Lorich DG. Malreduction of the tibiofibular syndesmosis in ankle fractures. Foot Ankle Int. 2006;27:788–92.
50. Elgafy H, Semaan HB, Blessinger B, Wassef A, Ebraheim NA. Computed tomography of normal distal tibiofibular syndesmosis. Skelet Radiol. 2010;39:559–64.
51. Prior CP, Widnall JC, Rehman AK, Weller DM, Wood EV. A simplified, validated protocol for measuring fibular reduction on ankle CT. Foot Ankle Surg. 2017;23:53–6.
52. Malhotra G, Cameron J, Toolan BC. Diagnosing chronic diastasis of the syndesmosis: a novel measurement using computed tomography. Foot Ankle Int. 2014;35:483–8.
53. Dikos GD, Heisler J, Choplin RH, Weber TG. Normal tibiofibular relationships at the syndesmosis on axial CT imaging. J Orthop Trauma. 2012;26:433–8.
54. Vasarhelyi A, Lubitz J, Gierer P, Gradl G, Rosler K, Hopfenmuller W, Klaue K, Mittlmeier TW. Detection of fibular torsional deformities after surgery for ankle fractures with a novel CT method. Foot Ankle Int. 2006;27:1115–21.
55. Tang CW, Roidis N, Vaishnav S, Patel A, Thordarson DB. Position of the distal fibular fragment in pronation and supination ankle fractures: a CT evaluation. Foot Ankle Int. 2003;24:561–6.
56. Phisitkul P, Ebinger T, Goetz J, Vaseenon T, Marsh JL. Forceps reduction of the syndesmosis in rotational ankle fractures: a cadaveric study. J Bone Joint Surg Am. 2012;94:2256–61.
57. Davidovitch RI, Weil Y, Karia R, Forman J, Looze C, Liebergall M, Egol K. Intraoperative syndesmotic reduction: three-dimensional versus standard fluoroscopic imaging. J Bone Joint Surg Am. 2013;95:1838–43.
58. Pelton K, Thordarson DB, Barnwell J. Open versus closed treatment of the fibula in Maisonneuve injuries. Foot Ankle Int. 2010;31:604–8.
59. de Cesar Netto C, Richter M. Use of advanced weightbearing imaging in evaluation of hallux valgus. Foot Ankle Clin. 2019. In Press.
60. Yildirim Y, Cabukoglu C, Erol B, Esemenli T. Effect of metatarsophalangeal joint position on the reliability of the tangential sesamoid view in determining sesamoid position. Foot Ankle Int. 2005;26:247–50.
61. Talbot KD, Saltzman CL. Assessing sesamoid subluxation: how good is the AP radiograph? Foot Ankle Int. 1998;19:547–54.
62. Smith RW, Reynolds JC, Stewart MJ. Hallux valgus assessment: report of research committee of American Orthopaedic Foot and Ankle Society. Foot Ankle. 1984;5:92–103.
63. Kuwano T, Nagamine R, Sakaki K, Urabe K, Iwamoto Y. New radiographic analysis of sesamoid rotation in hallux valgus: comparison with conventional evaluation methods. Foot Ankle Int. 2002;23:811–7.

Chapter 22
Clinical Examples of Weight Bearing Computed Tomography

Martinus Richter, Francois Lintz, Cesar de Cesar Netto, Alexej Barg, Arne Burssens, and Scott Ellis

Figures 22.1, 22.2, 22.3, 22.4, 22.5, 22.6, 22.7, 22.8, 22.9, 22.10, 22.11, 22.12, 22.13, 22.14, 22.15, 22.16, 22.17, 22.18, and 22.19 show different examples of clinical application of weight bearing computed tomography (WBCT).

M. Richter et al., *Weight Bearing Cone Beam Computed Tomography (WBCT) in the Foot and Ankle*, https://doi.org/10.1007/978-3-030-31949-6_22

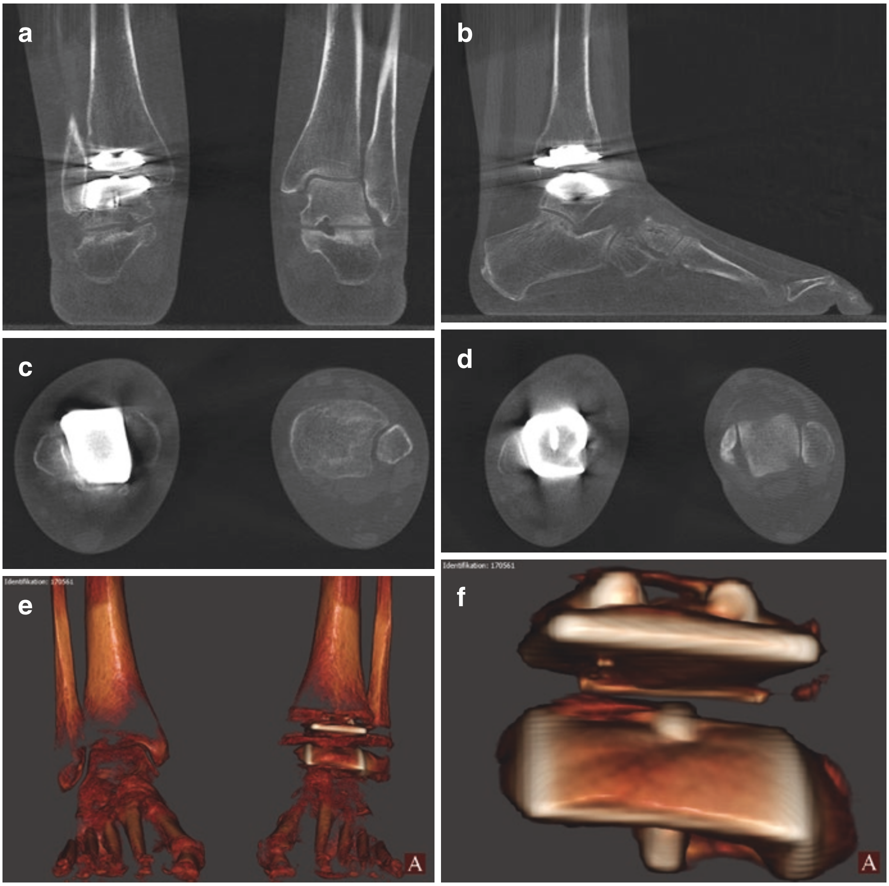

Fig. 22.1 (**a**–**f**) WBCT with implanted total ankle replacement (TAR) (STAR, Stryker, Kalamazoo, MI, USA). (**a**) show paracoronal reformation, (**b**) parasagittal reformation, and (**c**, **d**) axial reformations. The axial reformations (**c**, **d**) allow for assessment of rotational relationship between tibial component (**c**) and talar component (**d**). Especially for nonmobile bearing TAR models, incongruent rotational position of tibial and talar components might cause increased internal stress and wear. (**e**, **f**) show 3D reformations of TAR and surrounding bone (**e**) and TAR implant alone (**f**)

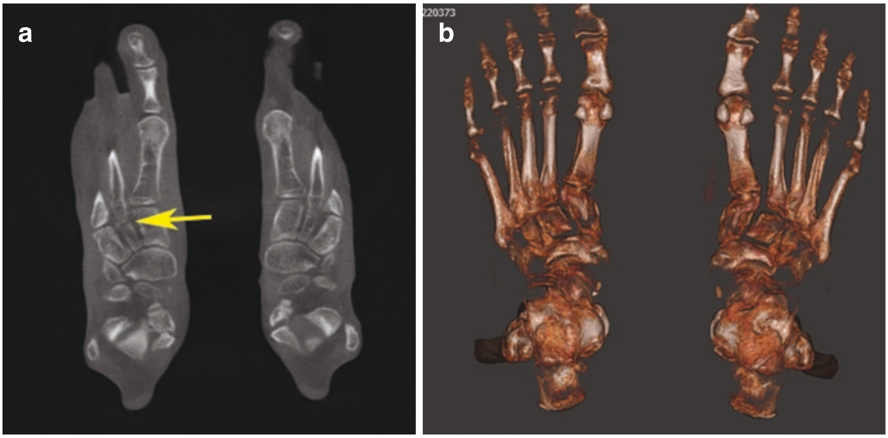

Fig. 22.2 (**a**, **b**) Subtle Lisfranc joint instability. (**a**) shows a lateral shift of the base of the second metatarsal in the second tarsometatarsal joint (arrow) which was not visible on conventional radiographs with weight-bearing or conventional CT without weight-bearing. (**b**) shows a 3D reformation

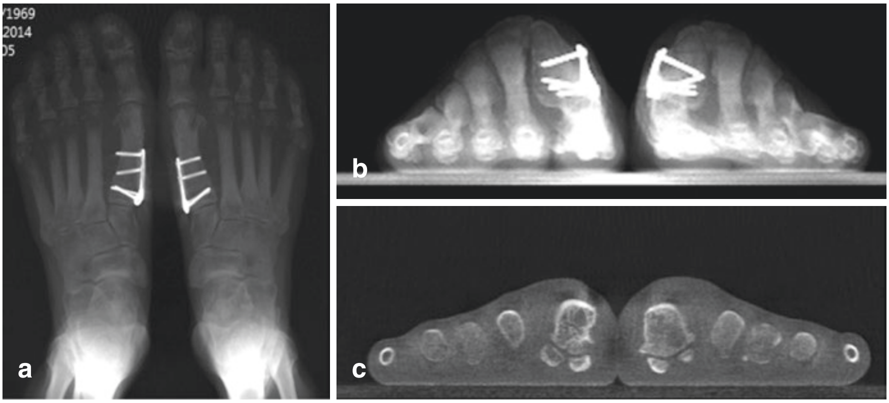

Fig. 22.3 (**a**–**c**) Assessment of bilateral hallux valgus correction. (**a**) shows a virtual dorsoplantar weight-bearing radiograph, generated from the WBCT-3D-dataset. (**b**) shows a generated Metatarsal-Skyline view, and (**c**) a paracoronal reformation. The rotation of the first metatarsal head and its position in relation to the sesamoids is better visible on the paracoronal reformation (**c**) than on the metatarsal-skyline view (**b**) which represents the former visualization with conventional weight-bearing radiographs

Fig. 22.4 (**a**–**c**) TAR (Salto, Wright Medical Group, Memphis, TN, USA). WBCT-based parasagittal (**a**), paracoronal (**b**), and axial (**c**) reformations allowing for optimal assessment of implant position and cyst size and location under weight-bearing conditions

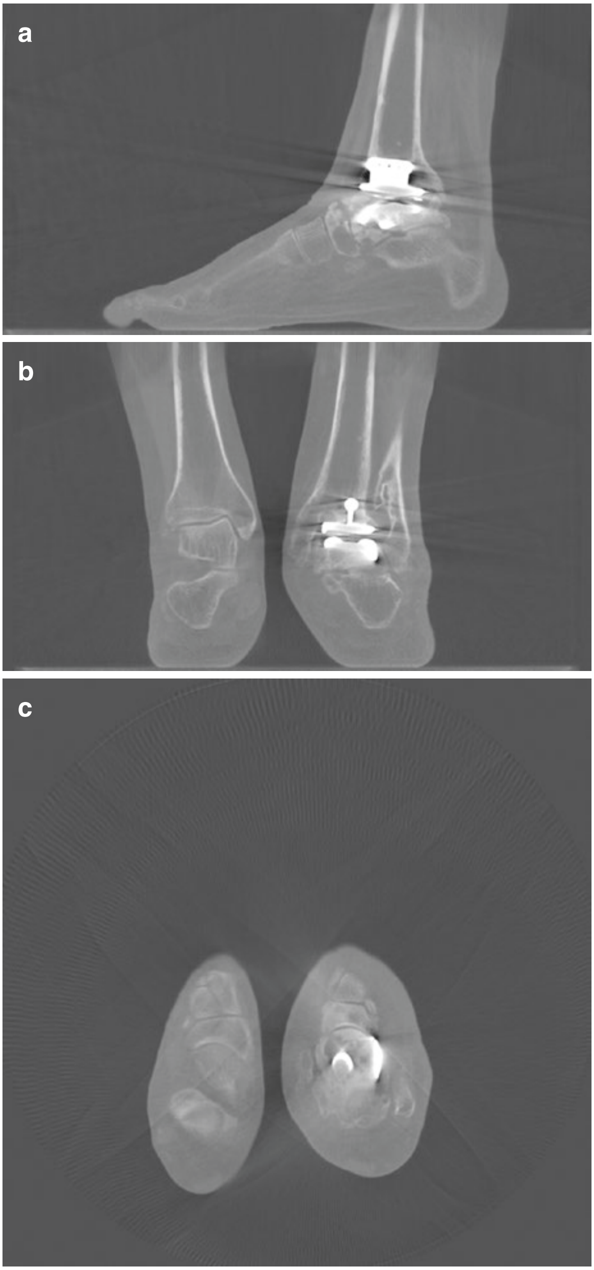

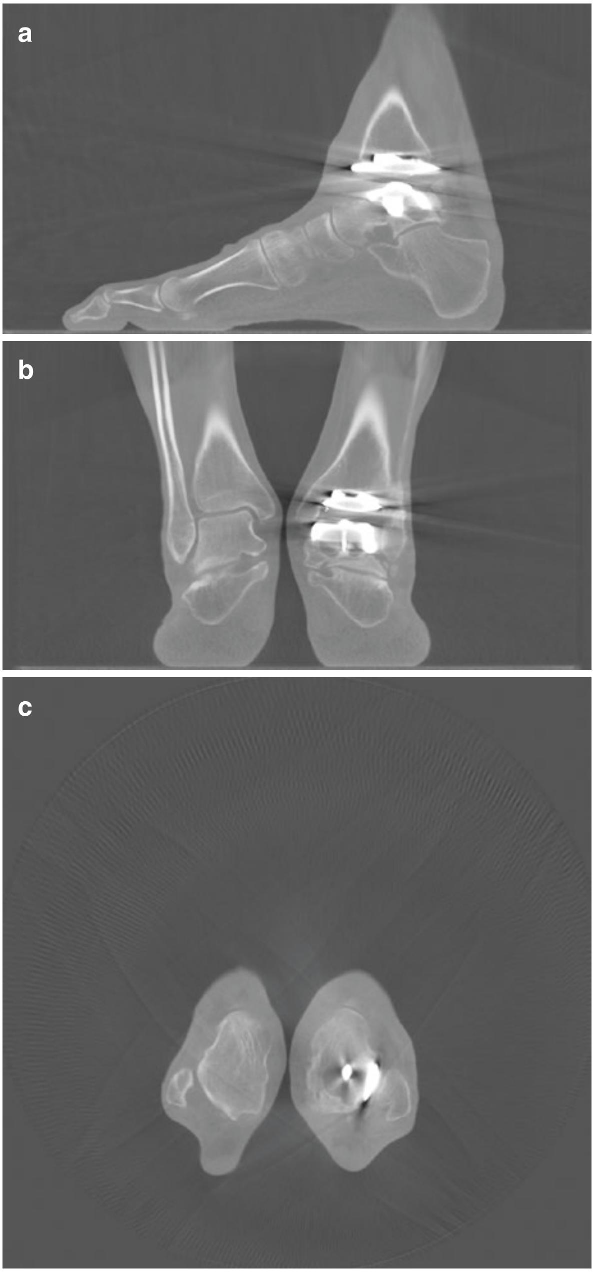

Fig. 22.5 (**a**–**c**) (STAR, Stryker, Kalamazoo, MI, USA). WBCT-based parasagittal (**a**), paracoronal (**b**), and axial (**c**) reformations allowing for optimal assessment of implant position and cyst size and location under weight-bearing conditions

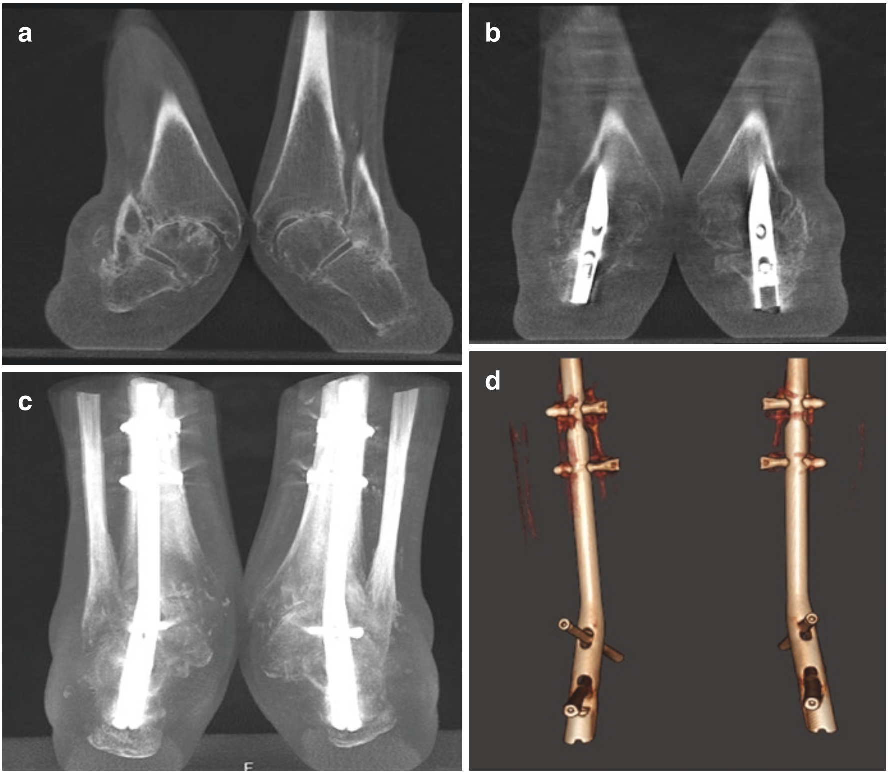

Fig. 22.6 (**a**–**d**) Charcot arthropathy at the hindfoot (Localization Sanders IV) before (**a**) and after bilateral hindfoot correction arthrodesis (**b**–**d**). The preoperative paracoronal reformation (**a**) shows severe hindfoot valgus and destruction of ankle and subtalar joints. (**b**) shows a paracoronal reformation after bilateral hindfoot correction arthrodesis with retrograde arthrodesis nail (A3, Stryker, Kalamazoo, MI, USA). (**c**) shows a generated virtual hindfoot radiograph (so-called Saltzman view) showing the hindfoot axis and the entire implant. (**d**) shows a 3D reformation of the implants with best visibility of the locking screws

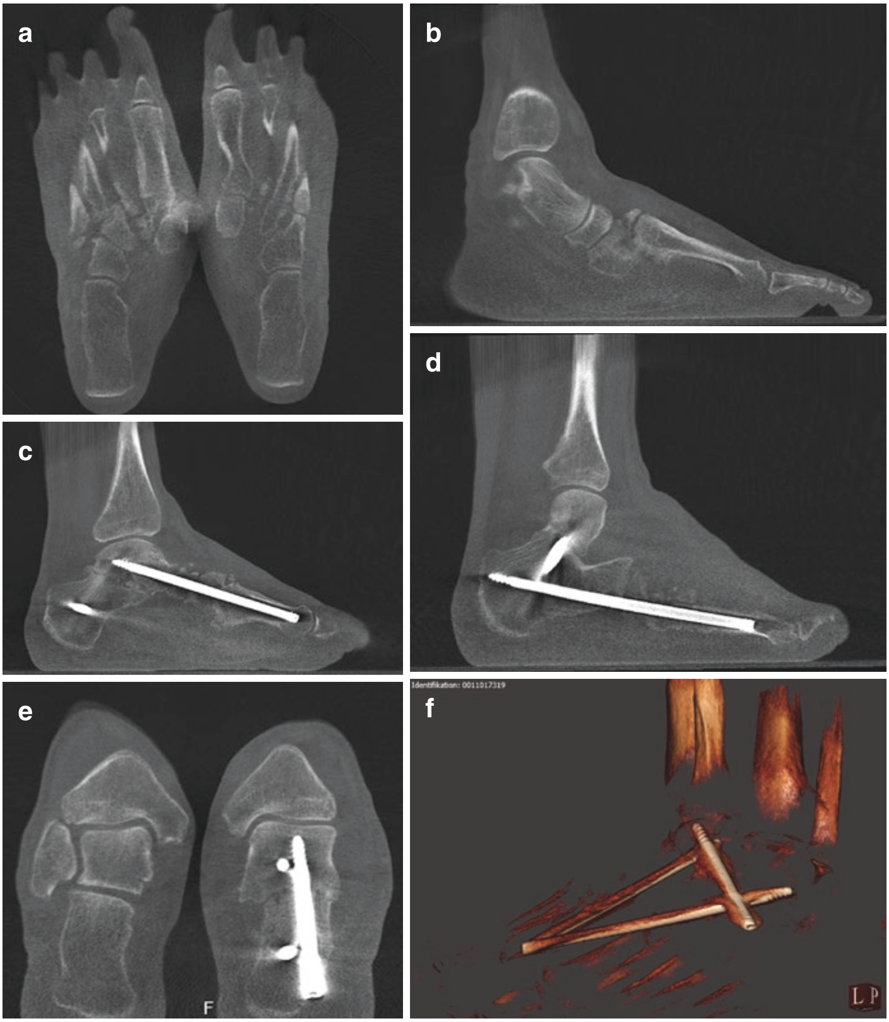

Fig. 22.7 (**a**–**f**) Charcot arthropathy at the midfoot (Localization Sanders II) before and after pan-correction-arthrodesis. (**a**, **b**) show axial and parasagittal reformations with severe destruction and deformity at and around the Lisfranc joint. (**c**–**e**) show the healed situation after plan-correction-arthrodesis involving the following joints: subtalar, talonavicular, calcaneocuboid, innominate 1–3, intercuneiform 1–2, intercuneiform 2–3, and tarsometatarsal 1–5. Midfoot fusion bolts (MFB, Depuy Synthes, Raynham, MA, USA) were used for fixation. (**c**) shows a MFT in the medial column, i.e., first metatarsal, cuneiform 1, navicular, and talus. (**d**) shows a MFB in the lateral column, i.e., fifth metatarsal, cuboid, and calcaneus. (**e**) shows a MFB in the hindfoot, i.e., calcaneus and talus. (**f**) shows a 3D reformation of the three MFBs with their spatial relationship in relation to each other

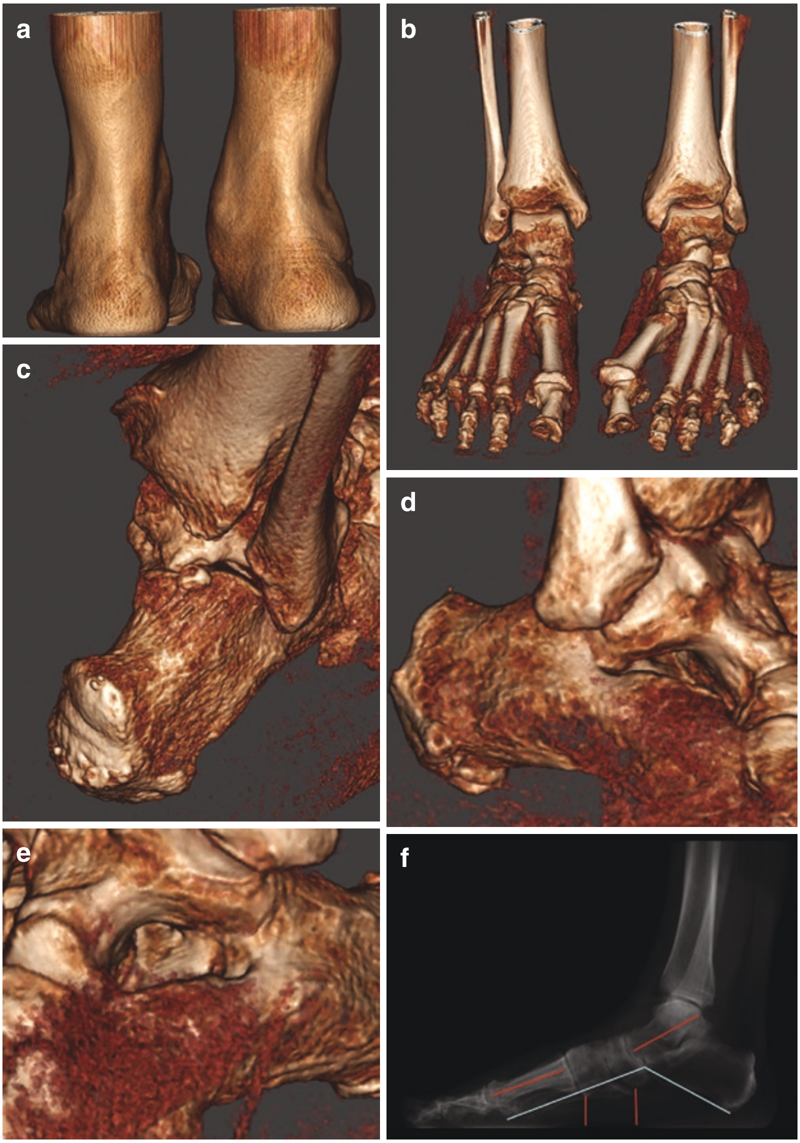

Fig. 22.8 Shows a posttraumatic case of acquired flatfoot following chronic subluxation of the tibialis posterior tendon. The bilateral posterior skin view shows deviation of the hindfoot (**a**). The AP 3D rendering bone view shows lateralization of the forefoot and plantar drop of the talus comparative to the asymptomatic side (**b**). We have added a posterior 3D bone view showing the enlarged medial groove consequence of chronic subluxation of the posterior tibial tendon (**c**). (**d**, **e**) show the talocalcaneal lateral impingement in the sinus tarsi on the symptomatic (**d**) and asymptomatic (**e**) sides. Conventional measurements are possible very rapidly using pre-programed and readily available DRR (digitally reconstructed radiographs) incidences such as this lateral 2D view (**f**) showing medial arch angle, Meary's angle, and navicular and medial cuneiform to floor distances. The TALAS (**g**) window shows the result of the semiautomatic hindfoot alignment software. In this case, the foot ankle offset value is 10.8%, advocating for a severe case of flatfoot

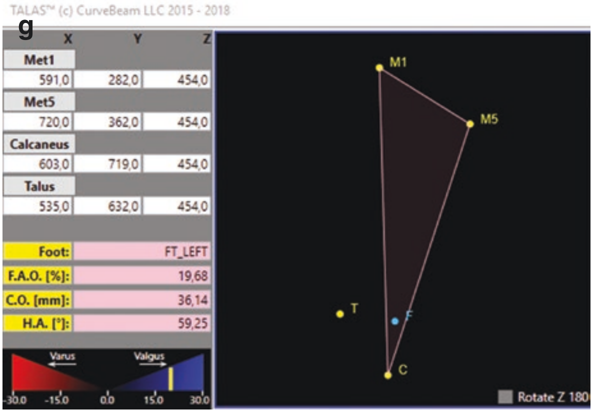

Fig. 22.8 (continued)

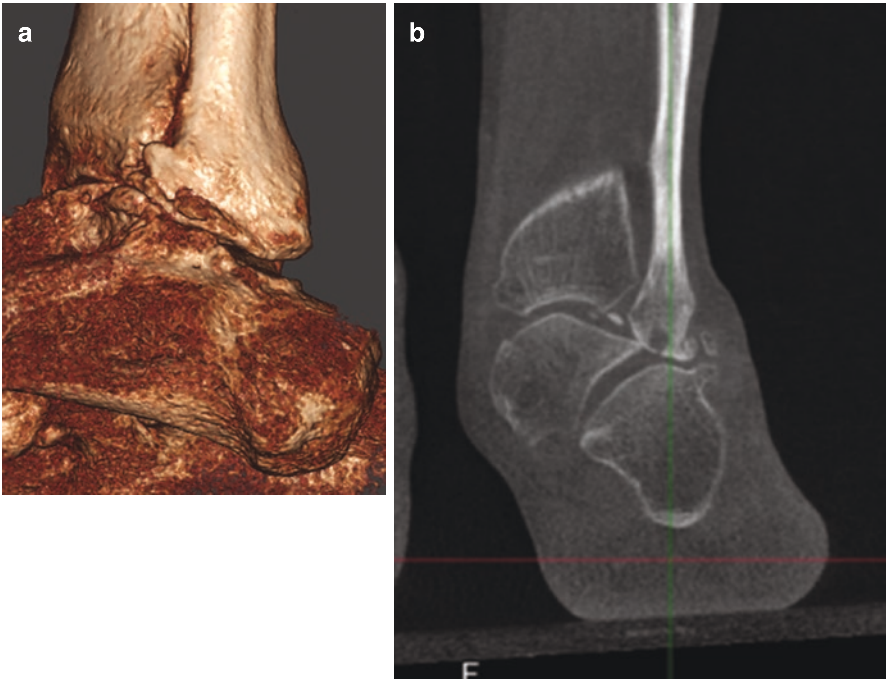

Fig. 22.9 Is a classic case of subfibular impingement. (**a**) shows the 3D rendering view on which the diagnosis is self-evident. We advocate for the use of the 3D rendering view to fulfill in the future the need for a "snapshot" view which before was provided by conventional radiographs. In the future, virtual reality and holographic projectors will probably provide for a comfortable and immediate interface valid for daily clinical use. (**b**, **c**) correspond to the coronal and sagittal views of the multiplanar windows. The TALAS (**d**) window in this case shows a major case of valgus, explaining this situation, with a close to 20% foot ankle offset. The FAO is given as a percentage of foot length, in order to be comparable across different patients. In this case, that means that the patient's mass is distributed with an offset so large that it is actually projected outside, on the medial side of the plantar surface. In physical terms, this means the foot tilts on each step, explaining the major subfibular impingement

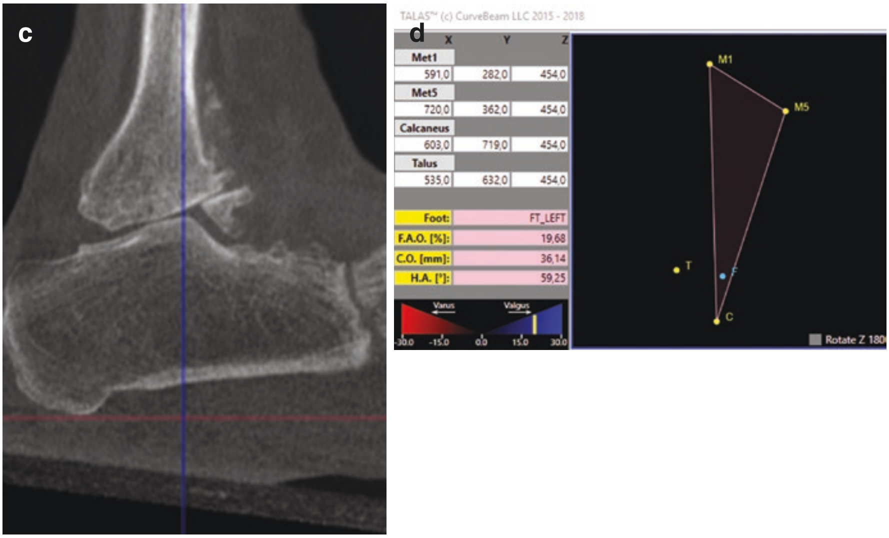

Fig. 22.9 (continued)

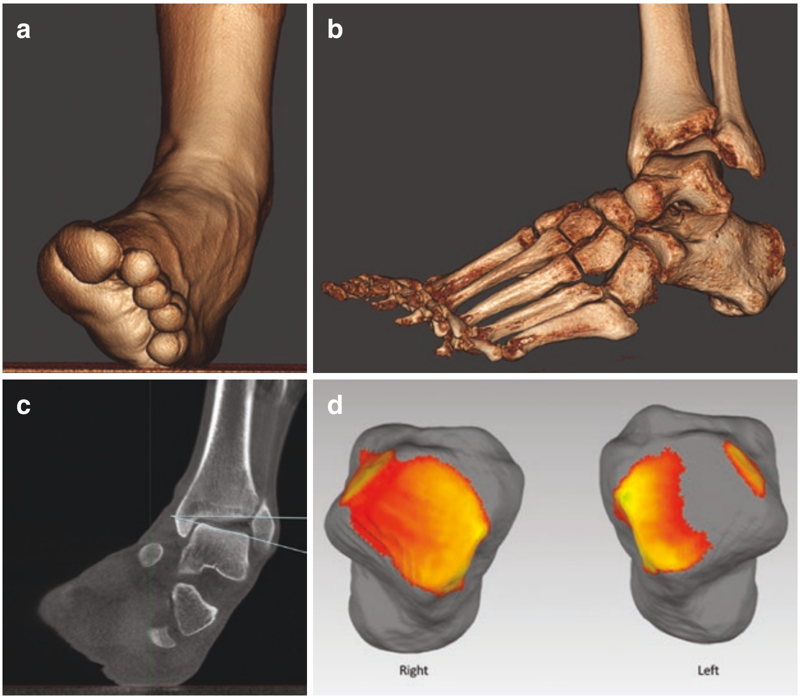

Fig. 22.10 Demonstrates the possibility in a large field of view cone beam WBCT to investigate dynamic postures such as varus in this case of chronic lateral ankle instability. An important intra-articular lateral talar tilt can be visualized and measured. The subtalar joint may be investigated in the MPR windows (**c**) or on the 3D rendering view (**a**, **b**). A distance mapping view (**d**, image courtesy of Pr Sorin Siegler, Drexel University, Philadelphia PA, USA) may be built from the harvested data. In this case the right side demonstrates good joint congruency, whereas the left side demonstrates approximation in the medial aspect of the tibiotalar joint and important distancing in the lateral aspect of the joint

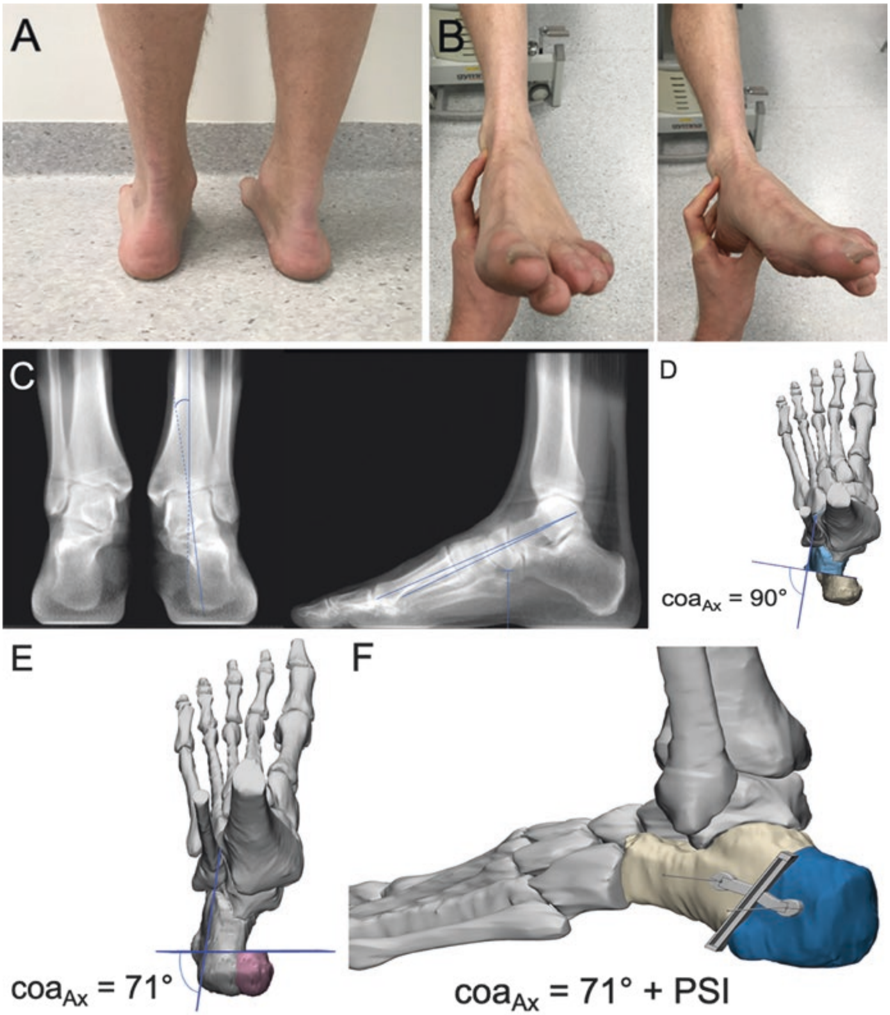

Fig. 22.11 (**a**–**f**) Preoperative computer-assisted planning of an adult-acquired flatfoot deformity correction based on weightbearing CT images. Left AAFD in a 52-year-old male patient (**a**). Tenderness over deltoid ligament, tibialis posterior, and fascia plantaris +++ (**b**). Digitally reconstructed images AP and lateral of the left AAFD (**c**). A medializing calcaneus osteotomy is simulated on a generated 3D model with a calcaneus osteotomy angle in the axial plane (coa_{Ax}) 90° (perpendicular) to the lateral wall of the calcaneus (**d**). Note a lengthening of the calcaneus, which needs to be avoided in this case, as the patient presents with a marked fasciitis plantaris (**e**). The coa_{Ax} is changed to 71° which corresponds to an isometric translation of the calcaneus. A patient-specific instrument (PSI) is constructed to obtain the correct osteotomy plane (**f**)

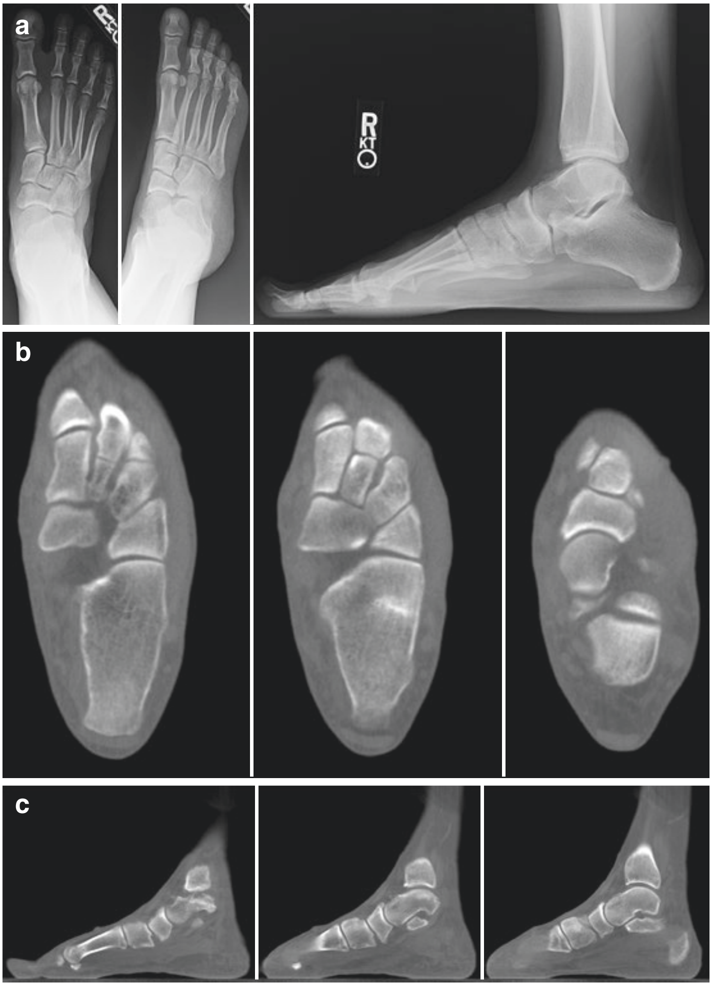

Fig. 22.12 Demonstrates the usage of WBCT in a 44-year-old male patient with painful midfoot osteoarthritis and concomitant deformity. (**a**) Weight bearing radiographs (from left to right: anteroposterior, oblique, and lateral views) demonstrate moderate midfoot osteoarthritis with a moderate abductus deformity. The lateral radiographic view demonstrates neutral overall alignment of the medial arch. (**b**) Axial WBCT demonstrates moderate degenerative changes in the midfoot, especially in the naviculocuneiform joints. (**c**) Sagittal WBCT demonstrates a severe breakdown of the medial arch at the level of the naviculocuneiform joint with visible degenerative changes. (**d**) Coronal WBCT confirms naviculocuneiform joint osteoarthritis and demonstrates an overall neutral hindfoot alignment with no substantial degeneration of associated structures. The patient underwent a diagnostic ultrasound-guided injection of the naviculocuneiform and medial intercuneiform joints resulting in immediate pain relief throughout the midfoot. In addition, arthrodesis realignment of the naviculocuneiform and medial intercuneiform joints was performed with the use of a proximal tibia bone graft (cancellous bone). (**e**) Non-weight bearing radiographs (from left to right: anteroposterior, oblique, and lateral views) demonstrate appropriate hardware positioning. A WBCT was taken during the 3-month postoperative follow-up prior to clearing the patient for full weight bearing conditions and to wear regular shoes. This postoperative (**f**) axial, (**g**) sagittal, and (**h**) coronal WBCT demonstrates progressive, near complete union of the naviculocuneiform and medial intercuneiform joints with restored alignment of the medial arch and appropriate hardware positioning. Additionally, the postoperative WBCT reveals diffuse osteopenia due to the patient's non-weight bearing rehabilitation following the operation

Fig. 22.12 (continued)

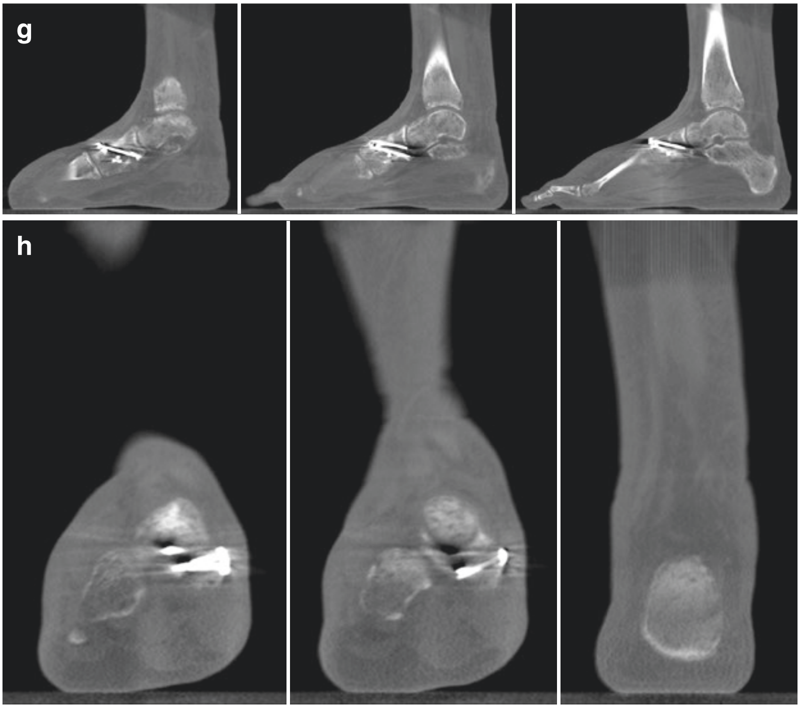

Fig. 22.12 (continued)

Fig. 22.13 Demonstrates the usage of WBCT in a 32-year-old male with painful midfoot nonunion. Five years ago, the patient missed a step during a hockey game and sustained a complex comminuted fracture of the navicular bone. Since this injury, he has undergone four surgeries chronologically listed as follows: (1) closed reduction and application of external fixator of the midfoot, (2) removal of external fixator, open reduction, and internal fixation using an allograft, (3) irrigation and debridement of a deep infection acquired postoperatively, and (4) arthrodesis attempt of the talonavicular and naviculocuneiform joints using an iliac crest autograft. All surgeries were performed in an outside facility within 9 months of the initial injury. (**a**) Weight bearing radiographs (from left to right: anteroposterior, oblique, and lateral views) demonstrate substantial nonunion of the talonavicular joint with partial loosening of implanted hardware. A reliable assessment of the naviculocuneiform arthrodesis is not possible using conventional radiographs. However, (**b**) axial WBCT does demonstrate a complete nonunion of the talonavicular joint with mature union of the naviculocuneiform arthrodesis. (**c**) Sagittal WBCT confirms these findings and demonstrates neutral overall alignment of the midfoot. (**d**) Coronal WBCT re-demonstrates complete nonunion of the talonavicular joint. This view also demonstrates an overall neutral hindfoot alignment with no substantial degeneration of associated structures. A deep debridement of the talonavicular nonunion with deep biopsies was performed along with the realignment of the medial column arthrodesis with use of proximal tibia bone graft (cancellous bone). (**e**) Postoperative non-weight bearing radiographs (from left to right: anteroposterior and lateral views) demonstrate appropriate hardware positioning. (**f**) At 9-month follow-up, weight bearing radiographs (from left to right: anteroposterior and lateral views of the foot, mortise view of the ankle, and hindfoot alignment view) were acquired and demonstrate progressive union of the medial column with appropriate hardware positioning. (**g**) Axial, (**h**) sagittal, and (**i**) coronal WBCT demonstrates complete union of the talonavicular joint with neutral overall alignment of the midfoot and hindfoot. Due to local discomfort, all hardware was removed 12 months after the index surgery. (**j**) Postoperative weight bearing radiographs (from left to right: anteroposterior, oblique, and lateral views) demonstrate a mature arthrodesis of the medial column with no remaining hardware present

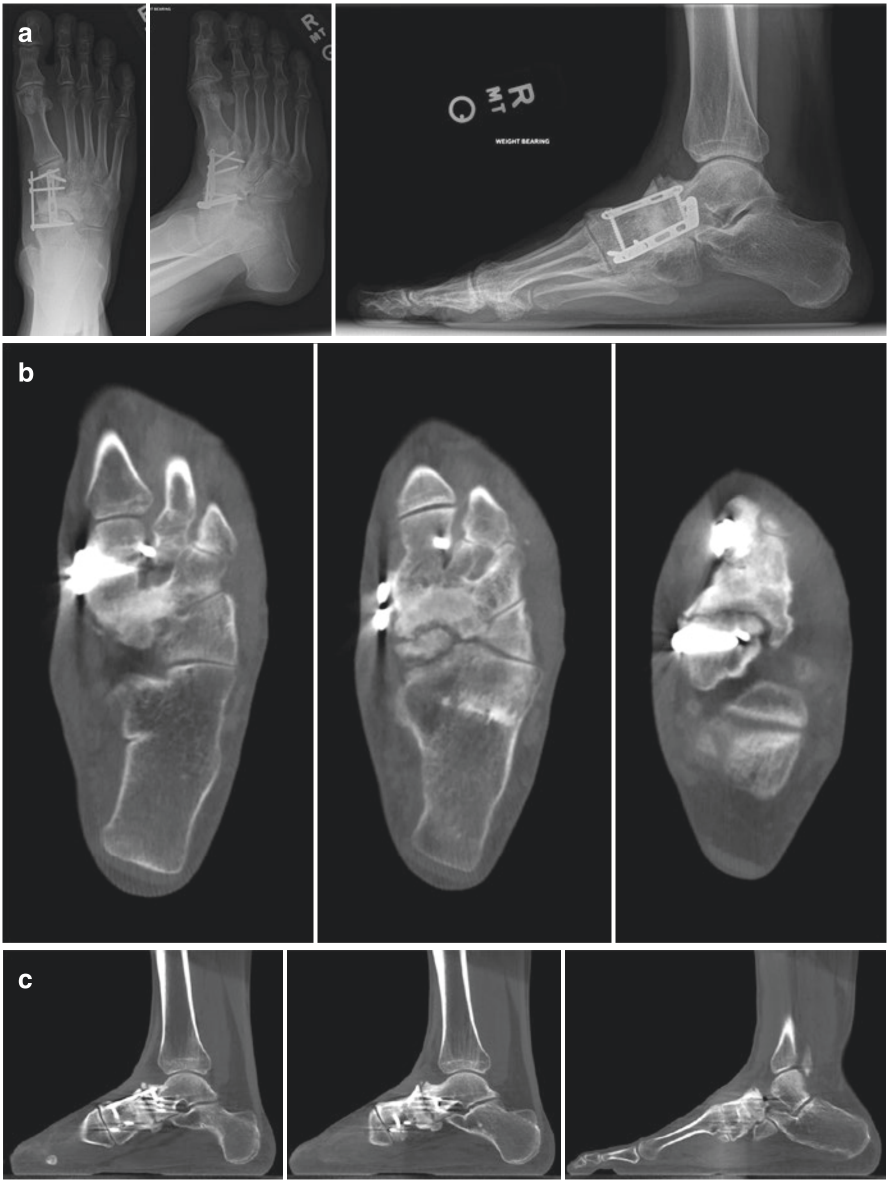
a
R
MT
WEIGHT BEARING
b
c

Fig. 22.13 (continued)

Fig. 22.13 (continued)

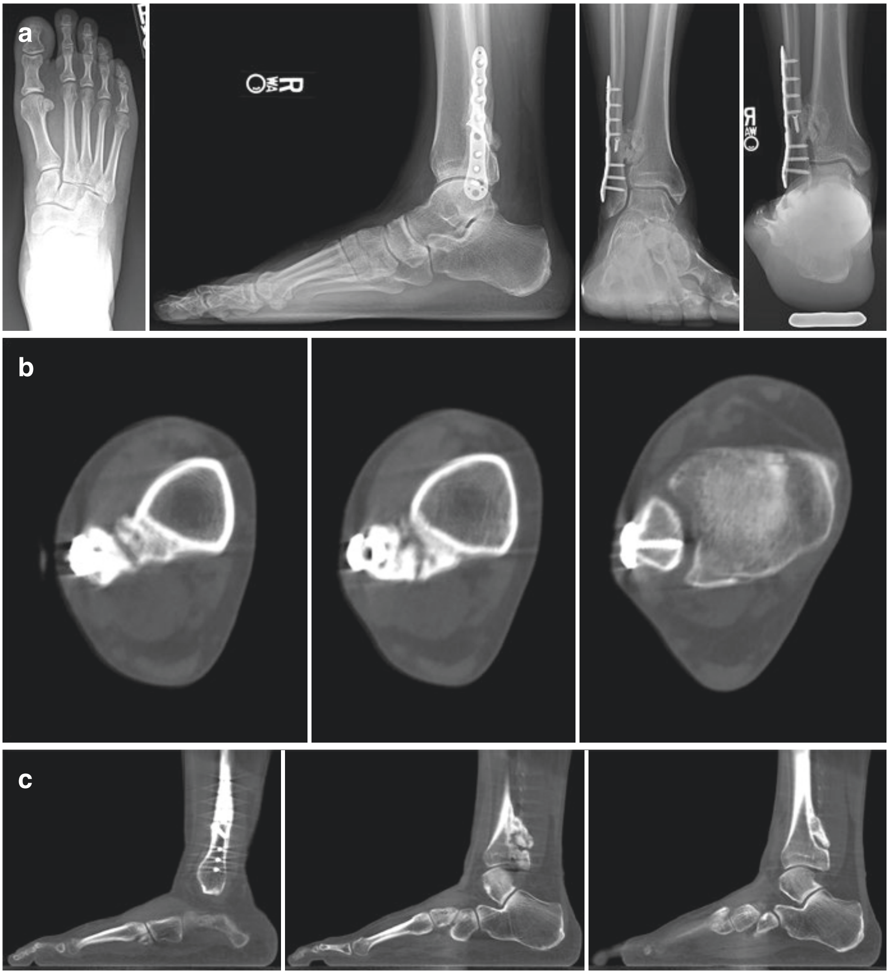

Fig. 22.14 Demonstrates usage of WBCT in a 35-year-old male with a missed syndesmosis injury. Three years ago, the patient underwent an open reduction and internal fixation of a distal fibula fracture in an outside facility. However, at the time of the surgery, the concomitant syndesmosis injury was not recognized. (**a**) Weight bearing radiographs (from left to right: anteroposterior and lateral views of the foot, mortise view of the ankle, and hindfoot alignment view) demonstrate complete union of the distal fibula fracture; however, they also demonstrate substantial degeneration of the distal tibiofibular joint a significant amount of heterotopic ossifications. (**b**) Axial, (**c**) sagittal, and (**d**) coronal WBCT demonstrate severe degeneration of the distal tibiofibular joint with subluxation of the fibula within the incisura. A deep debridement of the heterotopic ossification using a transfibular approach was performed. Additionally, a realigning arthrodesis of the distal tibiofibular joint with use of a proximal tibia bone graft (cancellous bone) was installed. (**e**) At the 4-month postoperative follow-up, weight bearing radiographs (from left to right: anteroposterior and lateral views of the foot, mortise view of the ankle, and hindfoot alignment view) were acquired and demonstrate progressive union of the distal tibiofibular arthrodesis and appropriate hardware positioning. However, conventional radiographs do not allow a reliable assessment of union degree or fibular alignment within the incisura. Due to this shortcoming, a postoperative (**f**) axial, (**g**) sagittal, and (**h**) coronal WBCT was acquired and demonstrates progressive, near complete union of the distal tibiofibular arthrodesis and anatomic alignment of the distal fibula in all three planes

Fig. 22.14 (continued)

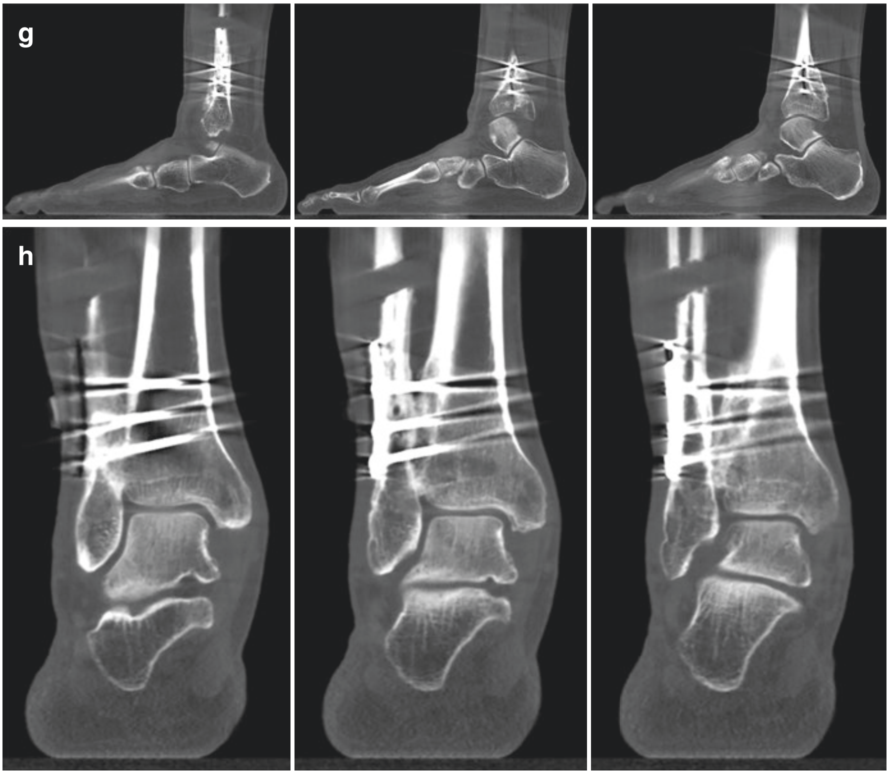

Fig. 22.14 (continued)

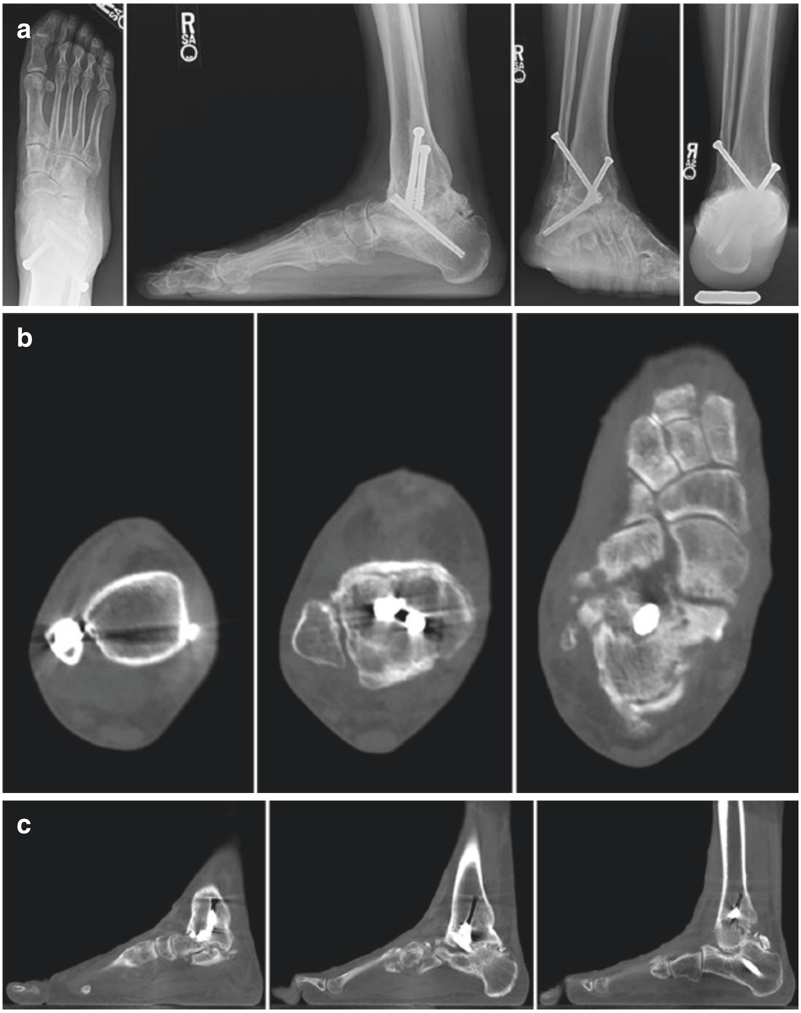

Fig. 22.15 Demonstrates the usage of WBCT with a 59-year-old male with painful hindfoot nonunion. Four years ago, the patient underwent hindfoot fusion in an outside facility. (**a**) Weight bearing radiographs (from left to right: anteroposterior and lateral views of the foot, mortise view of the ankle, and hindfoot alignment view) demonstrate status post hindfoot surgery with apparent nonunion of the subtalar and distal tibiofibular joints. (**b**) Axial, (**c**) sagittal, and (**d**) coronal WBCT confirms complete nonunion of the subtalar and distal tibiofibular joints, while the tibiotalar arthrodesis appears mature. A deep debridement of the subtalar and distal tibiofibular nonunion with deep biopsies was performed. Additionally, a realigning hindfoot revision arthrodesis with use of a proximal tibia bone graft (cancellous bone) was installed. (**e**) At the postoperative 6-month follow-up, weight bearing radiographs (from left to right: mortise and lateral views of the ankle) were acquired and demonstrate progressive union of the hindfoot arthrodesis and appropriate hardware positioning. However, conventional radiographs do not allow reliable assessment of union degree or alignment of the distal tibiofibular arthrodesis. Due to this shortcoming, a postoperative (**f**) axial, (**g**) sagittal, and (**h**) coronal WBCT was acquired and demonstrates progressive, near complete union of hindfoot arthrodesis and anatomic alignment of the distal fibula in all three planes

Fig. 22.15 (continued)

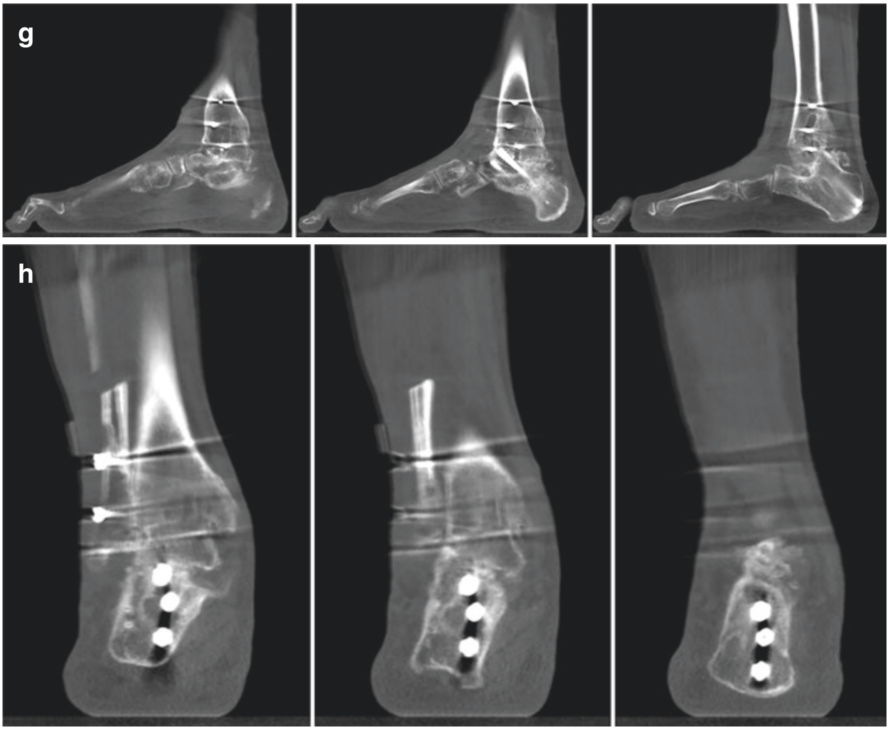

Fig. 22.15 (continued)

Fig. 22.16 Preoperative and postoperative assessment of hallux valgus using WBCT. (**a**) shows a preoperative sagittal reformation, (**b**) a preoperative coronal reformation, and (**c**) a preoperative WB AP radiograph of the foot. Preoperatively, the coronal reformation shows the rotation of the sesamoids and first metatarsal as the medial sesamoid is perched on the plantar ridge of the first metatarsal head. The visualization of the rotation on the first metatarsal seen on the scan helps to predict the surgical correction of the rotation; this could not be visualized on a standard radiograph. The scan also shows the contour of the first tarsometatarsal joint. The sagittal reformation shows mild elevation of the first ray as well as osteoarthritis in the first metatarsophalangeal joint and in the sesame-trochlear articulations. Understanding of the arthritis in the joint helps educate the patient in terms of potential for postoperative pain in the joint and range of motion. (**d**) shows a postoperative sagittal reformation, (**e**) a postoperative coronal reformation, and (**f**–**h**) postoperative WB radiographs. Postoperatively, the sagittal reformation shows bony bridging and union of the first tarsometatarsal fusion which is better visualized on WBCT. The coronal reformation shows the corrected alignment at the first metatarsophalangeal joint and corrected positioning of the medial and lateral sesamoids

Fig. 22.16 (continued)

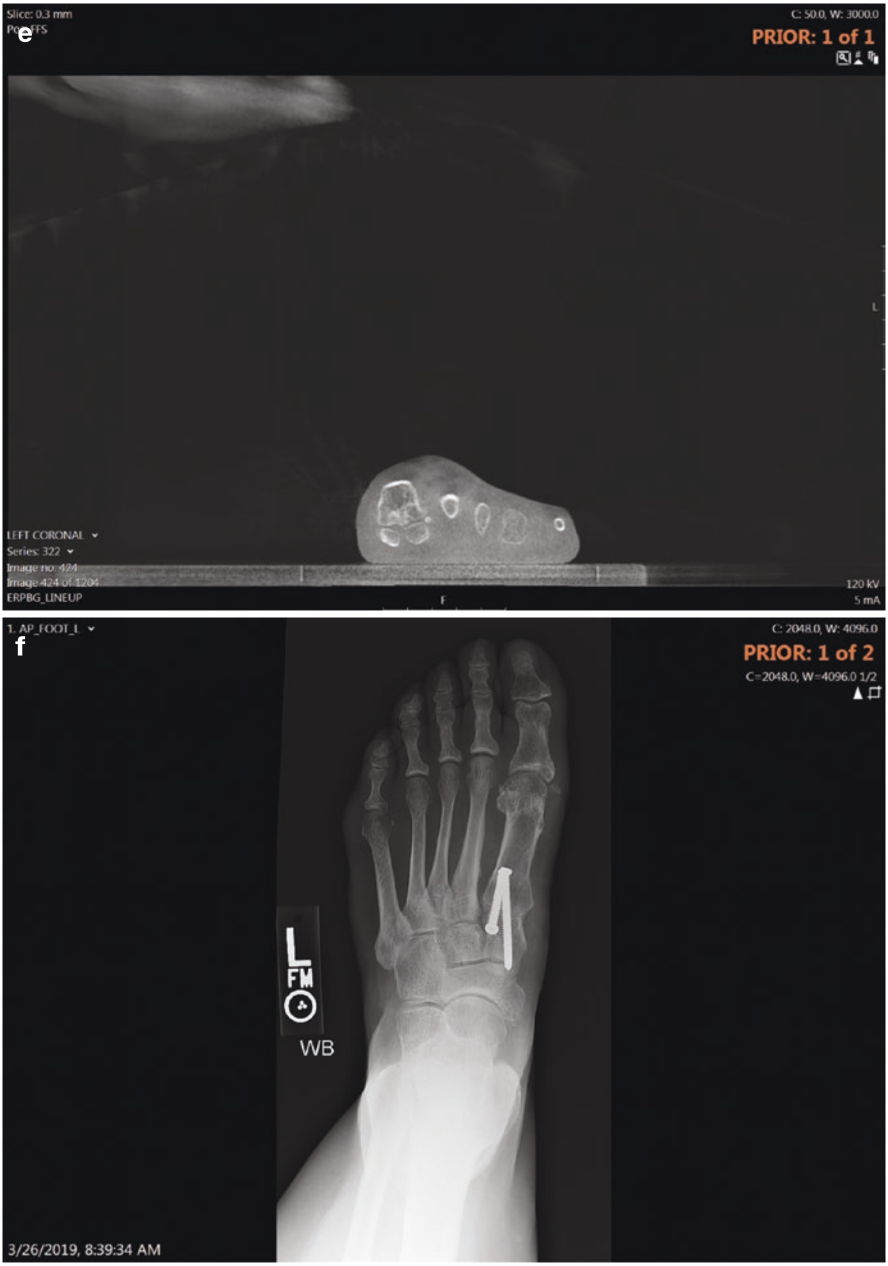

Fig. 22.16 (continued)

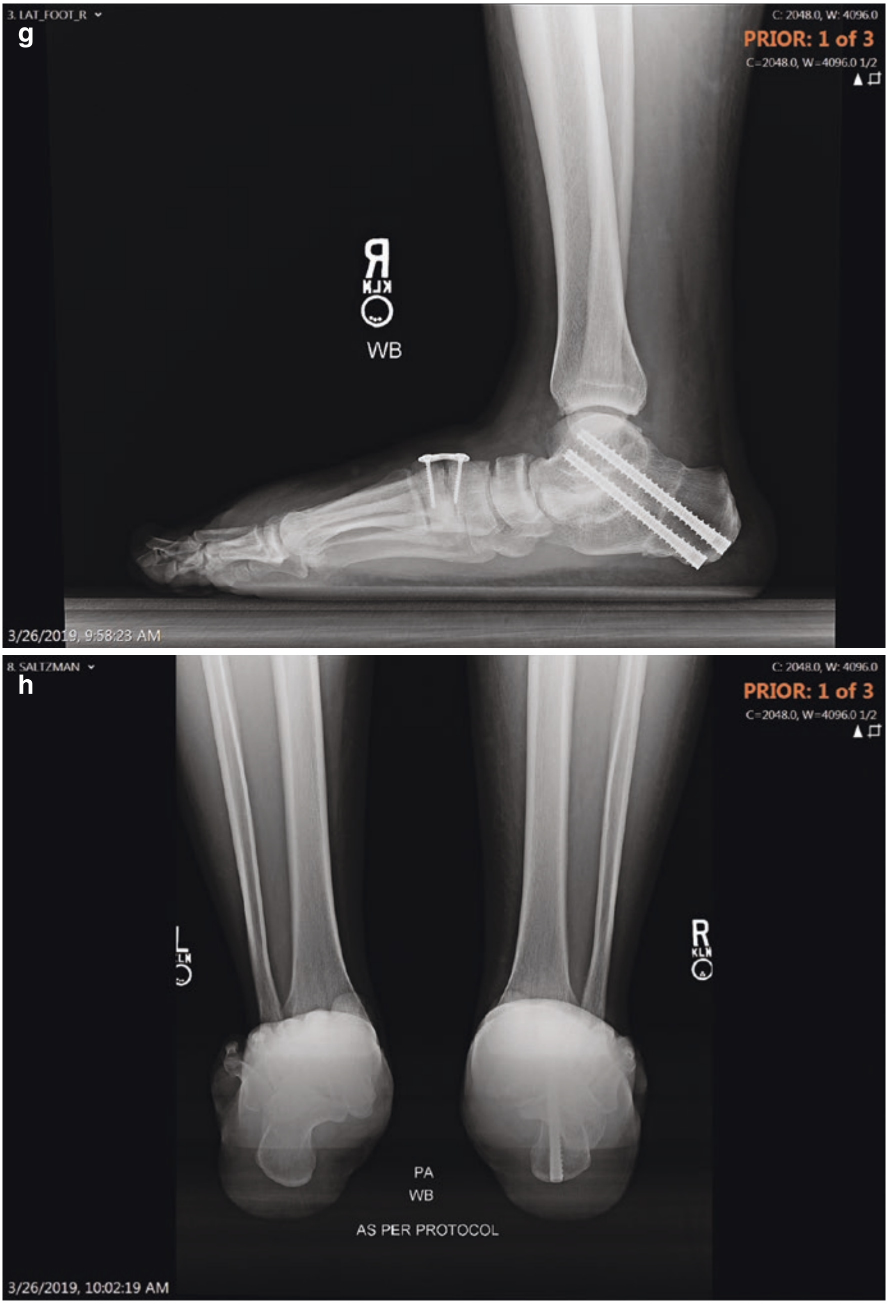

Fig. 22.16 (continued)

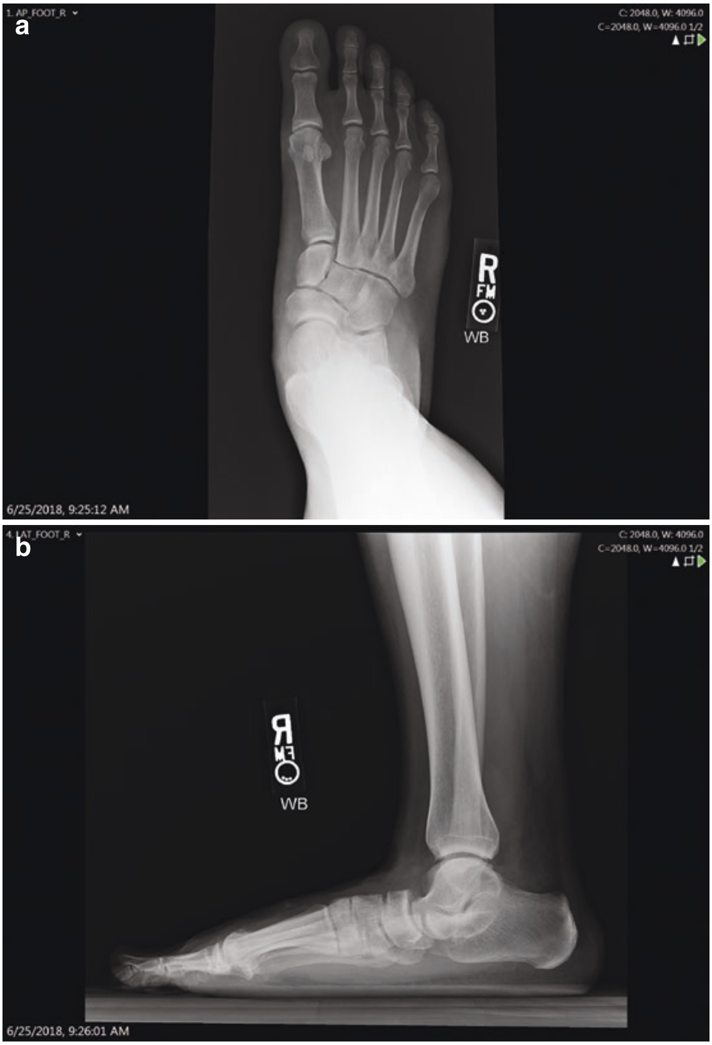

Fig. 22.17 Preoperative and postoperative assessment of acquired flatfoot deformity using WBCT. (**a**–**c**) show preoperative WB AP and, lateral and bilateral Saltzman radiographs, (**d**) shows a preoperative sagittal reformation, and (**e**) shows a preoperative coronal reformation. Preoperatively, the WB AP radiograph shows significant abduction of the talonavicular joint; the WB lateral radiograph shows impingement of the talus on the calcaneus and a large Meary's angle indicating severe deformity. The WB bilateral Saltzman radiograph demonstrates the heel alignment and shows a valgus heel on the right. The sagittal reformation shows severe impingement and cystic formation on both sides of the angle of Gissane, and the coronal reformation shows impingement and severe subluxation of the medial facet; this could not be visualized on standard radiograph. (**f**–**h**) Images show postoperative WB AP and lateral and bilateral Saltzman radiographs. Postoperatively, the WB AP radiograph shows good correction of abduction of the talonavicular joint. The WB lateral radiograph shows operative changes in the foot including a Cotton osteotomy, subtalar fusion, and calcaneal osteotomy. The WB lateral radiograph also shows good correction of the arch and shows improvement in talar coverage. The bilateral Saltzman radiograph demonstrates good correction of heel alignment on the right

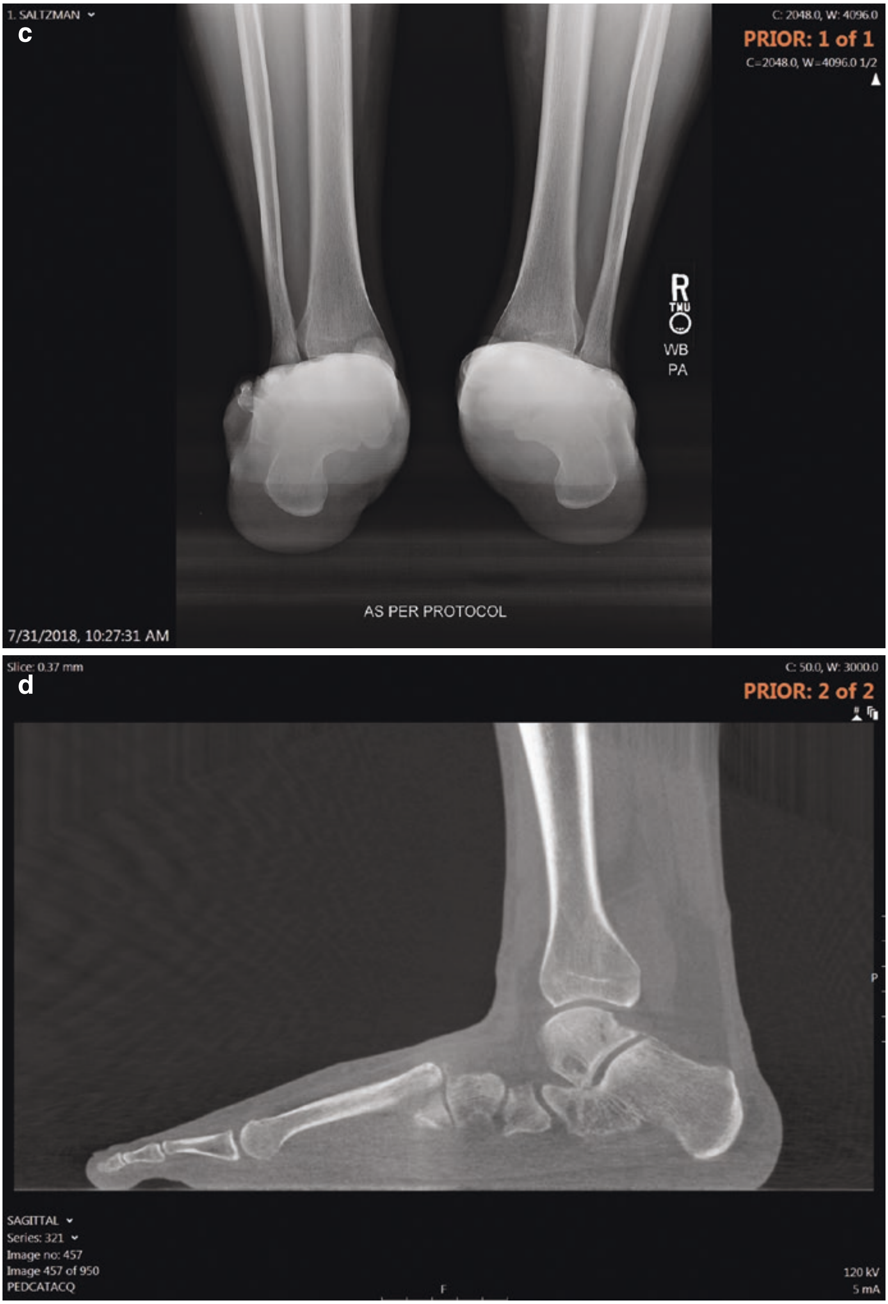

Fig. 22.17 (continued)

Fig. 22.17 (continued)

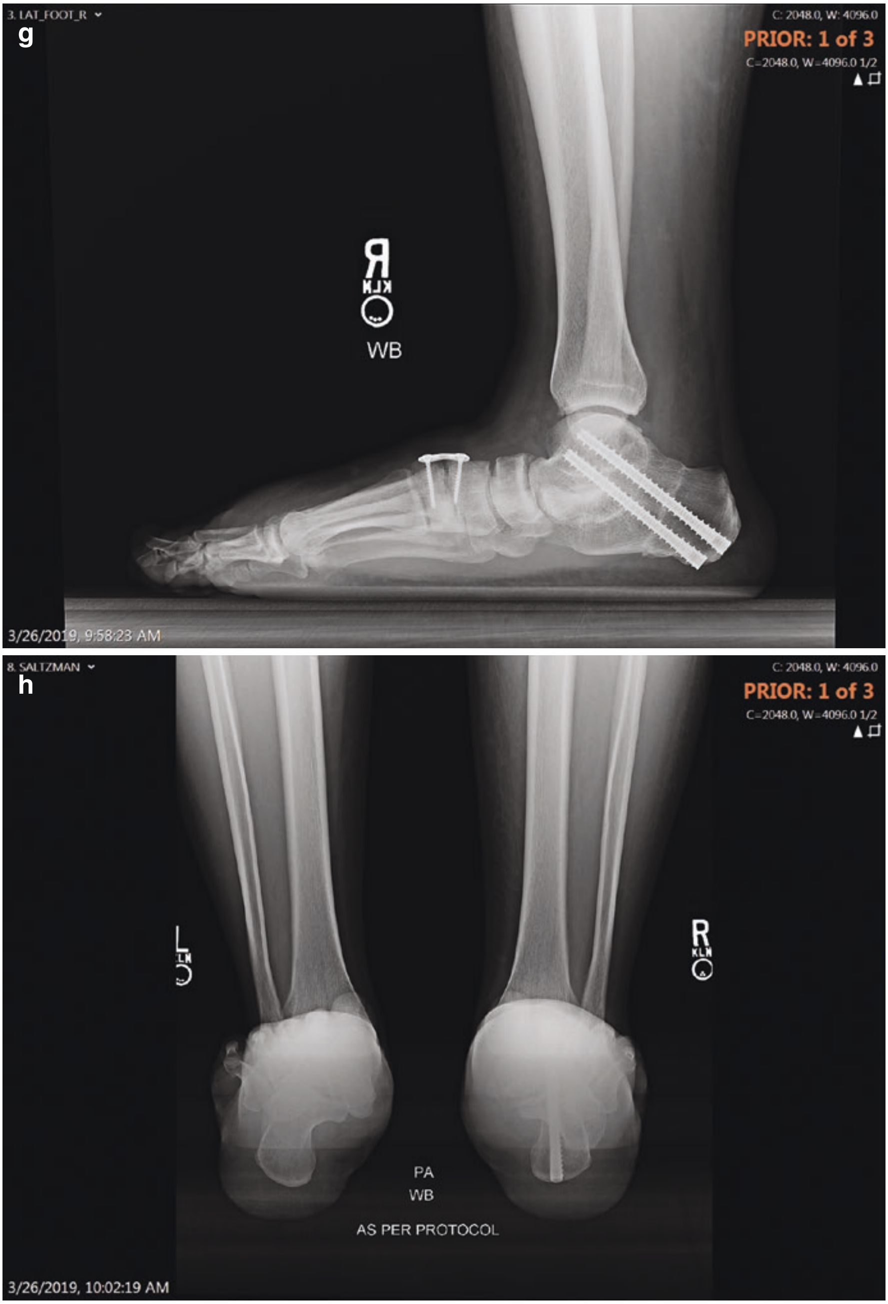

Fig. 22.17 (continued)

Fig. 22.18 Demonstrates the use of WBCT in a 54-year-old male patient with a history of partial injury of the left common peroneal nerve following a peripheral nerve block for a lateral ligament reconstruction of the left ankle. The patient developed mild cavus-varus deformity with symptoms along the lateral border of the foot and peroneal tendon's trajectory. (**a**–**d**) Clinical pictures demonstrate asymmetric left subtle cavus-varus deformity, with mild elevation of the longitudinal arch, neutral alignment of the hindfoot, and a positive peekaboo sign. The hindfoot varus was correctable during Coleman's block test, and the patient had a weakness for eversion (4/5). (**e**, **f**) WBCT three-dimensional (3D) reconstruction images show similar neutral hindfoot alignment, with mild elevation of the longitudinal arch. (**g**) Digitally reconstructed radiographs (DDRs), anteroposterior, lateral, and hindfoot alignment views demonstrate similar alignment findings, with presence of two metallic anchors in the distal fibular (from prior ankle lateral ligament reconstruction procedure) as well as an incidental finding of a dysplastic middle and anterior facet of the subtalar joint, consistent with incomplete tarsal coalition. (**h**) Multiplanar reformation (MPR) WBCT images of the harvesting of 3D coordinates of the weightbearing points of foot tripod and center of the ankle joint, from left to right: most distal voxel of the first metatarsal head, fifth metatarsal head, calcaneal tuberosity, and most central and proximal voxel of the talar dome. The harvested 3D coordinates are used by dedicated software (TALAS™, CubeVue™, CurveBeam©, LLC, Warrington, PA, USA) to calculate the foot ankle offset (FAO) automatically. The measurement is given as a percentage that gauges the shortest distance between the center of the ankle joint and a bisecting line of the foot tripod, normalized by the length of the foot. (**i**) Image of the harvested 3D data (X, Y, and Z planes) for this specific patient for the first (Met1/M1) and fifth metatarsals (Met5/M5), calcaneus (C) and talus (T). F-point represents a point in the bisecting line of the foot tripod, where the center of the ankle would be positioned in an ideal situation, centered in the foot tripod. T-point shows where the center of the ankle currently is, significantly laterally positioned in relation to the foot tripod, demonstrating important biomechanical malalignment in "varus." The measured FAO was −9.63. CO (calcaneal offset) is an estimate in millimeters how much one would have to displace the calcaneal tuberosity laterally to correct the deformity, in this case, a theoretical displacement of 17.6 mm. HA (hindfoot alignment) is an estimate of the hindfoot alignment angle projected in the floor plane, in this case, consistent with approximately a 33° of hindfoot varus malalignment. (**j**) Postoperative non-weightbearing conventional radiographs demonstrating adequate healing of a first metatarsal dorsiflexion osteotomy as well as Malerba calcaneal osteotomy. The WBCT findings with significantly more pronounced biomechanical malalignment in varus, represented by the severely altered FAO, when compared to the relatively mild findings of the clinical and radiographic evaluation of the patient has influenced the surgical treatment. The Malerba calcaneal osteotomy was also performed, to improve the surgical correction of the malalignment, even though Coleman's block test demonstrated that clinically the deformity could potentially be corrected with an isolated dorsiflexion osteotomy of the first ray

Fig. 22.18 (continued)

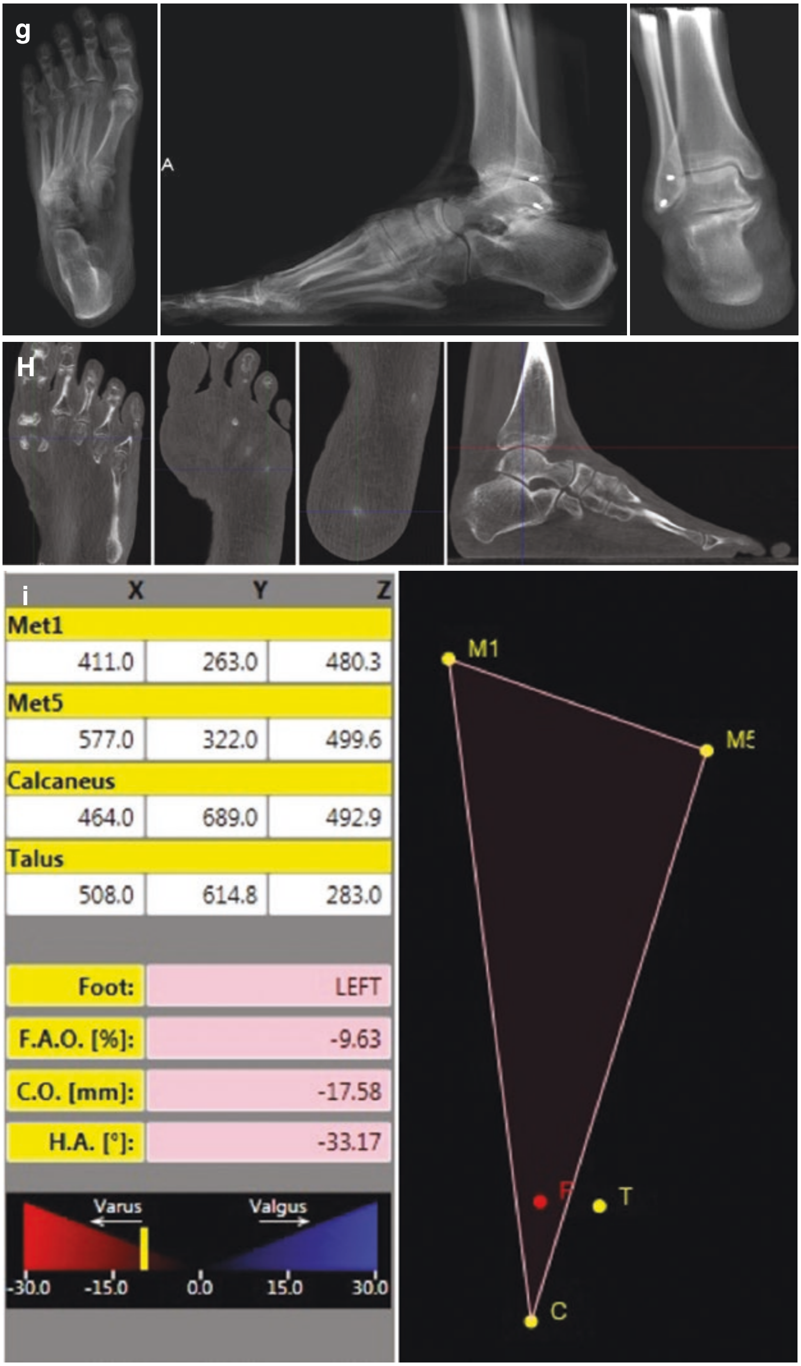

Fig. 22.18 (continued)

Fig. 22.18 (continued)

Fig. 22.19 Demonstrates the use of WBCT in a female 58-years-old patient with symptomatic adult-acquired flatfoot deformity. The patient had noticed progressive foot collapse for the last 2–3 years. She has been walking more on the medial border of the foot. The pain is mostly located laterally at the level of the subtalar joint and sinus tarsi, but the patient has relatively preserved range of motion of the triple joint complex. (**a**) Conventional weightbearing radiographs (from left to right: anteroposterior and lateral views of the foot) demonstrate significant abduction of the forefoot/midfoot, with uncoverage of the talar head, break in the talus-first metatarsal angle, and no apparent arthritic findings of the subtalar joint or pronounced sinus tarsi impingement. (**b**) Axial WBCT images confirm abduction of the forefoot/midfoot, with uncoverage of the talar head and a first tarsometatarsal joint with no arthritic findings. (**c**) From left to right, coronal WBCT images demonstrate increased valgus angulation of the posterior facet of the subtalar joint, evident signs of subluxation and asymmetry of the subtalar joint at its posterior facet as well as impingement of the lateral aspect of the calcaneus with the distal aspect of the fibula (subfibular impingement – yellow arrow, central image), and completely non-arthritic articular surface of the posterior facet. Likewise, there are evident findings of sinus tarsi impingement (yellow arrow, the image on the right), with sclerotic bone and opposing mirrored cystic formation in the lateral aspects of the talus and calcaneus, as well as more than 50% subluxation of the middle facet of the subtalar joint (parallel yellow lines). (**d**) Coronal WBCT image of the midfoot/forefoot shows the significant collapse of the longitudinal arch with a negative forefoot arch angle. (**e**) Sagittal WBCT images demonstrating the collapse of the longitudinal arch (with a break in the talus-first metatarsal angle), no arthritic findings or plantar gapping of the first tarsometatarsal joint, and signs of sinus tarsi impingement (yellow arrow). (**f**) MRI images in the axial, coronal, and sagittal planes, showing degeneration of the posterior tibial tendon (yellow arrow, picture on the left), high-grade tear/degeneration of the superomedial component of the spring ligament and talocalcaneal interosseous ligaments (yellow arrows, central image) and bone edema of the lateral process of the talus (yellow arrow, image on the right), consistent with sinus tarsi impingement. (**g**) Postoperative weightbearing conventional radiographs (from left to right: anteroposterior and lateral views of the foot) demonstrating adequate healing of medial displacement calcaneal osteotomy, subtalar joint fusion, Cotton osteotomy, flexor digitorum longus (FDL) tendon transfer to the navicular tuberosity, as well as reconstruction of the deltoid-spring ligament with Achilles tendon allograft. The decision on proceeding with the fusion even with no arthritic findings of the posterior facet of the subtalar joint was made based on the presence of significant hindfoot deformity, confirmed by the amount of subtalar joint subluxation (evaluated at both the posterior and middle facets), pronounced sinus tarsi impingement, but most importantly, by the presence of subfibular impingement

Fig. 22.19 (continued)

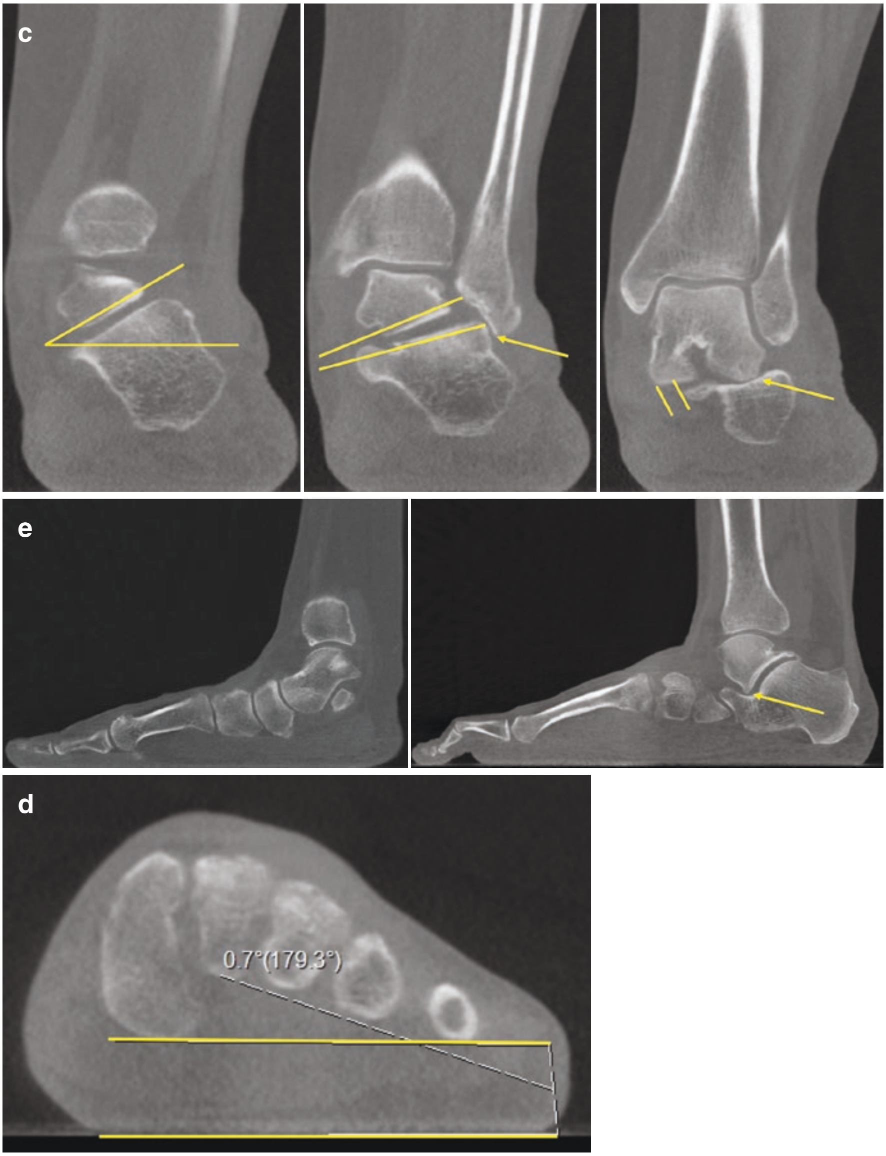

Fig. 22.19 (continued)

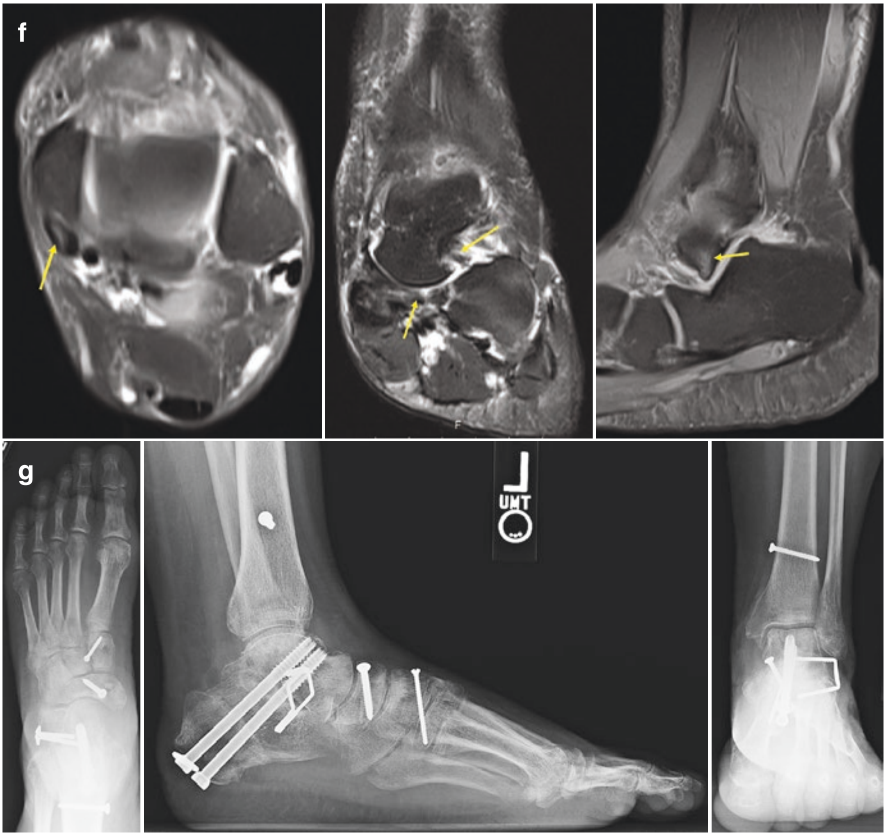

Fig. 22.19 (continued)

Chapter 23
Future Developments in Weight Bearing Computed Tomography

Martinus Richter

What is the future of WBCT in the foot and ankle? What are the needs and what is feasible? Regarding the WBCT scan, faster scanning times, lower radiation dose, larger scan volume, and better image quality will be the next reachable developments. More challenging will be dynamic scans, i.e., scanning the foot and ankle during the entire gait stance phase. Even though the actual standard imaging is also static, dynamic imaging would be desirable, for example, dynamic pedography or gait motion analysis [1]. Much faster scanning times like 20 scans per second and a very large scanning volume will be needed to allow for dynamic scan of the foot and ankle during the entire stance phase. An inclusion of dynamic pressure and force measurement will be an easy adjunct, as these methods do already exist (section "Angle Measurement: Differences Between Methods" and "Angle Measurement: Intra- and Interobserver Reliability") [2–4]. However, dynamic scanning and addition of other data (e.g., pedographic data) acquisition modalities will register excessively more data than to date. This calls into question how these data are stored, visualized, analyzed, and interpreted. The use of conventional two-dimensional monitors will not allow for adequate visualization of three-dimensional and maybe even dynamic instances. Holographic visualization could be helpful but could not be adequately developed so far (Fig. 23.1) [5]. This will require heavy investments from the industry. It requires even faster data transfer speeds and projection technology, including advanced interfacing, enabling surgeons to interact manually with the models, which to date is only in the development phase and far from being available in the daily clinical setting. However, surgeons have been inventive and are for now using existing technology such as third-party software, holographic lenses, or 3D printing solutions for better visualization. In any case, WBCT developers are making tremendous ongoing progress with their onboard software solutions to make datasets readily available and easy to navigate right on the spot of patient scanning. The next issue is data analysis. Automatic measurements are already possible (section "Shortcomings of the Study") and will be included in all software solutions in the near future. Further data analysis, for example, diagnosis of foot deformities, will require artificial intelligence (AI) for automatic analysis of

M. Richter et al., *Weight Bearing Cone Beam Computed Tomography (WBCT) in the Foot and Ankle*, https://doi.org/10.1007/978-3-030-31949-6_23

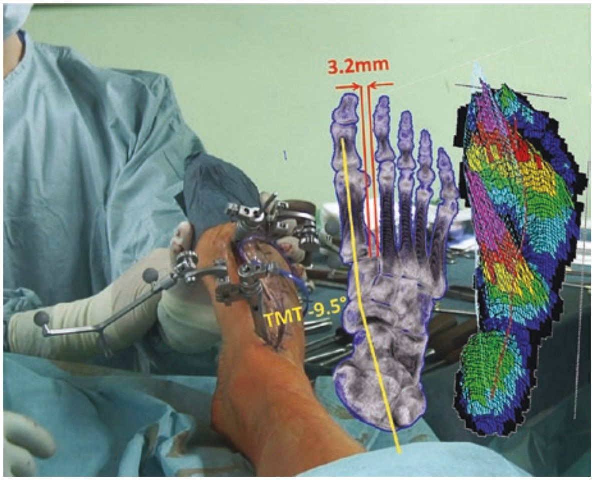

Fig. 23.1 Early example of a holographic intraoperative visualization of a foot skeleton and pedographic pattern including visualization of measures (angle and distance) as guide for the surgeon during a navigated foot correction. (From Ref. [5])

extensive data volumes. Enormous databases will be needed to build up a sufficient AI. New three-dimensional measurement modalities in addition to angles and distances between bones need to be defined; standard values will have to be assigned and guidelines adapted or created. At least a whole generation of foot and ankle surgeons will have to find all the solutions, and we are just at the start of this exciting process. A new era of foot and ankle imaging has started, and we are facing an exciting and promising future.

References

1. Cavanagh PR, Henley JD. The computer era in gait analysis. Clin Podiatr Med Surg. 1993;10(3):471–84.
2. Richter M, Lintz F, Zech S, Meissner SA. Combination of PedCAT weightbearing CT with pedography assessment of the relationship between anatomy-based foot center and force/pressure-based center of gravity. Foot Ankle Int. 2018;39(3):361–8.
3. Richter M, Zech S, Hahn S, Naef I, Merschin D. Combination of pedCAT for 3D imaging in standing position with pedography shows no statistical correlation of bone position with force/pressure distribution. J Foot Ankle Surg. 2016;55(2):240–6.
4. Schmiegel A, Vieth V, Gaubitz M, Rosenbaum D. Pedography and radiographic imaging for the detection of foot deformities in rheumatoid arthritis. Clin Biomech (Bristol, Avon). 2008;23(5):648–52.
5. Richter M. Computergestützte Fußchirurgie. Berlin/Heidelberg: Springer; 2012.

Correction to: Weight Bearing Cone Beam Computed Tomography (WBCT) in the Foot and Ankle

Correction to:
M. Richter et al., ***Weight Bearing Cone Beam Computed Tomography (WBCT) in the Foot and Ankle*****,**
https://doi.org/10.1007/978-3-030-31949-6

This book was inadvertently published with the wrong chapter author details in pdf and ePub version.

In the original version of all the chapter PDFs, the name of the author was missed to be mentioned and it has been corrected now by placing the author name in the chapter opening page.

In the original ePub version, several author names were provided instead of single chapter author name which is now corrected.

The updated online version of this book can be found at
https://doi.org/10.1007/978-3-030-31949-6

M. Richter et al., *Weight Bearing Cone Beam Computed Tomography (WBCT) in the Foot and Ankle*, https://doi.org/10.1007/978-3-030-31949-6_24

Index

A
Achilles tendon/calcaneal tuberosity angle (ATCTA), 201
Acute isolated syndesmotic injury, 138
Adult acquired flatfoot deformity (AAFD), 121, 181, 199, 213
  interobserver reliability, 218
  intraobserver reliability, 217
  material and methods, 214–218
    study design, 214
    subjects, 214
    WBCT imaging technique, 214–215
  measurements, 215
    axial plane measurements, 215
    coronal plane measurements, 215–217
    measurement differences, 218–223
    sagittal plane measurements, 217
American Orthopaedic Foot and Ankle Society(AOFAS), 7
Anatomical tibia axis (TA2D), 110
Anatomy based FC and force/pressure based COG
  biomechanical parameter, 62
  COG, 62
  customized pedography sensor, 56
  FC vs. COG, 57–59
  foot and ankle pathologies, 61
  gravitational line, 63
  image acquisition, 57
  inclusion and exclusion Criteria, 56–57
  pedography, 56, 57
  position differences, 61
  radiation dose, 65
  shortcomings, 64–65
  TALAS, 60
  triangular based pyramid model, 62
Ankle and hindfoot measurements, 111
Assessment of acquired flatfoot deformity, 292
Assessment of hallux valgus, 288
Axial and parasagittal reformations, 271
Axial CT images of cadavers, 147
Axial plane measurements, 184
Axial WBCT images, 276, 300

B
Bone position measurement, 27
  angle measurements
    calcaneal pitch angle, 31
    differences between methods, 32
    hindfoot angle, 31
    intermetatarsal angle, 30
    intra- and interobserver reliability, 32
  approval for use, 37
  calcaneal pitch angle, 35
  cost, 37
  1st– 2nd intermetatarsal angle, 34
  hindfoot angle, 35
  image acquisition, 29
  inclusion and exclusion criteria, 29
  radiation dose, 36
  results, 31–32
  standard imaging, 38–39
  time spent, 29
  TMT dorsoplantar, 34
  TMT lateral, 34

C
Calcaneal-fibular distance, 216
Calcaneal inclination angle, 22
Calcaneal pitch angle, 16

M. Richter et al., *Weight Bearing Cone Beam Computed Tomography (WBCT) in the Foot and Ankle*, https://doi.org/10.1007/978-3-030-31949-6

Calcaneofibular distance, 22
Calcaneus osteotomy, 275
Cartesian coordinate system and linear regression analysis, 129
Center of gravity (COG), 55
Central talus point (CTP), 110
Charcot arthropathy, 270, 271
Chronic lateral ankle instability and hindfoot varus
 ankle instability, 95
 central calcaneal varus angle, 94
 design, 88
 investigations and measurements, 89–90
  calcaneal offset, 90
  CubeView™, 89
  PedCAT™, 89
 limitations, 94
 log-linearity, 90
 risk factor, 95
 statistical analysis, 90
 study population, 88
Chronic subluxation, 272
Clinical application of weight bearing CT, 265, 276
Clinical hindfoot alignment angle (CHAA), 201
Coleman's block test, 296
Computed analysis of midfoot alignment, 126
Computed tomography (CT), 87, 181
Computer assisted surgery (CAS), 107
Computing medial translation, 125
Cone-beam computed tomography (CBCT), 6, 200, 241
 acquisition time, 242
 biases of conventional radiography, 246–247
 field of view, 242
 foot and ankle assessment, 243
 hounsfield unit, 242
 radon and fourier transforms, 243
 sinogram, 241
 3D environment, 244–245
  digitally reconstructed radiographs, 245–246
  multi Planar reconstruction, 245
  hounsfield's attenuation coefficient, 244
 3D models, 243
Cone beam technology, 5
Cone beam WBCT, 274
Confidence interval, 223
CONSORT diagram, 183
Conventional radiographs, 4, 152, 300
Coronal and axial planes, 221
Coronal plane measurements, 185
Coronal WBCT images, 276, 278, 300
Correlation analysis, 115
Correlation of bone position, 41
 angle measurement, 50
 bone position measurement, 44–45
 correlation analysis, 47–48
 correlation of WBCT, 47–51
 foot orientation, 41
 image acquisition, 44
 inclusion and exclusion criteria, 43–44
 intra- and interobserver reliability, 48
 pedography, 41, 44, 46
  parameters, 46–48
  sensor, 42
 radiation dose, 52
 shortcomings, 51–52
 WBCT and pedography parameters, 49
 WBCT parameters, 50
Cuboid-floor distance, 22, 216
Cuneiform–first metatarsal angle, 216
Cuneiform-floor distance, 22, 216
Curvebeam, 98

D
Deltoid ligament, tibialis posterior and fascia plantaris, 275
Digitally reconstructed radiographs (DRR), 170, 177
Distal tibio-fibular syndesmosis, 137, 167
 using CT, 137
 using plain radiographs, 136
Dorsoplantar radiograph, 80
DRR and IM1-2 angle measurement, 246

E
Effective radiation dose, 10
Enlarged medial groove, 272
European Foot and Ankle Society (EFAS), 7
Experimental setting, 139, 153, 169

F
Field of view, 242
Flat foot deformity, 275
Flexible adult acquired flatfoot deformity
 CBCT imaging technique, 182–183
 CT-based measurements, 189
 hindfoot valgus alignment, 191
 interobserver reliability, 188–189
 intraobserver reliability, 188
 low interobserver reliability, 193

materials and methods, 182–187
measurements, 183–184
axial plane measurements, 184
coronal plane measurements, 184–186
sagittal plane measurements, 186–187
source of funding, 187
statistical analysis, 187
asymptomatic control subjects, 193
intraobserver reliability, 187
spearman's correlation test, 187
subtalar horizontal angle, 193
study design, 182
WB radiograph measurements, 191
weightbearing and nonweightbearing CT, 190
Foot and ankle disorders, 11–13
Foot and ankle offset (FAO), 68, 82, 87
Foot center (FC), 55
Forefoot arch angle, 22, 216
Future developments
artificial intelligence, 305
dynamic scanning, 305
holographic visualization, 305

G

Graphical plots, 204

H

Hallux valgus correction, 267
Health insurance portability and accountability act (HIPAA), 78
Heterotopic ossifications, 282
Hind- and midfoot alignment
hindfoot alignment
pre- and postoperative comparison, 128
regression analysis, 128
intra- and interclass correlation coefficients, 130
midfoot alignment, 128–130
pre- and postoperative comparison, 128–130
regression Analysis, 130
pre- and post-operative hindfoot measurements, 128
pre- and post-operative midfoot measurement, 129
study population, design, 122–127
anatomical tibia axis, 123
cartesian coordinate system, 123
cloudcompare, 125
concomitant infra malleolar procedures, 122
rotation of the tibia, 123
supramalleolar procedures, 122
talocalcaneal axis, 123
surgical procedure, 127
broad osteotome, 127
pearson coefficient, 127
step plate, 127
Hindfoot alignment (HFA), 67, 77, 87, 124
AAFD (*see* Hindfoot alignment of AAFD)
measurements, 18
in 3D, 110
in 2D, 109
WBCT (*see* Hindfoot alignment, WBCT)
Hindfoot alignment, AAFD, 199
CBCT imaging technique, 201
cross sectional imaging modalities, 200
dynamic deformity, 200
hindfoot alignment evaluation, 208
hindfoot valgus measures, 204
intra- and interobserver reliability, 203
mean clinical hindfoot alignment angle, 204–206
radiographic assessment, 199
statistical analysis, 203
hindfoot alignment angulations, 208
hindfoot moment arm, 203
intraobserver and interobserver reliability, 203
study design, 200
T-test comparison, 205
WB CBCT measurements, 202
WB CBCT scans, 208
Hindfoot alignment, WBCT, 97
anatomical axis, 97
anatomical tibia axis (TA_x), 100
hindfoot alignment, 101–103
hindfoot characteristics, 103
hindfoot pathology, 97
independent student t-testing, 103
intra class correlation coefficients, 102
intrinsic varus configuration, 104
measurement method (HA_{IC}), 99, 102
morphological characterization, 104
patient characteristics, 98–101
podography study of cavanagh, 104
ROI density analysis, 103
spearman's coefficient, 101
study population and design, 98
talocalcaneal axis, 97
3D overview, 102
wilcoxon signed rank test, 101
Hindfoot alignment angle (HAA), 201, 206
Hindfoot angle measurement, 30
Hindfoot moment arm (HMA), 201, 206, 207

Hindfoot varus malalignment, 296
Holographic intraoperative visualization, 306

I
Imaging and measurements, 169–171
Impact on WBCT
  Control Group, 230
  cost-effectiveness, 230–231
  data acquisition, 230
  data analysis/control group, 231
  epidemiology, 232
  imaging time, 230
  R and CT sequences, 232
  radiation dose, 230
  RCT and WBCT groups, 232
  shortcomings, 234
  Study Design, 229
Inclination angle, 216
Interobserver agreement, 221
Interobserver reliability, 220
Interosseous talo-calcaneal ligament (ITCL), 151
Intraclass correlation coefficients (ICCs), 140, 156, 218

L
Lateral ligament reconstruction, 296
Lateral radiographs, 4
Lateral tarsometatarsal angle, 16
Linear regression analysis, 83
LineUp®, 252
Long axial method (HA_{LA}), 99

M
Magnetic resonance imaging (MRI), 9, 135
Malerba calcaneal osteotomy, 296
Mean values for subtalar horizontal angle measurements, 195
Measurements performed on CT, 155
Measurements using CT, 141, 161
Measurements using DRRs, 160
Measurements using single weight bearing CT, 162
Measurements, weight bearing CT, 255
  adult acquired flatfoot measurements, 255–256
    calcaneofibular distance, 256
    cuboid-to-floor distance, 256
    cuboid-to-skin distance, 255, 256
    cuneiform angle, 256
    cuneiform–first metatarsal angle, 256
    cuneiform-to-floor distance, 256
    forefoot arch angle, 255
    inclination angle, 256
    navicular-to-skin distance, 255
    talonavicular coverage angle, 255
    talus-first metatarsal angle, 255
  distal tibiofibular syndesmotic measurements, 258–259
    anterior tibiofibular distance, 258
    davidovitch translation, 259
    DELTAFIB, 259
    lateral clear space, 259
    medial clear space, 259
    phisitkul translation, 259
    posterior tibiofibular distance, 258
    syndesmotic diastasis, 258
    tang rotation, 259
    tibiofibular clear space, 258
    zwipp rotation, 259
  hallux valgus measurements, 259–260
    first metatarsal rotation alpha-angle, 260
    hallux valgus angle, 259
    intermetatarsal angle, 259
    interphalangeal angle, 259
    metatarsal head positioning, 259
    sesamoid rotation angle, 260
    stanmore classification system, 260
  hindfoot alignment measurements, 256–257
    foot and ankle offset, 256
    hindfoot alignment angle, 256, 257
    hindfoot moment arm, 257
    joint angle, 257
    tendon/calcaneal tuberosity angle, 257
    tuberosity angle, 257
    WBCT clinical hindfoot alignment angle, 256
  subtalar joint alignment measurements, 257–258
    incongruence angle, 258
    inferior talus-horizontal angle, 257
    inferior talus–superior calcaneal angle, 258
    inferior talus–superior talus angle, 257
    subtalar joint subluxation, 258
    subtalar vertical angle, 257
Medial clear space (MCS), 167, 173
Medializing calcaneal osteotomy (MCO), 121
MFB in the hindfoot, 271
MFB in the lateral column, 271
MFT in the medial column, 271
MPR and 3D rendering windows., 245

Multidetector computed tomography (MDCT), 181
Multiplanar reformation, 296

N
Navicular-cuneiform angle, 22
Navicular-floor distance, 22, 216
Navicular–medial cuneiform angle, 216
Navicular-skin distance, 22
Non-mobile bearing TAR-models, 266
Non-weight bearing (NWB), 182
  in axial plane, 190
  in coronal plane, 192
  radiographs, 276, 278
  in sagittal plane, 194

O
ONEWAY ANOWA radiographs, 32
Onsight 3D Extremity System, 250, 252

P
Painful hindfoot nonunion, 285
Paracoronal reformation, 270
Pathology location, 231
PedCAT, 15, 79, 109, 250
Plan-correction-arthrodesis, 271
Post Hoc Test WBCT vs. radiographs and CT, 32
Postoperative weight bearing radiographs, 278

R
Radiographic assessment
  forefoot, 17
  midfoot and hindfoot, 19–21
Region of interest (ROI), 101
Reliability and correlation analysis, 107
  ankle and hindfoot characteristics, 114–116
    centroidal axis, 116
    intraclass correlation coefficients, 116
    limitation of, 117
    medial distal tibia angle, 117
    multiplanar deformity, 117
    post-operative assessment, 117
    3D structural configuration, 117
  bony hindfoot structures, 116
  complex fracture patterns, 107
  hindfoot alignment, 114
  hindfoot measurements, 114
  Kolmogorov-Smirnov normality test, 113
  linear regression analysis, 113
  patient characteristics, 108
  study population, design, 108–113
    cartesian coordinate system, 112
    hindfoot angle, 109
    hindfoot measurements, 109
    intermalleolar axis, 111
    middle subtalar vertical angle, 111
    subtalar joint, 111
    tibiotalar joint, 111
    varus and valgus alignment, 110
    3D hindfoot angle (HA3D), 110

S
Single-photon emission computed tomography-CT (SPECT-CT), 9
Sagittal plane measurements, 186
Sagittal WBCT Images, 278, 300
Scientific overview
  foot and ankle imaging
    cone-beam CT technology, 10
    imaging modality, 9
    partial weight bearing, 10
    skeletal pathology, 9
  normal controls study
    ankle rotation, 13
    coronal planes, 10
    imaging acquisition, 13
    rotation of the talus, 13
    subtalar vertical angle, 10
  pathologic conditions
    asymptomatic controls, 14
    fibulocalcaneal distance, 15
    4-stage grading system, 15
    1st metatarsal alignment, 14
    forefoot and hindfoot alignment, 15
    hallux valgus deformity, 14
    hindfoot alignment angle, 14
    naviculocalcaneal distance, 15
    talar anatomy, 18
    3D biometric tool, 18
  radiographic measurements, 19–21
  standardization of measurements, 21
Single computed tomography (CT) images, 170
Sinogram, 241
Software screen view
  with FC, 58
  showing COG, 59
  with 3D-reformation, 43
Standard Triangulation Language (STL), 123

Statistical analysis, 171
Sub-fibular impingement, 273
Subtalar horizontal angle, 22, 185, 216
Subtalar joint instability, 151
  computed tomography scans, 158–161
  data source and specimens, 152–153
  experimental setting
    dynamometric wire tensioner, 153
    ilizarov apparatus, 155
    radiolucent polyoxymethylene, 153
  imaging and measurements, 155–156
    broden view, 155
    digitally reconstructed radiographs, 157–158
    ITCL transection, 158
    torque application, 158
  ligamentous stabilizers, 163
  linear mixed effect models, 156
  long-lasting instability, 151
  radiographs measurements, 157
  TT measurements, 163
  with and without load application, 157
  with and without torque application, 158, 159
Subtalar vertical angle in 3D, 112
Subtle lisfranc joint instability, 267
Syndesmotic injuries, 135
  ATFD, 144, 146
  cadaver models, 148
  conventional radiographs, 135
  data source, 136
  experimental setup, 139–140
    dynamometric wire tensioner, 139
    ilizarov apparatus, 139
    inter-observer agreement calculation, 140
    radiolucent frame, 139
  ICC, 142
  imaging and measurements, 140
  intra-observer agreement, 145
  linear mixed effect models, 142
  plantigrade position, 144
  post-traumatic condition, 147
  TFO, 145, 146
  tukey adjustment, 142
  weight bearing, 143
Systematic literature review, 14

T

Talocalcaneal axis (TCA_x), 100, 110
Talo-calcaneal lateral impingement, 272
Talonavicular coverage angle, 215, 216
Talus–first metatarsal angle, 215, 216
3D biometrics, HFA, 67
  design, 78
  FAO mean values, 82
  FAO measurement, 71
  foot length, 69
  gaussian distribution, 71, 82
  HACT mean values, 82
  intra and inter-observer ICC, 81
  intra- and interobserver reliability, 83
  kolmogorov-smirnov analysis, 81
  limitations of, 84
  meary's view, 83
  measurements of FAO and HA, 81
  patient assessment, 78–79
    angular measurement, 79
    foot and ankle orthopaedic surgery, 78
  PedCAT, 68
  quality assurance testing, 84
  schematic representation, 69
  spearman's correlation coefficient, 81
  statistical analysis, 70, 81
  3D views, 69
  tibiocalcaneal angle, 78
  torque ankle lever arm system, 68, 78
3D rendering, 245, 272
3D-reformation of three MFBs, 271
3D Weight bearing Computed Tomography (3D WBCT), 67
Tibial axis/calcaneal tuberosity angle (TACTA), 201
Tibial axis/subtalar joint angle (TASJA), 201
Tibio-fibular clear space (TFCS), 174
Tibio-fibular overlap (TFO), 174
Torque Ankle Lever Arm System (TALAS) algorithm, 57, 273
Torque application, syndesmotic injuries
  data source, 168
  digitally reconstructed radiographs, 172–175
  experiments, 168–169
    digitally reconstructed radiographs, 169
    distal tibial plafond, 170
    dynamometric wire tensioner, 168
    ilizarov apparatus, 168
    intact ankles, 168
    inter-observer agreement, 171
    intraclass correlation coefficients, 171, 172
    linear mixed effect models, 171
    tibio-calcaneal ligament, 168
    two-way mixed effect model, 171
  measurements, 173
  weight bearing CT scans, 175
    AITFL transection, 177
    cadaver model, 178

Total ankle replacement (TAR), 266, 268
Transection of the ligaments, 154
2D measurements to 3D angles, 113

V
Verity®, 251, 253

W
WB bilateral Saltzman radiograph, 292
WBCT-based parasagittal, 269
WBCT clinical hindfoot alignment angle (WBCT CHAA), 202
WBCT Cone Beam imaging, 244
WBCT -scan and software screen, 28, 45
Weight bearing (WB), 181
  in axial plane, 190
  in coronal plane, 192
  in sagittal plane, 194
Weight bearing computed tomography (WBCT), 77, 87, 214, 249
  academic affiliates, 6
  clinical hindfoot alignment angle, 201
  foot and ankle weight bearing CT, 249–251
  future of, 251–253
    multidisciplinary approach, 253
    3D deformity, 253
    3D measurements, 251
  high radiation dose, 249
  hologram-like visualization, 7
  international WBCT society, 7
  international WBCT study group, 6
  knee weight bearing CT, 251
  machine footprint, 243
  peritalar subluxation, 249
Weight bearing radiographs, 278, 282